

Manuscrit HDR

Pour obtenir le diplôme d'

HABILITATION à DIRIGER des RECHERCHES de l'UNIVERSITE SAVOIE MONT BLANC

Spécialité : **Physique**

Arrêtés ministériels des 23 novembre 1988 et 13 février 1992

Présenté par **Michał WAŚ**

A bang and a flash in the hubbub and haze

GW170817 / GRB 170817A and noises limiting gravitational wave detectors

HDR soutenue publiquement le **23 novembre 2023**,
devant le jury composé de :

Mme Lucia DI CIACCIO

Professeur, USMB, Annecy, Président

Mme Edwige TOURNEFIER

Directeur de recherche, LAPP, Annecy, Membre

M Matteo BARSUGLIA

Directeur de recherche, APC, Paris, Rapporteur

M Frédéric PIRON

Directeur de recherche, LUPM, Montpellier, Rapporteur

M Hartmut GROTE

Professeur, Cardiff University, United Kingdom, Rapporteur

M Michel LINTZ

Chargé de recherche HDR, Artemis, Nice, Membre

Contents

Introduction	5
1 Gravitational wave detectors	8
1.1 Gravitational Waves	8
1.2 Detection principle	10
1.3 Ground based detector network	11
2 Advanced Virgo	13
2.1 Optical configuration	13
2.2 Thermal noise	16
2.3 Mirror suspension	17
2.4 Quantum noise	19
2.5 Residual gas pressure	21
3 Noise budget and technical noises	23
3.1 A noise budget model	23
3.2 A selection of technical noises	26
3.2.1 Output mode cleaner length noise	26
3.2.2 Relative amplitude modulation noise	28
3.2.3 Demodulation phase noise	29
3.2.4 Laser frequency noise	30
3.2.5 Back-scattered light noise	33
3.3 O2 noise budget	35
3.4 O3 noise budget	36
4 Back-scattered light	39
4.1 Detector calibration with scattered light	39
4.2 Scattered light measurement	41
5 Gamma-ray bursts and gravitational waves	46
5.1 GW170817 / GRB 170817A	47
5.2 Short GRB population	50
6 Conclusions	54

Bibliography	59
A Upper-limit on the Advanced Virgo output mode cleaner cavity length noise	63
B Requirement on relative amplitude modulation noise for O4	74
C Interferometer Sensing and Control for the Advanced Virgo Experiment in the O3 Scientific Run	86
D End benches scattered light modelling and subtraction in advanced Virgo	108
E A high angular resolution interferometric backscatter meter	121
F Search for Gravitational Waves Associated with Gamma-Ray Bursts during the First Advanced LIGO Observing Run and Implications for the Origin of GRB 150906B	126
G Gravitational Waves and Gamma-Rays from a Binary Neutron Star Merger: GW170817 and GRB 170817A	145

Introduction

Gravitational waves are one of the early prediction of Einstein's theory of General Relativity [1, 2]. These are space-time deformation that propagate at the speed of light in free space, and are generated by accelerated quadrupole and higher order moments of the energy-momentum tensor.

Whether gravitational waves are a real physical effect or an artifact of the theory was debated for several decades with a milestone consensus reached at the 1957 Chapel Hill conference [3]. Later on, the physical nature of gravitational waves was confirmed by the discovery of the binary pulsar PSR 1913+16 by Hulse and Taylor in 1974 [4]. Radio observation of this close binary system (7.75 hours orbital period) have shown a slow orbital decay that matched accurately the energy loss expected from gravitational wave emission as shown on figure 1.

In parallel an experimental effort was launched to detect gravitational waves directly on Earth. First with narrow band mechanical resonators, which have then be surpassed in sensitivity by increasingly large interferometric detectors. This five decade long effort eventually led to the detection in 2015 of GW150914 by the two 4km advanced LIGO instruments. This event resulted from the merger of two $\sim 30 M_{\odot}$ black holes at distance of 410^{+160}_{-180} Mpc [6]. It confirmed that General Relativity holds true also in the high curvature and high speed regime of $\frac{v}{c} \sim 0.5$ [7].

Two years later Advanced Virgo joined the international gravitational wave detector network and enabled another breakthrough with the observation of GW170817 / GRB 170817A. This first observation of gravitational waves from a binary neutron star merger, was followed by observations in almost the whole electro-magnetic spectrum. Including a prompt gamma-ray burst and a day scale optical kilo-nova, which were then followed by X-ray and radio-wave emission over several months from the decelerating relativistic jet.

This truly multi-messenger and multi-wavelength event led to a wide array of results that combine information from multiple sources. Such as confirming that short gamma-ray bursts are at least in part due to binary neutron star mergers, verifying with exquisite precision that gravitational wave propagate at the speed of light, or allowing a new independent measure of the universe expansion rate.

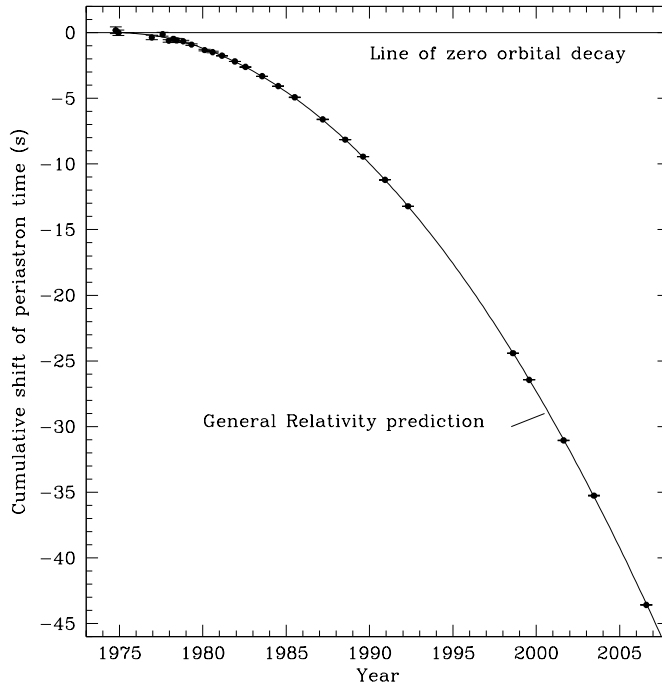


Figure 1: Plot of the cumulative shift of the periastron time of the binary pulsar from 1975 to 2007 [5]. The points are data with measurement error bars, the curve is the General Relativity prediction.

These two events left deep marks in the minds of the gravitational wave community, with each member recollecting the first hours after they have learned of the discovery. For me GW150914 was initially confusing, I was on the blind injection challenge committee in charge of adding artificial signals into the detector data without the rest of the collaboration being informed. The purpose was to make sure the collaboration performed a truly blind search, without knowing if any given signal was real or not. The day before the event, I had sent instructions to the detector sites on how to inject a binary black hole signal into the detector strain data, as that was the only astrophysically plausible signal given the detector sensitivity at the time. The real astrophysical event arrived before those instructions were executed rendering moot the whole blind injection activity.

In this manuscript I summarize the main lines of my research activity since rejoining the Virgo collaboration in 2013 and starting to work at the Laboratoire d'Annecy de Physique des Particules.

In chapter 1 I briefly introduce gravitational waves and the working principle of ground base gravitational wave detectors. Chapter 2 describes in

more details the configuration of Advanced Virgo in 2017-2020 and the main fundamental noises that result from that design. Chapter 3 concerns the technical noise of Advanced Virgo during that time period, which has been the core of my activity of leading the Virgo noise budget. I follow on with chapter 4 which is a more recent activity of scattered light and how it can be used as a tool instead of being just a noise source in optical measurements. Finally in chapter 5, I present my work on gravitational wave searches in association with gamma-ray bursts that has been reduced over time as I have transitioned to a larger involvement in detector construction and operation.

Chapter 1

Gravitational wave detectors

Einstein's theory of General Relativity describes gravitation not as a force but as a deformation of space-time. The presence of matter creates a deformation of space-time, and then object follows straight lines, geodesics, according to this deformed metric. For example Earth's rotation around the Sun is a straight line which turns out to be a circle in space due to space-time deformations caused by the Sun.

1.1 Gravitational Waves

At a given local coordinates point \mathbf{x} the metric tensor \underline{g} expresses the relation between infinitesimal changes in coordinates dx^μ and the corresponding infinitesimal change in length ds

$$ds^2(\mathbf{x}) = g_{\mu\nu}(\mathbf{x})dx^\mu dx^\nu. \quad (1.1)$$

A geodesics between the two coordinates is the shortest path achieved by integrating ds between the two coordinates in question. Special Relativity is a particular case where the metric is flat and coordinate independent. It is the *Minkowski metric* $\underline{\eta}$, whose expression in the usual time-space (ct, x, y, z) Cartesian coordinate system is

$$\eta_{\mu\nu} = \begin{pmatrix} -1 & 0 & 0 & 0 \\ 0 & 1 & 0 & 0 \\ 0 & 0 & 1 & 0 \\ 0 & 0 & 0 & 1 \end{pmatrix}. \quad (1.2)$$

This will be the starting point for understanding how an inteferometric gravitational wave detector works.

However, lets first derive how gravitational waves propagate. The starting point is the *Einstein's equation*

$$G_{\mu\nu} = \frac{8\pi G}{c^4} T_{\mu\nu}, \quad (1.3)$$

which relates \underline{G} , a second order differential operator of \underline{g} , with the the energy-momentum tensor field \underline{T} . Gravitational waves are derived as a solution of that equation assuming small perturbation \underline{h} around the Minkowski metric $\underline{\eta}$

$$g_{\mu\nu} = \eta_{\mu\nu} + h_{\mu\nu} \quad \text{with} \quad |h_{\mu\nu}| \ll 1. \quad (1.4)$$

Keeping only the first order terms in \underline{h} yields

$$\partial^\sigma \partial_\sigma h_{\mu\nu} - \partial_\lambda \partial_\mu h^\lambda{}_\nu - \partial_\lambda \partial_\nu h^\lambda{}_\mu + \partial_\mu \partial_\nu h^\lambda{}_\lambda = -\frac{16\pi G}{c^4} \left(T_{\mu\nu} - \frac{1}{2} \eta_{\mu\nu} T^\lambda{}_\lambda \right). \quad (1.5)$$

This equation can be simplified by an appropriate choice of coordinates, called *radiation coordinates*, which yields a simple wave equation

$$\partial^\sigma \partial_\sigma h_{\mu\nu} = -\frac{16\pi G}{c^4} \bar{T}_{\mu\nu}, \quad (1.6)$$

where the source term \bar{T} is the traceless part of \underline{T} .

We will not focus on how gravitational waves are produced by the source term, but only on their propagation once $\underline{T} = 0$. In that case the solutions are waves of the form

$$h_{\mu\nu}(x) = \text{Re} \left[H_{\mu\nu} \exp(ik_\lambda x^\lambda) \right]. \quad (1.7)$$

The coordinates can be then further specified to be in the so-called *transverse-traceless* gauge, and the wave solution must then obey the following four relations

$$k^\mu k_\mu = 0, \quad (1.8a)$$

$$k^\mu H_{\mu\nu} = 0, \quad (1.8b)$$

$$H^\mu{}_\mu = 0, \quad (1.8c)$$

$$H_{0\mu} = 0. \quad (1.8d)$$

The first simply states that gravitational waves are propagating at the speed of light, the second is the condition defining the radiation coordinates, the third is the traceless condition and the fourth the transverse condition.

In particular, if we choose a plane wave propagating along z -axis with an angular frequency ω the transverse-traceless solutions are of the form

$$h_{\mu\nu}^{TT} = \text{Re} \left\{ \begin{pmatrix} 0 & 0 & 0 & 0 \\ 0 & H_+ & H_\times & 0 \\ 0 & H_\times & -H_+ & 0 \\ 0 & 0 & 0 & 0 \end{pmatrix} \exp[i\omega(z/c - t)] \right\}. \quad (1.9)$$

This shows that gravitational waves have two independent polarizations, usually called $+$ and \times , which have effects in the transverse plane compared to the direction of propagation.

1.2 Detection principle

Interferometric gravitational wave detectors use laser light to measure the distance between two coordinate points. Light in General Relativity always travels along null geodesics, i.e. $ds^2 = 0$. In addition, the radiation coordinate choice results in objects such as mirrors remaining at fixed coordinates, while the speed of light propagation in terms of coordinates varies due to the metric.

Combining equations (1.9) and (1.1) we obtain the propagation of light in the interferometer along the x -direction

$$0 = g_{\mu\nu}^{TT} dx^\mu dx^\nu = -c^2 dt^2 + (1 + h_+(t)) dx^2. \quad (1.10)$$

Hence the propagation time τ_x between two coordinates distant by L_0 is equal to

$$\tau_x = \frac{1}{c} \int_0^{L_0} \sqrt{1 + h_+\left(t + \frac{x}{c}\right)} dx. \quad (1.11)$$

In the particular case of ground based interferometers, the current 3 – 4 km scale is much smaller than the gravitational wavelength they try to detect. This translates into a propagation time $\frac{x}{c} \leq \frac{L_0}{c} \sim 10 \mu\text{s}$ that is much smaller than the gravitational wave period of $100 \mu\text{s} - 100 \text{ms}$, hence we can approximate $h_+(t + \frac{x}{c}) \simeq h_+(t)$ and obtain

$$\tau_x \simeq \frac{1 + \frac{1}{2}h_+(t)}{c} L_0. \quad (1.12)$$

Consequently for a laser wavelength λ a round trip between two mirrors yields a phase difference

$$\varphi_x = 4\pi \frac{c}{\lambda} \tau_x = 4\pi \frac{L_0}{\lambda} \left[1 + \frac{1}{2}h_+(t) \right]. \quad (1.13)$$

Hence, in principle one could use a single arm interferometer to detect gravitational waves. However in practice the laser wavelength is not sufficiently stable, and would mask any gravitational wave effect, as fractional changes in wavelength $\frac{\delta\lambda}{\lambda}$ would need to be much smaller than the gravitational wave strain.

To avoid this issue, a second arm, which is usually orthogonal, is used in interferometric gravitational wave detectors. The same derivation for light propagating in the y -direction yields a phase difference

$$\varphi_y = 4\pi \frac{L_0}{\lambda} \left[1 - \frac{1}{2}h_+(t) \right], \quad (1.14)$$

and the difference in light phase between the two arms is

$$\Delta\varphi = \varphi_x - \varphi_y = 4\pi \frac{L_0}{\lambda} h_+(t), \quad (1.15)$$

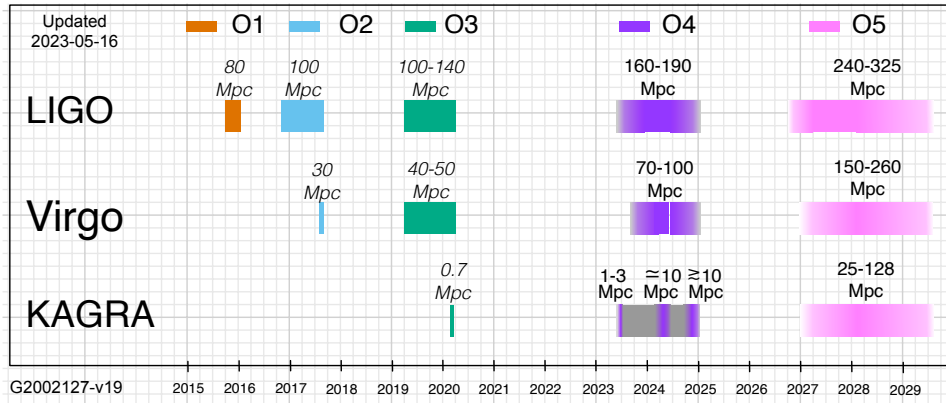


Figure 1.1: Past and future observing runs of the global network of ground based gravitational wave detectors, along with the achieved or planned average sensitive range to binary neutron mergers [8].

which in theory removes any issue with wavelength stability as all lasers satisfy $\frac{\delta\lambda}{\lambda} \ll 1$. The phase induced by the gravitational wave in two orthogonal arms has opposite sign, hence the phase difference between two arms removes at first order the laser wavelength (frequency) noise while adding the gravitational wave signal from each arm.

A simple optical configuration that implements the phase difference measurement of light propagating along two orthogonal arms is the Michelson interferometer. In fact, it forms the basis of all interferometric gravitational wave detectors constructed to date. Although alternative configuration such as the Sagnac interferometer are also being actively studied at a prototype level.

1.3 Ground based detector network

Over several decades a global network of several km scale detectors based on this principle was progressively built, commissioned and operated on synchronized observing runs. Two 4 km advanced LIGO detectors in the USA in Livingston and Hanford, and a 3 km Advanced Virgo detector in Cascina, Italy. These three detectors reuse the infrastructure of the initial LIGO and Virgo detectors that were operated in the 2003-2011 period. The 3 km KAGRA detector is commissioned in a new underground facility in the Kamioka mine in Japan. And finally the LIGO-India project will operate an advanced LIGO detector in a new infrastructure that is presently under construction in India.

Figure 1.1 summarizes the observations this network has performed so far with the O1, O2 and O3 observing runs, and the planned O4 and O5 observing runs. The synchronous operation is necessary, as it allows sky local-

ization of the gravitational wave sources and enabling their electro-magnetic followup observations. The localization is mainly performed through triangulation of the time of arrival at each detector.

In addition, having at least two non aligned detectors allows to measure independently the two gravitational wave polarizations, while three or more detectors are required to constrain any extra polarization not predicted by General Relativity.

The large gaps visible in this timeline are necessary to improve the detectors sensitivity by hardware upgrades and commissioning. The loss of observing time is more than compensated by the increase in sensitive range, which increases the observable volume of universe as the cube of the range, and increase the detection rate with the same proportion. The sensitivity improvement also enables to observe in greater detail any nearby events that may occur.

Chapter 2

Advanced Virgo

In this chapter we will make an overview of a ground based interferometric gravitational wave detectors based on the example of Advanced Virgo. Advanced Virgo is a gravitational wave detector build in Cascina, Italy, which has two 3 km long arms and uses a laser with 1064 nm wavelength.

2.1 Optical configuration

We have seen in section 1.2 that in principle a Michelson interferometer is well suited for detecting gravitational waves. In practice Advanced Virgo uses a power recycled Fabry-Perot Michelson interferometer configuration that is shown on figure 2.1. This more complex optical configuration is driven by a goal of reducing shot noise, i.e. noise from the quantum nature of light.

The power at the output of a Michelson interferometer with a phase difference $\varphi = \varphi_0 + \Delta\varphi$ is

$$P_{\text{out}} = P_{\text{in}} \frac{|1 - (1 - \epsilon_{\text{cd}})e^{i(\varphi_0 + \Delta\varphi)}|^2}{4} \quad (2.1)$$

$$\simeq P_{\text{in}} \left[\frac{\epsilon_{\text{cd}}^2}{4} + (1 - \epsilon_{\text{cd}}) \sin^2\left(\frac{\varphi_0}{2}\right) + \frac{1}{2} \sin(\varphi_0) \Delta\varphi \right], \quad (2.2)$$

where φ_0 is a chosen working point of the Michelson interferometer called *dark fringe offset*, $\Delta\varphi$ is a small perturbation due for instance to a gravitational wave and ϵ_{cd} is the interferometer contrast defect.

The number N of photons detected on a photo-detector in a given time τ is Poisson distributed with a standard deviation $\sigma_N = \sqrt{\langle N \rangle}$. Hence the detected power has fluctuation

$$\frac{\sigma_{P_{\text{out}}}}{P_{\text{out}}} = \frac{\sigma_N}{N} = \sqrt{\frac{h_{\text{p}} c}{\tau \lambda P_{\text{out}}}}. \quad (2.3)$$

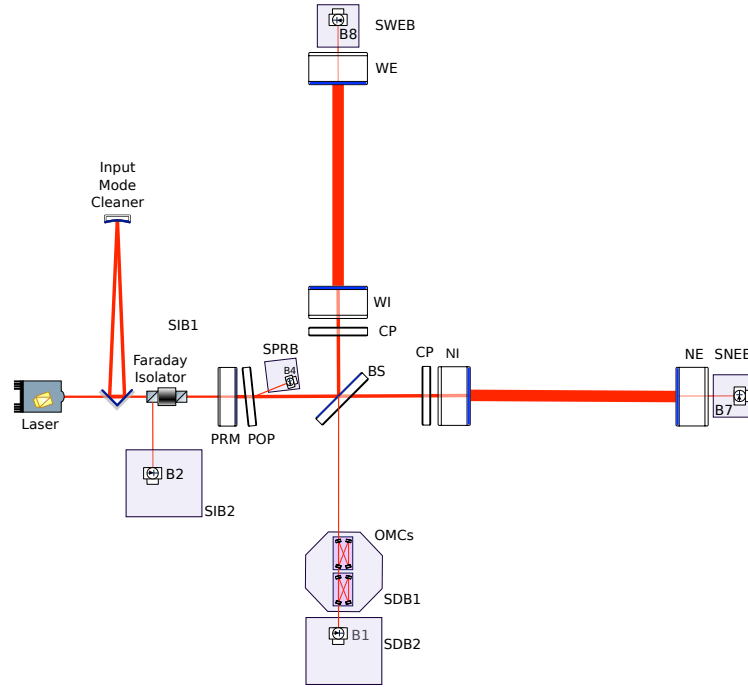


Figure 2.1: Optical layout of Advanced Virgo in 2017-2020, adapted from [9].

This translates into an optical phase noise

$$\sigma_{\Delta\varphi} = \frac{\sigma_{P_{\text{out}}}}{P_{\text{out}}} = \sqrt{\frac{h_P c}{\tau \lambda P_{\text{in}}}} \sqrt{\frac{4(1 - \epsilon_{\text{cd}}) \sin^2(\frac{\varphi_0}{2}) + \epsilon_{\text{cd}}^2}{\sin^2 \varphi_0}}, \quad (2.4)$$

where the second square root factor has a broad minimum equal to one for $\epsilon_{\text{cd}} \ll \varphi_0 \ll 1$. In other words, the best phase sensitivity of a Michelson interferometer is achieved close to the dark fringe, but with the output power due to the dark fringe offset much larger than the contrast defect contribution.

Reducing the contrast defect light is the main goal of the two output mode cleaner (OMC) cavities shown on figure 2.1. Their purpose is to transmit the TEM00 gaussian mode of the carrier light and to reject higher order modes of carrier light and all modes of radio-frequency sidebands.

During O3a for advanced Virgo the output power was roughly 200 mW for 700 W impinging on the beam splitter. That power is roughly equally split between higher order modes and RF sidebands [10], with only 2.8 mW due to the dark fringe offset. However after OMC filtering only 120 uW of light due to contrast defect remained [11]. An improvement by a factor ~ 1700 from $\epsilon_{\text{cd}}^2 = 1.1 \times 10^{-3}$ to $\epsilon_{\text{cd}}^2 = 6.9 \times 10^{-7}$.

The dark fringe configuration of the Michelson interferometer reflects most of the light back to the laser. The purpose of the power recycling (PR) mirror is to reuse that light by forming an optical cavity and increase the effective input power. The PR cavity of Advanced Virgo has an optical gain of $G_{\text{PR}} \sim 40$ which allowed in O3a to have 700 W impinging on the beam splitter with 18 W of input laser power, and consequently reduce the shot noise by a factor 6 as given by equation (2.4).

The last major element of the Advanced Virgo optical configuration are the Fabry-Perot cavity arms, whose purpose is to amplify the optical phase change due to a gravitational wave. One simple aspect is their large length of 3 km as the phase signal is proportional to arm length as shown in equation (1.15). The other is the use of Fabry-Perot cavities that results in many effective round-trips inside the arms and an accumulation of the phase change with a gain

$$G_{\text{arm}} = \frac{1 + r_{\text{IM}}}{1 - r_{\text{IM}}}, \quad (2.5)$$

where $r_{\text{IM}} = 0.993$ is the field reflectivity of the input mirrors (IM) of the arm cavities. For high finesse cavities this gain happens to also be the gain in power stored in the cavity.

However the arm cavities also act as a low-pass filter due to storage in the cavity, attenuating the phase shift for high frequency gravitational waves. The arms act as a simple pole with frequency

$$f_{\text{arm}} = \frac{1 - r_{\text{IM}}}{r_{\text{IM}}} \frac{c}{4\pi L_0} \simeq 55 \text{ Hz}. \quad (2.6)$$

Combining this with equations (1.15) and (2.4) we obtain a shot noise amplitude spectral density (ASD)

$$A_{\text{shot}}(f) = \frac{\lambda}{4\pi L_0} \frac{1}{G_{\text{arm}}} \sqrt{\frac{h_{\text{P}} c}{\lambda G_{\text{PR}} P_{\text{in}}}} \sqrt{1 + \left(\frac{f}{f_{\text{arm}}}\right)^2} \quad (2.7)$$

$$\simeq 2.3 \times 10^{-24} \frac{1}{\sqrt{\text{Hz}}} \frac{288}{G_{\text{arm}}} \sqrt{\frac{40}{G_{\text{PR}}}} \sqrt{\frac{18 \text{ W}}{P_{\text{in}}}} \sqrt{1 + \left(\frac{f}{f_{\text{arm}}}\right)^2}. \quad (2.8)$$

The product $G_{\text{arm}} f_{\text{arm}}$ is roughly independent of r_{IM} for a cavity, hence increasing the optical gain of the arm cavities does not change the shot noise at high frequency as the increased gain is compensated by the lower bandwidth of the arm response.

In this discussion we have neglected so far losses. The expected losses of the Advanced Virgo mirrors of 35 ppm are small compared to the transmission of the input mirrors ($T_{\text{NI}} = 1.37 \times 10^{-2}$) hence they have no significant impact on G_{arm} . More surprisingly they have an impact on the PR cavity gain, as the losses are amplified by the arm cavity gain G_{arm} before being compared to the PR mirror transmission ($T_{\text{PR}} = 4.84 \times 10^{-2}$). As a result

the lossless PR cavity gain of 80 is reduced to 40 by the arm cavity losses of 70 ppm per round trip. In practice due to point defects on the cavity mirrors that have excess absorption, the losses increased once the interferometer is operated to 90 ppm, leading to G_{PR} reduction to around 35 during O3a.

This configuration has changed for Advanced Virgo for the O4 observing run with the addition of a signal recycling mirror.

2.2 Thermal noise

Thermal noise is a fundamental limitation of interferometric gravitational wave detectors, as the thermal fluctuation cause motion of the mirror surface. For a system in thermal equilibrium that has a linear response $x(\omega)$ to external perturbation $F(\omega)$

$$\chi(\omega)x(\omega) = F(\omega), \quad (2.9)$$

the fluctuation-dissipation theorem [12] states that the effective thermal force is due to the friction part of the linear response $\text{Im}(\chi(\omega))$ through

$$F_{\text{therm}}^2(\omega) = \frac{4k_B T}{\omega} \text{Im}(\chi(\omega)). \quad (2.10)$$

The mirrors are placed in vacuum, and their dominant mechanical losses are due to internal friction. For an oscillator of mass m with a single degree of freedom this is well modeled [13] through a frequency independent ‘‘loss angle’’ ϕ that is equal to the inverse of the quality factor Q of the oscillator

$$\chi(\omega) = m \left(\omega_0^2 - \omega^2 + i \frac{\omega_0^2}{Q} \right). \quad (2.11)$$

This yield a thermal displacement noise

$$x_{\text{therm}}(\omega) = \frac{\omega_0^2}{\sqrt{(\omega_0^2 - \omega^2)^2 + \frac{\omega_0^4}{Q^2}}} \sqrt{\frac{\omega_0}{\omega}} \sqrt{\frac{4k_B T}{mQ\omega_0^3}} \quad (2.12)$$

that is concentrated around the system resonant frequency ω_0 , with a $\propto \frac{1}{\omega^{0.5}}$ dependence below the resonance and $\propto \frac{1}{\omega^{2.5}}$ dependence above the resonance.

This relation shows three handles for reducing thermal noise: increase the quality factor of the system, increase the mirror mass and decrease the temperature.

We have considered above the mirror bulk thermal noise. But there are in fact other more dominant contribution to thermal noise from the mirror suspension and from the thin di-electric coating layers that render the mirrors reflective.

To reduce losses the 42 kg mirrors of Advanced Virgo are suspended on fused silica fibers, the same material as the mirror itself, using bonded fused

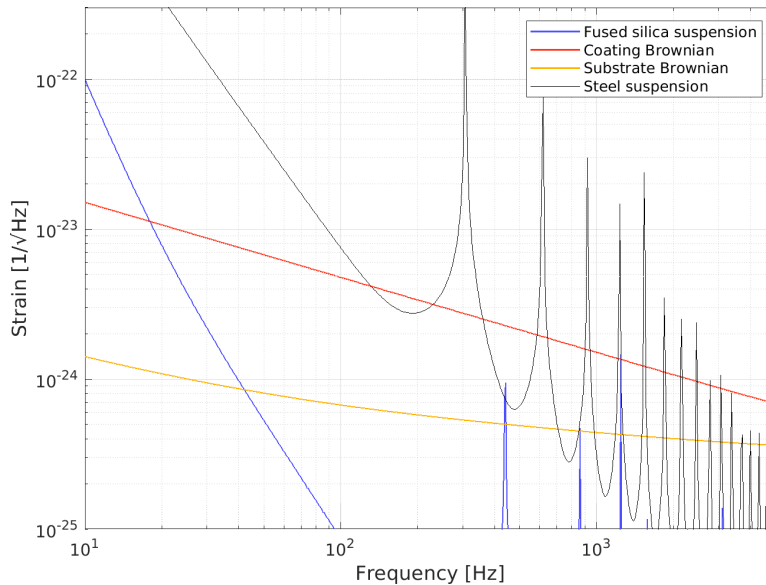


Figure 2.2: Suspension, coating and mirror contribution to the thermal noise of Advanced Virgo are shown. The estimated noise of the steel suspension used in O2 and the fused silica suspension used during O3 are shown.

silica ears and anchors. This achieved quality factors $Q \sim 10^7$, a considerable improvement over the $Q \sim 10^5$ steel wires that were used for initial Virgo and for the O2 observing run of Advanced Virgo.

The mirror coatings have a comparatively large loss angle $\phi \sim$ a few $\times 10^{-4}$, and contribute significantly to total thermal noise. This is shown on figure 2.2 which highlights that once the fused silica fiber suspensions were implemented the coating thermal noise become by far the dominant source of thermal noise at almost all frequencies.

2.3 Mirror suspension

Mirrors need to be isolated from the large ground motion. There are two aspects to take into account: the relatively small ground motion in the sensitive band of the detector that has a typical spectrum of

$$x(f) \sim 10^{-6} \left(\frac{1 \text{ Hz}}{f} \right)^2 \text{ m/Hz}^{1/2}, \quad \text{for } f > 10 \text{ Hz}, \quad (2.13)$$

and the large amplitude motion below a few Hz that is much larger than the laser wavelength.

In Virgo the seismic attenuation is achieved using a 7.3 m long isolation chain shown on figure 2.3 of mostly passive isolators that use a pendulum for horizontal isolation and metal blade spring for vertical isolation. The top

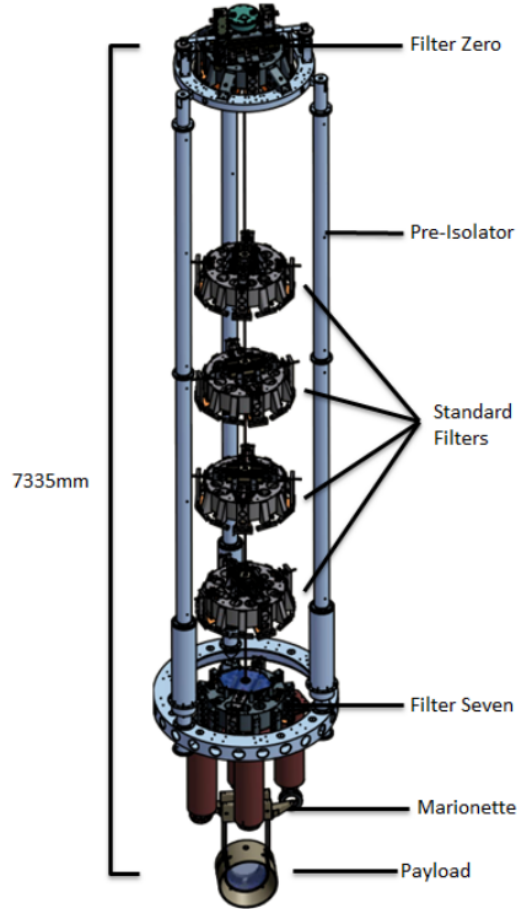


Figure 2.3: Virgo seismic attenuation chain composed of an inverse pendulum pre-isolator, a chain of isolators, and a steering marionette and the payload mirror.

(filter 0) and bottom (filter 7) are actively controlled to maintain a global relative positioning between mirrors and to damp mechanical resonances.

The latter is critical as mechanical resonances amplifies the motion in proportion to the quality factor

$$T(\omega) = \left| \frac{x(\omega)}{x_g(\omega)} \right| = \frac{\omega_0^2}{\sqrt{(\omega_0^2 - \omega^2)^2 + \frac{\omega_0^4}{Q^2}}} \quad (2.14a)$$

$$= 1 \quad \text{for } \omega \ll \omega_0 \quad (2.14b)$$

$$= Q \quad \text{for } \omega = \omega_0 \quad (2.14c)$$

$$\approx \frac{\omega_0^2}{\omega^2} \quad \text{for } \omega \gg \omega_0. \quad (2.14d)$$

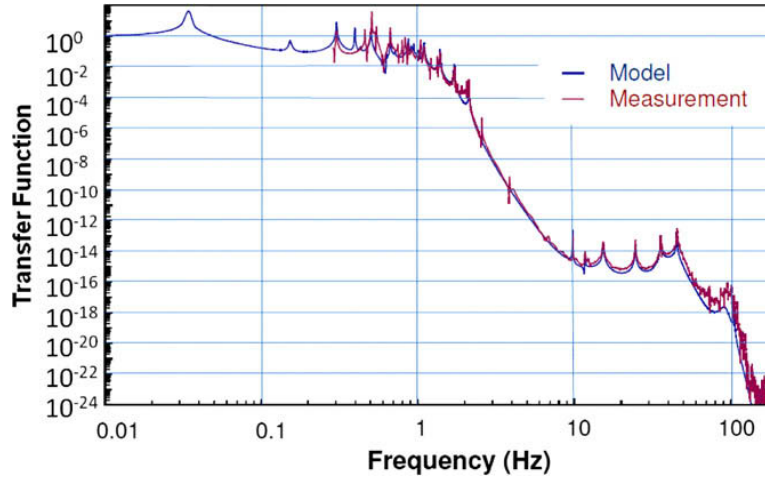


Figure 2.4: Total transfer function of the Virgo seismic attenuation between ground motion and motion of the suspended mirrors [14].

Hence in contrast to the mirror itself and the marionette which require very high quality factors to reduce thermal noise, the upper stages of the suspension need large intrinsic losses and active damping to prevent amplification of motion at low frequency.

The resulting ground motion isolation is shown on figure 2.3 with at least 12 orders of magnitude of ground motion reduction above 10 Hz. As a result the mirror motion due to ground motion is negligible compared to thermal noise above 10 Hz.

2.4 Quantum noise

We have seen in section 2.1 that the quantum shot noise of light limits the ability to measure the position of Advanced Virgo mirrors. A complementary aspect of quantum noise is that it can back act on the system. In our case quantum laser power fluctuations result in a fluctuating radiation pressure force that pushes on the mirrors.

It can be shown that the dominant source of quantum noise is due vacuum fluctuations entering through the anti-symmetric port of the interferometer and interfering with the light circulating in the arms [15]. This results in a readout shot noise contribution and in a radiation pressure contribution. The radiation pressure contribution is due to the shot noise impacting the 4

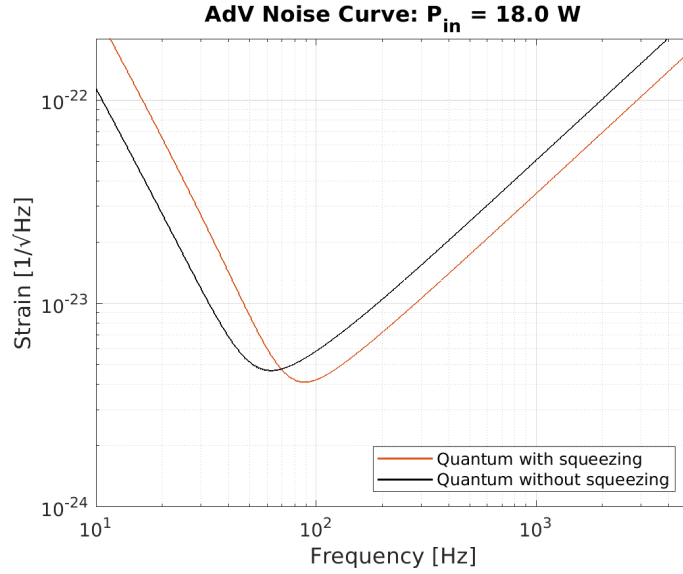


Figure 2.5: Quantum noise due to shot noise and radiation pressure noise during O3 for Advanced Virgo, both the case with squeezing enabled and disabled are shown.

mirrors of the arm cavities

$$A_{\text{rad}}(f) = \frac{4\sqrt{G_{\text{arm}}}}{L_0} \sqrt{\frac{P_{\text{arm}} h_P}{c\lambda}} \frac{2}{\chi(2\pi f)} \quad (2.15)$$

$$\simeq 1.2 \times 10^{-22} \frac{1}{\sqrt{\text{Hz}}} \frac{42 \text{ kg}}{M_{\text{mirror}}} \sqrt{\frac{G_{\text{arm}}}{288}} \sqrt{\frac{P_{\text{arm}}}{90 \text{ kW}}} \left(\frac{10 \text{ Hz}}{f}\right)^2, \quad (2.16)$$

and shows that increasing the mirror mass can reduce the radiation pressure noise, while increasing the power in the arms or the optical gain of the arms increases the radiation pressure noise.

The quantum noise level can be manipulated by changing the vacuum fluctuations entering the interferometer through the anti-symmetric port using a squeezed state of light. Due to the Heisenberg principle if one quadrature of the quantum noise is decreased the other quadrature is increased by the same factor.

The result for the Advanced Virgo O3 configuration is shown on figure 2.5. It shows that squeezing reduces shot noise by 3 dB while radiation pressure noise is increased by 7 dB. The difference is due to optical losses that reduce the amount of squeezing. Radiation pressure is only affected by optical losses on the path from the squeezed vacuum source to the interferometer and the losses inside the interferometer estimated to be 15% in total. While shot noise is in addition also affected by losses from the interferometer to the the DC read-out photodiodes that are estimated to be 25%.

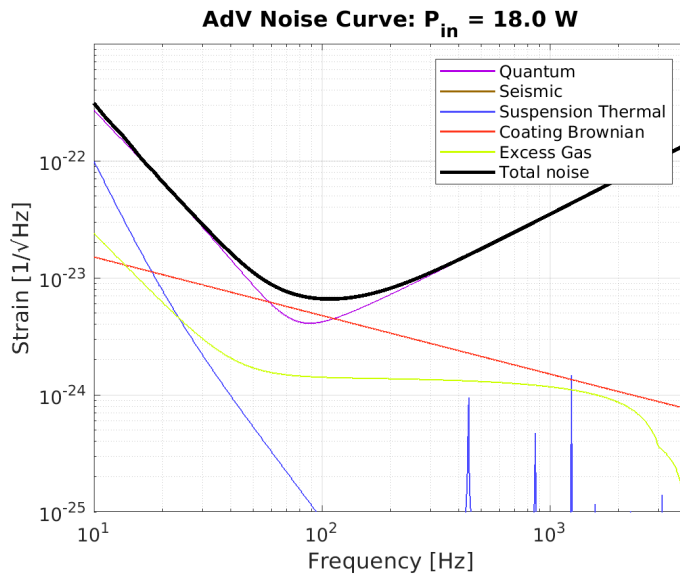


Figure 2.6: Fundamental noises of Advanced Virgo during O3 as modeled in AdVGWINC [16].

The squeezed vacuum state can be changed in a frequency dependent way using the reflection from a detuned auxiliary optical cavity so that the squeezing reduces the radiation pressure quadrature below the cavity detuning frequency and reduces the shot noise above the cavity detuning frequency. A 300 m long cavity has been commissioned at Advanced Virgo in preparation for the O4 observing run to be able to perform this frequency dependent change in the squeezing quadrature.

2.5 Residual gas pressure

Advanced Virgo is operated under vacuum with a residual gas pressure lower than $\sim 3 \times 10^{-9}$ mbar in the arms and $\sim 2 \times 10^{-8}$ mbar in the vacuum chambers hosting the arm cavity mirrors. This residual gas pressure has two effects:

- The laser beam in the arms interacts with gas molecules which creates optical index fluctuations, this effect is higher for larger molecules that tend to have larger polarisability.
- The gas molecules bouncing of the mirrors adds a random force pushing on the mirror.

The sum of these two noises arising from residual gas pressure is shown on figure 2.6, along with the 3 other noise sources discussed above: quantum

noise (radiation pressure and shot noise), thermal noise (bulk substrate and coating) and seismic noise. Note that the last is expected to be sufficiently reduced by the seismic isolation that it is several orders of magnitude below the axis on the figure.

These noises are often called “fundamental” as tackling them is the main cost of building gravitational wave detectors after basic infrastructure, and require a large R&D and engineering process to improve on. They are in many ways unavoidable regardless of the precise technologies used for building the detector.

In the next chapter we will move to the much wider and often obscure realm of “technical” noises, which are simply all of the other noises not listed so far.

Chapter 3

Noise budget and technical noises

The *noise budget* is the collection of different noise sources that are attempting to explain the noise amplitude spectrum density measured for an instrument, for example a gravitational wave detector. It is composed of the fundamental noises discussed in the previous chapter, which are usually well known in advance, and an ever incomplete list of technical noises that are often identified as the commissioning of a gravitational wave detector progresses.

3.1 A noise budget model

There are two a priori frequency dependent parts in estimating how a given noise source affects the detector sensitivity:

- The level of underlying noise in its natural units (electronic noise in volts, ground motion in meters, etc...).
- The transfer function from the noise source to the detector sensitivity. That transfer function may be non linear in some cases.

For each of these two components there are generally three approaches to estimate them

- a fully descriptive model,
- a model with some free parameters that are fitted to measurements,
- a direct measurement.

In practice depending on the noise in question different combinations of these three approaches are used for each of the two components in building a noise projection.

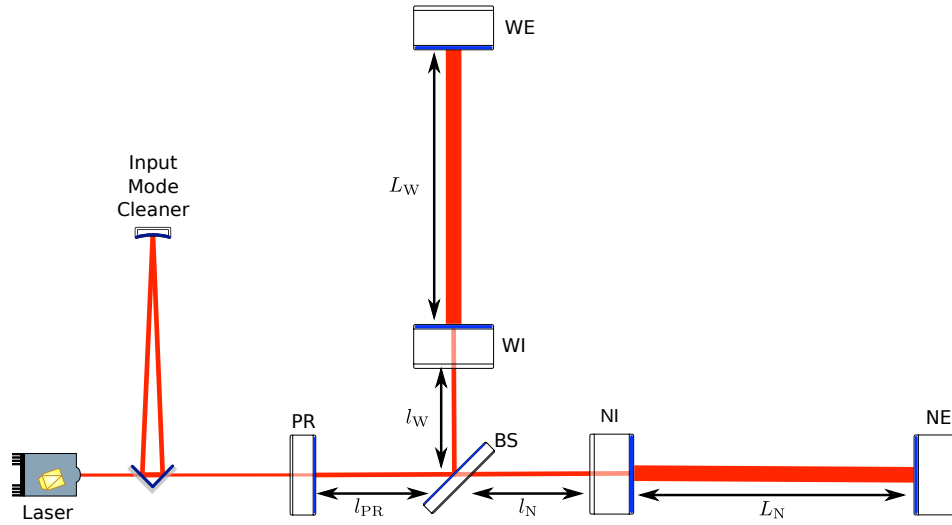


Figure 3.1: Longitudinal length definitions.

Models usually provide a better understanding of the underlying physics, and hence how to reduce the noise source or its coupling. For this reason to produce a noise budget of Advanced Virgo a complete model of the interferometer was built. It is a very simplified model that includes only the four main longitudinal degrees of freedom shown on figure 3.1.

DARM Differential arm length = $L_N - L_W$. This is the difference in length between the two arm cavities.

CARM Common arm length = $\frac{L_N + L_W}{2}$. This is the average length of the two arm cavities. In practice it is the same degree of freedom as the laser frequency, as the laser is locked onto CARM so that the CARM length is a multiple of the wavelength.

MICH Michelson = $l_N - l_W$. This is the difference in distance between the beam splitter and each arm cavity input mirror

PRCL Power recycling cavity length = $l_{PR} + \frac{l_N + l_W}{2}$. This is distance from the PR mirror to the average distance of the arm cavity input mirrors.

I have built the Advanced Virgo model in Matlab Simulink using the `SimulinNB` package [17]. There are three main parts: suspensions, optical response, and control filters. We will describe these briefly below.

For the suspension, only the two last stages are represented as a double pendulum system for the mirror itself and the marionette above it. The force exercised by the coils current on the magnets was measured and the response of the analog driving electronics was calculated. This gives the motion of a

mirror in meters as a function of the driving voltage in Volts from the digital to analog converters.

The optical response of the interferometer is simulated in `Optickle` [18]. It provides the response in Watts of power on various photodiodes as a function mirror displacement in meters. It only includes the main TEM00 mode of the carrier light and the RF sidebands, and it does include radiation pressure effects and computes quantum noise level including the effect of frequency independent squeezing.

Which error signals are used for controlling the interferometer is based on discussion with the commissioning team, and the control filters used were measured from the transfer function between the photodiodes signals and the correction signals of the digital to analog converters.

This model was built at the same time as the detector in 2016-2017, starting from modeling the lock of a single Fabry-perot cavity arm. It provided the only calibration of signals into GW strain during the first month of commissioning of the fully locked interferometer. And despite its largely a priori nature it managed to match within 10% the precise calibration that was performed later on with dedicated measurements. The model was also compared to measurements of the open loop gains transfer functions of each modeled degree of freedom.

Building such a model is a significant time investment but it provides a simple way of including many longitudinal noise source directly in their natural units:

- Thermal noise of all mirrors as a displacement noise.
- Noise of the coil driving electronics in Volts.
- Noise of the photodiode measured in dark conditions in Watts.
- Demodulation phase noise which bilinearly mixes the two quadratures of RF signals.
- Quantization noise due to limited precision of digital communication between different components.
- Quantum noise at the level of each photodiode.

It provides a noise budget not only from the main DARM degree of freedom of interest for gravitational wave detection, but also the three other modeled degrees of freedom. And it nicely incorporates the expected cross-couplings between the different degrees of freedom.

Other noise sources have been added independently of this model as additional noise contribution to DARM, which neglects their possible contributions to other degrees of freedom. In section 3.2 I discuss a selection of technical noise more in detail, then in section 3.3 and section 3.4 the Advanced Virgo budget at the end of respectively O2 and O3 is described.

The goal of this noise budget was to provide guidance to commissioning by highlighting which are the largest noises to tackle to improve performance, and following the commissioning evolution on a daily basis. This was done at the expense of not striving for high accuracy of each prediction, nor on the completeness of all the possible noises.

These further goals are beyond the possibility of any single person. During O3 the Virgo collaboration invested into a technical noise review process that involved ~ 30 different types of noises, and as many documents describing and evaluating them individually. The review was completed after the O3 run finished. For O4 this process is expanded to ~ 100 noises that could be identified, and about as many people to evaluate and document them precisely.

3.2 A selection of technical noises

In this section I will describe several technical noises that I have studied in more detail, and that led to publications or technical reports that are in the annex of this manuscript.

3.2.1 Output mode cleaner length noise

As we have seen in section 2.1 the role of the OMC is to reject higher order modes and radio-frequency sidebands to improve the interferometer contrast. However the OMC adds its technical noises to the interferometer in the process. The main mechanism is that OMC transmission is maximal when the cavity round trip length is a multiple of the wavelength and the cavity mode is aligned with the laser beam. This leads to a quadratic coupling of the OMC length and alignment fluctuations. We will focus here on the length case.

The Advanced Virgo OMC is an evolution of the Virgo OMC and uses a single piece of fused silica with four coated faces to form a bow-tie optical cavity. A concern is that the fused silica refractive index has thermal fluctuation which yield relatively large optical length fluctuations of

$$l_{\text{thermo-refractif}} \sim 10^{-15} \frac{10 \text{ Hz}}{f} \text{ m}/\sqrt{\text{Hz}} \quad (3.1)$$

above 10 Hz. However, the RMS of the OMC length is dominated by fluctuations below 1 Hz in practice mostly due to the laser frequency wavelength following the large common motion of the arm cavity arms. Hence the quadratic coupling is mostly bilinear in nature, with the thermo-refractive noise coupling proportionally to the OMC lock accuracy Δl_{rms}

$$\delta h \propto \frac{F_{\text{OMC}}^2 \Delta l_{\text{rms}} \delta l_{\text{th}}}{\lambda^2}, \quad (3.2)$$

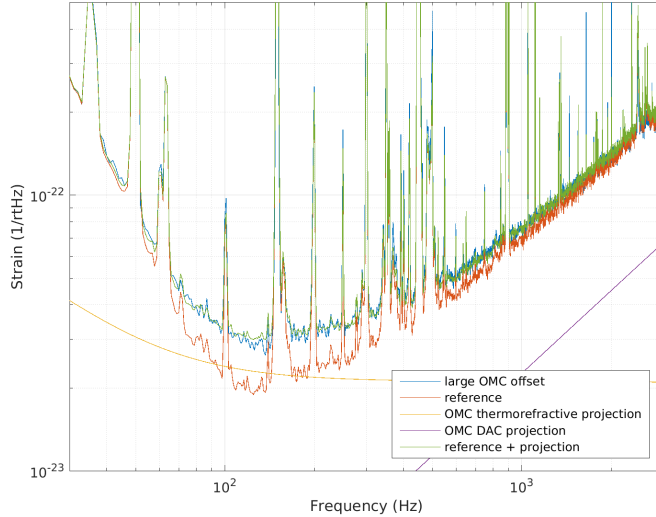


Figure 3.2: Projection of OMC length noise with the OMC lock intentionally mistuned by 4.5×10^{-10} m.

where F_{OMC} is the OMC cavity finesse.

I have experimentally studied the level of thermo-refractive noise and the lock accuracy before the OMC was installed in Advanced Virgo [19]. This had shown that previous estimates of the thermo-refractive noise were mistaken by a factor 2, and also establish that sufficient lock accuracy of $\Delta l_{\text{rms}} = 3.5 \times 10^{-13}$ m can be achieved to yield a thermo-refractive noise coupling to the advanced Virgo sensitivity almost 2 orders of magnitude below the sum of other noises. This paper is reproduced in appendix A.

This has been later on confirmed at the Virgo site by adding an intentional offset into the OMC lock of 4.5×10^{-10} m to render the OMC length noise dominant in the interferometer noise at ~ 100 Hz as shown on figure 3.2. The noise elevation followed the theoretical prediction of thermo-refractive noise of the OMC. In addition it has shown a small contribution of the digital to analog converter noise that drive the PZT that controls the OMC length. No additional length noise was observed, in particular no mechanical resonances.

The lack of spurious mechanical resonances, the low level of DAC noise and the robustness against transmission degradation due to optics contamination are the main advantages of a in glass resonance OMC such as the Advanced Virgo. The additional thermo-refractive noise is at a manageable level.

The uncertainty during the design stage on the thermo-refractive noise and the achievable lock precision led to an Advanced Virgo design with two

OMC cavities in series with a relatively low finesse of ~ 125 . The above experience allowed me to redesign the OMC for O4, and replace it with a single cavity of identical geometry but with a finesse ~ 1000 and cavity pole at ~ 800 kHz. This solution increases the thermo-refractive noise coupling, but allows to remove optical losses due to mis-match between the optical modes of the two cavities (mis-alignment, mode-size mismatch and polarization mismatch), and increases the filtering of radio-frequency sidebands, which were a dominating source of noise in Advanced Virgo during O3 as will be described in section 3.2.2.

Note however that this O4 design reaches the limit of how low a pole cavity frequency can be achieved with this technology. The measured OMC losses of the new design are $\sim 2\%$, half of which are due to Rayleigh scattering and absorption inside fused silica. Further reduction in optical losses or cavity pole frequency will require an open cavity solution with the beam resonating in vacuum. At other wavelengths, such as at 1550 nm where the fused silica optical losses are lower, an in-glass resonating cavity such as described above may still be viable, for instance for the proposed Einstein Telescope low frequency interferometers.

3.2.2 Relative amplitude modulation noise

The laser light is modulated at several RF frequency in order to generate optical beat signals between these sidebands and the carrier light that carry information on the different length degrees of freedom of the interferometer (MICH, PRCL, CARM). However this modulation is not perfectly constant, and the modulation amplitude fluctuates in time.

During O3 the dominant coupling of this relative amplitude modulation (RAM) noise was due to the 56 MHz sideband leaking through the OMC. The OMC transmitted power of the 56 MHz sideband was about 20 μ W for 60 mW of sideband power at the OMC input, so an OMC attenuation of the order of 3×10^{-4} . Due to RAM noise this power has relatively large fluctuations that are comparable to the shot noise of the DC read-out photodiodes.

Fortunately this fluctuations were also dominating in the light reflected from the OMC. Which allowed to measure them accurately and subtract from the interferometer sensitivity during the gravitational wave strain reconstruction procedure.

Figure 3.3 shows the projection of the RAM noise onto the sensitivity curve performed in two different ways. One approach is purely empirical, measuring the noise on the light reflected from the OMC and measuring the transfer function between that noise and the sensitivity curve. The other approach follows the noise from it source as follows. The RAM noise has been measured in the laboratory on a spare RF modulation generator and amplifier. Then this can be converted into light power fluctuations, which are filtered by the input mode cleaner that has a cavity pole at 520 Hz. The

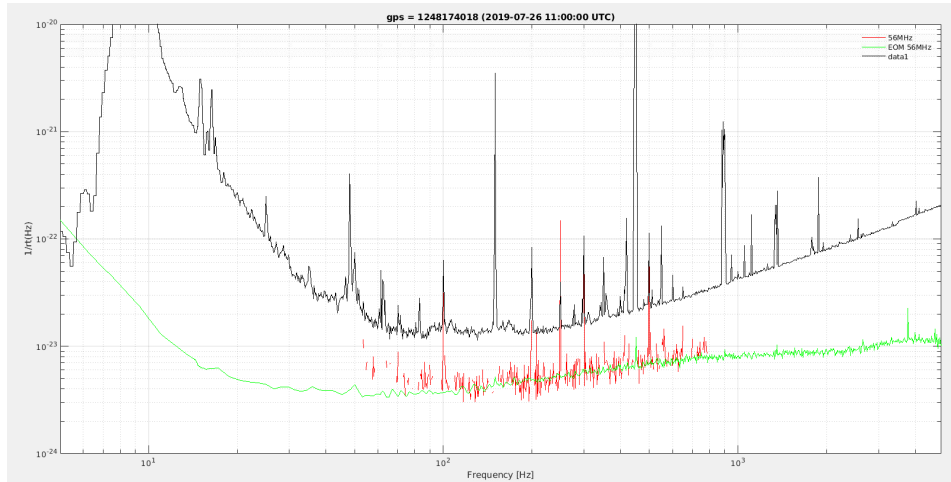


Figure 3.3: Projection of RAM noise onto the sensitivity curves using two approaches. An empirical measured noise level and coupling in red, and laboratory measured noise source and modeled coupling in green. The two projection match relatively well, and are compared to the sensitivity curve in black.

relative intensity fluctuations of the ~ 20 μ W of sideband power in transmission of the OMC can then be calibrated into strain using the interferometer optical response transfer function. The two approaches agree relatively well on the noise level, which gives confidence that the coupling path is well understood.

To solve this issue for O4 I have written a technical report with a detailed description of the RAM noise modeling and derived specifications for the RAM modulation scheme and the OMC. This report is reproduced in appendix B. The high finesse OMC upgrade described in section 3.2.1 will provide a factor 10 increase in filtering for this sideband, while an active RF modulation stabilization scheme will provide another factor 10. At the same time the power of the 56 MHz sideband will increase by a factor ~ 10 due to higher injected laser power and signal recycling increasing the sideband optical gain. In total a factor 10 noise reduction is expected which will keep this noise safely at least a factor 10 below the expected fundamental noises.

3.2.3 Demodulation phase noise

The control of most longitudinal and angular degrees of freedom of the interferometer relies on demodulating photodiodes signal at RF sideband frequencies. The phase noise of this demodulation mixes the two quadratures of the demodulated signal. This becomes an issue if one of the quadratures is large, for example when it is not used in any active control, or if interfer-

ometer optical defects result in the working point of the interferometer not corresponding to a zero of the demodulated signal.

This bilinear noise coupling is relatively simple to model in the time domain. If one denotes by I and Q the two quadratures of a given signal, and by $\delta\phi(t)$ the demodulation phase noise then each quadrature sees an additive noise source

$$\delta I(t) = Q(t)\delta\phi(t), \quad (3.3)$$

$$\delta Q(t) = I(t)\delta\phi(t). \quad (3.4)$$

This additional noise can be then propagated to the detector sensitivity using the same transfer functions as for the corresponding photodiode dark noise.

In Advanced Virgo the demodulation is performed digitally using high speed ADC (400 MHz) and FPGA computations. This systems suffers from noise added to the timing signal synchronizing the ADC during the propagation of this timing signal on copper wiring. This results in a relatively large phase noise of $3 \times 10^{-5} \sqrt{\frac{10\text{Hz}}{f}} \text{ rad}/\sqrt{\text{Hz}}$ for the higher frequency 56 MHz sideband [20].

This was a dominating noise source during the O3 commissioning, it was resolved by changing the interferometer control scheme to use two quadratures of the same photodiode for the MICH and CARM control, hence bringing both quadratures to zero. Also the timing distribution system was improved to use a clock sampled at 100 MHz instead of 10 MHz.

For angular controls intentional offsets are needed, so tackling the phase noise directly is required. This was resolved by measuring the phase noise using the $2f$ signal of a photodiode located on the same suspended bench, i.e. demodulating the photodiode signal at double the modulation frequency to measure the optical beat between the lower and upper sideband that in most cases is not contaminated by other noises. The photodiode used for the measurement was located in reflection of the OMC as it has its power dominated by the 56 MHz sidebands.

The phase noise measured from the $2f$ signal is double the phase noise of any $1f$ signal located on the same bench and can be subtracted using a feed-forward scheme as described in the O3 interferometer sensing and control paper reproduced in appendix C.

3.2.4 Laser frequency noise

The laser frequency (or wavelength) is locked to match the common arm length below ~ 10 kHz using a hierarchical scheme that involves: the input mode cleaner (IMC) cavity length adjusted by acting on the suspended mode cleaner mirror coils, the laser frequency up-stream of the IMC by acting on the master laser crystal temperature control and the crystal length using a piezo-electric transducer, and an electro-optic phase modulator.

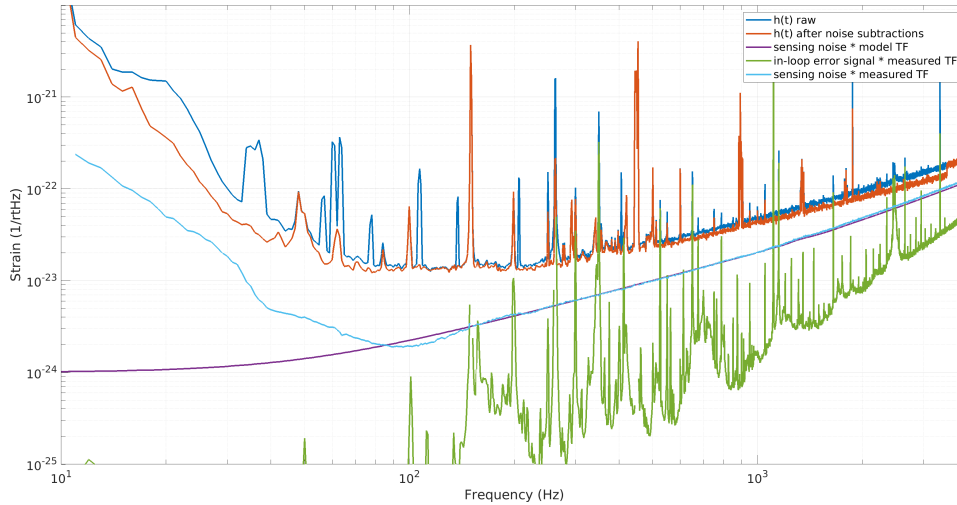


Figure 3.4: Projection of the laser frequency noise onto the sensitivity. Projection of the in-loop error signal (green) and the sensing noise projected using a modeled transfer function (purple) and a measured one (cyan). The raw $h(t)$ sensitivity is shown in blue while the curve in red shows the sensitivity after noise subtractions, including the subtraction of laser frequency noise.

The frequency noise coupling to the sensitivity is suppressed as it is common arm noise that is rejected by the differential nature of the gravitational wave measurement scheme. However the two arm cavities are not perfectly symmetrical. In particular in Advanced Virgo the input mirrors have both side curved with the same curvature, which forms an etalon, an optical cavity that can modulate the effective reflectivity of the input mirrors and hence the arm cavity finesse by $\sim 1\%$. This asymmetry can be controlled by adjusting the temperatures of the input mirrors, but this control scheme was only implemented in the second half of O3. The absence of control led to relatively large frequency independent coupling from CARM to DARM of up to $\sim 10^{-3}$ m/m.

Figure 3.4 shows a projection of the laser frequency noise at a time of large coupling due to a mistuned etalon. There are two noise components in this projection, the noise in the in-loop signal of the laser frequency control is shown in green, it present many resonant structures. The error signal sensing noise (photodiode quantum and dark noise) is shown in purple when projected using a modeled coupling transfer function. At most frequencies the sensing noise is larger than the in-loop signal, as the laser frequency control loop has high gain and suppresses the input laser frequency fluctuation below the sensing noise.

There is also an additional more surprising coupling path for the laser frequency noise. Frequency noise is polluting the error signal of the PRCL

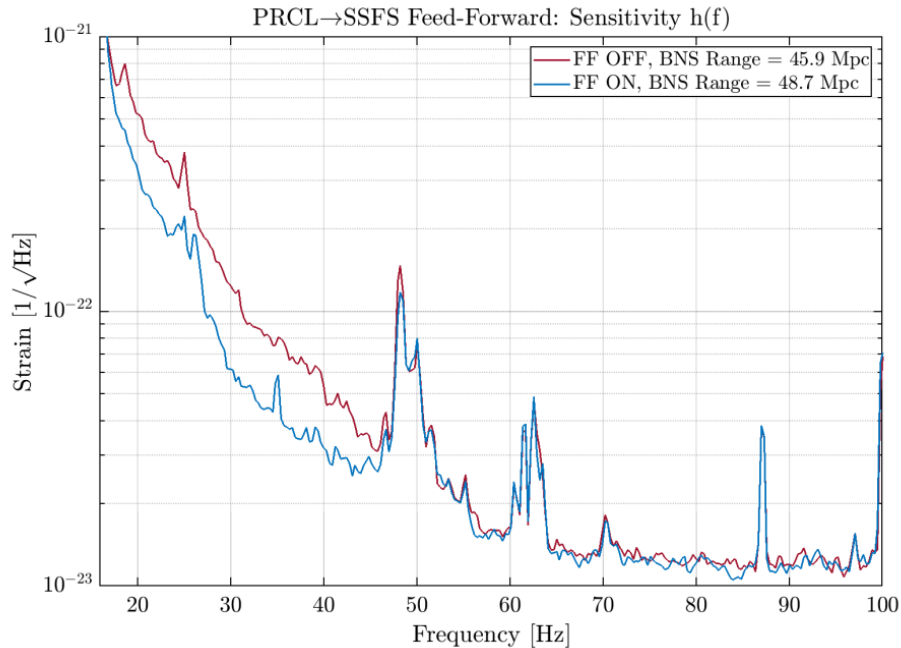


Figure 3.5: Comparison of gravitational wave strain sensitivity between the case where the feedforward from the PRCL correction to the laser frequency error signal is turned off and on.

control, which results in an increased motion of the PR mirror. That PR motion does not couple directly to the sensitivity, but instead pollutes the error signal of the laser frequency control. This additional coupling path explains the difference between the projection of the sensing noise using the measured transfer function shown in cyan and the modeled transfer function shown in purple that includes only direct coupling.

Hence this additional coupling path results from the imperfect diagonalization of the PRCL and laser frequency error signals. I have implemented a feed-forward scheme that successfully reduced this spurious coupling as described in the paper in appendix C and highlighted by figure 3.5.

The planned error signal for laser frequency control was affected by phase noise discussed in section 3.2.3, so instead an error signal with lower signal to noise ratio was used in practice. This meant that out-of-loop the laser frequency noise could be measured more accurately. I have used this error signal to perform a noise subtraction in the online $h(t)$ reconstruction. This allowed to mostly remove the residual frequency noise from the data after the fact, as highlighted by the difference at high frequency between the red and blue line in figure 3.4. The step at 3.5 kHz is solely due to the frequency noise subtraction being performed only up to that frequency.

3.2.5 Back-scattered light noise

Scattered light is a major limitation that is affecting all interferometric gravitational wave detectors built to date. We have already seen in section 2.1 that light scattered by the arm cavities mirrors is the dominant source of optical loss that reduce the power stored in the arm cavities by over a factor 2. In addition it reduces the effect of squeezing and hence increases quantum noise. In both cases the relevant quantity is the total integrated scatter (TIS) of the optics involved.

A more pernicious effect is back-scattered light: the small fraction of scattered light that is back propagated into the interferometer and superposed with the Gaussian mode resonating in the arm cavities. This back scattered light can have a large phase noise as it may involve for example the motion of the vacuum chamber walls, thus it can bypass the seismic isolation system. Even if the back scattered power is extremely small, it can interfere constructively with the large power in the arms, and lead to large effects.

Depending on the relative phase between the back-scattered light and the interferometer beam, the interference can be in the phase or amplitude quadrature. The former is a direct coupling as the interferometer detects relative phase between the beams in the two arms, while the latter is coupled through radiation pressure as it creates a fluctuating power pushing on the mirrors.

To put it into context, gravitational wave detector have an optical phase sensitivity of $\sim 10^{-12}$ rad/ $\sqrt{\text{Hz}}$ at the beam splitter. This means that back-scattered light with fractional power of 10^{-24} is sufficient to be a noise source above interferometer fundamental noises.

The coupling is also non-linear, as the ground motion is much larger than a wavelength and leads to fringe wrapping. This means that the large amplitude low frequency (<1 Hz) ground motion can be up-converted into the detectors sensitive frequency band.

The phase coupling of back-scattered light to the arm cavities can be written simply as

$$h_{\text{sc}} = \frac{\lambda}{4\pi} \frac{\sqrt{f_r}}{L_0} \sin \phi_{\text{sc}}, \quad (3.5)$$

where f_r is the fraction of the arm cavity power which is returning after being back scattered, while ϕ_{sc} is the phase difference accumulated by the back-scattered light. For back-scattered light that travels only once between the scattering object and the interferometer $\phi_{\text{sc}} = \frac{4\pi x_{\text{sc}}}{\lambda}$, where x_{sc} is the relative position of the scattering object with regard to the interferometer.

The non-linearity arises from the sine function, and leads to up-conversion up to maximum frequency of $2\frac{x_{\text{sc}}}{\lambda}$ for back-scattered that travels only once, but often reaches multiples of that frequency as light is back-scattered multiple times and travels back and forth several times between the scattering

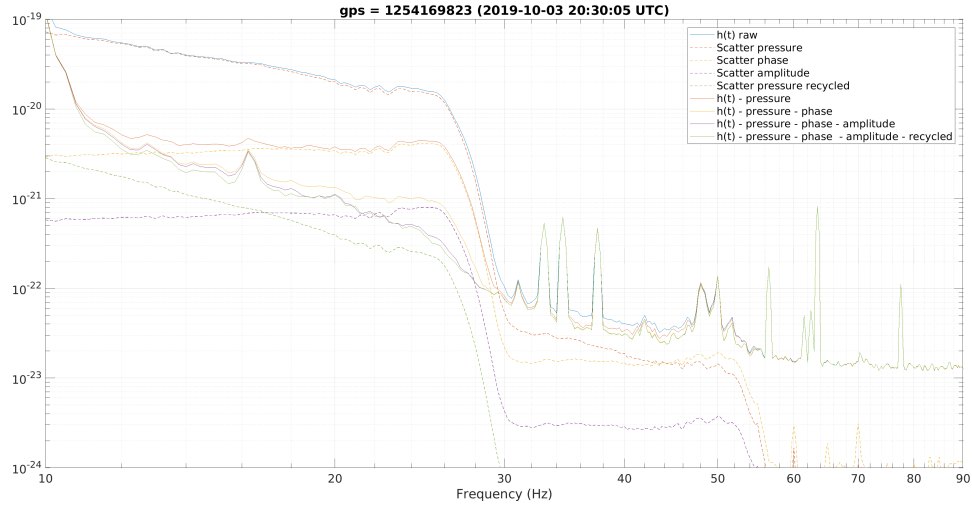


Figure 3.6: Strain data during an intentional suspended bench motion. The contribution of the different back scattered light mechanism is shown and subtracted step by step.

object and the interferometer.

Back-scattered light doesn't have to be a fatality, it can be well understood to reduce the back scattered fraction, the relative position of objects surrounding the interferometer can be controlled [21], and in some cases it can be measured and removed from the strain data after the fact.

In the article reproduced in appendix D I have studied in detail back-scattered light from suspended benches that detect light in transmission of the interferometer end mirrors. In addition to the direct phase coupling and radiation pressure coupling described above, there are also sub-dominant couplings due to the interferometer contrast defect and the arm power asymmetry.

Moreover, most of the back-scattered from the suspended benches is reflected by the end mirror back to the end mirror transmission photodiode. As a result that photodiode measures the scattered light with a signal-to-noise ratio greater than 10'000 and can be used to subtract back-scattered light noise from the strain data. This was done during O3 and improved the sensitivity up to a factor 4 at 20 Hz during times of bad weather when the ground motion is elevated.

Figure 3.6 shows the detector strain data during a time when the bench was intentionally shaken at low frequency to make scattering more apparent. The impact of the four back-scatter light coupling mechanism is shown, and the result of subtracting each one of them in the time domain results in a noise reduction of up to a factor 40.

Understanding the physical path of scattered light has also allowed to

measure the scattered light fraction from these benches to be $\sim 3 \times 10^{-8}$, much larger than expected from the optics on suspended benches [22]. The dominant source turned out to be quadrant photodiodes, as the measured scattering was reduced by a factor 7 when the quadrant shutter was closed. It has also shown a second order scattering (two round trips) that was independent of the quadrant shutter state and was different by two orders of magnitude between the two end benches ($\sim 1.5 \times 10^{-12}$ and 4×10^{-14}) despite the benches having nominally the same optical design. The culprit of this second order scattering remains an open question.

For O4 the suspension inertial sensors for the suspended benches have been replaced to improve the bench control. This should keep the first order scattering below 10 Hz, however the second order and higher scattering may still be a limitation at times of bad weather that will require continued use of the after the fact noise subtraction scheme.

I have also studied the back scatter from all other suspended benches in Advanced Virgo [23], but these were less of a concern due better suspension from the same long suspension chains as used for the arm cavity mirrors, or intrinsically lower coupling as they are located on less critical ports of the interferometer.

3.3 O2 noise budget

O2 was a brief observing run for Virgo that lasted only a few weeks at the end of a much longer observation run performed by LIGO. The noise budget of the interferometer a few weeks after the end of the data taking run is shown on figure 3.7. The noise budget is able to explain most of the noise measured in the interferometer, with the sum of known noise corresponding to a 35 Mpc binary neutron star (BNS) range, while the measured noise has a 14% lower sensitivity integrating to a 30 Mpc BNS range.

The dominant noise source below 25 Hz was angular sensing and control (ASC), where sensing noise of the quadrants and optical levers used to control the mirror angular degrees of freedom below 3 Hz is re-injected and shaking the mirrors more than they would naturally from ground motion filtered by the suspensions. There are also significant contribution from the length control of other degrees of freedom of the interferometer (mainly MICH and PRCL), and the demodulation phase noise discussed in section 3.2.3 affecting these longitudinal controls.

Between 25 Hz and 100 Hz the dominant source of noise is the thermal noise the steel suspension wires of the mirrors as discussed previously in section 2.2

Quantum noise discussed in section 2.4 is dominant above 100 Hz with many structures due mechanical vibrations and scattered light visible above quantum noise.

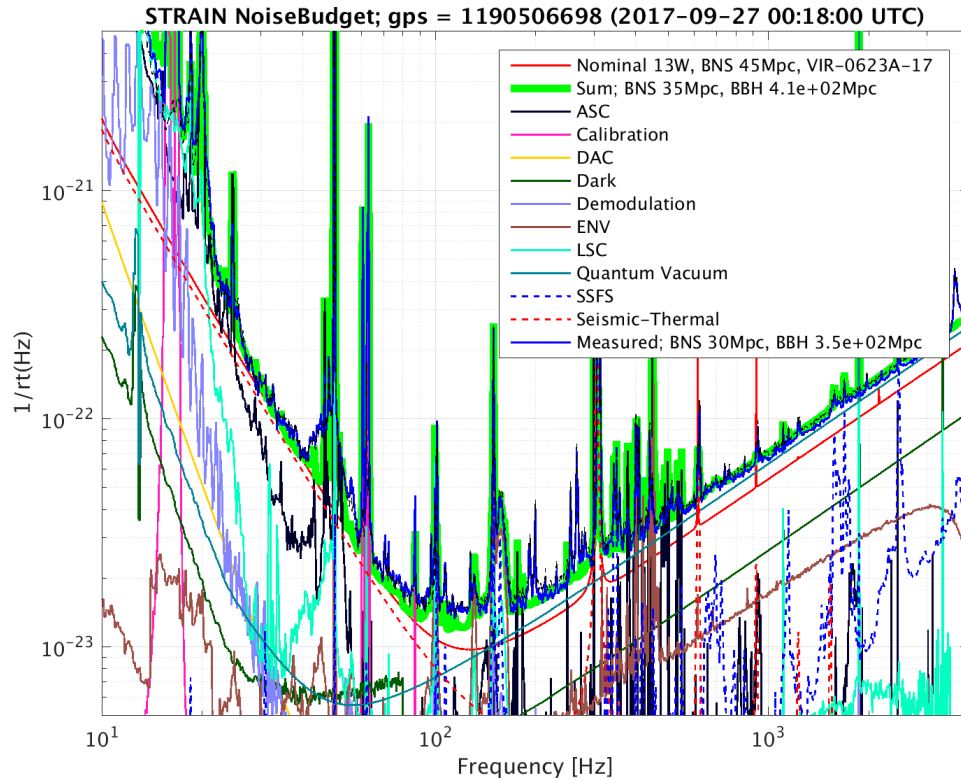


Figure 3.7: Virgo noise budget a few after the end of O2. The measured noise is shown in solid blue, while in green is shown the sum of known noises. Each family of noises contributing to this sum is shown in a different color line.

3.4 O3 noise budget

O3 was a much longer observing run that lasted almost one year, with a 1 month commissioning break in the middle of it. We discuss here the sensitivity near the end of that run when the sensitivity was about 20% higher than at the beginning.

One complication in discussing the noise budget is that several of the noises present at the interferometer output were identified and could be measured accurately enough to be subtracted from the data. Figure 3.8 compares the sensitivity before and after these subtractions. The control noise from the MICH and PRCL longitudinal loop is known, and its residual linear coupling can be subtracted. Also the relative amplitude modulation noise discussed in section 3.2.2 could be measured in reflection of the OMC and subtracted.

The remaining noise budget after these subtractions is shown on figure 3.9. The measured noise level integrated to a 59 Mpc BNS range is 11% higher than the sum of known noise sources that correspond to a 66 Mpc

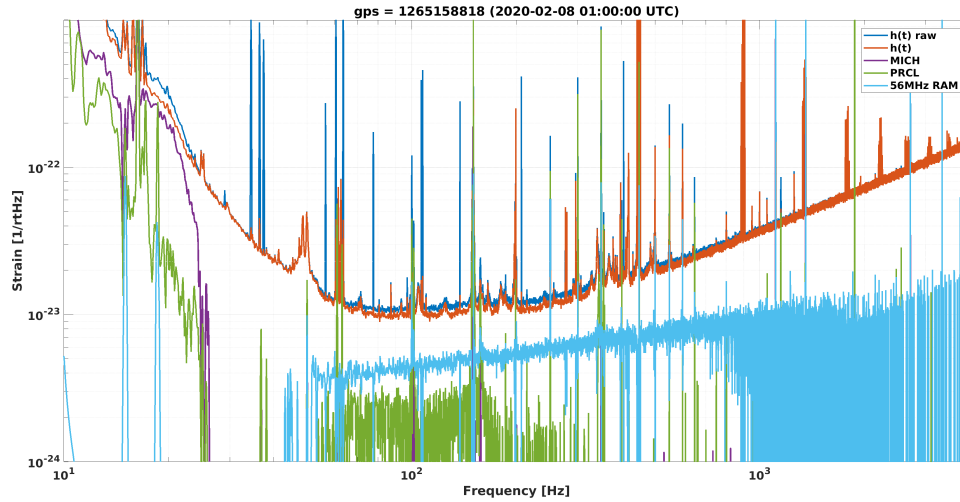


Figure 3.8: The detector noise as recorded is shown in blue, while the data after linearly subtracting coherent noise is shown in red. The three main subtracted noises are shown: MICH noise (purple), PRCL noise (green), 56 MHz relative amplitude noise (cyan). Also narrow calibration lines are subtracted, these are not shown to avoid cluttering the figure.

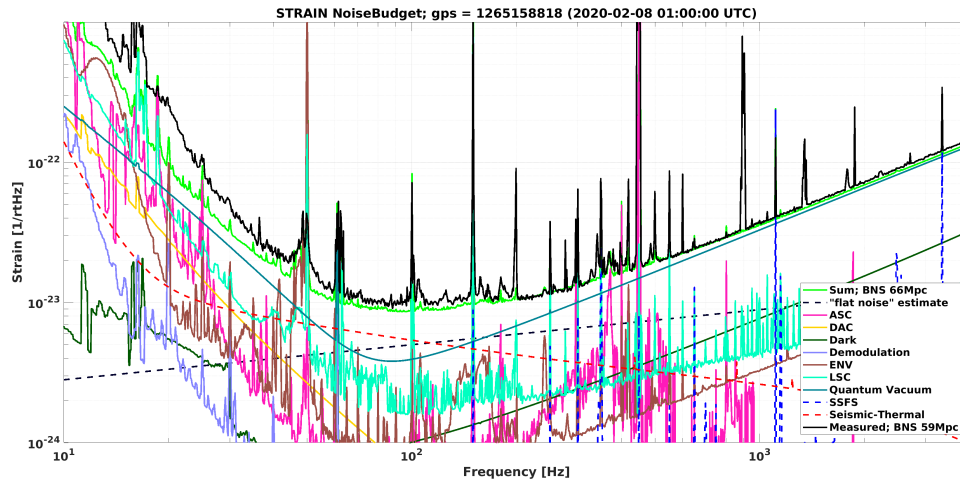


Figure 3.9: Virgo noise budget at the end of O3. The measured noise is shown in solid black, while in green is shown the sum of known noises. Each family of noises contributing to this sum is shown in a different color line.

BNS range.

Below 40 Hz most of the noise is not understood. The dominant known contribution come from quantum radiation pressure noise that is amplified by the frequency independent squeezing. Between 50 Hz and 200 Hz there are two additional significant noise sources beyond quantum noise: the thermal noise of the mirror coatings, and a “flat noise” that is not physically understood. The latter increases with the dark fringe offset and was limiting the BNS range to 35 Mpc in the initial stages of O3 commissioning. This higher level allowed to fit the frequency dependence of this noise, and estimate its level after dark fringe offset was reduced. Above 200 Hz the dominant noise source becomes again quantum noise, the shot noise component of which is reduced by frequency independent squeezing.

Chapter 4

Back-scattered light

We have already mentioned back-scattered light as an important source of noise in section 3.2.5. It can also be used as a tool for characterizing optically a gravitational wave detector or to measure the scattering from an optical component as we will describe it in this chapter.

4.1 Detector calibration with scattered light

Light back-scattered from end benches at Advanced Virgo is measured with great accuracy using photodiodes hosted on these benches, as most of the back scattered light from the bench is reflected back from the highly reflective end mirrors. Using a modified Hilbert transform and the direction of motion of the suspended bench (towards or away from the mirror), both quadratures of scattered light can be reconstructed from that photo-diode signal.

In simple terms, if the cosine of the scattered light phase is measured directly, then the sine of the phase can be obtained by shifting the phase either by $\pi/2$ forward or backward depending on whether the bench moves toward or away from the mirror. This transformation allows to measure back-scattered light coupling through the four mechanisms described in section 3.2.5, as each mechanism has a different quadrature or a different noise frequency dependence.

The amplitude quadrature is detected directly by the photodiode and can be used to measure the power stored in the arm cavities, the interferometer contrast defect and the arm power asymmetry. The phase quadrature obtained through the modified Hilbert transform can be used to measure the transmission of the end mirrors.

However this last parameter can be measured accurately in the laboratory after coating deposition and before mirror installation. Hence, the back-scattered coupling measurement can be used instead for an absolute strain data calibration. Indeed the phase quadrature shown in equation (3.5)

coupling is rather simple

$$h_{\text{sc}} = \frac{\lambda}{4\pi} \frac{\sqrt{f_r}}{L_0} \sin \phi_{\text{sc}}. \quad (4.1)$$

This can be rewritten as a function of the power P_{PD} detected on the photodiode on the suspended bench as

$$h_{\text{signal}} = \frac{1}{L} T_{\text{EM}} \frac{\lambda}{4\pi} \frac{1}{2} \mathcal{T}\mathcal{F} \left[\frac{\delta P_{\text{PD}}}{P_{\text{PD}}} \right], \quad (4.2)$$

where $\mathcal{T}\mathcal{F}$ is the modified Hilbert transform and T_{EM} is the end mirror transmission. Note that this relation involves only the relative power fluctuations on the photodiode, hence neither the absolute calibration of the photodiode nor the fraction of back scattered light are needed for determining the equivalent gravitational wave signal injected by scattered light. The only requirements are for the photodiode response to be flat or known accurately between DC and the 10 Hz-10 kHz band in which current gravitational wave detector operate, and for the end mirror transmission to be measured accurately. The other two quantities involved, the interferometer arm length L and laser wavelength λ are known with a precision better than 0.01% and are a negligible source of calibration uncertainty.

The Advanced Virgo end mirror have a transmission that was measured at LMA before installation of $T_{\text{WE}} = 4.3 \pm 0.2 \times 10^{-6}$ and $T_{\text{NE}} = 4.4 \pm 0.1 \times 10^{-6}$. These relatively large fraction errors of 2%-5% are not a fundamental limitation. For O4 the north end mirror has been replaced by a spare that has a measured reflectivity of $T_{\text{NE spare}} = 3.39 \pm 0.02 \times 10^{-6}$, a fractional error of 0.6%. This is level of precision would be competitive compared with other detector calibration methods.

There are currently three calibration methods used for gravitational wave detectors, all of them are relying on physically displacing the arm cavity mirrors.

The first approach relies on pushing on mirrors with electro-static or electro-magnetic actuator, and using ultimately the laser wavelength as the calibration reference. However, that reference is translated through a series of measurement starting from simple Michelson fringes. It relies on cross-calibrating several photodiodes, several mirror actuators and interferometer optical configurations, which leads to potential substation errors [24].

The second approach relies on pushing on mirrors with an auxiliary laser using radiation pressure. This requires them to have an accurate absolute calibration of this auxiliary laser, and of the power losses between the laser source and the mirror it impinges on. This is currently the standard method for absolute calibration of gravitational wave detectors with $\sim 1\%$ accuracy [25, 26], and it required a significant effort from metrology institutions to improve their accuracy of absolute light power calibration. It can be

limited at higher frequencies were the mechanical resonance modes of the mirrors (for example drum mode) can counteract the mirror pendulum displacement.

The third method relies on gravitational interaction between the mirror and a rotating mass moment. It is a method under development and promises a very good accuracy as the rotating object mass distribution can be simply measured, and the distance to the mirror confirmed by varying the distance between the rotator and the mirror. However it is limited by the rotor rotation frequency to frequencies lower than a few hundred Hz [27].

Scattered light is fundamentally different, as it relies on injecting a well calibrated light phase modulation, as gravitational wave would by modulating the effective distance between mirrors. It is not affected by the mechanical modes of the mirrors, and can be used to inject large signals at high frequency. However it cannot be used during science operation as the injection is intrinsically broadband, and cannot be concentrated at discrete frequencies such as used in other method to monitor the calibration throughout data taking.

Hence this could be complimentary to existing methods increasing the calibration robustness. Absolute detector calibration will become increasingly important for measuring parameters such as the Hubble constant using gravitational wave data, while the frequency dependence of the calibration at a few kHz is crucial for determining neutron star physical parameters such as the tidal deformability and the equation of state from the merger of two neutron stars.

4.2 Scattered light measurement

Scattered light fringe wrapping, while a large issue in gravitational wave detectors as it leads to upconversion, is also a great tool as it self calibrates the scattered light signal. It has a also a large signal to noise ratio as it involves the interference between the small amount of scattered light with a powerful reference beam. This can be used to make simple but very sensitive measurements of scattered light from different optical components.

Based on the Virgo scattered light experience from suspended benches, I have built a small table top scattered light measurement scheme at LAPP. It relies on balanced homodyne detection to remove the laser amplitude noise, and a bench position modulation of a few hundred μm is simply achieved by letting the bench gently swing on metal wires. This motions up-converts scattered light up to a few kHz where the photodiode signal is otherwise quantum shot noise limited. The setup is shown on figure 4.1 and its results are described in detail in appendix E

This setup allowed to understand coherent effects of back-scattered light interference. A scattering reference PTFE (Teflon) was used, which relies on

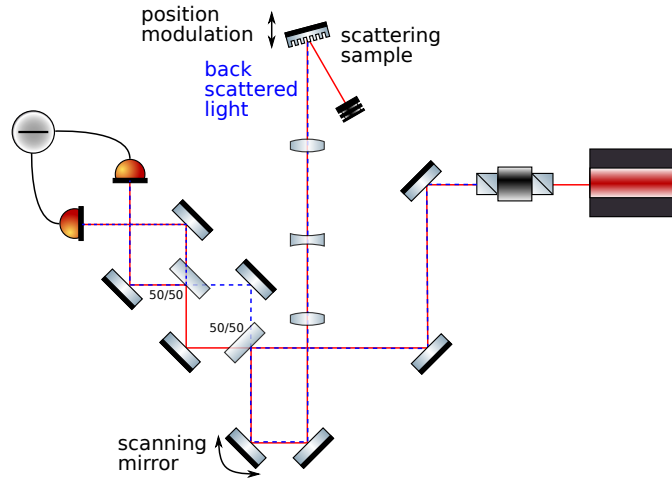


Figure 4.1: Optical layout of the interferometric scatter meter with balanced homodyne detection. The scattering sample is freely swinging on a pendulum suspended optical breadboard. The red line represent the laser beam, while the blue dashed line is the back scattered light optical path.

multiple scattering inside the material (similarly to snow) to generate a scatter that is almost perfectly independent of angle with a bidirectional reflectance distribution function (BRDF) that is equal to $\frac{1}{2\pi}$ for each polarization, i.e. a polarized beam is back scattered as unpolarized light.

There is a well known relation [28] between the interfering fraction of back-scattered light f_{sc} and the beam waist w_0 .

$$f_{sc} = \text{BRDF} \frac{\lambda^2}{\pi w_0^2} \quad (4.3)$$

It turns out that this relation holds also far from the waist when using the beam radius w instead of the beam waist, and this quadratic relation far from the waist can be measured experimentally. It also can be derived from first principle for simple cases such as back scatter from a point defect.

One can also measure that back-scattered light is sensitive to alignment. If one shifts the scattered light propagating in the balanced homodyne part of the experiment that is independent from the reference beam, then the measured interference falls off exponentially in the same way as a Gaussian beam would. This happens despite the incoherent power of the back-scattered light reaching the photodiodes remaining the same. That result highlights that scattering from one part of an optical setup to another is highly ineffective, and that direct back-scatter which counter-propagates along the beam path is in most cases the dominant source of scatter interference, as it is by construction aligned with the main beam.

Beyond these basic checks many different components can be measured

Component	BRDF (1/srad)	incidence angle	polarization
Neutral density	1.4×10^{-4}	3.3 deg	S-pol
Neutral density	5.2×10^{-6}	3.3 deg	P-pol
Neutral density	3.1×10^{-5}	19 deg	S-pol
Neutral density	5.6×10^{-6}	19 deg	P-pol
Silicon beam dump	1×10^{-4}	1 deg	S-pol
Silicon beam dump	3.8×10^{-6}	1 deg	P-pol
QPD, Excelitas, YAG-444-4A	3.5×10^{-3}	5 deg	S-pol
QPD, First Sensor, QP22-Q	3×10^0	5 deg	S-pol
PD, Excelitas, C30665GH	4.9×10^{-5}	20 deg	S-pol

Table 4.1: Back-scatter BRDF measurement of different opto-mechanical components used in Virgo. The incident beam is always S polarized while the polarization at which the measurement is performed is noted in the table. These measurements have $\sim 15\%$ statistical errors due to speckle averaging.

as shown in table 4.1. This allows to identify components that could be dominant sources of back-scatter on optical benches at Virgo. For example it confirmed that quadrant photodiodes from First Sensor are the dominant source of scattering on the Advanced Virgo end benches. The measured back-scatter from the bench corresponds well to the fraction of light back scattered by the bench once the beam size on these quadrants and the fraction of the incident beam reaching them is taken into account. It also shows that other quadrant photodiodes (from Excelitas) have back-scatter that is three orders of magnitude lower.

Another interesting result in that table is that back scatter in the P polarization can be several orders of magnitude smaller than in the S polarization. Showing that optics scatter mostly in the incident beam polarization. This is not very relevant for terrestrial gravitational wave detectors, but it is important for the future eLISA space gravitational wave telescope which use different polarization in the same beam expander for sending and receiving beams to the other spacecraft. Hence for example a powerful S polarized beam that is sent out, can through back scatter pollute the low power P polarized signal arriving from the distance spacecraft.

The interferometric approach used also allows back-scatter measurements at very small angle of incidence. The main reason is that only light that reach the scattering target will be phase modulated by the suspended bench motion, as it is the only component located on that suspended bench. Hence a telescope can be used to send a large beam with low divergence on the sample optic and amplify the angular separation between the specular reflection and the back scatter from the sample optic.

In practice with a simple magnification $\times 4$ telescope and a 2 mm waist

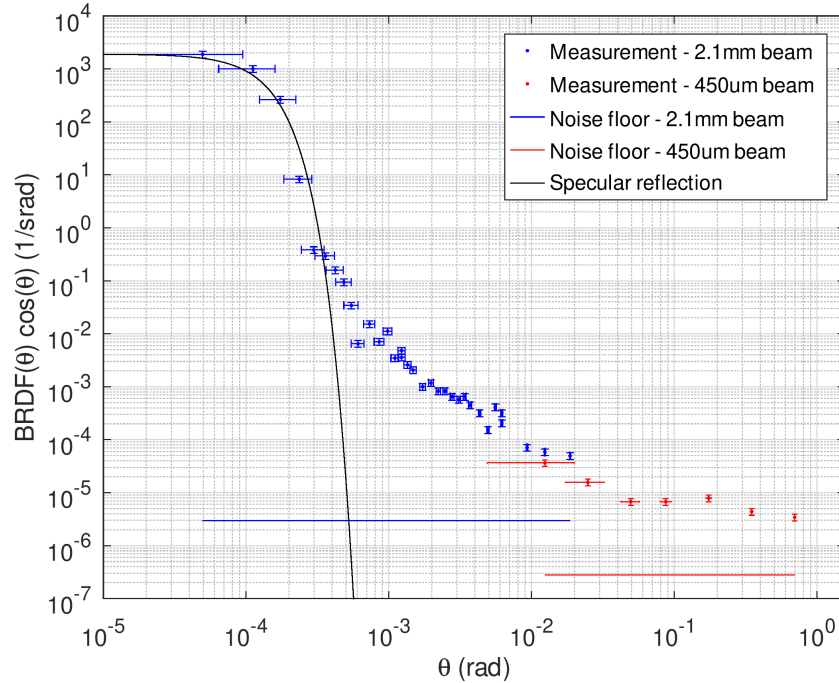


Figure 4.2: Measured BRDF using a 2.1 mm radius beam (blue points) and 450 μm radius beam (red points) as a function of incidence angle θ . The horizontal blue and red solid lines represents the corresponding measurement noise floor observed without a sample. The black solid line show the expected interference from the window 700 ppm specular reflection.

beam a 160 μrad angular resolution was achieved. This resolution is still limited by the beam divergence.

This performance is showcased on figure 4.2 where the results from measuring an anti-reflective coated optical window are shown. This window sample is a damaged spare of the vacuum windows used on Virgo suspended benches vacuum tanks. Up to 500 μrad the measurement is limited by the specular reflection from the window. The Gaussian fall-off from the specular reflection follows well the theoretical expectation, then above 500 μrad a roughly $\frac{1}{\theta^2}$ powerlaw fall-off is measured that corresponds to expectations from a highly polished optic, which then flattens at 30 mrad as the scattering becomes limited by small scale rugosity and point defects.

The small angle measurements are at present limited to samples with low specular reflectivity, such as lenses, beam dumps, sensors. The main reason is that for a highly reflective mirror the powerful specular reflection re-enters the telescope and back scatters from optics or mounts in the setup. This effect is easily identifiable, as back-scattered light following this path

encounters the suspended bench motion twice, which result in scattered light up-conversion at double the frequency of light back-scattered directly by the sample mirror. So this does not bias the measurements, but it can render the setup blind for small incidence angles on reflective optics. And there are prospects to resolve this issue by properly baffling the telescope, and more refined data analysis to separate back-scatter that sees the bench motion once or twice.

The telescope magnification could be increase further to obtain a beam of ~ 20 mm in radius. This would remain a factor few smaller than what is achieved with meter scaled telescopes on suspended benches at Advanced Virgo. That larger beam size should yield an angular resolution of $16 \mu\text{rad}$ and permit the study of back scatter at incidence angle of $100 \mu\text{rad} - 1 \text{ mrad}$. A poorly characterized scatter angle region, but critical as this is the angle where baffles closest to the beam are located within the gravitational wave detector Fabry-Perot arms [29, 30].

Chapter 5

Gamma-ray bursts and gravitational waves

Gamma-ray bursts (GRBs) are bright flashes of gamma-rays originating in distant galaxies. They were originally discovered in the 1970's by satellite monitoring the application of the treaty on nuclear tests ban. After several decades of study and the exclusion of hundreds of potential models two explanations remained for GRBs: extreme cases of core-collapse supernova for more massive and highly rotating progenitor stars, and the merger of a neutron star with another neutron star or a black hole.

These two models correspond to the two partially overlapping populations of observed GRBs. These two populations are differentiated by the GRB duration and spectral hardness, i.e. the relative contribution of more and less energetic gamma-rays to the total measured luminosity. Short-hard GRBs are less frequent and are thought to be due to neutron star mergers, while long-soft GRBs are associated with core-collapse supernova. The line separating the two classes of GRBs being at roughly 2 second duration. In both cases the GRB engine is thought to be a highly rotating compact object (either neutron star or black hole) that ejects some matter along its rotation axis at relativistic speeds. The emission from these jets is boosted to higher energies by the highly relativistic motion of the emitting matter.

Before gravitational wave observations the long GRB association with core-collapse supernova was more established. Most long GRBs are located in active star forming regions of galaxies, due to the short life span of massive stars of only a few million years. There were also several observations of supernova following the long GRB emission, starting with the first well established association of SN1998bw and GRB980425.

The short GRB association to neutron star mergers was more speculative. Short GRBs are less numerous, and due to their short duration they are harder to localize and the observation of its afterglow is more difficult. Hence the association relied observationally mostly on a small number of lo-

calized short GRBs that were in galaxies without much active star formation, and often with large offsets to the galaxy center. The presence in galaxies without active star formation would be explained by the long time necessary for the two neutron stars of the binary system to lose orbital energy and merge. While the large distance would be due to supernova kicks, when the neutron stars are formed by non perfectly symmetrical collapse. This collapse asymmetry impacts sufficient momentum to displace the binary system far from the galactic plane.

Neutron star mergers were identified early on as a prime candidate for gravitational wave detection. As a consequence searches for gravitational waves associated with GRBs have been performed since the first initial LIGO data taking runs [31]. This has continued for subsequent runs with two types of analysis. A modeled search using binary neutron star and neutron star – black hole coalescence template waveform that was focused on short GRBs, and broader scope analysis using time-frequency excess power methods to search for any gravitational wave transient associated with any of the GRBs. In both cases by the end of the S6/VSR2-3 runs in 2009-2010 the gravitational wave method were coherently combining data from several detectors [32]. This was enabled by the localization of GRBs by gamma-ray satellites, which greatly simplifies coherent searches as the relative time delay of arrival at different detector sites is known a priori.

By the time of the first Advanced LIGO and Virgo data taking run O1 in 2015-2016 the search methods were well established. And required mostly a transfer of knowledge from the initial LIGO/Virgo experience to a new generation of scientists. I have led this transfer by being the main editor of the collaboration paper on this topic that is reproduced in appendix F, and then coordinating the GRB working group for 5 years. The prospects of these analysis remained in question, as the expected rate was relatively low at 1 per year at aLIGO/Virgo design sensitivity due to the relativistic beaming which was expected to produce visible gamma-rays only for 10% or less of binary mergers.

5.1 GW170817 / GRB 170817A

The spectacular breakthrough occurred in 2017, with the discovery of the binary neutron star merger GW170817 in coincidence of GRB 170817A. The time and sky location association between the two was highly significant, at more than 5σ . It clearly confirmed that short GRBs are produced at least in some cases by binary neutron star mergers.

The gamma-ray arrival was delayed compared to the neutron star merger gravitational wave signal by 1.74 ± 0.05 s as shown on figure 5.1. Well within the expected delays of $[-1, 5]$ s derived by the LIGO/Virgo collaboration back in 2010. This short delay after ~ 43 Mpc of propagation corresponds to

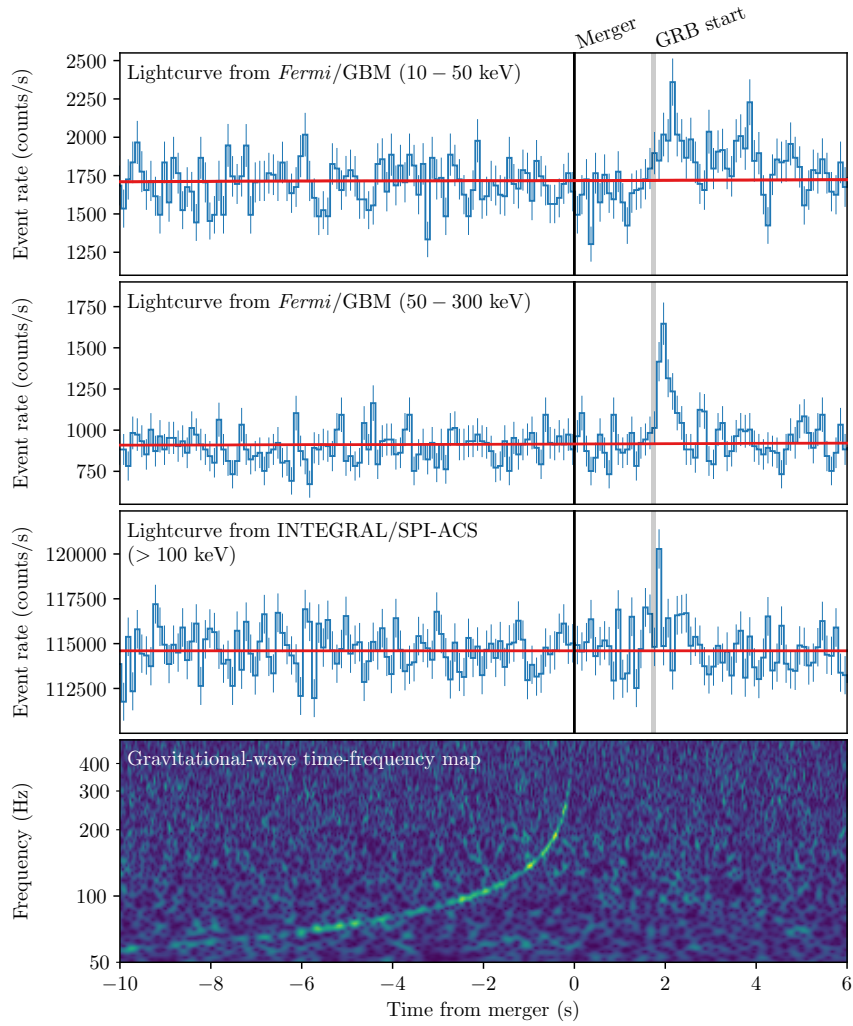


Figure 5.1: Joint multi-messenger detection of GW170817 and GRB 170817A. The top 3 panes show the gamma-ray flux measurement, while the bottom pane is the gravitational wave time-frequency map showing the characteristic chirp signal of a compact object binary merger.

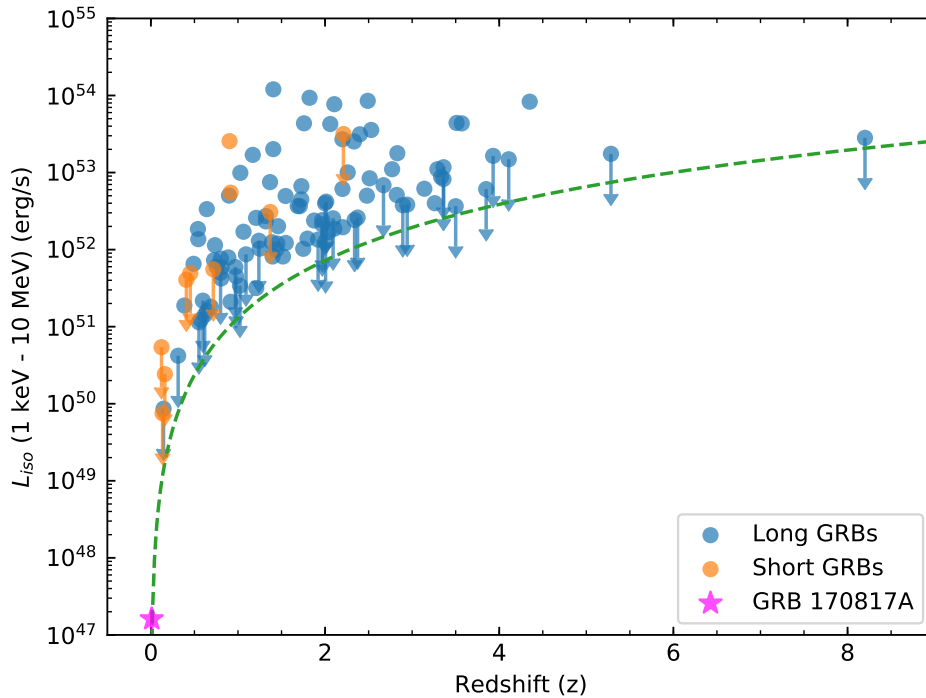


Figure 5.2: Equivalent isotropic luminosity of GRB 170817A compared to the luminosity of other GRBs as a function of redshift. The green dashed line shows the detection sensitivity of the GBM instrument on-board the Fermi satellite.

a fractional speed difference between light and gravitational waves of $\sim 10^{-15}$ or less. It also provides a strong test of the equivalence principle that electromagnetic radiation propagation is affected by the Milky Way gravitational potential in the same way as gravitational waves with a precision of $\sim 10^{-6}$.

This event provided also a large surprise, as the gamma-ray emission was 3 to 5 orders of magnitude less luminous than for other short GRBs, and could be detected only due to the proximity of the source. This suggested that GRB 170817A was observed slightly off-axis, which later on was confirmed by late time X-ray and radio afterglow brightening as the relativistic jet slowed down sufficiently to include Earth in its beaming angle.

This highlighted that the top-hat jet approximation, that GRBs emit only in a narrow cone with no emission outside of it is too simplistic. And that more complicated structures are needed to explain a non-negligible angular region with reduced but still significant gamma-ray emission. Another consequence was that observed luminosity models for short GRBs need to be extended down from 10^{49} erg/s to at least 10^{47} erg/s or lower, to include dim nearby short GRBs as shown on figure 5.2.

These results were derived between the LIGO, Virgo, Fermi/GBM and Integral collaboration in a paper written a few weeks after the event and reproduced in appendix G. As the Virgo editor for that paper, it was an intense and unexpected round the clock work for that time period, that followed the months long marathon and sprint of commissioning Virgo to start data taking only a few weeks before that event. This was a very different pace from previous LIGO/Virgo collaboration results that had taken a year or more to be written in a publication.

That event led also to a host of other results by studying in more detail the gravitational wave signal or combining it with other electro-magnetic observations. It provided a measure of the Hubble constant independent from the usual cosmic ladder [33], some interesting bounds on the neutron star radius and equation of state [34], or that neutron star mergers may explain most of the r-process heavy elements present in the Milky Way [35].

5.2 Short GRB population

This event changed some paradigms, as the limiting factor for joint observation becomes gamma-ray sensitivity for slightly off-axis events instead of gravitational wave. This prompted a more active developments of gamma-ray followup of gravitational wave events and joint gamma-ray / gravitational wave searches [36, 37]. Despite this no other neutron star merger event associated with a GRB has been discovered since GW170817 in the 2019-2020 O3 observing run, highlighting that GRB 170817A was a relatively exceptional event.

This was in many ways predicted after observing GRB 170817A. On figure 5.3 one can see that at redshift 0.03 corresponding to 135 Mpc, roughly the range of gravitational wave detectors during O3, one could expect between 3 and 30 binary neutron star detection per year, but only 0.2 and 1 detection that is associated with a short GRB. This is in line with what was actually discovered during O3 with the observation of one binary neutron star merger and three neutron star – black hole mergers [38, 39].

Nonetheless, the lack of further gravitational wave detections after GRB 170817A provides lower limits on the distance to the other observed short GRBs and put constraints on the population. Most short GRB population models were assuming a simple top-hat emission, with a large uniform gamma-ray flux inside a narrow emission cone, and no emission outside it. The equivalent isotropic luminosity inside that emission cone had a wide distribution, with a lower cut-off at a few 10^{49} erg/s and a decaying tail of rare high luminosity events extending to 10^{53} erg/s to cover the observed distribution of luminosity shown on figure 5.2.

Before GRB 170817A this top hat emission model was evaluated by a dozen different studies, an example of such a study and a comparison with

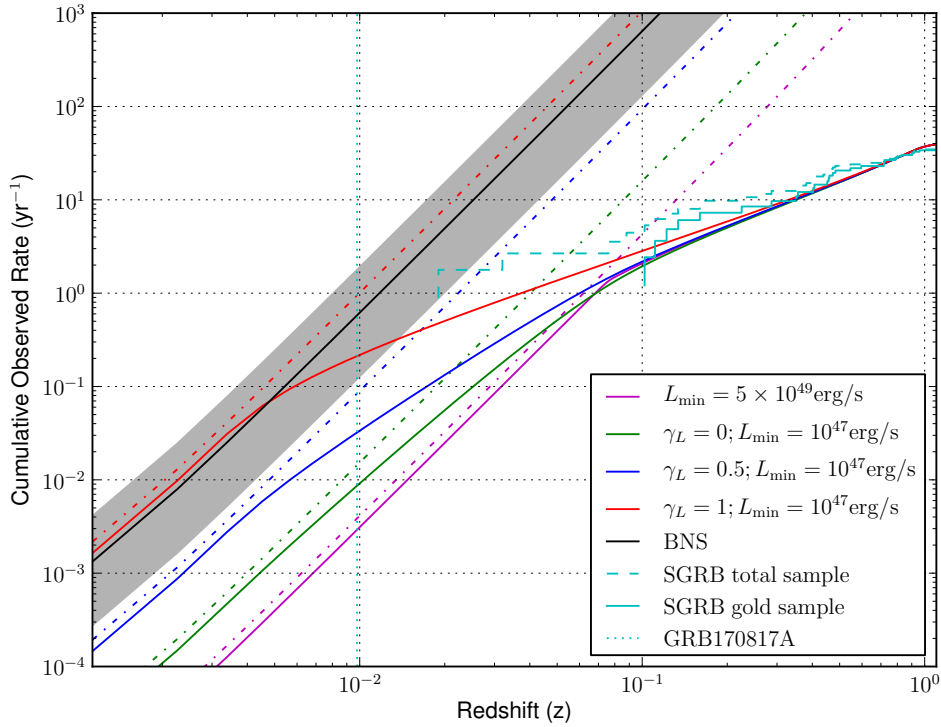


Figure 5.3: Predicted detection rates per year as a function of redshift. The purple curve shows an example luminosity distribution model before GRB 170817A was observed, while the three other model show extension to lower luminosity that would be more compatible with GRB 170817A. The gray band is the binary neutron star merger rate measured by the detection of GW170817.

others can be found in [40]. These models based on gamma-ray observations predict the product $\rho_0 f_b$ to be of the order of a few $\text{Gpc}^{-3}\text{yr}^{-1}$, where ρ_0 is the GRB rate in the local universe and f_b is the beaming factor representing the fractional solid angle of the top hat cone emission. This turned out to be compatible with the measured rate of BNS mergers through gravitational wave of 10 to 1700 $\text{Gpc}^{-3}\text{yr}^{-1}$ [41], as the beaming factor for short GRBs is expected to be of the order of 10 percent.

However these top-hat models remain unsatisfactory, as they do not include the low-luminosity of GRB 170817A. A simple solution is to extend to lower luminosities the luminosity distribution functions used in one of these

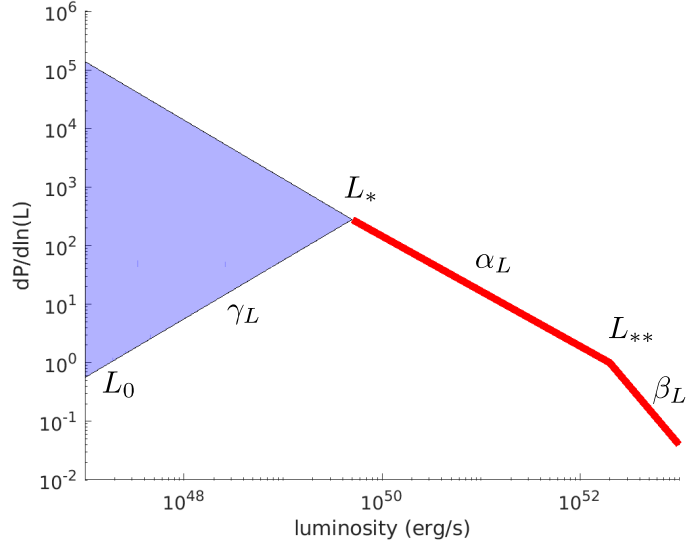


Figure 5.4: Luminosity distribution model, in red is shown a broken power law that fits short GRB observations, and in blue possible low luminosity extensions to take into account GRB 170817A with γ_L between -1 and 1. The labels describe the powerlaw slopes and break energies corresponding to equation (5.1).

models as shown on figure 5.4 and assume $f_b = 1$

$$\frac{dP}{d \ln(L_{\text{iso}})} \propto \begin{cases} \left(\frac{L_{\text{iso}}}{L_{**}}\right)^{-\gamma_L} \left(\frac{L_{**}}{L_*}\right)^{-\alpha_L} & L_0 \leq L_{\text{iso}} \leq L_{**} \\ \left(\frac{L_{\text{iso}}}{L_*}\right)^{-\alpha_L} & L_{**} < L_{\text{iso}} \leq L_* \\ \left(\frac{L_{\text{iso}}}{L_*}\right)^{-\beta_L} & L_{\text{iso}} > L_* \end{cases} \quad (5.1)$$

where the parameters $\alpha_L = 0.94$, $\beta_L = 2$, $L_* = 2 \times 10^{52} \text{ erg s}^{-1}$ and $L_{**} = 5 \times 10^{49} \text{ erg s}^{-1}$ are fixed by past studies of the GRB population, and the free parameters are the powerlaw slope γ_L of the low luminosity extension and the low luminosity cut-off L_0 .

This is an effective phenomenological model, and one should not assume that the GRBs have such a wide distribution of intrinsic luminosities. Instead the expected physical model would be that the intrinsic luminosity distribution is convolved with the angular distribution of the emission, which leads to the apparent low luminosity observed at Earth for sGRBs that have their core emission pointing in a different direction.

The LIGO-Virgo-KAGRA collaboration results are actually able to put some constraint on such a model [42], putting limits on the powerlaw slope γ_L of the low luminosity extension, and to a lesser extent on the low luminosity

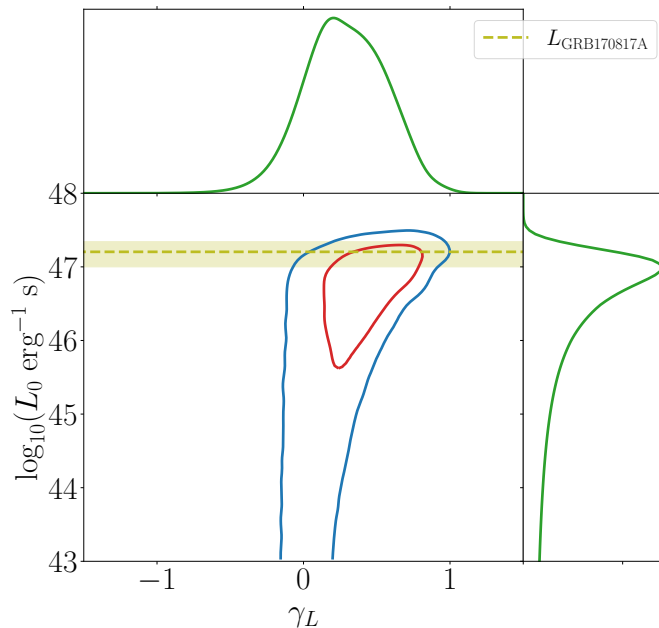


Figure 5.5: Posterior distribution on the low luminosity powerlaw slope γ_L and the low luminosity cut-off L_0 from gravitational wave followup of ~ 100 GRBs.

cut-off L_0 of that extension. The results of a Bayesian analysis are shown on figure 5.5, and constrain the slope to be between -0.17 and 0.73 , a much slower decrease compared to the higher luminosity part of the distribution that has a slope of 0.94 and further increasing to 2 at very high luminosity. The L_0 cut-off is constrained to be at most of $\sim 10^{47}$ erg/s in order to be able to explain GRB 170817A, but remains compatible with no cut-off down to at least 10^{43} erg/s. In other words, the are results compatible with an angular emission that continuously decreases from a high luminosity core to negligible gamma-ray emission far from the emission cone.

A future development would be to constrain directly parameters of such physical models of emission. For example, a simple two parameter model can be a Gaussian angular distribution of flux with the width of the Gaussian as a free parameter, and a powerlaw distribution of the intrinsic luminosity of the GRB, i.e. the flux along the axis of the emission jet. It is however likely that a more complex model, with additional parameters, would be needed to be compatible with the measured GRB luminosity distribution, and the constraints coming from observing one GRB in gravitational waves and putting lower limit of $100 - 200$ Mpc on the distance to ~ 100 other GRBs.

Chapter 6

Conclusions

I have summarized in this thesis my activity in the gravitational wave field between 2013 and 2022, which has covered two different topics: gravitational waves searches in association with gamma-ray bursts, and the construction, commissioning and operation of Advanced Virgo.

My research was initially focused on gravitational wave data analysis related to gamma-ray bursts. I have co-chaired the LIGO/Virgo GRB working group from 2016 to 2021, led the paper writing of the O1 LIGO/Virgo GRB follow-up in 2016, and was the Virgo collaboration editor for the paper on the joint gravitational wave and gamma-ray discovery of GW170817 / GRB 170817A. This extraordinary event, which has subsequently been observed at most electromagnetic wavelengths, changed many hypothesis into established facts. However it has not been confirmed since then by other observations during the O3 LIGO/Virgo observing run. The on-going O4 observing run, with its longer 18 months duration and better sensitivity will hopefully lead to another multi-messenger observation. This will either start confirming that GW170817 / GRB 170817A was a typical nearby event, or that the population of nearby GRB is diverse with much variability remaining to be understood. It should also shed some more light on the typical angular distribution of gamma-ray emission from binary neutron star mergers and the structure of the relativistic jet that powers that emission.

Over time I have increased my involvement in the Virgo detector instrumentation. I have characterized and commissioned the Advanced Virgo output mode cleaner. First in the optics laboratory, then installing it at Virgo, and commissioning it for science operations. I have also participated in developing and characterizing the upgraded O4 output mode cleaner. This has however reached the limit of performance in terms of optical losses per level of optical filtering, due to the Rayleigh scattering inside fused silica. Future upgrades to reduce further losses and increase the filtering of sidebands and higher order modes will require a change in technology, to a cavity in which

light resonates in vacuum. That technology is already used in the LIGO output mode cleaner, but developing the expertise to be able to implement it without additional mechanical resonances will be a challenge.

I have also been in charged of the Advanced Virgo noise budget since 2016, building a simplified but complete model of the longitudinal control of the interferometer, and integrating all noise sources into it. This has been a precious tool for understanding the instrument and guiding commissioning once lock is acquired and light resonates fully inside the interferometer.

During O2 and O3 this achieved a fairly complete explanation of the measured noise with only 10-15% remaining unexplained. However, given that noise sources add quadratically to the sensitivity, this strongly limits any long term planning of sensitivity improvement. This remaining unaccounted noise is sufficient to limit any improvement on the total sensitivity to at most a factor 2. As a result the sensitivity improvements, obtained from upgrades that aim to tackle understood noise sources, remain highly uncertain.

A more recent activity on scattered light is an off-shoot of studying the general noise budget. It resulted in a better understanding on how scattered light couples to the detector sensitivity, how it could be used for calibrating the gravitational wave strain data in an absolute way that is also accurate at high frequency, and finally how to measure accurately back-scattered light from individual component in the laboratory.

In particular the project of measuring back-scattered light at very small angles ($100 \mu\text{rad} - 1 \text{mrad}$) combined with direct measures and models of back-scatter from multiple scattering has been funded. And it will be developed over the next 3 years in a new R&D platform that is under construction at LAPP.

Also, the replacement of the north end mirror with one that has small errors in its transmission measurement promises a good test of using scattered light to calibrate a gravitational wave detector. I hope that there will be opportunity to test this during the O4 observing run.

In the mean time, since the start of writing this thesis I have been appointed deputy commissioning coordinator and the O4 commissioning of Advanced Virgo is slowly progressing and still underway. The main difficulty is the introduction of resonant sideband extraction through signal recycling. This has been in use at advanced LIGO since 2015, but Virgo has the additional complication of marginally stable recycling cavities due to space constraints in the building.

A marginally stable cavity corresponds roughly to a flat-flat configuration of a Fabry-Perot resonator. It is not selective and allows all spatial modes to resonate for the same cavity length in addition to the main TEM00 Gaussian beam. This can be contrasted with stable cavities, which have curved mirror and beam expansion within the cavity. For stable cavities each spatial mode resonate for a different length of the cavity due to the accumulation

of Gouy phase that is proportional to the order of the mode. In addition, the relatively large curvature of the mirrors, ensures that any defect due to manufacturing or thermal effect due to laser absorption remains small. This contrasts with a marginally stable cavity that can easily be pushed into the unstable region where all modes are diverging spatially and no mode can resonate.

The consequences of the lack of these two properties were not well understood at the start of the O4 commissioning. As result they were slowly uncovered, understood and mitigated over time, and can be briefly summarized as follows.

The correction of the signal recycling and power recycling curvature was initially performed using intentional thermal lenses in compensation plates in front of the input mirrors. The intention was to use the average of the two lenses to compensate the power recycling cavity curvature, while to use the difference of the two lenses to compensate the signal recycling cavity curvature. While this works from the point of view of radio-frequency sideband, it is not the case of the differential carrier light that contains the gravitational wave signal and is recycled by signal recycling. The latter is also controlled by the average of the two lenses. This issue was eventually resolved in the summer of 2022 by creating an additional thermal lens in the power recycling cavity, using a thermal projector that had been developed 10 years before for initial Virgo arm cavity mirrors, which enabled to act independently on the power and signal recycling cavity curvatures.

This allowed to achieve stable and repeatable operation of the detector, however the radio-frequency signals remained polluted by large offsets due to higher order modes and discrepancy between the sideband and carrier beam shapes and positions. These offsets could be eventually measured using carrier light only and mechanical dithering of the mirrors to obtain the correct longitudinal position of mirror. This was implemented in the spring 2022 for SRCL and in winter for MICH.

A consequence of these offsets are that they greatly increase the coupling of demodulation noises. The phase noise was known since O3, and the solution developed for O3 for angular degrees of freedom proved effective also for longitudinal ones. In addition, a demodulation amplitude noise was identified and eventually a solution was found to subtract in winter 2022. This was possible as the amplitude noise is common to radio-frequency lines demodulated using the same analog to digital converter, and noise measured at one radio-frequency could be used to subtract it from another frequency.

In parallel, another struggle was the signal recycling alignment. An overlooked consequence of marginally stable cavities is that higher order modes are also recycled and their power increased at the dark port of the interferometer by about a factor 7. Counter to the experience with other degrees of freedom, a good signal recycling alignment correspond to a higher brightness of the light at the dark port of the interferometer. In addition radio-frequency

quadrant signals do not provide useful signals due to the lack of Gouy phase in the signal recycling cavity.

Eventually a solution of dithering longitudinally the arm cavity mirrors and angularly the signal recycling mirror proved to be effective at aligning signal recycling although with limited bandwidth and accuracy.

An ongoing issue to resolve is the higher coupling of laser frequency noise due to this higher power at the dark fringe. The increased finesse of the output mode cleaner allows to achieve a reasonable rejection of the noise, but it critically depends on alignment and is limited by alignment fluctuations.

In parallel several other issues have contributed to slowing down the progress. An incident during vacuum pumping that broken a mirror suspension and one of the magnets bonded to the mirror, contamination of the output mode cleaner external surface with burned plastic, laser failures and unexplained excess noise of the new fibered laser, and many more smaller issues.

Overall, this puts in question the long term prospects of operating a marginally stable dual recycled interferometer at Virgo. Efforts have started to revisit the studies from circa 2010 of implementing stabled recycling cavities either through the construction of additional building or through more complex suspension schemes to fit many suspended mirrors in a small space. When and how could this be implemented will be an intense activity over the next few years.

With a longer perspective, I am also involved in the newly created Einstein Telescope collaboration that proposes to build a third generation underground gravitational wave detector, with construction starting in the 2030 decade. The purpose is to increase the sensitivity by an order of magnitude compared to current detectors and be able to measure already observed sources at cosmological distances, and study gravitational waves sources that remain to be detected such as supernova, pulsars and ringdowns of neutron star mergers.

With that perspective I am co-chair the Input Output Optics work package with the task of designing this part of the future instrument over the next few years. I hope to transfer some of the lessons I have learned working on commissioning the output optics of Virgo, coordinating the general commissioning of Virgo and managing the interferometer system in the Advanced Virgo+ project of upgrades for O4 and O5.

Bibliography

- [1] A. Einstein. Die grundlage der allgemeinen relativitätstheorie. *Annalen der Physik*, **354**:769, 1916.
- [2] A. Einstein. Näherungsweise integration der feldgleichungen der gravitation. *Sitzungsberichte der Preußischen Akademie der Wissenschaften*, page 688, 1916.
- [3] C. DeWitt. Conference on the role of gravitation in physics at the university of north carolina. Technical report, 1957. WADC Technical Report 57-216.
- [4] A. Hulse and J. Taylor. Discovery of a pulsar in a binary system. *Astrophys. J. Lett.*, **195**, 1975.
- [5] J. M. Weisberg, D. J. Nice, and J. H. Taylor. Timing measurements of the relativistic binary pulsar PSR B1913+16. *Astrophys. J.*, **722**:1030, 2010.
- [6] B. P. Abbott *et al.* Observation of gravitational waves from a binary black hole merger. *Physical Review Letters, Volume 116, Issue 6, id.061102*, **116**:061102, feb 2016.
- [7] B. P. Abbott *et al.* Tests of general relativity with gw150914. *Physical Review Letters, Volume 116, Issue 22, id.221101*, **116**:221101, jun 2016.
- [8] Observing scenario timeline graphic. LIGO-G2002127.
- [9] F. Acernese *et al.* Status of advanced virgo. *EPJ Web of Conferences*, **182**:02003, 2018.
- [10] M. Was, Virgo logbook 47115. <https://logbook.virgo-gw.eu/virgo/?r=47115>.
- [11] M. Was, Virgo logbook 46956. <https://logbook.virgo-gw.eu/virgo/?r=46956>.
- [12] R. Kubo. The fluctuation-dissipation theorem. *Rep. Prog. Phys.*, **29**:255, 1966.

-
- [13] P. R. Saulson. Thermal noise in mechanical experiments. *Phys. Rev. D*, **42**:2437, 1990.
- [14] F. Acernese *et al.* Measurements of Superattenuator seismic isolation by Virgo interferometer. *Astropart. Phys.*, **33**:182, 2010.
- [15] C. M. Caves. Quantum-mechanical noise in an interferometer. *Phys. Rev. D*, **23**:1693, 1981.
- [16] Advanced Virgo GWINC. <https://git.ligo.org/virgo/virgoapp/advgwinc>.
- [17] Wipf, C. SimulinkNb. <https://github.com/cwipf/SimulinkNb>.
- [18] Evans, M. Optickle. <https://github.com/Optickle/Optickle/tree/Optickle2>.
- [19] R. Bonnard *et al.* Upper-limit on the advanced virgo output mode cleaner cavity length noise. *Class. Quantum Grav.*, **34**:175002, 2017.
- [20] A. Masserot and M. Was, Virgo logbook 48718. <https://logbook.virgo-gw.eu/virgo/?r=48718>.
- [21] S Soni *et al.* Reducing scattered light in LIGO’s third observing run. *Class. Quantum Grav.*, **38**(2):025016, jan 2021.
- [22] B. Canuel, E. Genin, G. Vajente, and J. Marque. Displacement noise from back scattering and specular reflection of input optics in advanced gravitational wave detectors. *Optics Express*, **21**(9):10546, apr 2013.
- [23] M. Was and R. Gouaty. AdV+ noise review DET – SDB1/SDB2/SPRB/SNEB/SWEB scattered light noise. Technical Report VIR-1155B-19, 2020.
- [24] F Acernese *et al.* Calibration of advanced virgo and reconstruction of the gravitational wave signal $h(t)$ during the observing run o2. *Class. Quantum Grav.*, **35**(20):205004, sep 2018.
- [25] S. Karki, D. Tuyenbayev, S. Kandhasamy, B. P. Abbott, T. D. Abbott, E. H. Anders, J. Berliner, J. Betzwieser, C. Cahillane, L. Canete, C. Conley, H. P. Daveloza, N. De Lillo, J. R. Gleason, E. Goetz, K. Izumi, J. S. Kissel, G. Mendell, V. Quetschke, M. Rodruck, S. Sachdev, T. Sadecki, P. B. Schwinberg, A. Sottile, M. Wade, A. J. Weinstein, M. West, and R. L. Savage. The advanced LIGO photon calibrators. *Review of Scientific Instruments*, **87**(11):114503, nov 2016.
- [26] D. Estevez, P. Lagabbe, A. Masserot, L. Rolland, M. Seglar-Arroyo, and D. Verkindt. The advanced virgo photon calibrators. Technical Report VIR-0705A-20, 2020.

-
- [27] D Estevez, B Lieunard, F Marion, B Mours, L Rolland, and D Verkindt. First tests of a newtonian calibrator on an interferometric gravitational wave detector. *Classical and Quantum Gravity*, **35**(23):235009, nov 2018.
- [28] F. J. Raab and S. E. WHITCOMB. Estimation of special optical properties of a triangular ring cavity. Technical Report LIGO-T920004, 1992.
- [29] Y. Drori, J Eichholz, T Edo, H Yamamoto, Y Enomoto, G Venugopalan, K Arai, and R X Adhikari. Scattering loss in precision metrology due to mirror roughness. arXiv:2201.05640, 2022.
- [30] Alba Romero-Rodríguez, Mario Martínez, Lluïsa M. Mir, and Hiroaki Yamamoto. Determination of the stray light-induced noise from the baffle in the cryogenic trapping area of advanced virgo in o5. *Galaxies*, **10**(4):86, aug 2022.
- [31] B. Abbott *et al.* Search for gravitational waves associated with 39 gamma-ray bursts using data from the second, third, and fourth LIGO runs. *Phys. Rev. D*, **77**:062004, 2008.
- [32] J. Abadie *et al.* Search for gravitational waves associated with gamma-ray bursts during LIGO science run 6 and Virgo science run 2 and 3. *Astrophys. J.*, **760**:12, 2012.
- [33] B. P. Abbott *et al.* A gravitational-wave standard siren measurement of the Hubble constant. *Nature*, 2017.
- [34] B.P. Abbott *et al.* GW170817: Measurements of neutron star radii and equation of state. *Phys. Rev. Lett.*, **121**(16), oct 2018.
- [35] B. P. Abbott *et al.* Estimating the contribution of dynamical ejecta in the kilonova associated with GW170817. *Astrophys. J.*, **850**(2):L39, dec 2017.
- [36] E. Burns *et al.* A fermi gamma-ray burst monitor search for electromagnetic signals coincident with gravitational-wave candidates in advanced LIGO’s first observing run. *Astrophys. J.*, **871**(1):90, jan 2019.
- [37] R. Hamburg *et al.* A joint fermi-GBM and LIGO/virgo analysis of compact binary mergers from the first and second gravitational-wave observing runs. *The Astrophysical Journal*, **893**(2):100, apr 2020.
- [38] R. Abbott *et al.* GWTC-2: Compact binary coalescences observed by LIGO and virgo during the first half of the third observing run. *Physical Review X*, **11**(2):021053, jun 2021.

- [39] R. Abbott *et al.* GWTC-3: Compact Binary Coalescences Observed by LIGO and Virgo During the Second Part of the Third Observing Run, 2021. arXiv: 2111.03606.
- [40] David Wanderman and Tsvi Piran. The rate, luminosity function and time delay of non-collapsar short GRBs. *MNRAS*, **448**(4):3026, mar 2015.
- [41] R. Abbott *et al.* Population of merging compact binaries inferred using gravitational waves through GWTC-3. *Physical Review X*, **13**(1):011048, mar 2023.
- [42] R. Abbott *et al.* Search for gravitational waves associated with gamma-ray bursts detected by fermi and swift during the LIGO–virgo run o3b. *Astrophys. J.*, **928**(2):186, apr 2022.

Appendix A

Upper-limit on the Advanced Virgo output mode cleaner cavity length noise

Upper-limit on the Advanced Virgo output mode cleaner cavity length noise

**R Bonnard, M Ducrot, R Gouaty, F Marion, A Masserot,
B Mours, E Pacaud, L Rolland, M Was**

Laboratoire d'Annecy-le-Vieux de Physique des Particules (LAPP), Université Savoie Mont Blanc, CNRS/IN2P3, F-74941 Annecy, France

E-mail: michal.was@lapp.in2p3.fr

Abstract. The Advanced Virgo detector uses two monolithic optical cavities at its output port to suppress higher order modes and radio frequency sidebands from the carrier light used for gravitational wave detection. These two cavities in series form the output mode cleaner. We present a measured upper limit on the length noise of these cavities that is consistent with the thermo-refractive noise prediction of 8×10^{-16} m/Hz^{1/2} at 15 Hz. The cavity length is controlled using Peltier cells and piezo-electric actuators to maintain resonance on the incoming light. A length lock precision of 3.5×10^{-13} m is achieved. These two results are combined to demonstrate that the broadband length noise of the output mode cleaner in the 10-60 Hz band is at least a factor 10 below other expected noise sources in the Advanced Virgo detector design configuration.

PACS numbers: 04.80.Nn, 95.55.Ym

1. Introduction

Advanced interferometric gravitational wave detectors, such as Advanced Virgo [1], advanced LIGO [2], or GEO-HF [3] are making first detections or are about to start observations. All these detectors are using a special case of homodyne detection called DC readout [4, 5] to extract the differential arm length signal from the light at the interferometer output, that is the carrier light. A crucial element in the DC readout detection scheme is an output mode cleaner (OMC), which is a non-degenerate optical cavity that transmits only the fundamental Gaussian mode at the carrier frequency. The purpose is to keep only light which leaves the interferometer due to a gravitational wave signal and remove higher order modes caused by interferometer mirror defects and radio-frequency sidebands used for the control of auxiliary degrees of freedom.

One drawback of this scheme is that any length noise of the OMC cavity is imprinted on the transmitted light if the cavity length is not perfectly adjusted to the carrier frequency. The coupling factor is proportional to the root-mean-square of the difference between light carrier frequency and cavity resonant frequency.

A very low cavity length noise of a few 10^{-17} m/Hz^{1/2} at 1 Hz has been obtained for rigid cavities [6], however these have no means to tune the cavity length to follow the light frequency at the output of the interferometer. Although a scheme has been proposed to remove the need for cavity length actuator [7], all current detectors have actuators on the OMC length that may introduce additional length noise.

For advanced LIGO and GEO-HF the OMC is a 4-mirror bow-tie cavity with one of the mirrors directly mounted on a piezo-electric actuator (PZT) [2, 8], an upper limit of 2×10^{-14} m/Hz^{1/2} on the cavity length noise introduced by this PZT has been measured in the 1-7 kHz band [8]. Advanced Virgo chose an alternative, more compact design with a single piece of fused silica forming a 4 surface bow-tie cavity [1] (see figure 1), based on previous experience from Virgo [9]. The cavity optical length can be controlled with two actuators, a Peltier cell that thermally changes the refractive index in the cavity and hence the optical length, and a PZT pressing the OMC transversely and allowing a fast control of the refractive index but with a low dynamic range. This choice should have the advantage of reducing noise from mechanical vibration and from the PZT, but has the drawback of light circulating in the substrate instead of vacuum, which among other things introduces additional thermal noise [10]. In order to obtain sufficient light filtering without introducing high thermal noise and large scattered light losses, two monolithic cavities are placed in series instead of a single cavity with high finesse.

In this paper we present an upper limit on the Advanced Virgo OMC length noise and the achieved precision of the OMC length control in a table top measurement. By combining these two measurements we derive the expected contribution of the OMC length noise to the Advanced Virgo measurement noise. In section 2 we discuss in detail the expected thermal length noise of the OMC and its coupling to the gravitational wave measurement, then in section 3 we describe the test measurement setup. Section 4 presents the length noise upper limit and section 5 the length control precision.

2. Advanced Virgo Output Mode Cleaner

The optimization of parameters for the Advanced Virgo OMC led to a design composed of two monolithic fused silica cavities in series [10], which allows good radio frequency

refractive index	n	1.44963
refractive index temperature dependence	β	-10^{-5} K^{-1}
density	D	2200 kg/m^3
thermal conductivity	κ	$1.38 \text{ W m}^{-1} \text{ K}^{-1}$
temperature	T	300 K
specific heat	C	$746 \text{ J K}^{-1} \text{ kg}^{-1}$

Table 1. Fused silica parameters for thermo-refractive noise calculation (5)

filtering with low finesse and short cavities. Each OMC cavity is a single piece of fused silica with an elongated hexagon shape. The cavity has an effective length $L = 0.124 \text{ m}$ (half of the round-trip length) which corresponds to an optical path length $l_0 = nL$ where n is the fused silica refractive index. The cavity finesse was measured to be $F \simeq 125$ and internal cavity losses at $\sim 1.5\%$ [11]. One of the cavity surfaces is curved, with a radius of 1.7 m, and the beam resonating in the cavity has a waist $w_0 = 321 \mu\text{m}$ located at the cavity input surface.

The cavity couples the fluctuations in optical path length l to power fluctuations δP of the transmitted light

$$\frac{\delta P}{P_0} = \frac{1}{1 + \left(\frac{2F}{\pi}\right)^2 \sin^2 \frac{2\pi l}{\lambda}} - 1, \quad (1)$$

where $\lambda = 1064 \text{ nm}$ is the laser wavelength. In practice the optical path fluctuations are dominated by low frequency fluctuations, hence we decompose the cavity length fluctuations into a large dynamic, low frequency (below 10 Hz) component with root-mean-square (RMS) Δl_{rms} and a small component δl in the sensing band of Advanced Virgo (10 Hz–10 kHz)

$$l = l_0 + \Delta l_{\text{rms}} + \delta l. \quad (2)$$

Using this decomposition, (1) can be approximated above 10 Hz by

$$\frac{\delta P}{P_0} \simeq -32 F^2 \frac{\Delta l_{\text{rms}} \delta l}{\lambda^2}. \quad (3)$$

The corresponding noise on the gravitational wave signal is directly given by the power fluctuations in transmission of the OMC divided by interferometer response transfer function O_{TF} . Hence the OMC length noise coupling into the gravitational wave signal is

$$\delta h = -32 \sqrt{2} \frac{F^2 \Delta l_{\text{rms}} \delta l}{\lambda^2 O_{\text{TF}}}, \quad (4)$$

where the additional factor $\sqrt{2}$ comes from adding in quadrature the length noise of the two OMC cavities, which is expected to be caused by statistical fluctuations in the substrate temperature and therefore independent.

Indeed, compared to a 4 mirror cavity design, a monolithic cavity has additional thermal fluctuations from the medium in which light circulates. Given that the thermal expansion coefficient of fused silica $\alpha = 5 \times 10^{-7} \text{ K}^{-1}$ is small compared to the changes of the refractive index as a function of temperature $\frac{dn}{dT} = \beta = -10^{-5} \text{ K}^{-1}$, the dominant thermal length noise is thermo-refractive noise. There is also a contribution from Brownian noise and from all coatings thermal noises, but these are also negligible compared to thermo-refractive noise.

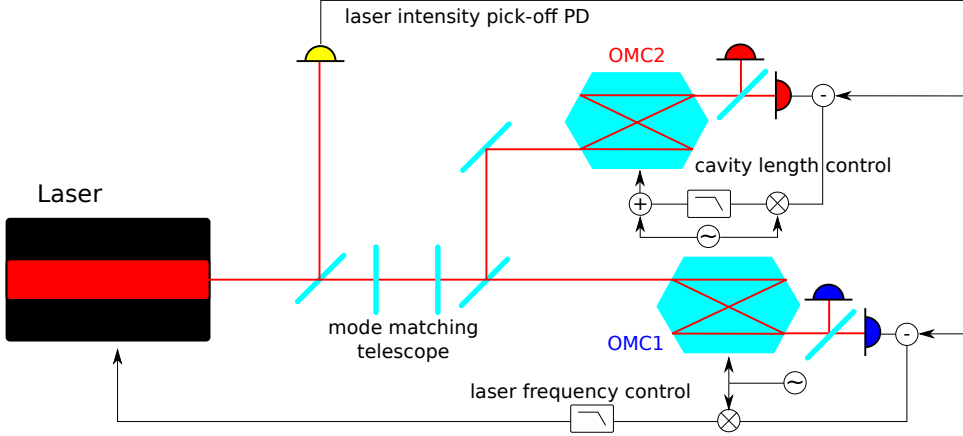


Figure 1. Schematic of the optical test setup (not to scale). The two OMC cavities OMC1 and OMC2 are set in parallel and each receives 45% of the laser beam, which in transmission of each cavity is split equally onto an in-loop and an out-of-loop PD. The flow of signal for the subtraction of laser intensity noise, the laser frequency control and the cavity length control is shown by arrows.

Thermo-refractive noise has been computed as a function of frequency f for an infinite plane of thickness L in appendix E of [12] and can be rewritten as

$$\delta l_{\text{thermo-refractive}}(f) \simeq \frac{2\beta T \sqrt{L k_B \kappa}}{DC \sqrt{\pi}} \frac{1}{(w_0/\sqrt{2})^2 2\pi f} \left[\int_0^\infty \frac{x dx}{1 + \frac{4r_{\text{th}}^2}{w_0^2} x^2} e^{-x} \right]^{1/2}, \quad (5)$$

where k_B is the Boltzmann constant, $r_{\text{th}} = \sqrt{\kappa/(2\pi f DC)}$ is the thermal path length, $L = 0.124\text{ m}$ is half of the cavity round-trip length and the values of the different parameters for fused silica are given in table 1. The integral term equates to 1 in the adiabatic limit where $r_{\text{th}} \ll w_0$. At low frequencies where $r_{\text{th}} \gg w_0$, the integral term is $\propto f$, hence the thermo-refractive noise remains bounded at low frequency. The transition between the two regimes occurs at $f \sim 1.3\text{ Hz}$ for the OMC cavity. The same result has been obtained more recently for a finite cavity of cylindrical geometry [13], which restrains its validity to the range where r_{th} is much larger than the wavelength and much smaller than the transverse size of the cavity (1 cm). This corresponds to a valid frequency range of 10 mHz–100 kHz, which covers well the frequency range of interest here. The principle of these computations has been confirmed by measuring thermo-refractive noise in a very different geometry of whispering-gallery mode of microspheres [14].

In section 4 we measure that the cavity length noise at 10 Hz is not larger than the one predicted by (5).

3. Experimental setup

The OMC cavity length fluctuations are measured using a dedicated optical test setup. The setup is located on a passively isolated optical bench, enclosed in aluminium and plexiglas covers placed on a tubular structure to prevent beam jitter from the clean room air flow. A schematic of the optical layout is shown on figure 1. A small

fraction (10%) of the light from a 2 W Mephisto laser [15] at 1064 nm is picked-off to a photo-diode (PD) to measure the laser intensity noise; the main part of the beam is matched with a telescope to two cavities set in parallel. This is different from the Advanced Virgo case where the two cavities are placed in series, and allows a simple measurement where light seen by one cavity is not directly affected by the other. For each cavity two PDs measure the transmitted power, which is between 30 mW and 80 mW depending on the PD.

To obtain an error signal for the cavity length, a dithering sine-wave, at a dozen kHz is applied to each cavity by a PZT. The cavity length error point is the PD signal demodulated at the dither frequency. This signal is limited by the laser intensity noise at the dither frequency. With the active power stabilization loop enabled (“noise eater” [15]), the laser intensity noise at a dozen kHz has a relative intensity $\sim 2 \times 10^{-7} \text{ Hz}^{-1/2}$. This laser intensity is measured by a pick-off PD and subtracted before demodulation.

The length error point is calibrated by scanning linearly the laser frequency over several cavity free spectral ranges, each free spectral range corresponding to a cavity length change of $\lambda/2$, as can be seen from (1). The measurement has an absolute statistical error of 2–3% and the systematic error from using the cavity length as a reference is less than 1%. Consequently the relative calibration is adjusted by several percent to obtain a good cancellation of common frequency noise between the two cavities. This cancellation is described in section 4.

4. Cavity length noise measurement

In our measurement the laser frequency noise is dominant. Hence we lock the laser onto the length of OMC1 with a bandwidth of $\sim 250 \text{ Hz}$ to reduce the frequency noise, and leave the OMC1 cavity length free. The OMC2 length is locked onto the laser frequency using Peltier cells and the PZT actuator with a loop unity gain frequency around 0.2 Hz.

Laser frequency noise $\delta\nu$ couples to transmitted light fluctuation δP in the same way as cavity length noise as shown in (1). The spectra of the two cavities length error points are shown on figure 2 and are dominated by laser frequency noise. This frequency noise is equivalent to cavity length noise δl_{laser} using the relation

$$\frac{\delta\nu}{\nu} = -\frac{\delta\lambda}{\lambda} = \frac{\delta l_{\text{laser}}}{l_0}, \quad (6)$$

with $\nu = 2.82 \times 10^{14} \text{ Hz}$ the light frequency. With this notation and dismissing other noise contributions the cavity calibrated error point can be written as

$$\text{EP}_{\text{OMC}} = \delta l_{\text{OMC}} + \delta l_{\text{laser}}. \quad (7)$$

Hence the difference between the two cavities

$$\text{EP}_{\text{diff}} = \text{EP}_{\text{OMC1}} - \text{EP}_{\text{OMC2}} = \delta l_{\text{OMC1}} - \delta l_{\text{OMC2}} \quad (8)$$

should be a good measure of the differential length, free of the common laser frequency noise. This is a true representation of the cavity differential length above 10 Hz as the OMC1 length is free and the OMC2 length control loop has a gain well below 1. However, some of the laser frequency noise is re-injected by PZT feedback of the OMC2 length control, as the loop gain at 10-100 Hz is ~ 0.02 and not zero. This means that in addition to OMC2 free cavity length noise there is a loop feedback contribution $\delta l_{\text{OMC2}} = \delta l_{\text{OMC2, free}} + \delta l_{\text{OMC2, PZT}}$. The latter can be easily subtracted as the

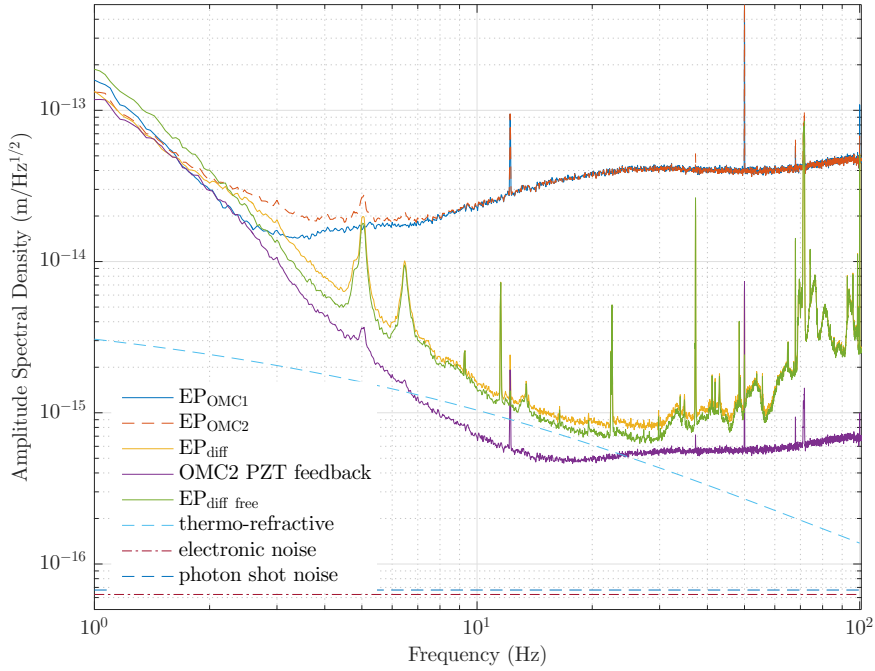


Figure 2. Differential OMC length noise measurement over 1.5 hours of data. Shown are the calibrated length error points for OMC1 and OMC2, their difference (8), and the difference with the OMC2 PZT feedback subtracted (9). For reference the expected thermo-refractive noise is shown along with electronic and photon shot noise.

feedback voltage is known and the cavity has a flat response of $\chi = 2.6 \times 10^{-11}$ m/V at these frequencies, hence we define the loop corrected differential length as

$$EP_{\text{diff free}} = EP_{\text{OMC1}} - (EP_{\text{OMC2}} - \chi PZT_{\text{OMC2}}) = \delta l_{\text{OMC1,free}} - \delta l_{\text{OMC2,free}}. \quad (9)$$

These noise curves are shown on figure 2 averaged over 1.5 hours of data, and we have checked that this noise level is stationary at the few minutes time scale. Also shown are the PD electronic noise measured with the laser switched off and the expected photon shot-noise. For comparison the thermo-refractive noise of the two cavities from 5 added in quadrature is also shown. The measured cavity differential length shows many lines due to mechanical resonances of components on the optical bench, especially above 60 Hz the measurement is completely spoiled. At lower frequencies, the broad lines at 5 Hz and 6.5 Hz come from the tubular posts that hold plexiglas covers to prevent air-flow, and their coupling depends on the torque applied to the PZT clamping. Below 10 Hz there are large fluctuations that are not understood. Nonetheless in the 10-20 Hz band the measured noise is within 10% of the thermo-refractive prediction, and is an upper-limit that no length noise is larger than this prediction.

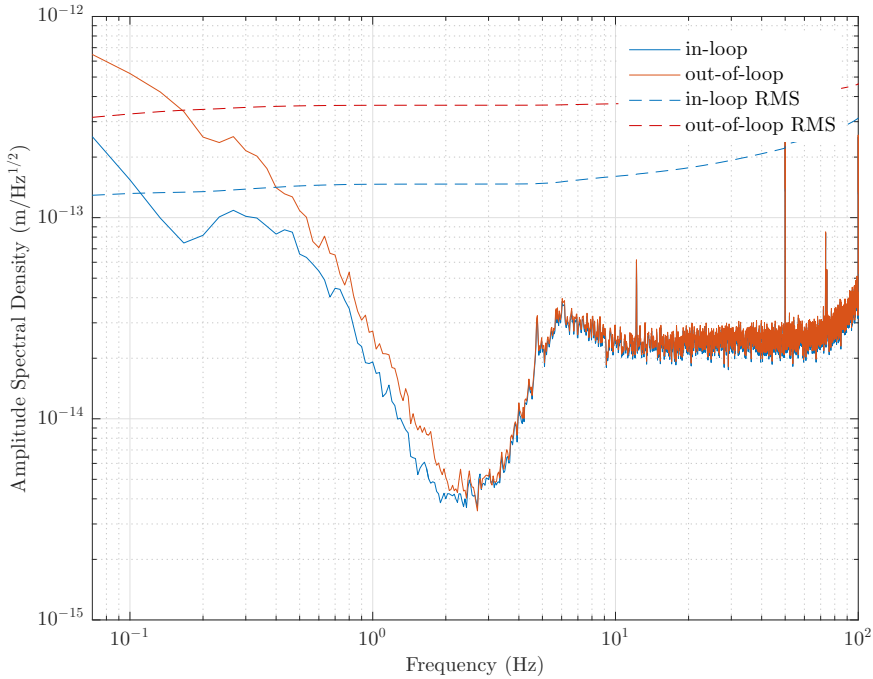


Figure 3. Spectra of the in-loop and out-of-loop measures of the OMC2 cavity length. The integrated low-frequency RMS of both signals are also shown. Above 5 Hz the signal is dominated by laser frequency noise, which is slightly lower than in figure 2 due to higher gain laser frequency control. Below that frequency the out-of-loop length RMS is 3.5×10^{-13} m.

5. Length control precision

The cavity length fluctuations couple to the gravitational wave detector sensitivity through (4), where the lock precision Δl_{rms} is a critical parameter. In section 4 we used a low gain on the OMC2 cavity length control to limit re-injecting frequency noise with the loop and to simplify the result interpretation. To improve the lock precision, the OMC is operated with a factor 10 higher loop gain and a unity gain at a few Hz. As in the previous section the loop feedback is dominated by the Peltier cells temperature feedback below 0.1 Hz and by the PZT feedback above this cross-over frequency. Figure 3 shows the OMC2 error point spectrum for a high gain loop using the in-loop and out-of-loop PD. This achieves $\Delta l_{\text{rms}} = 3.5 \times 10^{-13}$ m for the out-of-loop signal, over 3 times lower than the design requirement [1].

In Advanced Virgo the precision of the laser lock onto the reference cavity is ~ 1 Hz RMS [1], which through 6 is equivalent to 4.4×10^{-16} m, that is a laser frequency control orders of magnitude better than the one achieved here. Therefore in the real case the laser frequency should not be dominant as in the test setup presented here, and the OMC lock precision should be easily reproduced even with a lower control loop gain.

Using 4 we combine the achieved lock precision Δl_{rms} and the measured upper limit on cavity noise δl shown in figure 2 to obtain the expected contribution of OMC length noise to the Advanced Virgo measurement noise shown on figure 4.

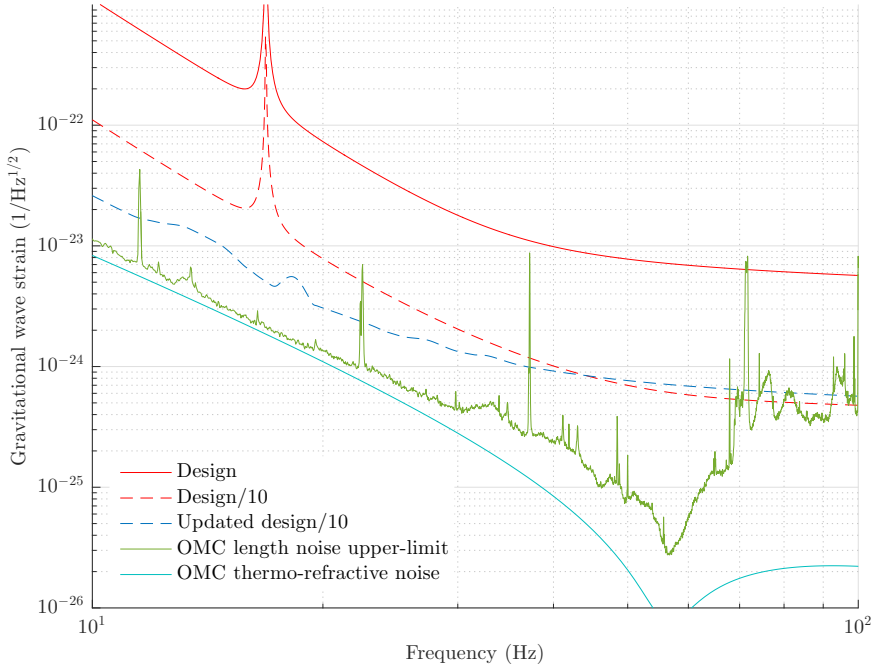


Figure 4. Projection of the upper-limit on OMC length noise from figure 2 onto the Advanced Virgo design noise curve assuming a lock precision of 3.5×10^{-13} m and a detuned signal recycling configuration. The original design and updated design Advanced Virgo noise curves are shown.

Below 60 Hz this expected broadband noise is at least 10 times smaller than the Advanced Virgo design sensitivity [10] or the updated sensitivity expectation using more accurate suspension thermal noise models [1]. Above 60 Hz the measured OMC length noise upper limit is dominated by mechanical resonance of the measurement setup, nonetheless it remains below the design sensitivity curve. In Advanced Virgo these resonances should not be present as the OMC will be placed on a suspended bench in vacuum.

The prominent lines at 11.53 Hz, 22.53 Hz and 37.23 Hz are narrow, with respective linewidths of 30 mHz, 100 mHz and 30 mHz. Hence regardless of whether these are real length noise or a sensing noise of this particular measurement, these lines will not have an impact on the broadband gravitational wave sensitivity that is relevant for most gravitational wave signals, such as coming from compact binary coalescences [16].

Note that in the initial broadband configurations [10] the constraints on the OMC length noise are ~ 10 weaker than in the configuration optimized for binary neutron star detection. Indeed, without signal recycling or with signal recycling tuned the optical gain at 10 Hz is about an order of magnitude higher, hence the OMC length noise coupling in these cases is 10 times smaller at low frequency than presented here.

6. Conclusions

We have measured an upper limit on the Advanced Virgo OMC cavity length noise. In the 10-20 Hz band this upper limit is consistent with the thermo-refractive noise prediction, confirming that there is no other significant length noise in this cavity design.

We achieved a lock precision of $\Delta l_{\text{rms}} = 3.5 \times 10^{-13}$ m, which is a factor 17 better than obtained previously for the Virgo OMC [10]. Combining these two results we have shown that the OMC length noise contribution to the Advanced Virgo measurement should be at least a factor 10 below other expected noise sources in the 10-60 Hz band, which is most challenging for technical noises. This gives confidence that the OMC noise should not be a limiting factor in the forthcoming Advanced Virgo observations.

The achieved gap between the expected OMC noise contribution and Advanced Virgo noise opens the prospects of further parameter optimization depending on the issues encountered during the first Advanced Virgo operations. For example the radio-frequency sideband filtering could be improved by an order of magnitude by increasing the OMC finesse by a factor 2. This would increase the thermo-refractive noise by a factor 4 but it would still remain a factor 10 below other expected noises.

Acknowledgments

We would like to thank our Advanced Virgo collaborators for numerous discussions that lead to the design and optimization of the OMC cavities discussed here.

References

- [1] F. Acernese et al. Advanced Virgo: a second-generation interferometric gravitational wave detector. *Class. Quantum Grav.*, 32:024001, 2015.
- [2] J. Aasi et al. Advanced LIGO. *Class. Quantum Grav.*, 32:074001, 2015.
- [3] K. L. Dooley et al. GEO 600 and the GEO-HF upgrade program: successes and challenges. *Class. Quantum Grav.*, 33:075009, 2016.
- [4] S. Hild et al. DC-readout of a signal-recycled gravitational wave detector. *Class. Quantum Grav.*, 26:055012, 2009.
- [5] T. Fricke et al. DC readout experiment in Enhanced LIGO. *Class. Quantum Grav.*, 29:065005, 2012.
- [6] K. Numata, A. Kemery, and J. Camp. Thermal-noise limit in the frequency stabilization of lasers with rigid cavities. *Phys. Rev. Lett.*, 93:250602, dec 2004.
- [7] G. Vajente and J. Marque. Controlling advanced gravitational wave detector output mode cleaners acting on the laser frequency. *Astropart. Phys.*, 41:45, 2012.
- [8] M. Prijatelj et al. The output mode cleaner of GEO 600. *Class. Quantum Grav.*, 29:055009, 2012.
- [9] F. Beauville et al. Improvement in the shot noise of a laser interferometer gravitational wave detector by means of an output mode-cleaner. *Class. Quantum Grav.*, 23:3235, 2006.
- [10] T. Accadia et al. Advanced Virgo Technical Design Report. Technical report, 2012. VIR-0128A-12.
- [11] M. Ducrot et al. Measurements of Advanced Virgo OMC cavities finesse. Technical report, 2014. VIR-0458A-14.
- [12] V. B. Braginsky and S. P. Vyatchanin. Corner reflectors and quantum-non-demolition measurements in gravitational wave antennae. *Phys. Lett. A*, 324:345, 2004.
- [13] D. Heinert, A. G. Gurkovsky, R. Nawrodt, S. P. Vyatchanin, and K. Yamamoto. Thermorefractive noise of finite-sized cylindrical test masses. *Phys. Rev. D*, 84:062001, 2011.
- [14] M. L. Gorodetsky and I. S. Grudin. Fundamental thermal fluctuations in microspheres. *J. Opt. Soc. Am. B*, 21:697, 2004.
- [15] *Mephisto Product Line User's Manual*, 2003.

- [16] B. P. Abbott et al. Binary Black Hole Mergers in the First Advanced LIGO Observing Run. *Phys. Rev. X*, 6:041015, 2016.

Appendix B

Requirement on relative amplitude modulation noise for O4

Requirement on relative amplitude modulation noise for O4

M. Waş, J. Casanueva, F. Nocera, M. Mantovani
VIR-1225B-19

December 9, 2019

Abstract

The relative amplitude modulation noise of the 56MHz sideband is affecting the Advanced Virgo sensitivity during the O3 run. Here we compute the requirement on this noise for O4 that is needed to prevent it from limiting the sensitivity.

1 Introduction

In this technical note we discuss the contribution of the relative amplitude modulation noise to the Advanced Virgo noise curve during O3, and compute the requirements for this noise for O4. The requirement is summarized in figure 7, and corresponds to a factor 10 reduction in the relative amplitude noise in order to keep it a factor 10 below the noise curve during O4. It is mandatory to have this improvement for the radio frequency sidebands that resonate inside the central interferometer (nominally 6 MHz and 56 MHz), but it is preferable to have it for all sidebands that are transmitted by the input mode cleaner, so also the 8 MHz sideband.

2 Level of relative amplitude modulation noise

The noise of the LNFS generator and RF amplifier has been measured in the laboratory [1]. The measurement is shown on figure 1, and it is in terms of RF voltage amplitude fluctuation divided by the mean amplitude of the voltage. It shows that the LNFS generator is the dominating noise contributor up to 500 Hz, above the 2 W amplifier adds another noise to it. Note that this additional bump at ~ 4 kHz is not present for the 1 W RF amplifier.

This amplitude modulation noise is then applied to the electro-optic modulator that generate RF sidebands around the carrier laser light. The relative amplitude noise of this sidebands is equal to the relative amplitude modulation noise. As the intensity of the sideband is equal to the square of the amplitude, the relative intensity noise (RIN) of the sideband is double the relative amplitude noise. Indeed, if we denote by W the light intensity and by V the light amplitude then

$$\frac{W + \delta W}{W} = \frac{(V + \delta V)^2}{V^2} \simeq \frac{V^2 + 2V\delta V}{V^2} \quad (1)$$

$$\frac{\delta W}{W} = 2 \frac{\delta V}{V}. \quad (2)$$

The sidebands are then filtered by the input mode cleaner (IMC) that has a cavity pole measured to be

at 520 Hz [2], which attenuates the amplitude fluctuations at high frequency. The sidebands are resonating in the central interferometer but are rejected by the arms, as the central interferometer cavities are shorter and lower finesse than the IMC. Hence the sideband amplitude noise arrives almost unchanged at the output of the interferometer.

This is confirmed by measurements. The B1s1 photodiode receives the light reflected by the first output mode cleaner (OMC). Above 30 Hz the spectrum is dominated by the 56 MHz sideband RAM as demonstrated by varying the 56 MHz modulation index which changes the level of noise observed on the B1s1 and B1p photodiodes [3]. Moreover, by scanning the first OMC, the amount of power for the upper and lower 56 MHz sideband impinging on the OMC can be measured, which allows to normalize the measured spectrum of power fluctuation into a RIN. Figure 2 shows the measured RIN on B1s1, for comparison the RIN at the output of the EOM, and after filtering by the IMC is also shown. The measured RIN at the interferometer output matches perfectly the expectation from the measured 2W amplifier output filtered by the IMC.

3 Filtering of RAM by OMC

The 56 MHz filtering by the OMC has been measured on two occasions [4]. In January 2019, by injecting a narrow band line into the 56 MHz modulation amplitude noise, and in August 2019 by injecting a broadband noise into the 56 MHz modulation amplitude noise. By observing the height of the narrow band line or broadband noise before and after each OMC the filtering of each OMC can be estimated. For the January 2019 this yielded a factor 230 for OMC1 and a factor 25 for OMC2. In August 2019 it yielded a factor 130 for OMC1 and a factor 10 for OMC2. The January 2019 results correspond to $10 \mu\text{W}$ of 56 MHz light reaching the B1 photodiodes.

The theoretical filtering by an OMC is given by

$$T_{\text{OMC}} = \frac{1}{(1 + (2F/\pi)^2 (\sin(-2\pi f_{\text{mod}} l_{\text{opt}}/c))^2)}, \quad (3)$$

where $l_{\text{opt}} = 2 \times 1.44963 \times 62$ mm is the OMC optical

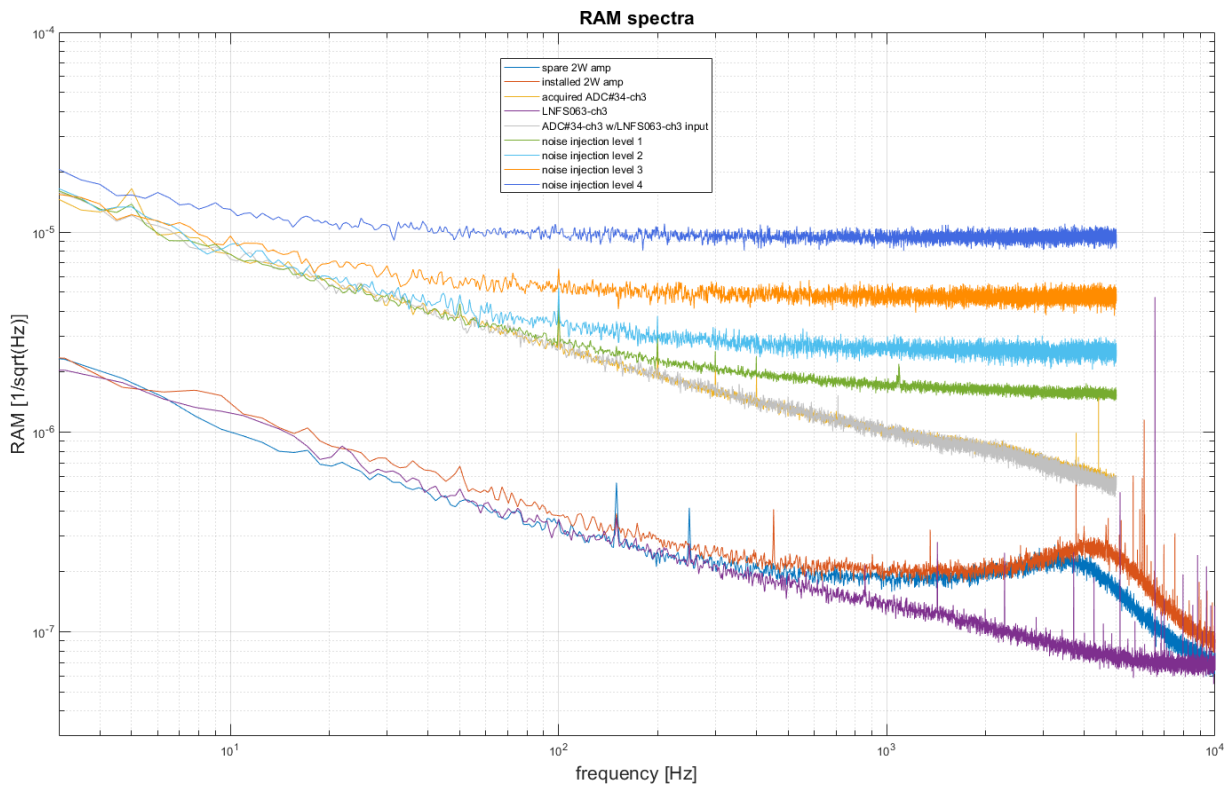


Figure 1: RAM noise measured for the LNFS and after amplification by the 2W amplifier. The noise of the LNFS generator is in purple, and the noise once amplified by the 2W amplifier is shown in red (installed amplifier) and blue (spare amplifier).

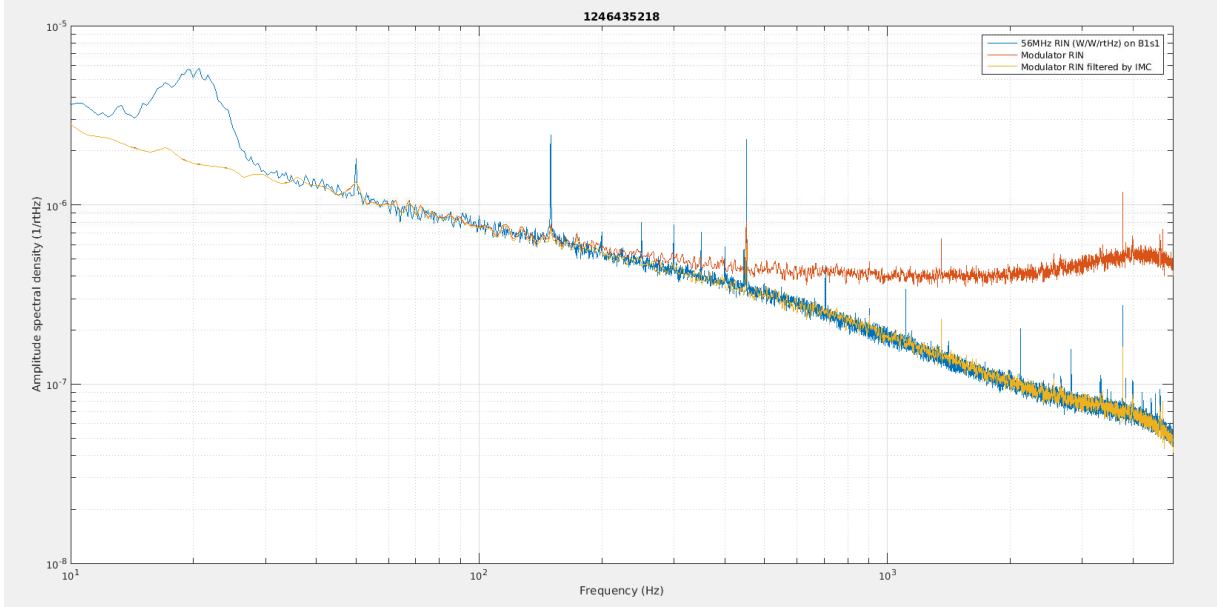


Figure 2: RIN

length, $F = 125$ is the finesse, $f_{mod} = 56$ MHz is the modulation frequency and c is the speed of light. This yields $T_{OMC} = 3.5 \times 10^{-3}$, compared to the best measure value of $T_{OMC} = 4.3 \times 10^{-3}$. The most surprising is why the OMC2 filtering is so much worse than OMC1. This has been understood, as the transmission of OMC1 is dominated by the order 1 mode of the 56 MHz which is ~ 10 times filtered by an OMC cavity than the order 0 mode [5].

In any case the measured filtering by the two OMCs is in between 1.7×10^{-4} and 7.7×10^{-4} , taking the average of these two 4.7×10^{-4} matches well the measured coupling of the 56 MHz sideband RAM into the sensitivity curve. Figure 3 shows the projected 56 MHz RAM assuming the measured 60 mW of 56 MHz sideband reaching the interferometer output and the B1 photodiode shot noise level for 2.8 mW of carrier light passing through the OMCs. Note that in practice the shot noise is a factor $\sqrt{2}$ smaller due to squeezing, so the sideband RAM is at the same level as shot noise at 100 Hz.

This projection has also been integrated into the

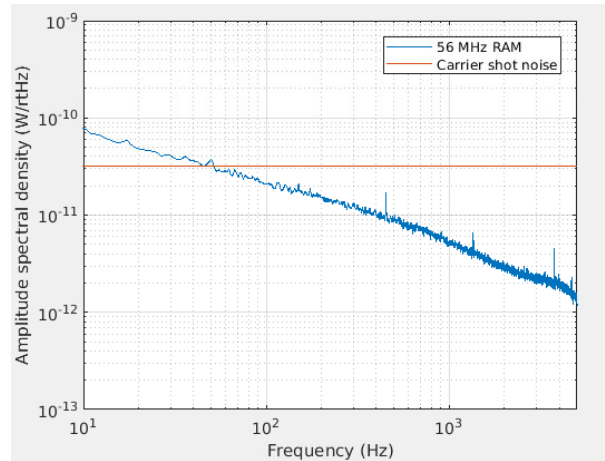


Figure 3: 56 MHz sideband RAM projection compared to the unsqueezed B1 shot noise

global noise budget. Figure 4 shows the projection based on the computation above, and a projection based on measuring directly the transfer function between the B1s1 photodiode and the sensitivity, as the two are coherent. The two projections agree well with each other

4 O4 simulations

To specification for O4 on the RF sideband RAM lets start by repeating the above projection for the O4 configuration with 40 W of input laser power and 40% transmittivity of the signal recycling mirror. We will conservatively assume a modulation index of $m = 0.25$ as this the modulation currently used for the 56 MHz sideband. We also assume a dark fringe offset yielding 2.8 mW of carrier TEM00 light at the interferometer output. We consider the nominal 6 MHz and 56 MHz sidebands, but also the tentative plans of replacing the 6 MHz modulation with either a modulation at 31 MHz or 44 MHz.

The results are summarized in in table 1, in particular there is 10 mW of 6 MHz power (upper and lower sideband added together) and 599 mW of 56 MHz power (upper and lower sideband added together) at the interferometer output. These powers do not depend significantly on the exact value of the dark fringe offset. Independent simulations were performed with Finesse that yield results within 10% of these.

For O4 the plan is to replace the double output mode cleaner (OMC) with a single OMC of higher finesse ($F \sim 1000$), which is expected to transmit 4.4×10^{-3} of the 6 MHz sideband and 5.5×10^{-5} of the 56 MHz sideband.

The simulations to obtain the sideband powers are performed calling a script¹ These are then input into the projection using a function in gwinc² These yield figure 5 where the coupling is almost the same for all sidebands. This is in line with the power on the B1 photodiode given in table 1. The reason is that

¹https://svn.ego-gw.it/svn/advsw/NoiseBudgets/simulinkNoiseBudget/DRITF/run_DRITF_NB.m

²<https://git.ligo.org/michal-was/advgwinc/blob/master/noise/technical/RIN56MHz.m>

for higher frequencies the Schnupp asymmetry has a larger impact, so a larger sideband power leaks to the anti-symmetric port of the interferometer. However the larger frequency sideband are better filtered by the OMC, and the two effects compensate each other.

In addition to the TEM00, there might be higher order mode on the sidebands. We consider here the order 1 and order 2 modes, taking into account that the OMC radius of curvature is 1.7 meters, and assuming there is 10% of power in the order 1 mode and order 2 mode each. During O3 the 56 MHz order 1 mode has about 10 times less power than the TEM00 [5]. The result is shown on figure 6, only the order 1 mode of the 56 MHz is relevant.

5 O4 specification

To derive a specification we assume that only the 56 MHz and 6 MHz sideband are present, and that the two are added in quadrature. The case when the 6 MHz is replaced by 31 MHz or 44 MHz are very similar. On figure 7 are the requirements in order for the RAM noise to be a factor 10 below the expected O4 sensitivity.

The sideband RAM is also polluting the power stabilization error signal, this has been evaluated [6], the result is shown on figure 8. The RAM contribution is a factor 2 above the power stabilization error signal shot noise. The power stabilization noise itself is a factor ~ 30 below the current sensitivity curve [7], but it would preferable to keep the error signal clean, by reducing the RAM noise by a factor 10. The factor 10 is in any case the requirement given on figure 7. This would require to implement this solution for all sidebands used in low noise operations, in particular also for the 8 MHz sideband.

The RAM specification seem feasible, in the Advanced Virgo TDR a prototype active stabilization is shown that has a noise level of $3 \times 10^{-8} \frac{1}{\sqrt{\text{Hz}}}$, and for LISA pathfinder an active stabilization was implemented that has an out of loop noise of $1 \times 10^{-8} \frac{1}{\sqrt{\text{Hz}}}$ (see figure 9). During O4, an active stabilization of RAM noise will be necessary for the two sidebands resonating in the central interferometer (nominally 6 MHz and 56 MHz), without it the sensitivity will

be significantly impacted between 20 Hz and 200 Hz. It would also be preferable for the sidebands that are transmitted by the input mode cleaner and reach the power stabilization photodiodes (nominally 6 MHz, 8 MHz and 56 MHz).

Note that this specification assumes that the new high finesse OMC will perform as well as the theory predict, so an even lower RAM noise might be needed if the new OMC is under performing. This would of course push the requirements on the RAM stabilization even further down in an attempt to compensate for the OMC flaws. While, as reported, a factor a few times better than what already achieved in the past seems within reach, it is important not to consider this as a silver bullet. First of all, recent communication from the LNFS-100 manufacturer have rule out the possibility of improving performance at the source (they are going to be exactly what they currently are) and some sort of red flag has been raised as far as the impact of an amplitude stabilization scheme could have on the synthesizer performance in term of Phase Noise. Although measurement made to that end at the time of AdV TDR writing did not find any impact on the generator Phase Noise, we can not rule out at this time that further improvement in the amplitude noise stabilization could be detrimental to the phase noise. In addition to that, the stabilization scheme under consideration is not far from reaching the best performance theoretically possible with such solution. So in the worst case scenario that the new OMC design is a failure, further improvement on RAM suppression would be needed compared to what is shown in figure 7, but with the caution expressed above.

References

- [1] B. Montanari, F. Nocera, F. Paoletti, logbook entry 46555
- [2] E. Genin, M. Mantovani, G. Pillant, logbook entry 31879
- [3] M. Was, logbook entry 43030
- [4] M. Was, logbook entry 46637
- [5] M. Was, logbook entry 47115
- [6] M. Was, logbook entry 47080
- [7] W. Chaibi, A. Chiummo, for AdV+ PSL/INJ team, VIR-0899A-19

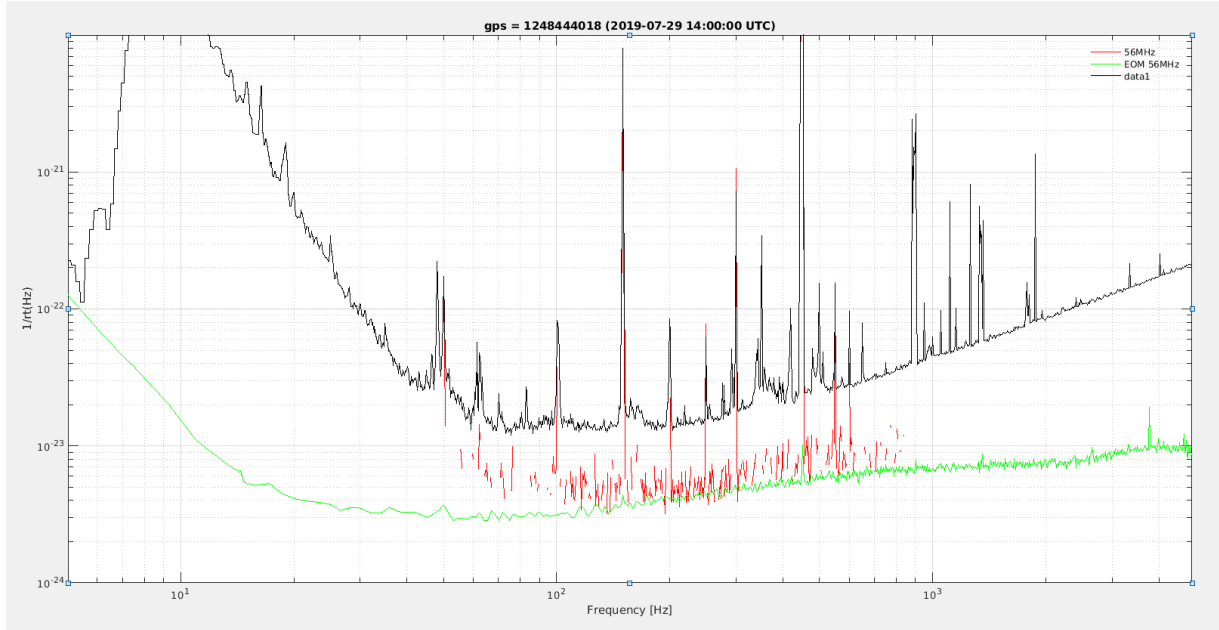


Figure 4: Amplitude spectral density of $h(t)$ in black, of the projection based on the computed coupling of the generator RAM in green, and the measured coupling between the B1s1 and $h(t)$ in red. The last two agree very well with each other and are a factor ~ 4 below the sensitivity curve.

sideband frequency	modulation index	ITF output power	OMC transmission	B1 PD power
6 MHz	0.25	10 mW	4.4×10^{-3}	44 μ W
56 MHz	0.25	599 mW	5.5×10^{-5}	33 μ W
31 MHz	0.25	227 mW	1.8×10^{-4}	41 μ W
44 MHz	0.25	404 mW	9.1×10^{-5}	37 μ W

Table 1: Table of sideband parameters and simulation results

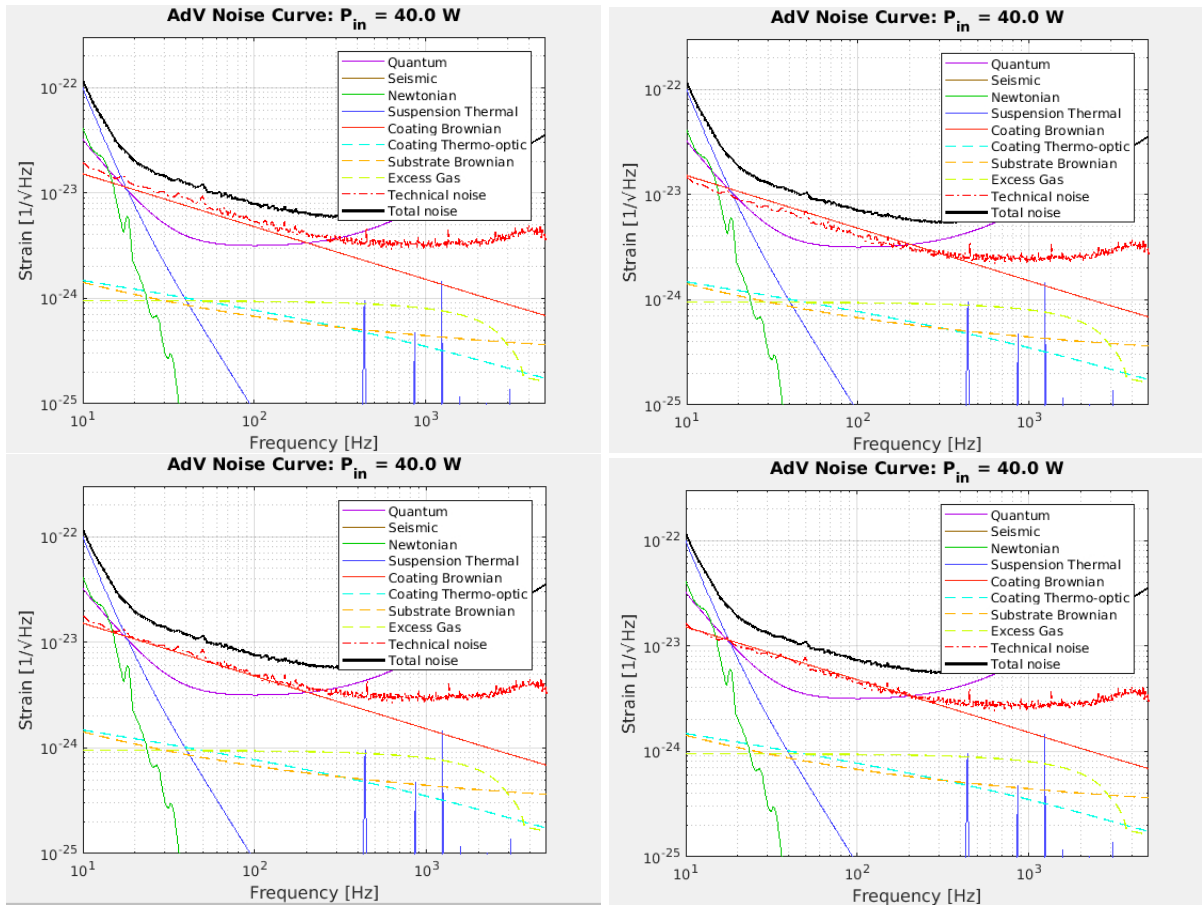


Figure 5: Projection of the 6 MHz RAM (top left), the 56 MHz RAM (top right), the 31 MHz RAM (bottom left) and the 44 MHz RAM (bottom right).

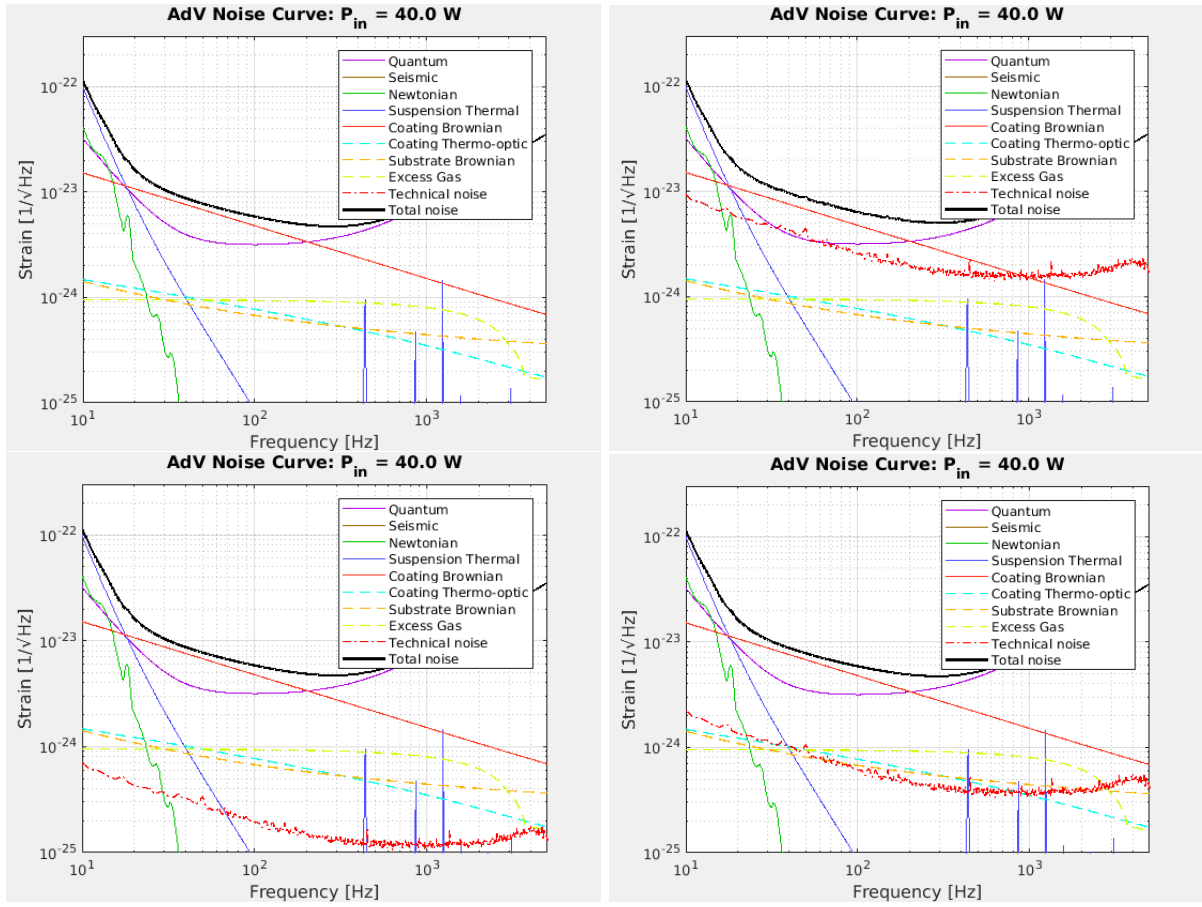


Figure 6: Projection of the higher order mode 1 and 2 of the sidebands 6 MHz RAM (top left), the 56 MHz RAM (top right), the 31 MHz RAM (bottom left) and the 44 MHz RAM (bottom right).

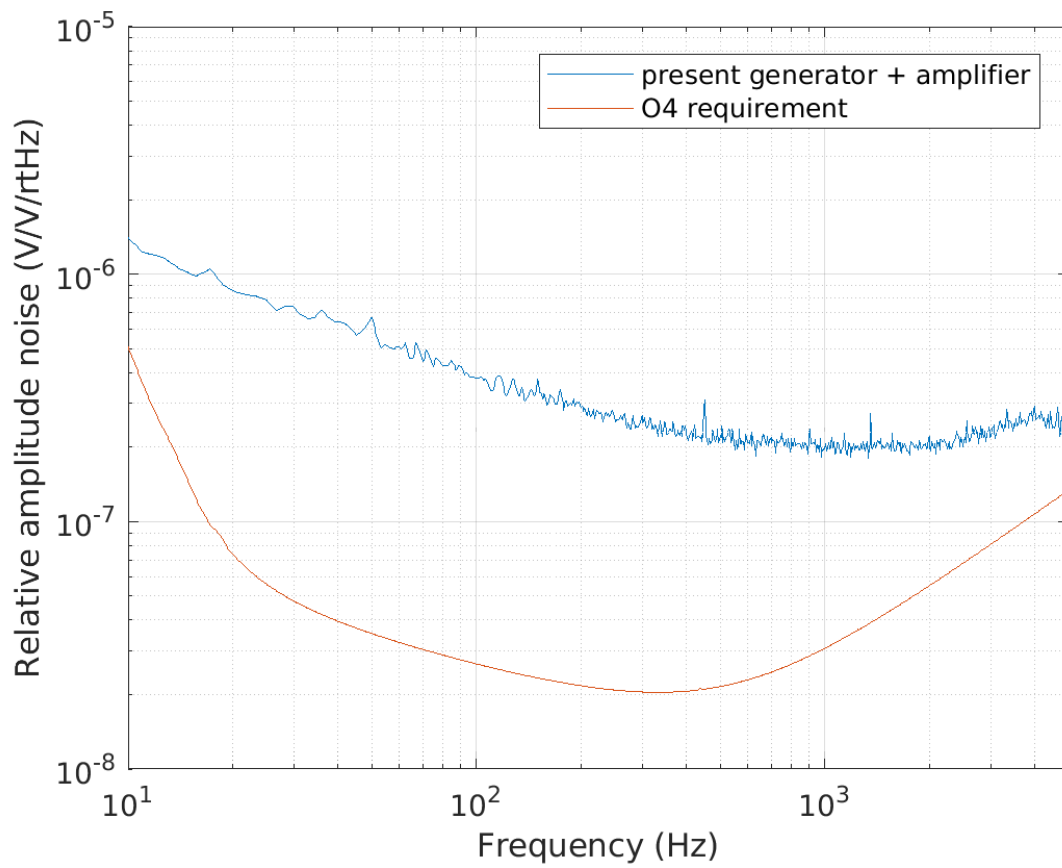


Figure 7: Requirement on the relative amplitude noise at the output of the amplified generator signal. Assumes the 6 MHz and 56 MHz sideband are used and includes 10% of power on the order 1 and 2 higher order modes.

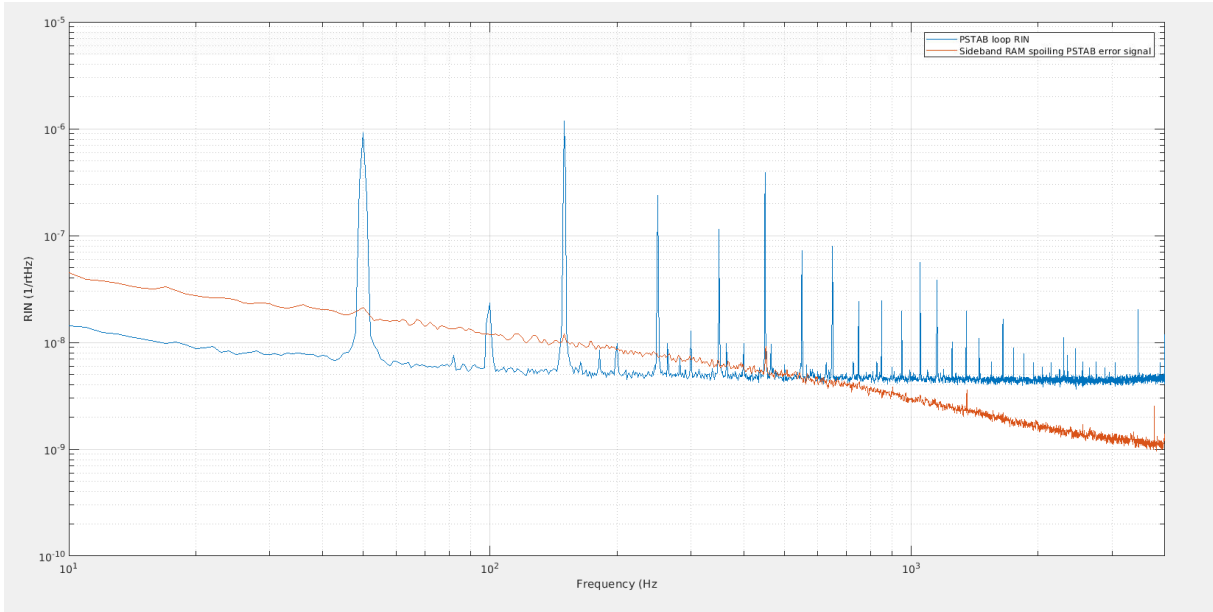


Figure 8: Impact of sideband RAM on the power stabilization error signal.

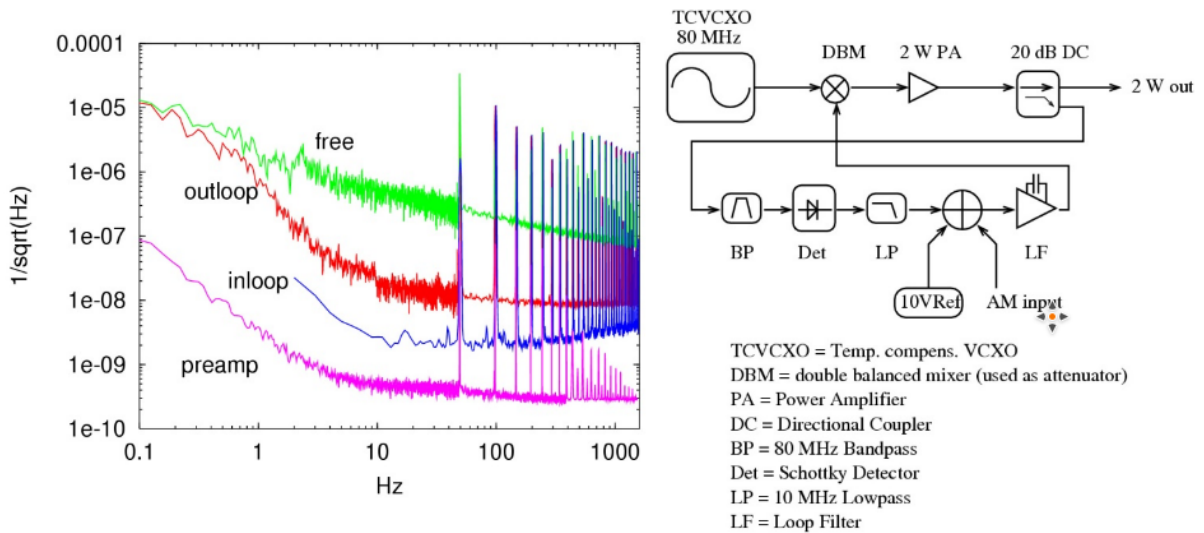









Figure 9: Performance of radio frequency amplitude stabilization in LISA pathfinder.

Appendix C

Interferometer Sensing and Control for the Advanced Virgo Experiment in the O3 Scientific Run

Article

Interferometer Sensing and Control for the Advanced Virgo Experiment in the O3 Scientific Run

Annalisa Allocca ^{1,2,*} , Diego Bersanetti ^{3,*} , Julia Casanueva Diaz ⁴ , Camilla De Rossi ⁴,
Maddalena Mantovani ⁴ , Alain Masserot ⁵, Loïc Rolland ⁵ , Paolo Ruggi ⁴, Bas Swinkels ⁶ ,
Enzo Nicolas Tapia San Martin ⁶, Marco Vardaro ^{6,7} and Michal Was ⁵ 

¹ Dipartimento di Fisica “E. Pancini”, Università di Napoli “Federico II”, Complesso Universitario di Monte S. Angelo, I-80126 Napoli, Italy

² INFN, Sezione di Napoli, Complesso Universitario di Monte S. Angelo, I-80126 Napoli, Italy

³ INFN, Sezione di Genova, I-16146 Genova, Italy

⁴ European Gravitational Observatory (EGO), Cascina, I-56021 Pisa, Italy; julia.casanueva@ego-gw.it (J.C.D.); camilla.derossi@ego-gw.it (C.D.R.); maddalena.mantovani@ego-gw.it (M.M.); paolo.ruggi@ego-gw.it (P.R.)

⁵ Laboratoire d’Annecy de Physique des Particules (LAPP), Université Grenoble Alpes, Université Savoie Mont Blanc, CNRS/IN2P3, F-74941 Annecy, France; Alain.Masserot@lapp.in2p3.fr (A.M.); loic.rolland@lapp.in2p3.fr (L.R.); was@lapp.in2p3.fr (M.W.)

⁶ Nikhef, Science Park 105, 1098 XG Amsterdam, The Netherlands; swinkels@nikhef.nl (B.S.); E.Tapia@nikhef.nl (E.N.T.S.M.); m.vardaro@nikhef.nl (M.V.)

⁷ Institute for High-Energy Physics, University of Amsterdam, Science Park 904, 1098 XH Amsterdam, The Netherlands

* Correspondence: annalisa.allocca@unina.it (A.A.); diego.bersanetti@ge.infn.it (D.B.)

Received: 31 October 2020; Accepted: 3 December 2020; Published: 8 December 2020



Abstract: Advanced Virgo is a 2nd-generation laser interferometer based in Cascina (Italy) aimed at the detection of gravitational waves (GW) from astrophysical sources. Together with the two USA-based LIGO interferometers they constitute a network which operates in coincidence. The three detectors observed the sky simultaneously during the last part of the second Observing Run (O2) in August 2017, and this led to two paramount discoveries: the first three-detector observation of gravitational waves emitted from the coalescence of a binary black hole system (GW170814), and the first detection ever of gravitational waves emitted from the coalescence of a binary neutron star system (GW170817). Coincident data taking was re-started for the third Observing Run (O3), which started on 1st April 2019 and lasted almost one year. This paper will describe the new techniques implemented for the longitudinal controls with respect to the ones already in use during O2. Then, it will present an extensive description of the full scheme of the angular controls of the interferometer, focusing on the different control strategies that are in place in the different stages of the lock acquisition procedure, which is the complex sequence of operations by which an uncontrolled, “free” laser interferometer is brought to the final working point, which allows the detector to reach the best sensitivity.

Keywords: gravitational waves; control systems; longitudinal control; feed-forward; angular control; laser interferometer; advanced virgo

1. Introduction

The detection of gravitational waves is based on the physical principle of the interference pattern of a Michelson interferometer, where different configurations of the length difference between the two arms can lead to an interference pattern ranging from constructive (*bright fringe*) to destructive (*dark fringe*) at the output port of the interferometer. The latter is the standard working condition of a gravitational wave laser interferometer where only a very small amount of light reaches the output

port, because of the detection scheme adopted in 2nd-generation detectors [1,2]. Instead, should a gravitational wave pass and interact with the detector, it would locally stretch the space-time metric and thus change, in a differential way, the length of the two arms of the interferometer; in this case, the interference pattern would deviate from the dark fringe and a signal would be detected at the output port of the interferometer, allowing reconstructing the properties of the gravitational wave and to investigate its source.

Advanced Virgo [3], together with other 2nd-generation gravitational wave interferometers, has a much more complicated optical scheme with respect to the one of the Michelson interferometer (cfr. Figure 1 in Section 2): the terminal mirrors of the Michelson interferometer are replaced with optical resonators, namely Fabry-Pérot resonant cavities; this allows increasing the effective arm length by a factor $\frac{2\mathcal{F}}{\pi} \approx 300$, where $\mathcal{F} \approx 460$ is the Finesse of the arm cavities. Moreover, the dark fringe operating condition has the consequence that almost all the light is rejected back from the interferometer towards the input port; in order to further increase the amount of light circulating in the interferometer, another mirror is put in place between the laser and the main interferometer: this Power Recycling (PR) mirror allows recycling the back-reflected light and re-inject it in the interferometer. However, this behaviour happens only if another resonance condition is met in this Power Recycling cavity, made of the PR mirror on one side and the two arm cavities input mirrors on the other side.

To reach (and then keep) the correct operating point, such as the Power Recycling cavity and Fabry-Pérot cavities on resonance, and the relative mirror angular orientation with respect to the main laser beam, a series of control loops is needed, which maintain the correct microscopic working point of each optic both in relative position (*longitudinal controls*) and relative orientation (*angular controls*). These loops are engaged during a complex sequence which brings the interferometer from a free uncontrolled state to the final working point; such sequence is called lock acquisition. After the end of the lock acquisition, additional control loops and algorithms are switched on in order to improve the performance of the detector and to reduce the effect of several technical noises which affect it.

In this paper, these main topics will be addressed: in Section 2 the new noise subtraction techniques for the longitudinal controls are described, while for the general description of the longitudinal control scheme we refer to [4,5]. In Section 3 the full scheme of the angular controls is described, with all the different approaches which are used in the several steps of the lock acquisition, together with a noise subtraction technique specific for the angular controls. Finally, Section 4 reports the effect of both the longitudinal noise subtractions and the angular controls on the sensitivity curve and the duty cycle, which are the final figures of merit for the performance of the detector.

2. Longitudinal Control Scheme

As introduced in Section 1, a laser interferometer GW detector is a compound optical system which is based on the Michelson interferometer as its working principle, with in addition several technological improvements (like resonant optical cavities) which are useful to both increase its performance and to reduce some of the technical noises it is affected by. The optical scheme of Advanced Virgo in O3 is unchanged with respect to O2; it is pictured in Figure 1 and a thorough description can be found in [4].

Here we recall very briefly its main points: the several optical cavities, made by suspended mirrors, define several characteristic longitudinal degrees of freedom (DOF), which have to be kept in a definite working point via an active feedback control system; taking the Beam Splitter mirror (BS) as the origin of the coordinate system, such DOFs are the following (cf. Figure 1):

- $MICH = l_N - l_W$, the length difference of the short arms of the Michelson, it defines the interference condition;
- $PRCL = l_{PR} + \frac{l_N + l_W}{2}$, the Power Recycling cavity length;
- $CARM = \frac{l_N + l_W}{2}$, the Common, average length of the long Fabry-Pérot arm cavities;
- $DARM = L_N - L_W$, the length Difference of the long Fabry-Pérot arm cavities; this is the most important degree of freedom, as it is the one which is sensitive to the passage of gravitational waves.

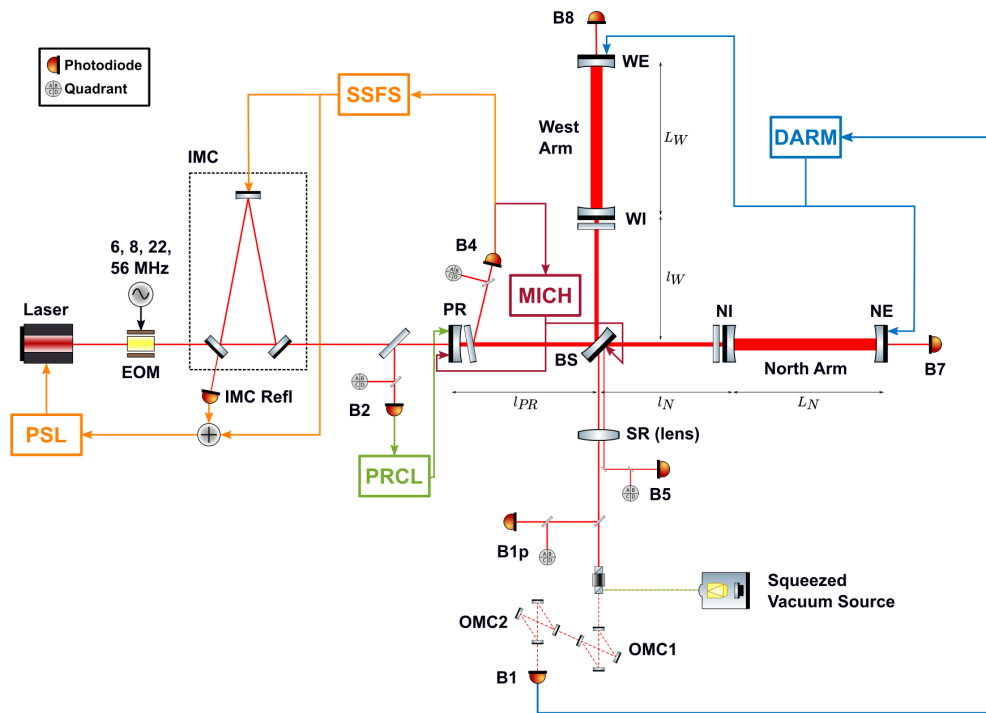


Figure 1. Optical layout of Advanced Virgo during O3. Each depicted Quadrant Photodiode (QPD) actually represents a set of two different physical sensors [6]. Acronyms used only in the plot: PSL (Pre-Stabilized Laser), IMC (Input Mode Cleaner), NI (North Input mirror), NE (North End mirror), WE (West End mirror), SR (Signal Recycling mirror). The image uses the graphic library from [7].

The main longitudinal control technique of Advanced Virgo, which is used to control all the aforementioned DOFs, is the Pound-Drever-Hall (PDH) technique [8,9], and the control scheme does not differ from the one that was used in O2 [4,5]. This technique is based on the generation of radio-frequency sidebands, which are used to phase modulate the carrier light, and the demodulation of the photodiode (PD) signals at such frequencies; in Advanced Virgo the sidebands are generated via an Electro-Optic Modulator (EOM) and the characteristic frequencies are 6 MHz, 56 MHz (with the corresponding sidebands anti-resonant in the arms) and 8 MHz (with the corresponding sideband completely reflected by the interferometer). Therefore, each DOF is sensed by a signal extracted from one PD (or, in general, by a linear combination of signals extracted from different PDs), demodulated at a given sideband frequency (or frequencies). The notable exception to this scheme is the sensing of the DARM DOF, which does not use a radio-frequency demodulated signal but a DC signal, due to the detection scheme used in 2nd-generation detectors, called *DC Readout* [2].

The sensing of the CARM DOF is instead peculiar for a different reason: one of the most sensitive sensors which is used for such DOF (B4 in Figure 1) is equivalently sensitive to a common movement of the arm cavities lengths and to a change in the frequency of the main laser (i.e., frequency noise). For this reason such sensor is used with a nested control loop which acts on both the mechanical movement of the mirrors and the laser's frequency; this latter loop is called Second Stage of Frequency Stabilization (SSFS) [10].

For the longitudinal controls, the main novelty for O3 has been the introduction of feed-forward techniques, which are aimed to the reduction of noise couplings from a known source either directly to the DARM DOF, or to one of the auxiliary ones; while in the former case the benefit is evident, also in the latter case the reduction of such a noise coupling gives a benefit in the overall noise level of the DARM DOF since the main contributors to the DARM noise level are exactly the other longitudinal DOFs.

The two feed-forward techniques which are going to be presented here are the one devoted to the reduction of the PRCL noise from the SSFS error signal (the so-called *PRCL to SSFS*) and the one devoted to the *adaptive* reduction of the noise coming from the 50 Hz main electricity line and affecting directly the DARM DOF (named *Adaptive 50 Hz*).

2.1. PRCL to SSFS Feed-Forward

The purpose of this technique is to reduce the noise coupling between two auxiliary DOFs, PRCL and CARM (in its control implementation, the SSFS loop), which is then propagated to DARM. The source noise is due to the residual longitudinal motion of the PR mirror, which is at least in part induced by sensing noise (above 10 Hz) caused by scattered light. Such noise is then propagated commonly inside the two arms, as they see the same disturbance coming from the input port of the interferometer; this common disturbance can be sensed by the B4 PD, which is a pick-off of the Power Recycling cavity and it is used to sense the SSFS.

The SSFS loop on its own is quite effective in reducing the frequency noise sensed by the B4 sensor, and it has 10 kHz of Unity Gain Frequency (UGF), which is much higher than the UGF of all the other loops, which range between 10 Hz to 100 Hz of control bandwidth. Therefore, the residual frequency noise sensed by the B4 PD is quite low. On the other hand the PRCL loop, because of the residual motion of the PR mirror, induces a spurious signal on the SSFS sensor within the SSFS control bandwidth; therefore, the SSFS loop considers it as legitimate frequency noise and tries to correct it, actually doing the opposite and re-introducing this length noise as frequency noise.

For this reason, it was decided to implement a noise-cancellation feed-forward system which adds, to the SSFS controller, an additional term which depends on the PRCL loop and on the cross-coupling between the two loops. Such additional term is tuned in order to cancel the effect of the spurious noise.

More in detail, the coupling mechanism between two DOFs can be described in the following way: given a diagonal controller C and a plant P which is non-diagonal, i.e., it has cross couplings,

$$C = \begin{pmatrix} c_{11} & 0 \\ 0 & c_{22} \end{pmatrix}, \quad P = \begin{pmatrix} p_{11} & p_{12} \\ p_{21} & p_{22} \end{pmatrix}, \quad (1)$$

the two cross-couplings terms p_{12} e p_{21} are not controlled and cannot be suppressed. If instead one wants to reduce one of the two terms (for instance, p_{12}), the controller takes the following form:

$$C = \begin{pmatrix} c_{11} & x \\ 0 & c_{22} \end{pmatrix}. \quad (2)$$

In this case, the product PC , which represents the coupled open-loop transfer function, is

$$PC = \begin{pmatrix} p_{11}c_{11} & xp_{11} + p_{12}c_{22} \\ p_{21}c_{11} & xp_{21} + p_{22}c_{22} \end{pmatrix} \quad (3)$$

and, in order to cancel the noise coupling term, the non-diagonal term of the controller is defined as

$$x = -\frac{p_{12}}{p_{11}}c_{22} \quad (4)$$

and PC becomes

$$PC = \begin{pmatrix} p_{11}c_{11} & 0 \\ p_{21}c_{11} & -p_{12}p_{21}c_{22}/p_{11} + p_{22}c_{22} \end{pmatrix}. \quad (5)$$

The stability of the loops is dependent on the eigenvalues of the PC matrix: given that PC is triangular, the eigenvalues are simply the diagonal terms. What happens is that one diagonal term (relative, in this case, to the PRCL loop) is modified by the introduction of this feed-forward control

term, as it changes from being simply $c_{22}p_{22}$ to the form $c_{22}(p_{22} - p_{21}p_{12}/p_{11})$, which changes, but not in a dramatic way, the shape of the PRCL loops itself.

The term x can be found from quantities which are either known (c_{22} , the PRCL controller) or can be modeled (p_{11} and p_{12}) in frequency domain as optical transfer functions, with their overall gain measured with standard noise injections in the loops. From a procedural point of view, what is done is to take the correction of the PRCL loop, filter it following the shape of the cross-coupling term and then add it to the SSFS sensing matrix; the filter used to match the cross coupling term has the form depicted in Figure 2.

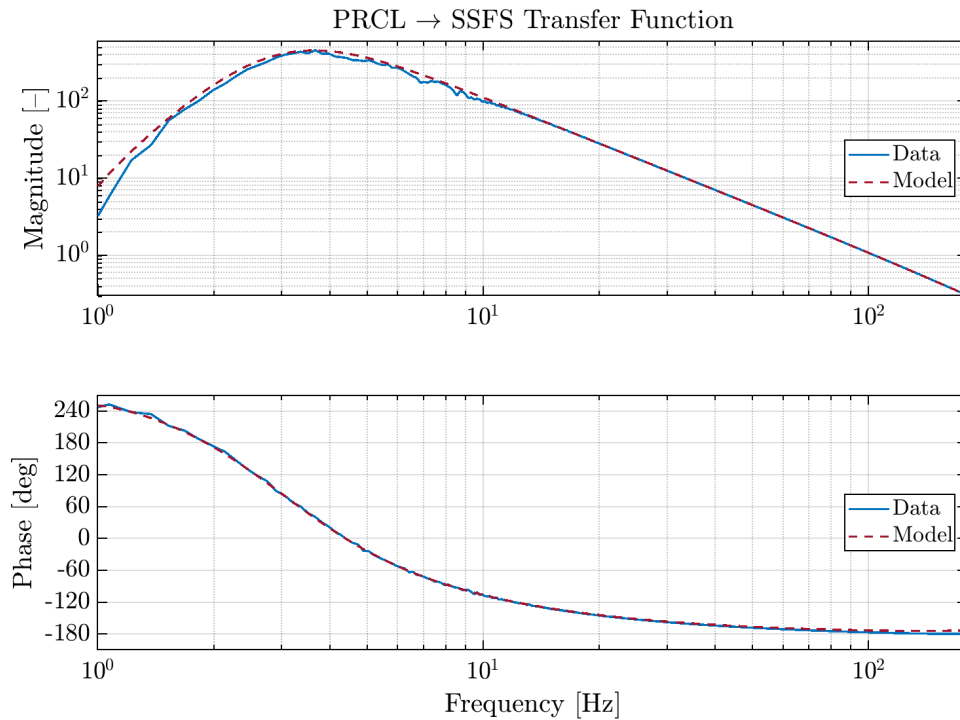


Figure 2. PRCL to SSFS Feed-Forward: cross-term of the open loop transfer function.

The application of this *PRCL to SSFS* feed-forward technique is appreciable in Figure 3, where the transfer function and the coherence between the PRCL and the DARM DOFs are shown during two separate noise injections, in order to make a precise measurement of the coupling of PRCL to DARM: as it was explained in Section 2, the reduction of the coupling between auxiliary DOFs does have an effect on the noise level of DARM as, for example in this case, the reduction of the PRCL contribution to the frequency noise level assures that the contribution to DARM of the SSFS itself is effectively reduced.

The effect of the feed-forward on the sensitivity curve $h(t)$ of the interferometer will be presented in Section 4, which is devoted to the performance improvements brought by all the techniques described in this paper. In addition, future possible improvements can be done by reducing the PRCL control noise by mitigating the source of the noise and improving the roll-off of the control filter.

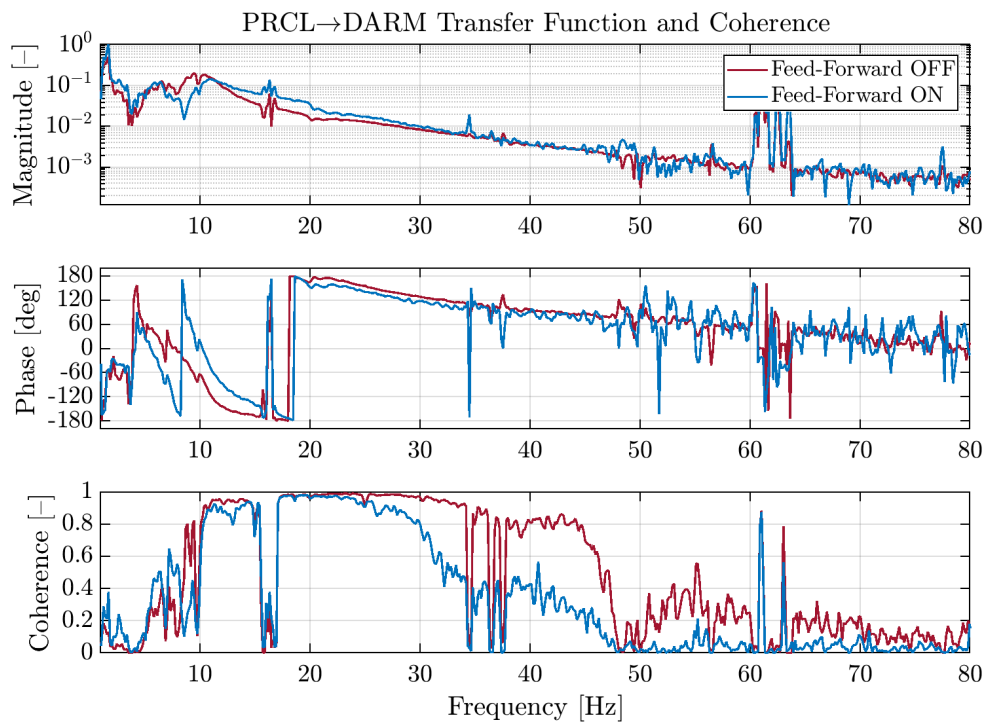


Figure 3. PRCL to SSFS Feed-Forward, from top to bottom: transfer function and coherence between PRCL and DARM.

2.2. Adaptive 50 Hz Feed-Forward

The second feed-forward technique which was used for the longitudinal controls of Advanced Virgo during the O3 Run was devoted to the suppression of the noise line at 50 Hz, which is due to the electrical mains. This control is quite different with the one described in Section 2.1, as here the target is directly the primary DOF (DARM) and the disturbance is not coming from an auxiliary control loop but it is an independent, known noise source. In addition, the disturbance is not broadband, but theoretically it is at a very definite frequency.

In order for a feed-forward to be accurate, it is necessary to find a good witness of such disturbance, so that it can be used to build a viable error signal for the feed-forward itself; in this case, it was found that the probe of one of the three phases of the Uninterruptible Power Supply (UPS) system present in Virgo's Central Building was a good candidate, so it was chosen as witness channel.

The working principle of this kind of control is the following:

- the level of the 50 Hz mains line is measured using, as a probe, one phase of the UPS system present in Virgo's Central Building;
- a gain and a phase are applied to the signal coming from the probe, in order to match the noise that is seen by the target channel, which is the main longitudinal degree of freedom, DARM;
- in order to compute the correction, this quantity is filtered using a resonant filter with 50 Hz as characteristic frequency: in this way, it is possible to avoid the introduction of additional noise (due to this control) at frequencies different from the target one;
- the correction is then sent to the actuators (which are the coil-magnet pairs of the West Input (WI) mirror) in order to effectively cancel the effect of the noise at 50 Hz directly in DARM.

One important point, which is crucial in determining the performance of the control, is the following: this feed-forward is *adaptive*, meaning that the gain and phase which have to be found for a matching correction to be computed are not static, so two control loops are constantly *adapting* online their value in order to follow any change of the noise coupling, which is not perfectly stationary itself.

The error signals for these two loops (gain and phase) are the two quadratures of the demodulation of the DARM signal itself with respect to the witness, i.e., one phase of the UPS system of the Central Building. As it is shown in Figures 4 and 5, using an adaptive strategy allows reducing the noise level, described by the band-limited root mean square (RMS) of DARM around 50 Hz, with respect to the static case. Such strategy is also quite fast to engage (with a bandwidth of around 50 mHz), as the loops converge rapidly (cfr. Figure 5) while the band-limited RMS of the DARM DOF drops by two orders of magnitude with respect to the case with no feed-forward engaged.

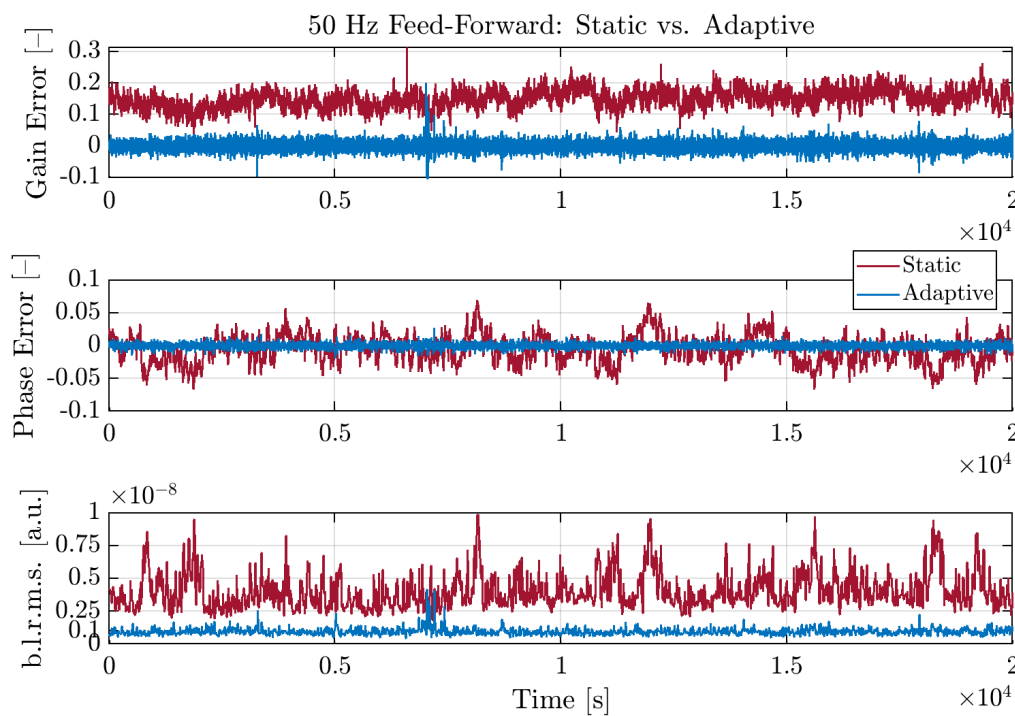


Figure 4. 50 Hz Feed-Forward: Improvement of the band RMS around 50 Hz of the DARM error signal by using an *adaptive* control strategy. From top to bottom: error signal for the gain and phase of the feed-forward control; band RMS of DARM around 50 Hz.

One other important point is to find the best possible match between the witness channel and the disturbance, i.e., having the transfer function between the two signals as flat as possible in the band of interest, as it is expected. This means that the information provided by the witness is replicated correctly with the actuation without distortions, and this provides two linked advantages:

- it reduces the possibility to actually re-inject noise outside the narrow band of interest, as the feed-forward would try to subtract spurious, non-physical effects;
- it allows reducing the Q factor of the resonant filter, resulting in a less narrow band on which it can operate.

Since the mains frequency is not perfectly stable on its own account but it has some jitter, having a larger band is helpful as it eases the requirements on the in-loop parameters of the adaptive feed-forward, as the frequency jitter of the disturbance directly affects the computation of the phase of the feed-forward. Moreover, the effect of the subtraction can be extended in a small band around the mains line itself.

This has been achieved, as shown in Figure 6, where it can be seen that the transfer function has become very flat not only at 50 Hz, but also in a non-negligible band around the mains frequency. The effect on the coherence with the DARM signal will be shown in Section 4, which is devoted to the performance improvements due to the different techniques described in the paper.

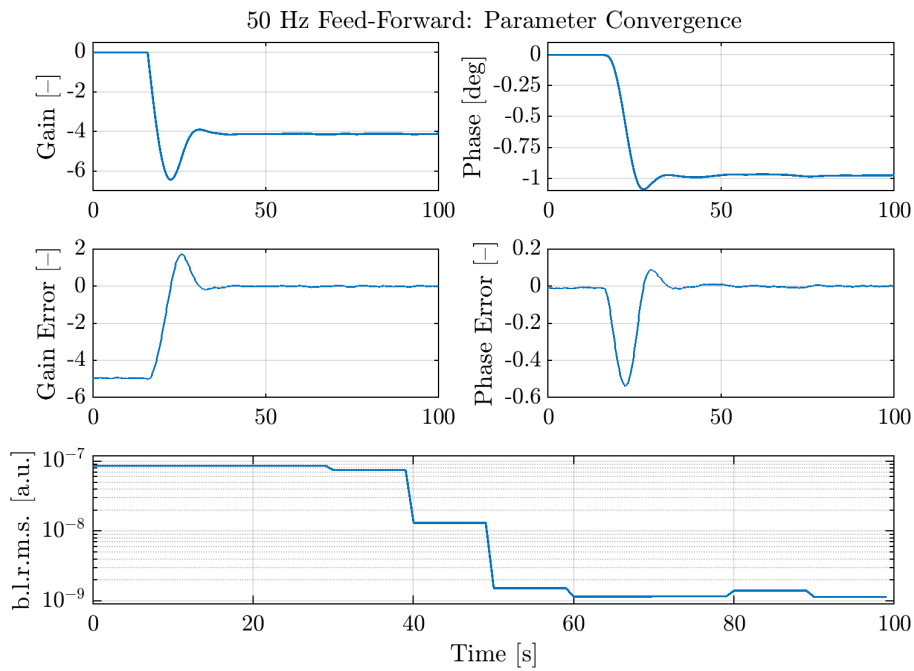


Figure 5. 50 Hz Feed-Forward: Convergence of the loop parameters and reduction of the DARM band-limited RMS by two orders of magnitude.

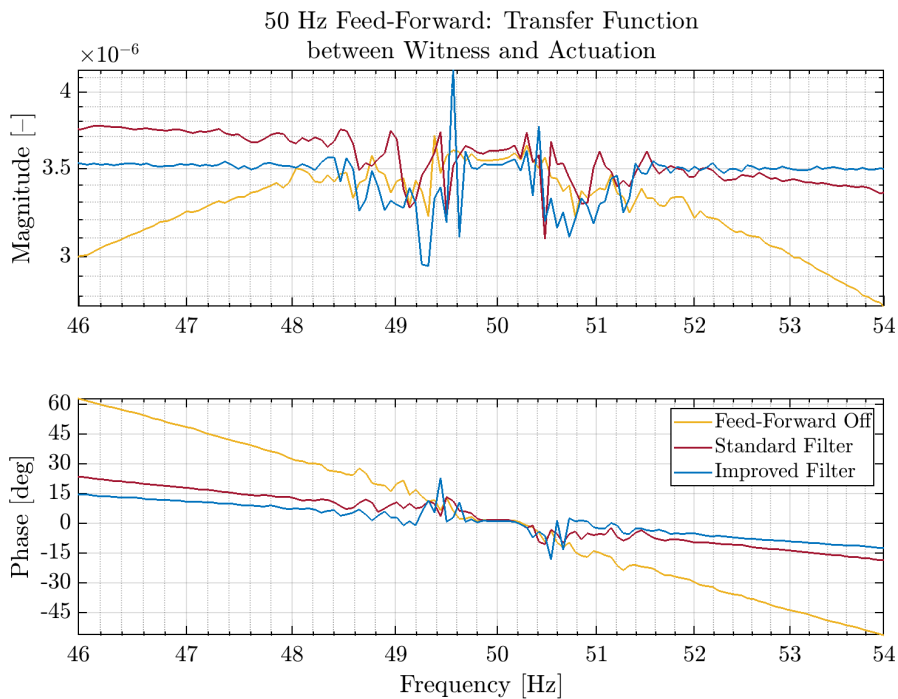


Figure 6. 50 Hz Feed-Forward: transfer function between witness and actuation. It can be observed how in the initial transfer function, with the feed-forward not engaged (yellow trace), the actuation could reproduce the information from the witness channel only at 50 Hz; a progressively better filtering of the witness signal (red and blue traces) brought to a flatter transfer function, minimizing the risk of reintroducing noise and allowing a broadening of the bandwidth of the feed-forward itself.

3. Angular Control Scheme

For the interferometer to reach the maximum sensitivity, DARM residual motion must be kept below 10^{-16} m RMS. To accomplish this requirement, the Fabry-Pérot cavity length control is not sufficient, as also the mirrors angular stability plays a role.

All the mirrors are free to oscillate around their main axes. In particular, we define the x and y axes as the two perpendicular directions on the plane of the mirror Highly Reflective (HR) surface, with horizontal and vertical orientation respectively. Mirror oscillations around x and y are therefore called θ_x and θ_y .

A first mitigation of the seismic noise is obtained by hanging each mirror to the so-called *Superattenuator* [11], a long chain of pendulums which provides a seismic noise suppression in the beam direction of $\frac{1}{f^{2n}}$, where f is the frequency and n the number of pendulum stages. This yields a passive overall noise reduction by a factor 10^{-14} starting from a few Hz.

A misalignment of the cavity mirrors can induce a tilt/shift of the optical axis with respect to the beam direction. It can be shown [12] that while the geometrical displacement can be compensated by the longitudinal lock, on the other hand the first-order transverse optical modes can be excited and therefore spoil the destructive interference of the beams at the interferometer output. Furthermore, being the mirrors spherical, if the optical axis does not overlap with the mirror center, a coupling with the longitudinal DOFs of any residual angular motion is observed, with a subsequent worsening of the detector sensitivity.

As explained in Section 1, in Advanced Virgo, where about 25 W of input power are injected in the interferometer, three main optical resonators can be identified: the two 3 km arm cavities, with a Finesse of about 460 and a circulating power of about 130 kW, and the Power Recycling cavity, the additional compound optical resonator composed of the PR mirror on one side and the two arm cavities input mirrors on the other side. This latter cavity, also referred to as CITF (*Central Interferometer*), has a much lower Finesse (around 60) with respect to the arm cavities with a total circulating power of about 1 kW.

Second generation interferometers, with respect to first generation, have to deal with an additional effect due to high circulating power: the radiation pressure effect. If a static misalignment is present, the optical axis does not hit the geometrical centers of the mirrors. As a consequence, the laser beam exerts on them a torque with a force proportional to the circulating power.

Such effect can be modeled as an optical spring connecting the cavity mirrors. This optically induced torsional stiffness changes the cavity mechanical transfer function as a function of the circulating power, and can be even larger than the stiffness of the mirror suspensions.

Radiation pressure effects can be described in terms of the torsional stiffness matrix, which in turn depends on the cavity g -factor and on the circulating power. This matrix becomes diagonal in the normal mode basis, which are the *plus* (+, which increases the suspension frequency and makes the mode stiffer) and *minus* (−) DOFs [13]. It can be shown [13] that the resonance frequency of the latter mode can become imaginary: in this condition, the system becomes unstable and the control filter has to be properly shaped as to guarantee the stability [14].

In the arm cavities, where the largest amount of power is stored, the radiation pressure effect is higher, while mirrors in the central interferometer are less concerned.

Both slow drift and faster oscillations of the cavity mirrors must be kept under control: this determines the bandwidth of the control loops, which should range from DC up to a few Hz. The actuation is performed using the second to last stage of the Superattenuator, called *marionette*: this allows a larger force to be driven while filtering the correction signal by a pendulum stage before reaching the mirror, reducing the actuation noise.

To guarantee an optimal working point for the interferometer, the alignment of two angular DOFs for each of the six mirrors has to be controlled, aside from the input beam direction tilt and shift. To fulfill the requirements, the estimated needed precision is hundreds of nrad for the (−) modes, tens of nrad for the PR and BS mirrors and reduces down to a few nrad for the (+) modes [15,16].

3.1. Degrees of Freedom Definition and Interferometer Sensors

To better describe the alignment control scheme of the Advanced Virgo detector, it is convenient to define the interferometer angular DOFs.

In the Power Recycling cavity, the radiation pressure is not strong enough to couple the angular DOFs, thus PR and BS can be treated independently. Concerning the arm cavities, the radiation pressure effect plays a very significant role, resulting in an optical spring between cavity mirrors. Hence, a basis of *common* and *differential* DOFs, both (+) and (−), is more suitable for the arm cavities misalignment description as it is the basis which diagonalizes the sensing.

The four DOFs (effectively eight if the rotations around x and y axes are considered) are depicted in Figure 7. In particular:

- COMM(+): common tilt of the arm cavities resulting in the two beams recombining in the same spot on the BS;
- DIFF(+): differential tilt of the arm cavities resulting in two spots recombining on the two opposite sides of the BS;
- COMM(−): common shift of the arm cavities resulting in the two beams recombining in the same spot on the BS;
- DIFF(−): differential shift of the arm cavities resulting in two spots recombining on the two opposite sides of the BS.

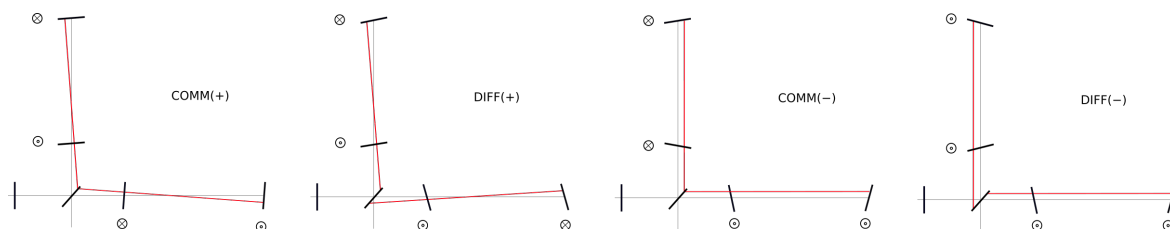


Figure 7. Scheme of the angular DOFs of the arms.

In addition to the optical cavities, also the input beam tilt and shift with respect to the interferometer plane have to be controlled. However, only one of them (tilt) is kept in loop, since the local controls (see next paragraph) for the shift are compliant with the accuracy requirements.

Different types of controls are used for the interferometer alignment:

- *Local Controls*—A first stage of control on the mirrors is performed by engaging the so-called *local controls*. The error signals are obtained with a system of optical levers, a setup made of a Superluminescent Diode (SLED) hitting the mirror and focusing on a Position Sensing Device (PSD), able to monitor the angular and longitudinal position of the mirrors. The local controls can achieve a precision of $\approx 0.2 \mu\text{rad h}^{-1}$ RMS for the mirror angular control. These sensors are ground-based and can only provide a local reference. Optical levers noise has the advantage of being fairly flat out of the control bandwidth (about 10 Hz): its level is about $5 \times 10^{-10} \text{ rad}/\sqrt{\text{Hz}}$ at the marionette level and it is filtered down by an additional f^2 factor due to the last pendulum stage before reaching the mirror.
- *Dithering Control*—The basic principle of the dithering technique is that a coupling between longitudinal and angular DOFs is observed if the cavity axis does not hit the mirror rotation center of actuation [6]. The error signal is obtained, once the longitudinal DOFs are locked, by exciting both angular DOFs (θ_x and θ_y) of each test mass at a determined frequency, all

different for each DOF and each test mass (below 10 Hz for arm cavity mirrors). Then the cavity longitudinal correction is demodulated at the same frequency: the amplitude of the signal is thus proportional to the angular-to-length coupling. This allows obtaining a set of angular signals suitable to sense mirror angular displacements. To cancel them, the mirrors angular position which minimizes the coupling is chosen. This technique allows achieving a good tuning of the resonators working point, although its noise performance is not good enough to meet the noise and accuracy requirements for the most critical DOFs, namely the (+) modes and the central interferometer angular modes. This is due to the fact that the dithering error signal is blended at 50 mHz with the local control signals, which are much noisier than the QPD signals, used for the Full Bandwidth Global Control, which is described below.

- *Full Bandwidth Global Control*—The *Global Alignment* control takes advantage of the *Ward technique* [17], which exploits the modulation frequencies used for the PDH technique in the longitudinal lock [8]. We recall (cf. Section 2) that for the longitudinal lock the carrier light is phase modulated at three different frequencies: 6 MHz and 56 MHz, which are resonant in the CITF and anti-resonant in the arms, and 8 MHz, completely reflected by the interferometer. In presence of a misalignment, the off-axis modes of carrier and sideband fields are reflected and are sensed by a QPD, which has four separated areas to be sensitive to high order modes power distribution. Besides the demodulated signals, also the QPD DC signal is used for the angular control, as it provides a good indication about the beam position. QPDs are the most sensitive sensors, as they are able to measure the relative displacement between the beam and the cavity axis. Moreover, their noise level is much lower than the one of the PSDs, which allows using high loop gains avoiding to spoil the sensitivity by re-introducing control noise.

In the final interferometer configuration (science mode), the most critical DOFs are controlled using this kind of sensors, while the others make use of a mix of signals coming from optical levers and dithering.

3.2. Alignment Control Evolution

As described in [4], the interferometer working point is reached through the *Variable Finesse* technique. This lock acquisition strategy consists of different steps, which will be briefly recalled in the next subsections. Since each step requires a suitable alignment accuracy, different alignment schemes are applied.

3.2.1. Phase I: Arms Drift Control

In the first step of the lock acquisition, all the mirrors are under local controls. The PR is misaligned, so as to avoid the effect of the Power Recycling cavity, the two Fabry-Pérot arm cavities are brought to resonance and the MICH DOF is controlled at an intermediate interference condition (*half fringe*). In this configuration, shift and tilt of the input beam with respect to the interferometer plane have to be controlled, together with optical axis shift and tilt of the two arms, in a single cavity basis.

The input beam is controlled through the *Beam Pointing Control* system [18], which allows reaching a shift accuracy of 20 μm RMS and a tilt accuracy of 0.5 μrad RMS.

The arm cavities optical axes are geometrically centered through the dithering technique described in Section 3.1. The same technique is also applied to maximize the overlap between input beam direction and arms optical axes, which is the tilt of the input beam with respect to the interferometer plane. To do this, the Anti-Reflective (AR) surface strong curvature of the PR mirror (3.62 m) is exploited: indeed, shifting the PR along horizontal and vertical directions, a tilt to the beam not hitting the PR mirror center is applied along θ_y and θ_x , respectively. Dithering of PR mirror x and y position and demodulating the line in the arm transmitted power yields an error signal for the mutual tilt between input beam and cavity axis: the optimum point is obtained for the maximum arm transmitted power. This procedure is well suited for the North arm cavity, which is in the direction of the beam transmitted by the BS mirror, while the pointing to the West arm cavity depends on the BS orientation.

To achieve an equally good tuning also for the West arm cavity, the dithering is applied also to the θ_x and θ_y of the BS mirror, in order to steer the beam toward the West cavity. The error signal for the West arm alignment is therefore achieved by demodulating the BS angular lines in the West arm transmitted power. The input beam impinging on the cavity is then steered by translating the PR mirror, for North and West cavities, and tilting the BS mirror, for the West cavity.

3.2.2. Phase II: PR Mirror Alignment and Variable Finesse

During the second phase of the lock acquisition, the PR mirror is aligned and the Power Recycling cavity becomes fully effective; then, the Michelson fringe is reduced to attain the destructive interference working point (*dark fringe*). These operations result in an enhancement of the interferometer circulating power.

In this phase the drift control is switched off, as it is affected by the power increase in the arms. This is possible because any drift of the cavity mirrors would be too slow with respect to the duration of the fringe reduction procedure.

On the other hand, being the Power Recycling cavity very critical because of its small Gouy phase [1], the PR mirror optimal working point must be reached and kept throughout the whole procedure; therefore, its angular control is performed by using a QPD in reflection of the interferometer (B2 QPD, see Figure 1 in Section 2), demodulated at 8 MHz.

This alignment scheme is kept until the last step before going to dark fringe: just before the interferometer reaches the dark fringe condition, this alignment is switched off. As soon as the dark fringe configuration is reached and the power circulating in the arms is not changing drastically anymore, the drift control is immediately turned back on, but only for the four Fabry-Pérot mirrors.

3.2.3. Phase III: Final Working Point Angular Control

So far we have described the alignment scheme in the mirror basis. However, once the dark fringe configuration is achieved, the interferometer signals are much more entangled. In the final working point, a distinction can be made between the Power Recycling cavity alignment loops and the arms control loops. For the latter, it is convenient to switch to the *Common* and *Differential* basis described in Section 3.1. In the dark fringe configuration, the interferometer provides very good error signals for the COMM(+) and DIFF(+) DOFs. In particular, a good accuracy and a high gain are required for the destructive interference to be as good as possible: this is obtained by using the B1p QPD error signals demodulated at 56 MHz, and an accuracy of about 1 nrad is achieved. Furthermore, the beam spot residual motion has to be minimized on the test masses, and this is controlled with the COMM(+), which uses the DC of the B5 QPD as error signal. On the contrary, in this configuration, interferometer signals are not good enough to provide a sensitive error signal for the DIFF(−) and COMM(−) DOFs, and the drift of such DOFs is controlled with the dithering technique. Finally, in the central interferometer, B5 QPD signals demodulated at 56 MHz are used for PR and BS angular controls. Furthermore, the PR horizontal and vertical centering, which act on the input beam tilt, are controlled using the B2 QPD demodulated at 8 MHz. The interferometer plane is defined by the COMM(+) and the two (−) modes reference.

The overall accuracy of the angular controls can be observed in Figures 8 and 9, for the θ_x and θ_y DOFs respectively; in order to reduce the software communication paths between the suspensions, the two (−) DOFs are reconstructed in the North/West single cavity bases.

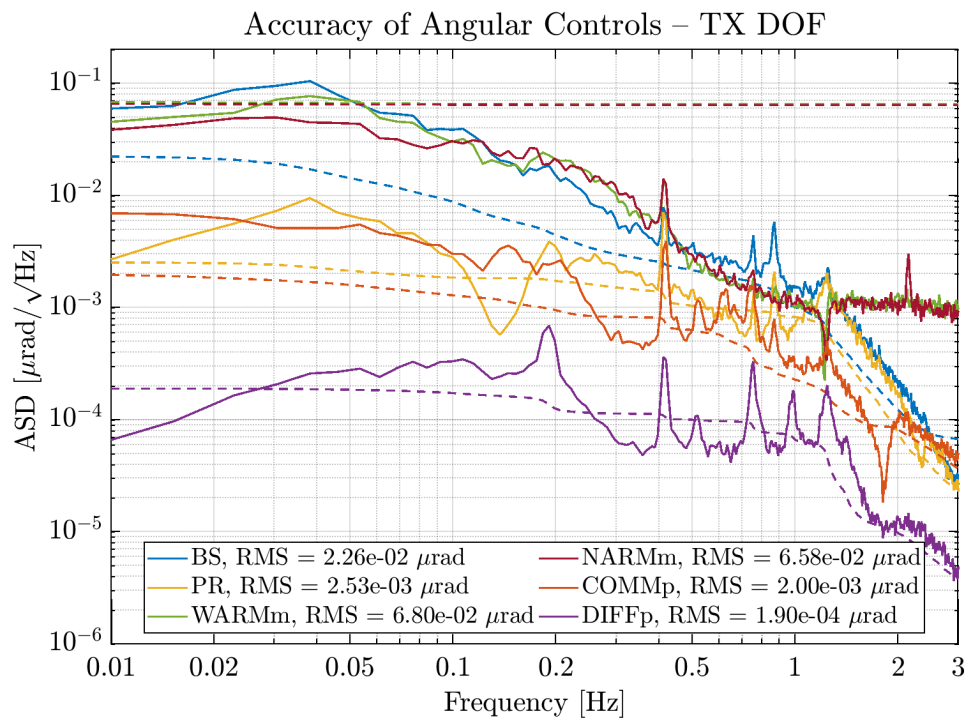


Figure 8. Amplitude Spectral Density (ASD) of the accuracy of Angular Controls in Phase III, θ_x DOFs. (–) modes are defined in the single cavity basis (see text). Dashed lines are the RMS of the signal of the same colour.

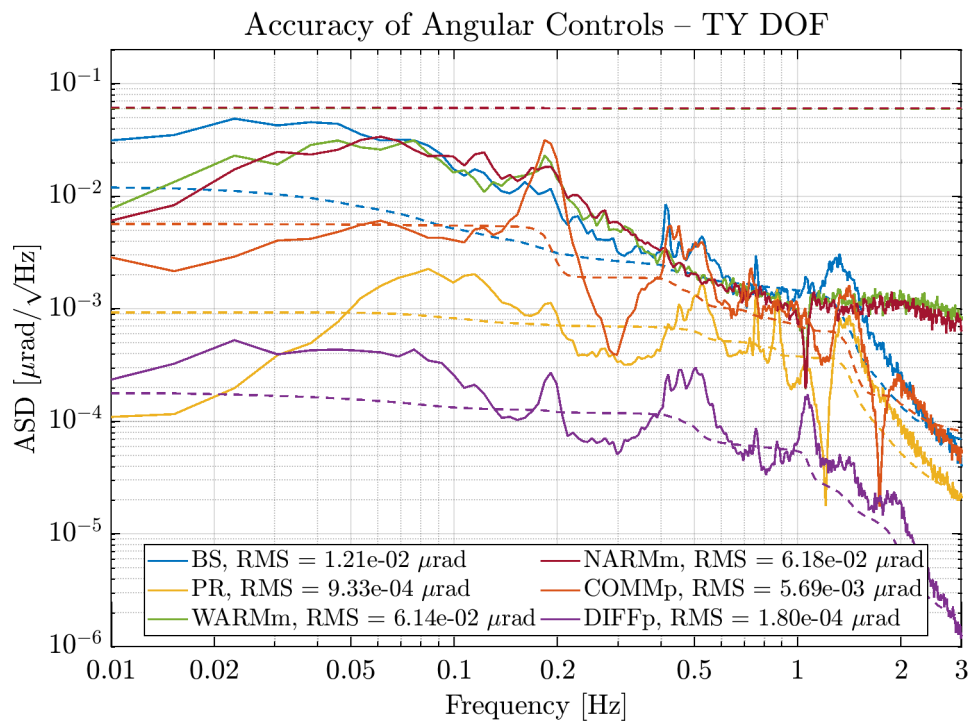


Figure 9. Amplitude Spectral Density (ASD) of the accuracy of Angular Controls in Phase III, θ_y DOFs. (–) modes are defined in the single cavity basis (see text). Dashed lines are the RMS of the signal of the same colour.

3.3. Phase Noise Subtraction

The QPD signals demodulated at 56 MHz show excess of phase noise that is added in the digital demodulation process, which can be summarized as follows. The electromagnetic field of the light impinging on a PD can be written as

$$E(t) = E_0 + E_{\text{LSB}} e^{-i\omega t} + E_{\text{USB}} e^{i\omega t}, \quad (6)$$

where E_0 , E_{LSB} , and E_{USB} are the complex amplitudes of respectively the carrier, lower sideband and upper sideband. The electric signal produced by the PD is proportional to the power impinging on the PD, which is

$$\begin{aligned} P(t) &= |E(t)|^2 \\ &= |E_0|^2 + |E_{\text{LSB}}|^2 + |E_{\text{USB}}|^2 \\ &\quad + 2 \operatorname{Re} \left[(E_0 \bar{E}_{\text{LSB}} + \bar{E}_0 E_{\text{USB}}) e^{i\omega t} \right] + 2 \operatorname{Re} \left(\bar{E}_{\text{LSB}} E_{\text{USB}} e^{i2\omega t} \right) \\ &= P_0 + P_1 \cos(\omega t + \phi_1) + P_2 \cos(2\omega t + \phi_2), \end{aligned} \quad (7)$$

where P_0 , P_1 and P_2 are the powers of the carrier, 1st and 2nd order sideband fields respectively.

The digital demodulation process consists of multiplying the $P(t)$ signal digitized at 400 MHz with a sine and cosine at the sideband frequency and taking an average with a sampling frequency of 1 MHz to obtain the P_I and ϕ_1 signals.

The generated sine and cosine signals have also an error $\delta\phi(t)$ in the phase compared to the modulation imposed on the laser beam. That phase error is predominantly due to a digital timing jitter, hence the phase error can be written as $\delta\phi(t) = \omega\delta\tau(t)$. This results in the two quadrature signals P_I and P_Q to be of the form

$$\begin{aligned} P_I(t) &= \langle P(t) \cos[\omega t + \delta\phi(t)] \rangle_t = \frac{P_1(t)}{2} \cos[\delta\phi(t) - \phi_1(t)] \\ &\simeq \frac{P_1(t)}{2} [\cos\phi_1(t) + \delta\phi(t) \sin\phi_1(t)] \simeq \frac{P_1(t)}{2} \cos\phi_1(t) - P_Q(t) \delta\phi(t), \\ P_Q(t) &= \langle P(t) \sin[\omega t + \delta\phi(t)] \rangle_t = \frac{P_1(t)}{2} \sin[\delta\phi(t) - \phi_1(t)] \\ &\simeq \frac{P_1(t)}{2} [-\sin\phi_1(t) + \delta\phi(t) \cos\phi_1(t)] \simeq -\frac{P_1(t)}{2} \sin\phi_1(t) + P_I(t) \delta\phi(t), \end{aligned} \quad (8)$$

with a spurious signal created in both quadratures by the phase noise $\delta\phi(t)$. The coupling of the phase noise depends on the signal in the quadrature, i.e., for $P_I(t)$ the noise coupling is proportional to the value of $P_Q(t)$ and vice-versa.

However, the same timing jitter $\delta\tau(t)$ is also affecting the signal demodulated at twice the sideband frequency ($2f$ signal):

$$\begin{aligned} P_{2I}(t) &= \langle P(t) \cos[2\omega(t + \delta\tau(t))] \rangle_t = \frac{P_2(t)}{2} \cos[2\delta\phi(t) - \phi_2(t)], \\ P_{2Q}(t) &= \langle P(t) \sin[2\omega(t + \delta\tau(t))] \rangle_t = \frac{P_2(t)}{2} \sin[2\delta\phi(t) - \phi_2(t)], \end{aligned} \quad (9)$$

which yields a measure $2\delta\phi(t) - \phi_2(t)$. By rotating $(P_I(t), P_Q(t))$ by the $\delta\phi(t) - \frac{\phi_2(t)}{2}$ angle we obtain

$$\begin{aligned} P_{I,\text{rot}}(t) &= \frac{P_1(t)}{2} \cos \left[\frac{\phi_2(t)}{2} - \phi_1(t) \right], \\ P_{Q,\text{rot}}(t) &= \frac{P_1(t)}{2} \sin \left[\frac{\phi_2(t)}{2} - \phi_1(t) \right], \end{aligned} \quad (10)$$

which replaces the demodulation phase noise $\delta\phi(t)$ by the $2f$ signal phase $\phi_2(t)$.

Moreover, the dominant contribution of the timing jitter $\delta\tau(t)$ is common to all PDs and QPDs situated on the same bench, as this noise is added when propagating the information on the timing to a given bench. Hence any PD signal can be used to correct the demodulation phase of all other PDs.

In practice, at the end of the second part of O3 (named O3b) the $2f$ signal of the light rejected by the Output Mode Cleaner (OMC) was used to correct the demodulation phase of the B5 and B1p QPDs. The correction is done separately for each segment of each quadrant. The effect on the alignment error signal noise can be seen in Figure 10, which compares data in the same lock of the interferometer before and after applying the phase noise correction. Phase noise creates characteristic bumps in the spectrum, that are especially visible in the BS θ_x signal (ASC_BS_TX), due to the larger offset in the signal in its quadrature. A reduction in this noise of up to a factor 10 is observed.

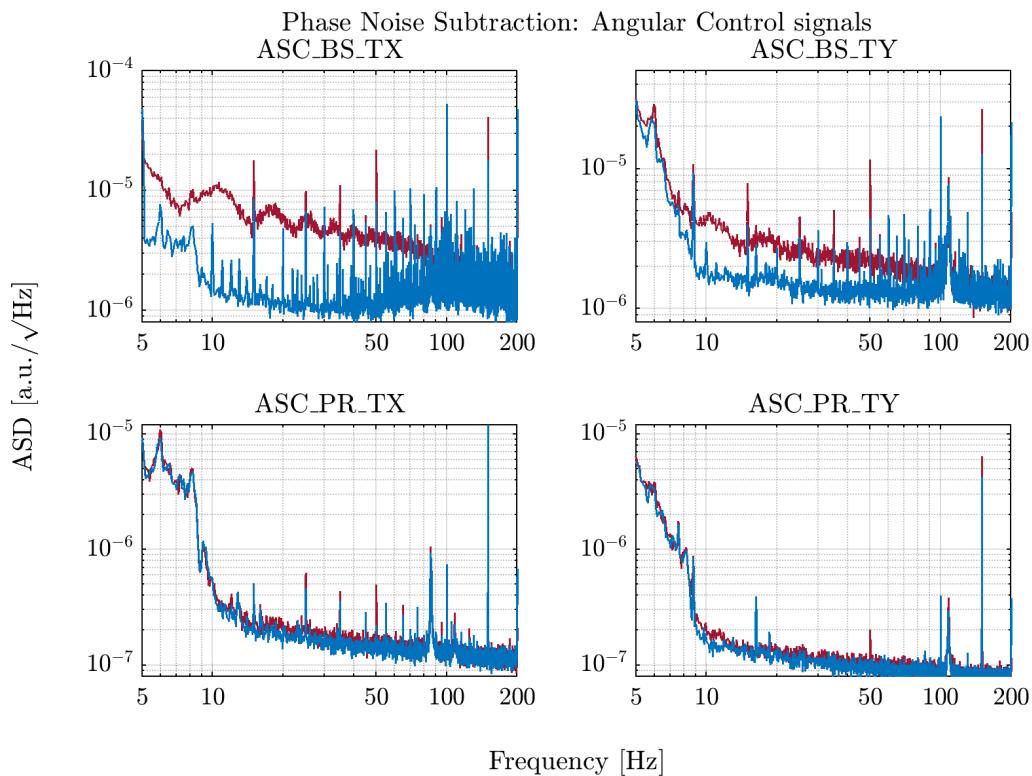


Figure 10. Angular error signals for the BS and PR mirror control, before (in red) and after (in blue) the implementation of the phase noise subtraction.

4. Performance

4.1. Effect of the PRCL to SSFS Feed-Forward

As it was explained in Section 2.1, the PRCL to SSFS feed-forward removes the coupling of the frequency noise to the DARM DOF (and therefore the sensitivity $h(t)$), which originates from the PRCL DOF and then propagates to the SSFS loop; the band of interest is therefore the one where the noise coming from the PRCL loop is most dominant, i.e., between 20 and 60 Hz; in Figure 11 the effect of the feed-forward can be appreciated, resulting in an increase of the Binary Neutron Star (BNS) Range of about 3 Mpc.

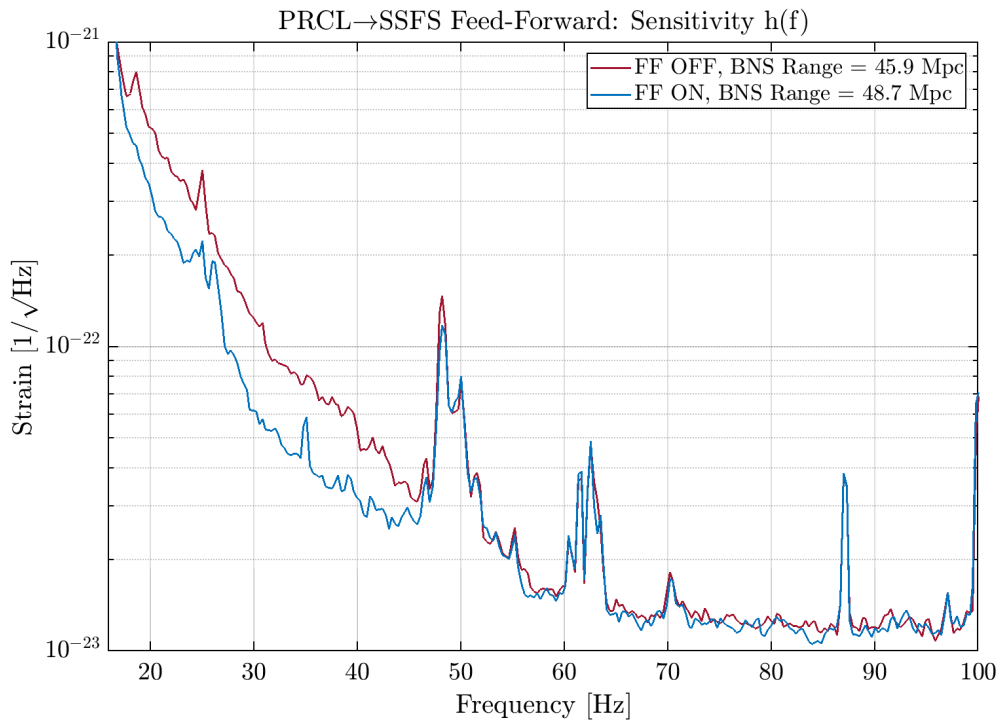


Figure 11. PRCL to SSFS Feed-Forward: improvement to the sensitivity $h(t)$.

4.2. Effect of the Adaptive 50 Hz Feed-Forward

Differently from the *PRCL to SSFS* feed-forward, the *Adaptive 50 Hz* feed-forward is theoretically aimed at a very definite frequency, which is exactly 50 Hz; looking at Figure 12, and because of the technical qualities described in Section 2.2, it is noticeable that the mains line is completely removed from DARM, and the coherence is greatly reduced in a band which is wider than the simple line itself, with a reduction factor in the range 2 to 8 in the band ranging from around 49 Hz to 51 Hz.

4.3. Effect of the Angular Controls

The main effect of the global angular controls is to have a reliable and optimal working point which allows having a high stability and duty cycle of the lock, which can be kept virtually indefinitely.

The effect of the residual angular motion on the sensitivity is reported in Figure 13; these data correspond to a period when the interferometer reached a stable sensitivity of about 55 Mpc BNS Range, and the Phase Noise Subtraction technique (cf. Section 3.3) was engaged. The data plotted here is only the one where a coherence with the sensitivity $h(t)$ of at least 0.3 was found.

The noise level of all the angular DOFs is well below both the measured sensitivity and the O3 target from the Observing Scenario paper [19], which guarantees no loss of performance due to angular controls. In Figure 13 also the projection of the sensitivity for the next O4 Scientific Run is shown: it can be seen that the sum of angular noises does not limit the foreseen sensitivity band, although it is not below a 1/10 safety margin for some frequency regions with respect to the sensitivity projection; therefore, an improvement of the angular controls is to be considered in view of the future O4 Scientific Run.

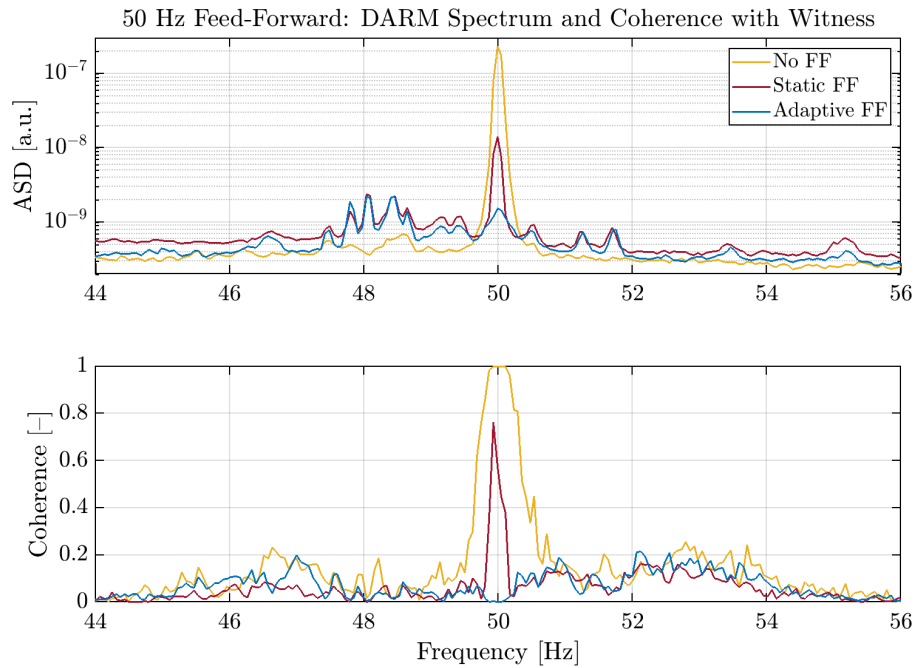


Figure 12. 50 Hz Feed-Forward: improvement to the DARM spectrum.

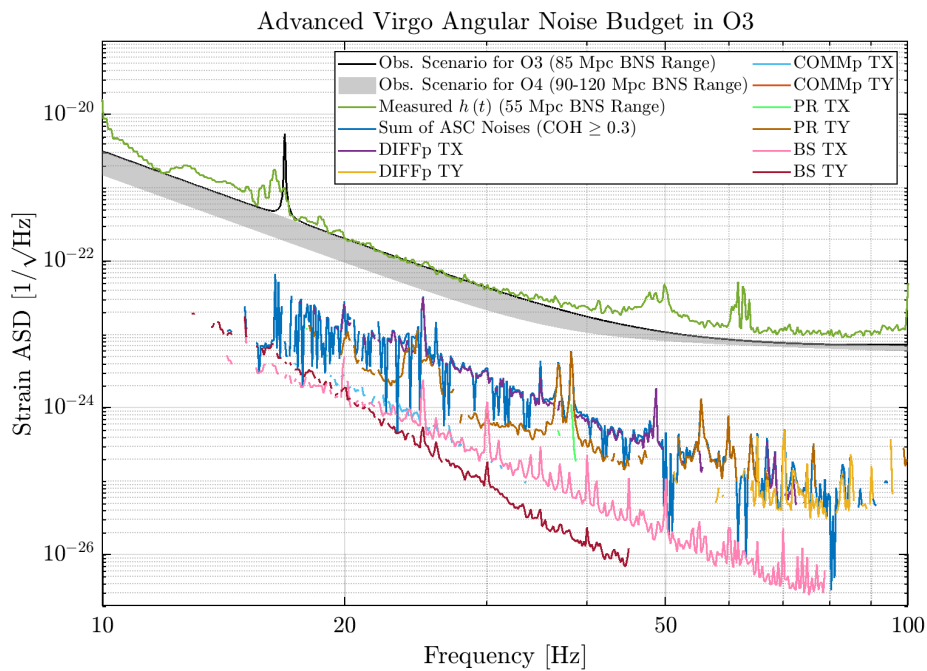


Figure 13. Angular Noise Budget for Advanced Virgo in O3. The Observing Scenario [19] target is set to 85 Mpc BNS Range. No angular DOF is impacting the sensitivity.

4.4. Overall Performance of the Advanced Virgo Detector in O3

Among the many improvements to different sub-systems of the detector, the new and the improved techniques of both longitudinal and angular controls here presented contributed to the improvement of the overall performance of the Advanced Virgo detector in the O3 Scientific Run.

In Figure 14 are reported the main figures of merit of the performance of Advanced Virgo in the O3 Scientific Run:

- the **sensitivity** to the strain induced by the passage of gravitational waves has increased considerably with respect to the O2 Run, reaching a peak value of 60 Mpc (which was set as the target for the run) and a steady value of 59 Mpc in O3b;
- the **duty cycle** of the detector has proved to be high, with Advanced Virgo in observing mode for more than 75 % of the time, allowing reaching high double and triple coincidence network duty factors;
- the **longest lock** of the run peaked at about 132 h of duration (almost twice of what has been achieved during the O2 Run [4]), which is basically the maximum achievable as it is constrained only by the scheduled time windows for the weekly Maintenance and Calibration of the detector; this result has been achieved in the week between 1–7 January 2020.

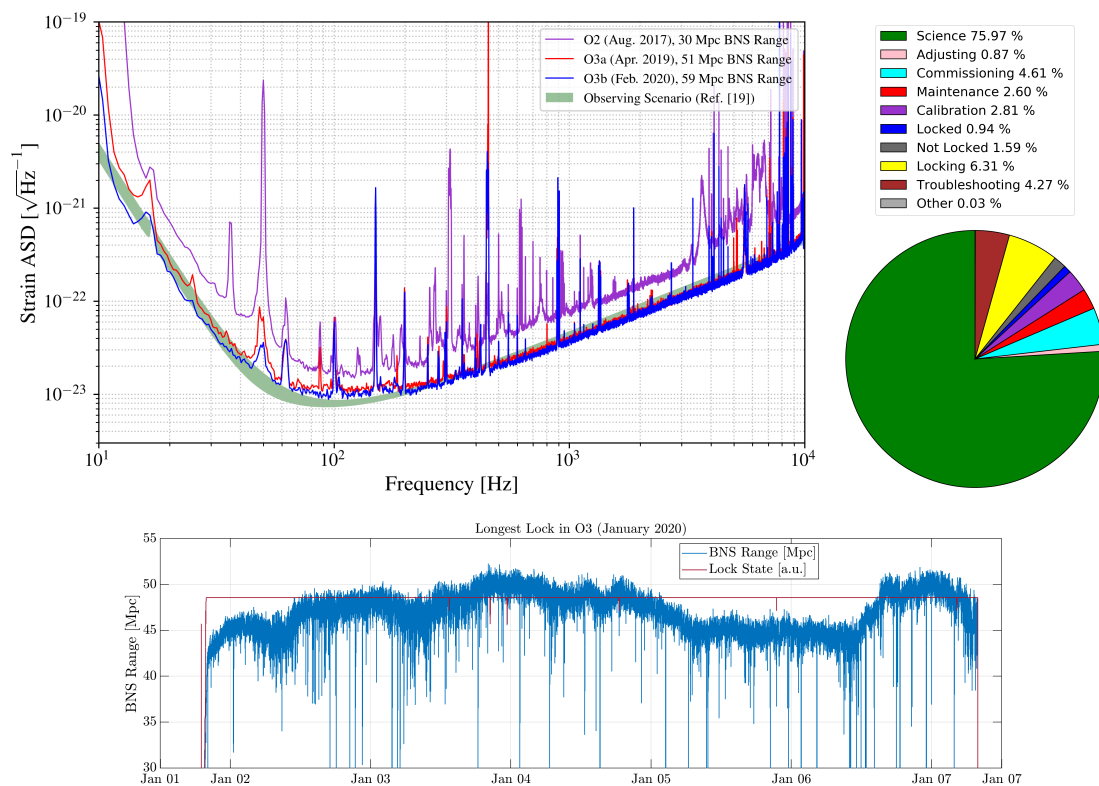


Figure 14. Snapshot of the performance of the Advanced Virgo detector in O3. **Top Left:** Sensitivity curve of Advanced Virgo in the two phases of the O3 Run, and comparison to the design sensitivity (Observing Scenario [19]) and the sensitivity during the O2 Run. **Top Right:** Overall duty cycle of Advanced Virgo during O3. **Bottom:** longest lock stretch of ≈ 132 h, from 1–7 January 2020, represented by the BNS Range and the Lock State flag of the detector.

5. Conclusions

This paper presented the main novelties of the control strategies which were implemented in the Advanced Virgo detector for the O3 Run. In particular, we were devoted to an extensive and focused description of: the noise subtraction techniques for the control of the longitudinal DOFs of the interferometer, either the gravitational wave channel or the auxiliary ones; the full description of the control scheme for all the angular DOFs of the interferometer in the several steps of the lock acquisition sequence, with in addition the implementation of a noise subtraction technique which improves the rejection of the angular control noise.

Finally, a brief description of all the improvements due to the previously described items to the sensitivity and the performance of the detector was presented.

In conclusion, it can be stated that the *Interferometer Sensing & Control* subsystem of Advanced Virgo provided several improvements to its core functionalities, which allowed to contribute to the overall improvement of the performance and the stability of the Advanced Virgo detector in the O3 Observing Run.

Author Contributions: Conceptualization, D.B., J.C.D., M.M., P.R. and M.W.; methodology, M.M., P.R. and M.W.; software, D.B., J.C.D., A.M., L.R., P.R., B.S. and M.W.; validation, M.M., P.R. and M.W.; formal analysis, A.A., D.B., J.C.D., C.D.R., M.M., P.R., M.V. and M.W.; investigation, A.A., D.B., J.C.D., C.D.R., M.M., P.R., M.V. and M.W.; resources, A.M., L.R., P.R. and B.S.; data curation, D.B., P.R. and M.W.; writing—original draft preparation, A.A., D.B. and M.W.; writing—review and editing, D.B., M.M. and P.R.; visualization, A.A., D.B. and E.N.T.S.M.; supervision, M.M.; project administration, M.M. All authors have read and agreed to the published version of the manuscript.

Funding: This research received no external funding.

Acknowledgments: The authors gratefully acknowledge the Italian Istituto Nazionale di Fisica Nucleare (INFN), the French Centre National de la Recherche Scientifique (CNRS) and The Netherlands Organization for Scientific Research, for the construction and operation of the Virgo detector and the creation and support of the EGO consortium. The authors also gratefully acknowledge research support from these agencies as well as by the Spanish Agencia Estatal de Investigación, the Consellera d’Innovació, Universitats, Ciència i Societat Digital de la Generalitat Valenciana and the CERCA Programme Generalitat de Catalunya, Spain, the National Science Centre of Poland and the Foundation for Polish Science (FNP), the European Commission, the Hungarian Scientific Research Fund (OTKA), the French Lyon Institute of Origins (LIO), the Belgian Fonds de la Recherche Scientifique (FRS-FNRS), Actions de Recherche Concertées (ARC) and Fonds Wetenschappelijk Onderzoek—Vlaanderen (FWO), Belgium. The authors gratefully acknowledge the support of the NSF, STFC, INFN, CNRS and Nikhef for provision of computational resources. *We would like to thank all of the essential workers who put their health at risk during the COVID-19 pandemic, without whom we would not have been able to complete this work.*

Conflicts of Interest: The authors declare no conflict of interest.

Abbreviations

The following abbreviations are used in this manuscript:

GW	Gravitational Wave
PSL	Pre-Stabilized Laser
EOM	Electro-Optic Modulator
IMC	Input Mode Cleaner
PR	Power Recycling mirror
NI	North Input mirror
NE	North End mirror
BS	Beam Splitter mirror
WI	West Input mirror
WE	West End mirror
SR	Signal Recycling mirror
HR	Highly-Reflective coating
AR	Anti-Reflective coating
CITF	Central InTerFerometer
OMC	Output Mode Cleaner
DOF	Degree Of Freedom
MICH	length difference between the arms of a MICHelson interferometer
PRCL	Power Recycling Cavity Length
CARM	Common ARM displacement
DARM	Differential ARM displacement
UGF	Unity Gain Frequency
COMM	COMMOn tilt/shift
DIFF	DIFFerential tilt/shift

PDH	Pound-Drever-Hall
SSFS	Second Stage of Frequency Stabilization
SLED	SuperLuminEscent Diode
PSD	Position Sensing Device
QPD	Quadrant PhotoDiode
PD	PhotoDiode
ASD	Amplitude Spectral Density
UPS	Uninterruptible Power Supply
RMS	Root Mean Square
BNS	Binary Neutron Star

References

1. The Virgo collaboration, Advanced Virgo Technical Design Report. Virgo Internal Document VIR-0128A-12. Available online: <https://tds.virgo-gw.eu/ql/?c=8940> (accessed on 4 December 2020).
2. Hild, S.; Grote, H.; Degallaix, J.; Chelkowski, S.; Danzmann, K.; Freise, A.; Hewitson, M.; Hough, J.; Luck, H.; Prijatelj, M.; et al. DC-readout of a signal-recycled gravitational wave detector. *Class. Quant. Grav.* **2009**, *26*, 055012. [[CrossRef](#)]
3. Acernese, F.; Agathos, M.; Agatsuma, K.; Aisa, D.; Allemandou, N.; Allocca, A.; Amarni, J.; Astone, P.; Balestri, G.; Ballardin, G.; et al. Advanced Virgo: A second-generation interferometric gravitational wave detector. *Class. Quant. Grav.* **2015**, *32*, 024001. [[CrossRef](#)]
4. Acernese, F.; Agathos, M.; Aiello, L.; Allocca, A.; Aloy, M.A.; Amato, A.; Antier, S.; Arène, M.; Arnaud, N.; Ascenzi, S.; et al. The Advanced Virgo longitudinal control system for the O2 observing run. *Astropart. Phys.* **2020**, *116*, 102386. [[CrossRef](#)]
5. Bersanetti, D.; Casanueva Diaz, J.; Allocca, A.; Heitmann, H.; Hoak, D.; Mantovani, M.; Ruggi, P.; Swinkels, B. New algorithm for the Guided Lock technique for a high-Finesse optical cavity. *Astropart. Phys.* **2020**, *117*, 102405. [[CrossRef](#)]
6. Acernese, F.; Alshourbagy, M.; Antonucci, F.; Aoudia, S.; Arun, K.G.; Astone, P.; Ballardin, G.; Barone, F.; Barsuglia, M.; Bauer, T.S.; et al. Automatic Alignment for the first science run of the Virgo interferometer. *Astropart. Phys.* **2020**, *33*, 131–139. [[CrossRef](#)]
7. Franzen, A. ComponentLibrary (A Vector Graphics Library for Illustrations of Optics Experiments). 2015. Available online: <http://www.gwoptics.org/ComponentLibrary/> (accessed on 4 December 2020). Licensed under a [Creative Commons Attribution-NonCommercial 3.0 Unported License](#).
8. Drever, R.W.; Hall, J.L.; Kowalski, F.V.; Hough, J.; Ford, G.M.; Munley, A.J.; Ward, H. Laser phase and frequency stabilization using an optical resonator. *Appl. Phys. Lasers Opt.* **1983**, *13*, 97–105. [[CrossRef](#)]
9. Black, E.D. An introduction to Pound–Drever–Hall laser frequency stabilization. *Am. J. Phys.* **2001**, *69*, 79. [[CrossRef](#)]
10. Acernese, F.; Alshourbagy, M.; Antonucci, F.; Aoudia, S.; Arun, K.G.; Astone, P.; Ballardin, G.; Barone, F.; Barsotti, L.; Barsuglia, M.; et al. Laser with an in-loop relative frequency stability of 1×10^{-21} on a 100-ms time scale for gravitational-wave detection. *Phys. Rev. A* **2009**, *79*, 053824. [[CrossRef](#)]
11. Acernese, F.; Antonucci, F.; Aoudia, S.; Arun, K.G.; Astone, P.; Ballardin, G.; Barone, F.; Barsuglia, M.; Bauer, T.S.; Beker, M.G.; et al. Measurements of superattenuator seismic isolation by Virgo interferometer. *Astropart. Phys.* **2010**, *33*, 182–189. [[CrossRef](#)]
12. Anderson, D.Z. Alignment of resonant optical cavities. *Appl. Opt.* **1984**, *23*, 2944–2949. [[CrossRef](#)] [[PubMed](#)]
13. Sidles, J.A.; Sigg, D. Optical torques in suspended Fabry-Perot interferometers. *Phys. Lett. A* **2016**, *354*, 167–172. [[CrossRef](#)]
14. Mantovani, M. for the Virgo Collaboration. The Advanced Virgo Interferometer Sensing and Control for the O3 Scientific Run. Virgo Internal Document VIR-0736A-19. Available online: <https://tds.virgo-gw.eu/ql/?c=14570> (accessed on 4 December 2020).
15. Mantovani, M.; Vajente, G. Alignment Accuracy Requirements for Advanced Virgo. Virgo Internal Document VIR-0247A-10. Available online: <https://tds.virgo-gw.eu/ql/?c=7228> (accessed on 4 December 2020).

16. Mantovani, M. Automatic Alignment Sensing and Control scheme for Advanced Virgo MSRC configuration. Virgo Internal Document VIR-0201A-11. Available online: <https://tds.virgo-gw.eu/ql/?c=8255> (accessed on 4 December 2020).
17. Morrison, E.; Meers, B.J.; Robertson, D.I.; Ward, H. Automatic alignment of optical interferometers. *Living Rev. Relativ.* **1994**, *33*. [[CrossRef](#)] [[PubMed](#)]
18. Canuel, B.; Genin, E.; Mantovani, M.; Marque, J.; Ruggi, P.; Tacca, M. Sub-nanoradiant beam pointing monitoring and stabilization system for controlling input beam jitter in gravitational wave interferometers. *Appl. Opt.* **2014**, *53*, 2906–2916. [[CrossRef](#)] [[PubMed](#)]
19. Abbott, B.P.; Abbott, R.; Abbott, T.D.; Abraham, S.; Acernese, F.; Ackley, K.; Adams, C.; Adya, V.B.; Affeldt, C.; Agathos, M.; et al. [KAGRA, LIGO Scientific and Virgo collaborations], Prospects for observing and localizing gravitational-wave transients with Advanced LIGO, Advanced Virgo and KAGRA. *Living Rev. Relativ.* **2020**, *23*. [[CrossRef](#)] [[PubMed](#)]

Publisher’s Note: MDPI stays neutral with regard to jurisdictional claims in published maps and institutional affiliations.



© 2020 by the authors. Licensee MDPI, Basel, Switzerland. This article is an open access article distributed under the terms and conditions of the Creative Commons Attribution (CC BY) license (<http://creativecommons.org/licenses/by/4.0/>).

Appendix D

End benches scattered light modelling and subtraction in advanced Virgo

End benches scattered light modelling and subtraction in advanced Virgo

M Waż* , R Gouaty and R Bonnard

Laboratoire d'Anney de Physique des Particules (LAPP), Univ. Grenoble Alpes,
Université Savoie Mont Blanc, CNRS/IN2P3, F-74941 Anney, France

E-mail: michal.was@lapp.in2p3.fr

Received 15 November 2020, revised 10 February 2021

Accepted for publication 17 February 2021

Published 11 March 2021



CrossMark

Abstract

Advanced Virgo end benches were a significant source of scattered light noise during the third observing run that lasted from April 1 2019 until March 27 2020. We describe how that noise could be subtracted using auxiliary channels during the online strain data reconstruction. We model in detail the scattered light noise coupling and demonstrate that further noise subtraction can be achieved. We also show that the fitted model parameters can be used to optically characterized the interferometer and in particular provide a novel way of establishing an absolute calibration of the detector strain data.

Keywords: gravitational waves, scattered light, calibration

(Some figures may appear in colour only in the online journal)

1. Introduction

Interferometric gravitational wave detectors have their sensitivity affected by scattered light, especially when microseism ground motion is elevated at times of rough seas. Examples of ground motion coupling to the sensitivity of detectors through scattered light have been previously described for initial Virgo [1, 2], GEO-HF [3] and most recently advanced LIGO [4, 5].

In this paper we focus on the coupling of light scattered by the end suspended benches to the sensitivity of advanced Virgo. This was a significant source of scattered light noise during the third observing run (O3) that lasted from April 1 2019 until March 27 2020. However, it was sufficiently well measured that scattered light noise could be subtracted after the fact from the gravitational wave strain data.

*Author to whom any correspondence should be addressed.

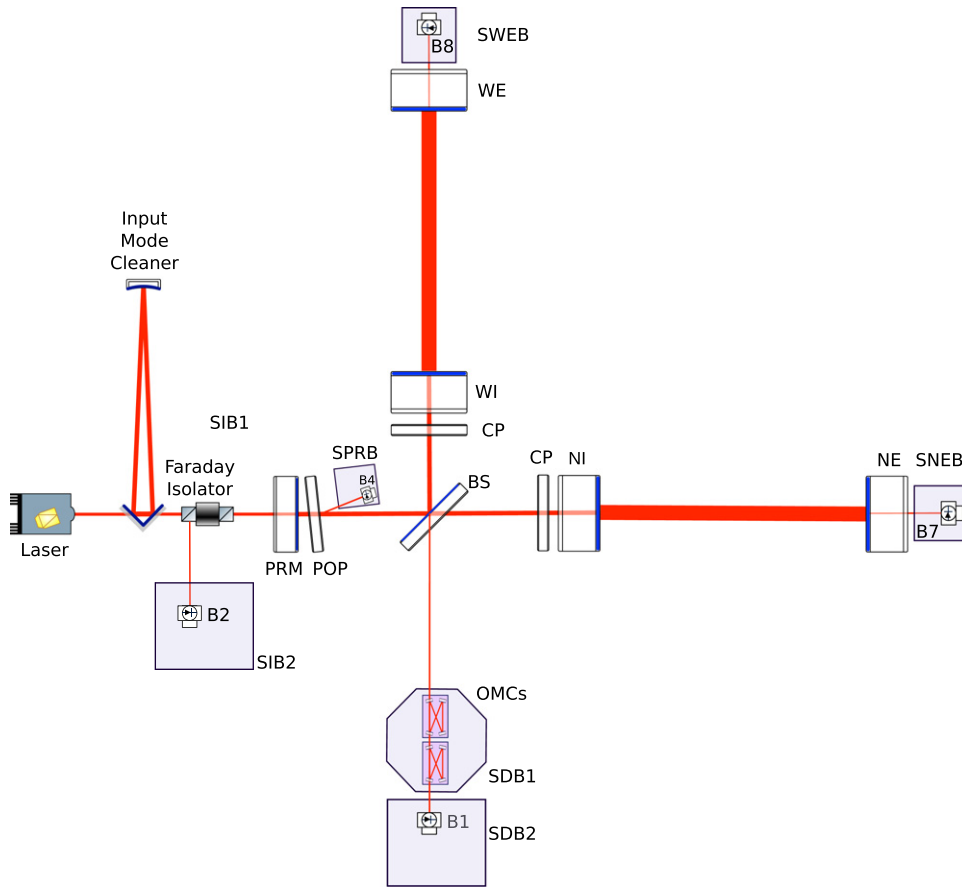


Figure 1. Optical layout of advanced Virgo during O3, adapted from [6] with kind permission of the European Physical Journal.

This paper is organized as follows. In section 2 we describe the theory of scattered light coupling from the suspended benches, in section 3 we show that scattered light can be measured using photodiodes located on these benches, in section 4 we demonstrate how these signals can be used to subtract scattered light noise from the strain data, and in section 5 we propose how to use scattered light as a new method to calibrate the strain data.

2. End benches scattered light theory

A simplified optical layout of advanced Virgo during O3 is shown on figure 1. It is a power recycled Fabry–Perot Michelson interferometer with 3 km arms. The interferometer transforms gravitational wave strain into audio frequency power fluctuations on the anti-symmetric port photodiode denoted B1. In transmission of the north end (NE) mirror and respectively the west end (WE) mirror are located the suspended north end bench (SNEB) and respectively the suspended west end bench (SWEB). Each of these benches host among others a photodiode denoted respectively B7 and B8.

Let E_0 be the electromagnetic field inside the west Fabry–Perot cavity at the highly reflective (HR) surface of the WE mirror of power transmission $T_{WE} \simeq 4.3 \times 10^{-6}$ [7], and x be the

distance between that surface and the scattering surface located on SWEB which reflects a fraction f_r of the impinging light. The electromagnetic field inside the Fabry–Perot cavity is in the fundamental Gaussian transverse mode, hence the field forward propagating on the bench is also in this mode, in particular light reaching photo-diodes. On the contrary light is scattered at all angles, the fraction f_r considers only the small portion of scattered light that is back scattered in the fundamental Gaussian mode and mode matched with the light inside the Fabry–Perot cavity. This is the only scattered light which will efficiently interfere with the dominant field in the arm cavities and on the photodiodes. As T_{WE} and f_r are small in the following we will keep only the leading term in $\sqrt{T_{WE}}$ and $\sqrt{f_r}$.

The scattering surface create a field E_{sc} that at the HR surface of the WE mirror is

$$E_{sc} = \sqrt{T_{WE}f_r}E_0 e^{i\phi_{sc}}, \quad (1)$$

where $\phi_{sc} = 4\pi\frac{x}{\lambda}$ is the phase delay due to the round trip propagation and λ is the laser wavelength. A small fraction of that light is transmitted through the HR coating yielding a total field

$$E_{tot} = E_0 + \sqrt{T_{WE}}E_{sc} = E_0 \left(1 + T_{WE}\sqrt{f_r} e^{i\phi_{sc}}\right), \quad (2)$$

while the majority is reflected back yielding a field E_{B8} towards the B8 photodiode

$$E_{B8} = \sqrt{T_{WE}}E_0 + E_{sc} = \sqrt{T_{WE}}E_0 \left(1 + \sqrt{f_r} e^{i\phi_{sc}}\right). \quad (3)$$

The field perturbation inside the arm cavity is amplified by the Fabry–Perot cavity in a frequency dependent way by

$$G(f) = \frac{1}{1-r} \frac{1}{1 + i\frac{f-f_{arm}}{f_{arm}}}, \quad (4)$$

where $r = \sqrt{1 - T_{WI} - \Lambda_{arm}} \sim 0.993$ [8] is the effective field reflectivity of the WI mirror taking into account the arm cavity round trip losses Λ_{arm} ,

$$f_{arm} = \frac{1-r}{r} \frac{c}{4\pi L} \simeq 55 \text{ Hz} \quad (5)$$

is the arm cavity pole frequency and $L = 3$ km is the arm cavity length. This yields a field inside the cavity

$$E_{cavity} = E_0 \left(1 + GT_{WE}\sqrt{f_r} e^{i\phi_{sc}}\right). \quad (6)$$

The interferometer is operated in DC read-out [9, 10] with an offset in the differential arm length. Let us denote ψ the differential phase offset and h the amplitude of a putative gravitational wave. The field inside the cavities becomes

$$E_{cavity, west} = E_0 e^{i\left(\frac{\psi}{2} + 2\pi G\frac{hL}{\lambda}\right)} \left(1 + GT_{WE}\sqrt{f_r} e^{i\phi_{sc}}\right) \quad (7)$$

$$E_{cavity, north} = E_0 e^{-i\left(\frac{\psi}{2} + 2\pi G\frac{hL}{\lambda}\right)} \quad (8)$$

where $L = 3$ km is the cavity length. A fraction $T_{IM} = 0.0138$ [8] of these fields returns through the input mirrors and recombines at the beam splitter, which yield at the anti-symmetric port

of the interferometer a power

$$\begin{aligned} P_{B1} &= T_{\text{IM}} |E_{\text{cavity, west}} - (1 - \epsilon)E_{\text{cavity, north}}|^2 \\ &= T_{\text{IM}} |E_0|^2 \left[\psi^2 + \epsilon^2 + 2\psi 4\pi G \frac{\hbar L}{\lambda} \right. \\ &\quad \left. + 2\psi GT_{\text{WE}} \sqrt{f_r} \sin \phi_{\text{sc}} + 2\epsilon GT_{\text{WE}} \sqrt{f_r} \cos \phi_{\text{sc}} \right], \end{aligned}$$

where ϵ accounts for asymmetries between the two arms that yield a contrast defect of the interferometer.

Thus scattered light directly mimicks a gravitational wave signal through phase and amplitude coupling

$$h_{\text{sc, phase}} = \frac{1}{L} T_{\text{WE}} \sqrt{f_r} \frac{\lambda}{4\pi} \sin \phi_{\text{sc}} \quad (9)$$

$$h_{\text{sc, amplitude}} = \frac{\epsilon}{\psi} \frac{1}{L} T_{\text{WE}} \sqrt{f_r} \frac{\lambda}{4\pi} \cos \phi_{\text{sc}}. \quad (10)$$

However, there are additional coupling path as scattered light modulates the power inside the west arm cavity

$$P_{\text{cavity}} = |E_0|^2 \left(1 + 2GT_{\text{WE}} \sqrt{f_r} \cos \phi_{\text{sc}} \right), \quad (11)$$

which through radiation pressure displaces in opposite directions the WI and WE mirrors and create an additional spurious signal

$$h_{\text{sc, pressure}} = \frac{2}{L} \frac{2\delta P_{\text{cavity}}}{c} \text{WE}_{F \rightarrow z} \quad (12)$$

$$= \frac{G}{L} \text{WE}_{F \rightarrow z} \frac{8|E_0|^2}{c} T_{\text{WE}} \sqrt{f_r} \cos \phi_{\text{sc}}, \quad (13)$$

where c is the speed of light and

$$\text{WE}_{F \rightarrow z}(f) = \frac{1}{M} \frac{1}{\Omega^2 - (2\pi f)^2} \quad (14)$$

is the mechanical response of the suspended WE mirror with M the mass of the mirror and Ω the mirror suspension pendulum angular frequency. Note that we omit here optical spring effects that have a negligible effect above 10 Hz as shown by the comparison to numerical simulation described at the end of this section.

These power fluctuations are further amplified and filtered in the combined power recycling and arm cavity by

$$G_{\text{combined}}(f) = \frac{\sqrt{T_{\text{IM}}}}{(1-r)(1-r_{\text{PR}}) + r_{\text{PR}}\Lambda_{\text{arm}}} \frac{1}{1 + i\frac{f}{f_{\text{combined}}}}, \quad (15)$$

where $r_{\text{PR}} = \sqrt{1 - T_{\text{PR}} - \Lambda_{\text{PR}}} = 0.975$ [11] is the effective field reflectivity of the PR mirror taking into account the power recycling cavity round trip losses Λ_{PR} and

$$f_{\text{combined}} = \frac{(1-r)(1-r_{\text{PR}}) + r_{\text{PR}}\Lambda_{\text{arm}}}{r + r_{\text{PR}} - \Lambda_{\text{arm}}} \frac{c}{4\pi L} \simeq 1.0 \text{ Hz} \quad (16)$$

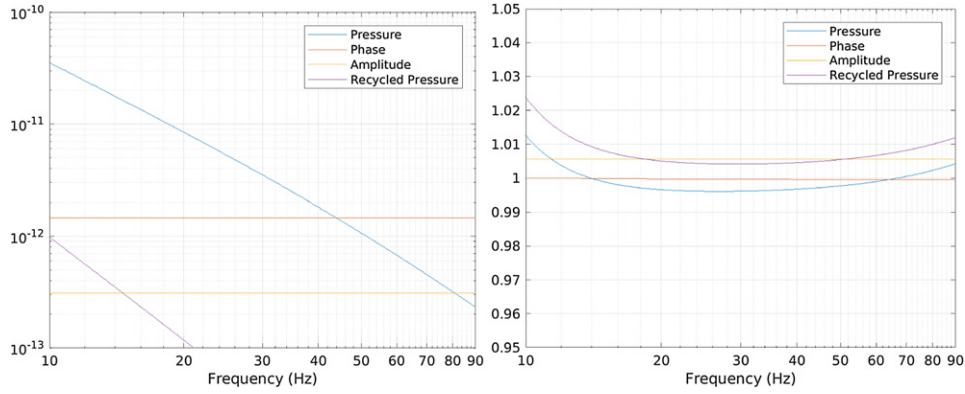


Figure 2. Left pane shows the scattering coupling transfer functions for the three coupling paths: radiation pressure given by equation (13), phase given by equation (9), amplitude given by equation (10), and recycled radiation pressure given by equation (17). The right pane shows the ratio between the transfer function numerically computed using *Optickle* and the analytical computation shown on the left pane.

is the combined cavity pole frequency. The displacement caused by the radiation pressure of these fluctuations is common to both arms, hence *a priori* the lengths of both arms is changed by the same amount not yielding any differential signal. However the power in the arms is not exactly equal, it may differ by a small fraction ρ , which will yield a differential effect as radiation pressure displacement is proportional to the power in the given arm. This creates a spurious signal

$$h_{sc, \text{ pressure recycled}} = \rho \sqrt{T_{WI}} \frac{G_{\text{combined}}}{2} h_{sc, \text{ pressure}}, \quad (17)$$

where the factor $\frac{1}{2}$ accounts for the recycled power being split between the two arms.

The power inside the arm cavities is estimated to be $|E_0|^2 = 90 \text{ kW}$ for a laser input power of 18 W used in the first half of O3. While the dark fringe power was set to be $P_{B1} = 2.8 \text{ mW}$ and the contrast defect light in the TEM00 mode in transmission of the output mode cleaner was measured to be $120 \pm 20 \mu\text{W}$ [12], which yields $\epsilon/\psi = 0.21$. The power ratio between the two arms has not been accurately measured, but it varied by $\sim 1\%$ during the run which sets an order of magnitude for ρ . These measurements allows us to evaluate the relative contributions of the four coupling paths as shown on figure 2 assuming a fiducial scattering $f_r = 10^{-6}$. The radiation pressure is dominant below 45 Hz while the phase coupling is dominant above. Note that in a previous estimate [13] of the scattered light coupling a factor 2 was missing for the radiation pressure and phase coupling path, and the amplitude and recycled radiation pressure coupling paths were completely neglected.

These analytic computations have been verified to be accurate with an interferometer simulation performed with the *Optickle* simulation software [14]. The only deviation is that in simulation the radiation pressure effects include the optical spring at $\sim 4 \text{ Hz}$, which causes a small deviation at low frequency of 2% in amplitude and 1 degree in phase at 10 Hz as shown on figure 2. In the following section we use the optical simulation results scaled by the parameters derived analytically to perform fits.

Fortunately the scattered light interference also produces a signal on the B8 photodiode

$$P_{B8} = \alpha T_{WE} |E_0|^2 \left(1 + 2\sqrt{f_r} \cos \phi_{sc} \right), \quad (18)$$

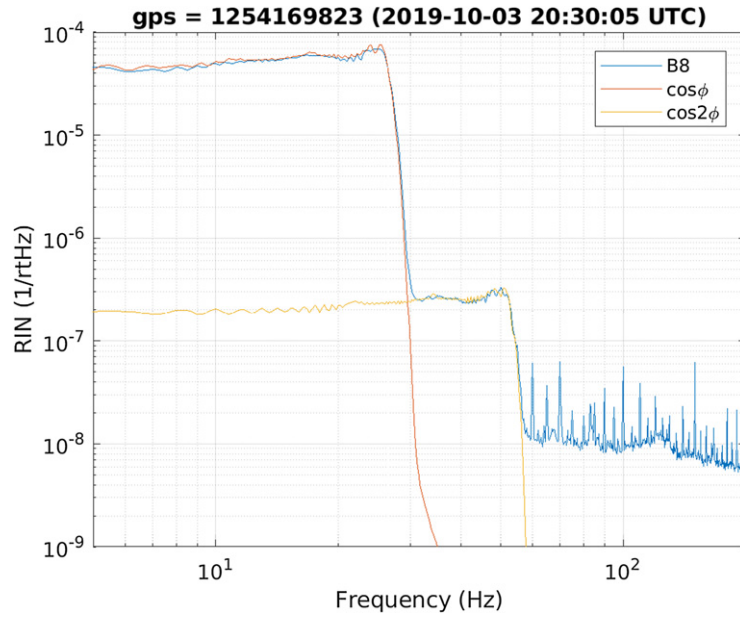


Figure 3. RIN of P_{B8} with superposed fringe wrapped relative motion between SWEB and WE during the time of intentional SWEB motion with the quadrant shutters open.

where α accounts for the light losses between WE and the B8 photodiode due to pick-offs for quadrant photodiodes and cameras, photodiode quantum efficiency, and other loss mechanisms. In particular the relative intensity noise (RIN) of P_{B8} yields a direct measurement of the scattered light fraction

$$\frac{\delta P_{B8}}{P_{B8}} = 2\sqrt{f_r} \cos \phi_{sc}. \quad (19)$$

3. Measurement of scattered light fraction

Large amplitude slow motion of the bench, especially at the microseism peak at 300 mHz, is up converted to the sensitive band of the detector (above 10 Hz) by the sine and cosine function of $\phi_{sc} = 4\pi\frac{x}{\lambda}$. This yields a noise with characteristic arch shape in a time-frequency representation of the data with a time dependent frequency $f(t) = \frac{2|\dot{x}(t)|}{\lambda}$ proportional to the bench speed. The variation in distance x between SWEB and WE can be directly measured from the ground connected local controls of SWEB (linear variable differential transformers) and of WE (optical levers), where the ground motion is removed at first order by taking the difference of these sensors.

To study scattering coupling the SWEB bench has been intentionally moved with large amplitude to increase the scattered light noise signal in the detector. In total four measurements of 3 min in duration have been performed over a 30 min time span. Two with an intentional motion of SWEB and two with an intentional motion of SNEB. In each case one of the measurement was with the quadrant shutters open and one with the quadrant shutters closed.

Table 1. Fitted scattered power for four different measurements with intentional large amplitude motion of either SWEB or SNEB, and with quadrant photodiode shutters on given bench either open or closed.

	f_r	f_{2r}
SWEB, open	4.0×10^{-8}	1.50×10^{-12}
SWEB, closed	6.0×10^{-9}	1.50×10^{-12}
SNEB, open	2.50×10^{-8}	3.0×10^{-14}
SNEB, closed	3.50×10^{-8}	5.0×10^{-14}

Using equation (19) we fit the scattering fraction f_r to match the RIN of P_{B8} . In addition, the second order scattering fraction f_{2r} is clearly visible, which correspond to light that makes two round trips between the mirror and the bench. An example is shown on figure 3, and the fit parameters for all four measurements are shown in table 1.

Note that closing the quadrant shutters reduces the SWEB scattering by almost an order of magnitude from $f_r = 4.0 \times 10^{-8}$ to $f_r = 6.0 \times 10^{-9}$. When the shutters are closed the beam is dumped on anti-reflective coated black glass on the bench which has low scattering, which explains the reduction in scattering. However, for SNEB the scattering increases from $f_r = 2.5 \times 10^{-8}$ to $f_r = 3.5 \times 10^{-8}$. This is due to the lack of these beam dumps on SNEB, the beam is sent instead on the vacuum chamber wall that appears to have a scattering similar in magnitude to the back scatter from the quadrant photodiode sensor.

4. Subtraction of scattered light

The RIN of P_{B8} give us direct access to the coherent sum of $\cos \phi_{sc}$ and $\cos 2\phi_{sc}$ with the appropriate scattering fraction coefficient. In addition, the $\sin \phi_{sc}$ term which couples through (9) can be reconstructed from the Fourier decomposition of $\cos \phi_{sc}$ and the bench speed as follows

$$\cos \phi_{sc}(t) = \int_{-\infty}^{\infty} \hat{\phi}_{sc}(\omega) e^{i\omega t} d\omega \quad (20)$$

$$\sin \phi_{sc}(t) = i \operatorname{sign} \left[\frac{d\phi_{sc}(t)}{dt} \right] \int_0^{\infty} \left[\hat{\phi}_{sc}(-\omega) e^{-i\omega t} - \hat{\phi}_{sc}(\omega) e^{i\omega t} \right] d\omega. \quad (21)$$

We will not attempt a formal derivation of that relation, instead we show that it is able to coherently subtract the observed scattering noise.

In practice we use the local controls to obtain the bench speed in $\mu\text{m/s}$, and use the tanh function instead of sign to avoid a discontinuity when the speed is low. For low speeds the exact value of $\sin \phi_{sc}(t)$ does not matter as its contribution will remain below 10 Hz.

We have verified that this reconstruction method of $\sin \phi_{sc}(t)$ does not introduce any bias in amplitude or phase using surrogate data as follows. We create a bench motion time series by filtering white Gaussian noise with a resonant pole at 0.1 Hz with a quality factor of 30. This yields a simulation of an imperfect intentional motion of the bench. We add a white noise three orders of magnitude lower than the cosine of the bench phase to simulate the sensing noise of the B8 photodiode. Using the method above we reconstruct the sine of the bench phase and compare it to the direct computation. The obtained reconstruction errors are lower than 0.1% in the 10–30 Hz band.

We then apply this $\sin \phi_{sc}(t)$ reconstruction method to the real detector data described in section 3. We use the transfer functions given by equations (9), (10) and (13) to subtract the

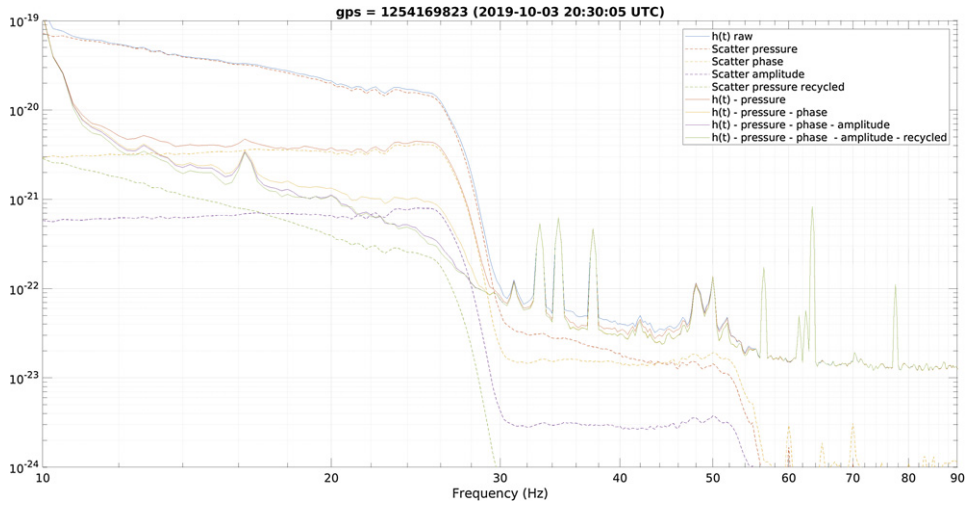


Figure 4. Spectrum of strain data during an intentional motion of SWEB. Shown are the original strain data, the projections of the radiation pressure, phase and amplitude couplings, alongside the successive subtraction in time domain of each of these contributions.

Table 2. Fitted interferometer parameters for four different measurements with intentional large amplitude motion of either SWEB or SNEB, and with quadrant photodiodes shutters on given bench either open or closed. For comparison the expected value of these parameters from other measurements is also shown.

	T_{WE} (ppm)	T_{NE} (ppm)	$ E_0 ^2$ (kW)	Contrast defect (μW)	ρ (%)
SWEB, open	4.34 ± 0.04	—	92.1 ± 0.7	95 ± 8	1.41 ± 0.06
SWEB, closed	4.36 ± 0.17	—	92.1 ± 5.1	82 ± 31	1.73 ± 0.10
SNEB, open	—	4.45 ± 0.08	91.6 ± 1.8	132 ± 19	1.05 ± 0.17
SNEB, closed	—	4.46 ± 0.05	91.3 ± 1.2	180 ± 12	1.26 ± 0.04
Expected					
[7, 12, 16]	4.3 ± 0.2	4.4 ± 0.1	90 ± 5	120 ± 20	~ 1

scattering noise measured by P_{B8} and the reconstructed phase quadrature during a time of intentional motion of SWEB. The result is shown on figure 4 and demonstrate up to a factor 40 reduction in scattered light noise. Also the second order scattering between 30 Hz and 55 Hz is correctly removed. To be able to fit these theoretical transfer functions to measurements, we diagonalize the measured transfer functions using the cross correlation matrix between $\cos \phi_{sc}$ and $\sin \phi_{sc}$, as performed in gravitational wave strain noise subtractions [15].

In total four measurements of 3 min in duration have been performed. Two with an intentional motion of SWEB and two with an intentional motion of SNEB. In each case one of the measurement was with the quadrants shutters open and one with the quadrants shutters closed.

To achieve this high subtraction efficiency we fitted the interferometer parameters as listed in table 2. The measurement errors were estimated by splitting the 3 min of available data into six blocks of 30 s, and repeating the complete analysis and fit separately on each of them. However these do not include systematic errors for example due to the frequency dependent response of the photodiodes, which could add $\sim 2\%$ errors on the leading parameters of T_{WE} ,

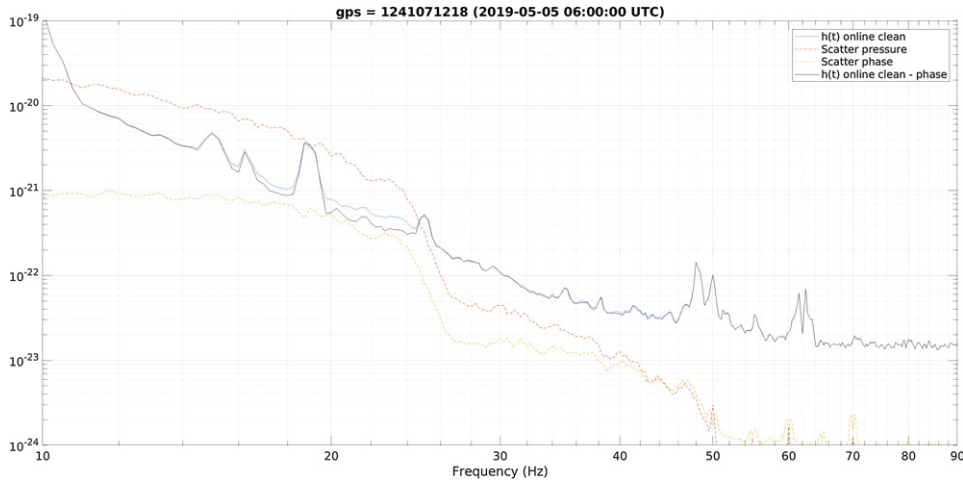


Figure 5. Spectrum of strain data during bad weather. Shown are the strain data after online noise cleaning, the projections of the radiation pressure and phase couplings of SWEB motion, and the effect of subtracting the phase coupling from the already cleaned data.

T_{NE} and $|E_0|^2$, and potentially larger errors in the sub-dominant parameters. This is a likely explanation for the inconsistency in the measured contrast defect and arm power asymmetry ρ between the SNEB and SWEB measurements.

The model and method described above have not been used to subtract scattered light noise from O3 online strain data used for gravitational wave analysis. Instead a simpler model independent approach has been used in the reconstruction process of the strain data to subtract several different noises [17]. This was performed by measuring the transfer function between auxiliary channels and the strain data over a 500 s long stretch of data, and using these transfer functions on the following 500 s of data to subtract the noise from these auxiliary channels. The measured power P_{B8} and P_{B7} were among the auxiliary channels to subtract noise, which allowed to subtract the combined contribution of radiation pressure, recycled radiation pressure and amplitude coupling. P_{B8} was more critical as the SWEB suspension suffered from a reduced isolation leading to larger motion during bad weather times.

On figure 5 we show that this noise subtraction was effective at removing the radiation pressure contribution of scattered light from SWEB that is coherent with P_{B8} , leading to sensitivity improvement of up to a factor 4. However that method was not able to remove the phase coupling path which is not coherent with B8. Using equation (21) to reconstruct the phase coupling we are able to reduce the noise by a further 30% at 20 Hz.

The strain data after subtraction are incoherent with the two subtracted components (proportional to $\cos \phi_{sc}$ and $\sin \phi_{sc}$), hence the residual strain data noise adds in quadrature with these components. Given the overall factor 5 decrease in noise at 20 Hz, it means that the scattered light noise measured by P_{B8} has been removed with $\sim 98\%$ efficiency, consistent with the factor 40 reduction in noise observed during intentional motion of the benches.

5. Interferometer absolute calibration

The measurement of T_{WE} and T_{NE} described above are derived from equation (9) and assumed that the calibration of the strain data was accurate. However the transmission of the end mirrors

have also been measured at LMA before installation [7, 16] ($T_{\text{WE}}^{\text{LMA}} = 4.3 \pm 0.2 \times 10^{-6}$ and $T_{\text{NE}}^{\text{LMA}} = 4.4 \pm 0.1 \times 10^{-6}$). Comparing the two measurement of the mirror transmission yields a measurement of the accuracy of the strain data calibration.

Indeed, combining equations (9) and (19) we obtain that scattered light introduces an absolutely calibrated signal

$$h_{\text{signal}} = \frac{1}{L} T_{\text{WE}} \frac{\lambda}{4\pi} \frac{1}{2} \mathcal{T}\mathcal{F} \left[\frac{\delta P_{\text{B8}}}{P_{\text{B8}}} \right], \quad (22)$$

where $\mathcal{T}\mathcal{F}$ is the transform from $\cos \phi_{\text{sc}}$ to $\sin \phi_{\text{sc}}$ given in equation (21). The arm length L and the laser wavelength λ are known with precision better than 0.01%, which introduces a negligible error. We also assume that the photodiode frequency response is corrected to be flat between DC and the measurement band of 10–30 Hz. In this case the ratio of the calibrated scatter light signal with the calibrated strain data after reconstruction h_{rec} is directly equal to the ratio of the two estimates of the WE mirror transmissions

$$\frac{h_{\text{rec}}}{h_{\text{signal}}} = \frac{T_{\text{WE}}}{T_{\text{WE}}^{\text{LMA}}} = \frac{4.34 \pm 0.04 \times 10^{-6}}{4.3 \pm 0.2 \times 10^{-6}} = 1.009 \pm 0.05. \quad (23)$$

Analogously for the NE mirror transmission estimates yields $\frac{h_{\text{rec}}}{h_{\text{signal}}} = 1.014 \pm 0.025$. The dominant source of error in these measurements comes from the 2%–5% uncertainty in the end mirror coating transmission, the statistical error is of the order of 1% and could be reduced by longer measurements.

The current calibration of LIGO and Virgo is performed using a *photon calibrator* [18, 19], an auxiliary laser that pushes on the mirrors through radiation pressure. A fundamental issue of that method is the absolute calibration of the laser power of that auxiliary laser, as the references standards in different countries are in disagreement by several percent. For O3 this has been addressed by inter-calibrating the LIGO and Virgo power references, which removes a calibration bias between the instruments but leaves the possibility of an absolute bias of the calibration of the gravitational wave detector network. The method described above could allow an absolute calibration of the detectors which do not rely on these power reference standards. Instead the method relies on precise measurement of the transmission of the end mirrors before their installation, a relative power measurement that has been performed with a few percent precision. However, in principle that precision could be significantly improved by developing the corresponding metrology.

6. Conclusions

We have shown how both quadratures of the scattered light from suspended end benches can be reconstructed from the signal of the photodiode located on that bench and from the information on the sign of the bench displacement speed. We derive a model of the main coupling mechanism for scattered light from these benches to the detector sensitivity, which allows to fit real data and subtract the scattered light noise contribution by up to a factor 40.

Moreover, the fitted interferometer parameters demonstrate how scattered light injections can be used to characterize the interferometer, as they provide self calibration injections of light field fluctuations directly into each arm cavity. In particular they are able to measure the power circulating in the interferometer and the interferometer contrast defect.

We have also shown that scattered light noise can be used to accurately calibrate the absolute response of the detector. This method is completely independent of previously proposed

methods such as the ‘free Michelson’ method [17], the photon calibrator or *Newtonian calibrator* [20]. We stress that measurement described above was opportunistic and performed for a different purpose. Dedicated measurements would yield more robust results. For instance by performing scattered light injection over a longer time with a faster motion to cover frequencies up to at least 100 Hz, which more clearly separates the different coupling mechanism that are dominant at different frequencies.

Acknowledgments

The authors gratefully acknowledge the Italian Istituto Nazionale di Fisica Nucleare (INFN), the French Centre National de la Recherche Scientifique (CNRS) and the Netherlands Organization for Scientific Research, for the construction and operation of the Virgo detector and the creation and support of the EGO consortium. The authors also gratefully acknowledge research support from these agencies as well as by the Spanish Agencia Estatal de Investigación, the Consellera d’Innovació, Universitats, Ciència i Societat Digital de la Generalitat Valenciana and the CERCA Programme Generalitat de Catalunya, Spain, the National Science Centre of Poland and the Foundation for Polish Science (FNP), the European Commission, the Hungarian Scientific Research Fund (OTKA), the French Lyon Institute of Origins (LIO), the Belgian Fonds de la Recherche Scientifique (FRS-FNRS), Actions de Recherche Concertées (ARC) and Fonds Wetenschappelijk Onderzoek—Vlaanderen (FWO), Belgium. The authors gratefully acknowledge the support of the NSF, STFC, INFN, CNRS and Nikhef for provision of computational resources.

Data availability statement

The data that support the findings of this study are available upon reasonable request from the authors.

ORCID iDs

M Wąs  <https://orcid.org/0000-0002-1890-1128>

References

- [1] Aasi J *et al* 2012 The characterization of Virgo data and its impact on gravitational-wave searches *Class. Quantum Grav.* **29** 155002
- [2] Accadia T *et al* 2010 Noise from scattered light in Virgo’s second science run data *Class. Quantum Grav.* **27** 194011
- [3] Dooley K L *et al* 2016 GEO 600 and the GEO-HF upgrade program: successes and challenges *Class. Quantum Grav.* **33** 075009
- [4] Abbott B P *et al* 2018 Effects of data quality vetoes on a search for compact binary coalescences in advanced LIGO’s first observing run *Class. Quantum Grav.* **35** 065010
- [5] Soni S *et al* 2020 Reducing scattered light in LIGO’s third observing run *Class. Quantum Grav.* **38** 025016
- [6] Acernese F *et al* 2018 Status of advanced virgo *EPJ Web Conf.* **182** 02003
- [7] Pinard L 2015 Advanced Virgo end mirror characterization report- em03 (coatings c14042/20 + c14035/20) *Technical Report VIR-0270A-15*
- [8] Pinard L 2014 Advanced Virgo input mirror characterization report- im02 (coatings c14081 + c14087) *Technical Report VIR-0543A-14*

- [9] Hild S *et al* 2009 DC-readout of a signal-recycled gravitational wave detector *Class. Quantum Grav.* **26** 055012
- [10] Fricke T T *et al* 2012 DC readout experiment in enhanced LIGO *Class. Quantum Grav.* **29** 065005
- [11] Pinard L 2015 Advanced Virgo power recycling mirror characterization report- pr01 (coatings c14097 + c14101) *Technical Report VIR-0029A-15*
- [12] Was M 2019 Virgo logbook 46956 <https://logbook.virgo-gw.eu/virgo/?r=46956>
- [13] Ottaway D J, Fritschel P and Waldman S J 2012 Impact of upconverted scattered light on advanced interferometric gravitational wave detectors *Opt. Express* **20** 8329
- [14] Optickle source code: <https://github.com/Optickle/Optickle/tree/Optickle2>
- [15] Davis D, Massinger T, Lundgren A, Driggers J C, Urban A L and Nuttall L 2019 Improving the sensitivity of advanced LIGO using noise subtraction *Class. Quantum Grav.* **36** 055011
- [16] Pinard L 2015 Advanced Virgo end mirror characterization report- em01 (coatings c14042/10 + c14035/10) *Technical Report VIR-0270A-15*
- [17] Acernese F *et al* 2018 Calibration of advanced virgo and reconstruction of the gravitational wave signal $h(t)$ during the observing run O2 *Class. Quantum Grav.* **35** 205004
- [18] Karki S *et al* 2016 The advanced LIGO photon calibrators *Rev. Sci. Instrum.* **87** 114503
- [19] Estevez D, Lagabbe P, Masserot A, Rolland L, Seglar-Arroyo M and Verkindt D 2020 The advanced Virgo photon calibrators *Technical Report VIR-0705A-20*
- [20] Estevez D, Lieunard B, Marion F, Mours B, Rolland L and Verkindt D 2018 First tests of a Newtonian calibrator on an interferometric gravitational wave detector *Class. Quantum Grav.* **35** 235009

Appendix E

A high angular resolution interferometric backscatter meter

High-angular-resolution interferometric backscatter meter

M. WAS*  AND E. POLINI

Laboratoire d'Annecy de Physique des Particules (LAPP), Univ. Grenoble Alpes, Université Savoie Mont Blanc, CNRS/IN2P3, F- 74941 Annecy, France

*michal.was@lapp.in2p3.fr

Received 17 February 2022; revised 29 March 2022; accepted 29 March 2022; posted 30 March 2022; published 27 April 2022

Backscatter limits many interferometric measurements, including gravitational wave detectors, by creating spurious interference. We describe an experimental method to directly and quantitatively measure the backscatter interference. We derive and verify experimentally a relation between backscatter interference, beam radius, and the scattering sample bidirectional reflectance distribution function. We also demonstrate that our method is able to measure backscatter from high-quality optics for angles as low as 500 μrad with an angular resolution of 160 μrad . © 2022 Optica Publishing Group

<https://doi.org/10.1364/OL.456391>

Introduction. Scattered light is a limitation to many high-sensitivity interferometric measurements. In particular, it is an issue in gravitational wave detectors such as LIGO and Virgo, which are kilometer-scale Fabry–Perot Michelson interferometers with power and signal recycling [1,2]. Scattered light affects these detectors in two ways: by introducing optical loss that lowers the optical power and reduces the efficiency of quantum noise reduction through squeezing [3]; and by introducing spurious interference between backscattered light and the main interferometer beam [4]. The latter has been a limitation to the sensitivity for all interferometric gravitational wave detectors operated to date and introduces non-stationary non-Gaussian noise [5–8]. This is due to the extreme sensitivity of these detectors where a 10^{-24} fraction of the main beam recombining after a spurious beam path can significantly affect the sensitivity.

This highlights the importance of understanding backscattered light, i.e., light that leaves the main interferometer beam path, propagates to a scattering surface, and then backpropagates to recombine coherently with the main interferometer beam. In particular, light backscattered at angles of a few milliradians is relevant for beam expanding telescopes [9], and at angles between $\sim 100 \mu\text{rad}$ and a few degrees is relevant for core optics baffles [4]. Scattering at these small angles is rarely measured and hard to access by the available methods [3].

The angular distribution of light reflected and backscattered by a surface is usually characterized by the bidirectional reflectance distribution function (BRDF). The BRDF is usually measured by directly detecting the scattered light power using a photodetector or a camera, and varying the relative orientation of the sensor and the scattering sample relative to the probe light beam. These systems can reach a sensitivity of 10^{-9}srad^{-1} and

an angular resolution of $300 \mu\text{rad}$ with up to 15 orders magnitude of dynamic range [10–12]. With similar systems, scattered light can also be imaged with lower angular resolution to identify individual point defects contributing to scattering [13–15]. However, in most cases, these systems cannot study light that is backscattered directly in the direction of the incoming beam. Direct backscatter measurement can easily be limited by the scattering from the measurement setup reaching only sensitivities of 10^{-4}srad^{-1} [16].

In this paper, we present a backscatter measurement that relies on laser interference and position modulation of the scattering sample under consideration. A similar approach, but with a more complex modulation approach and poorer angular resolution, has been used for scattered light measurements for the future space borne LISA gravitational wave detector [17]. An alternative that uses a wide-spectrum light source [18] has achieved a good angular resolution but two orders of magnitude poorer sensitivity.

Measurement setup. The measurement optical layout is shown schematically in Fig. 1. A single-mode S-polarized Nd:YAG laser beam with wavelength $\lambda = 1064 \text{ nm}$ and power of 70 mW is split using a 50/50 beam splitter located at the beam waist. The beam transmitted by the beam splitter is used as a local oscillator beam for the balanced homodyne detection (BHD), while the reflected beam is sent to the scattering sample. The incident beam is translated across the surface of the scattering sample using a motorized mirror (Newport AG-M100N). The beam propagating toward the scattering sample is expanded from a waist of $300 \mu\text{m}$ to 2.1 mm using a telescope composed of three lenses. The last two lenses of focal length -100 mm and 400 mm compose a Galilean telescope with magnification $\times 4$. The first lens with a focal length of 500 mm is a relay, which adds a degree of freedom to simultaneously obtain a collimated beam and to transform the angular displacement of the motorized mirror into pure beam translation on the scattering sample. As a result for lateral beam translations of $\pm 6 \text{ mm}$, the changes of beam tilt on the sample are smaller than $\pm 30 \mu\text{rad}$.

Backscattered light propagates back through the telescope toward the first 50/50 beam splitter, where half of the power is sent toward the BHD and the other half is lost. The difference in power received by the two photodetectors yields a signal

$$P_1(t) - P_2(t) = \frac{P_0}{\sqrt{2}} \sqrt{f_{\text{sc}}} \cos\left(2\pi \frac{\Delta L(t)}{\lambda}\right), \quad (1)$$

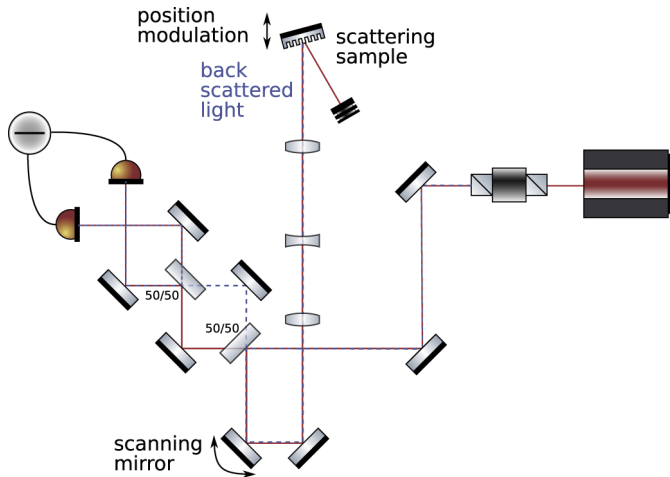


Fig. 1. Optical layout of the interferometric scatter meter with balanced homodyne detection. The scattering sample is freely swinging on a pendulum suspended optical breadboard.

where P_0 is the power provided by the laser, f_{sc} is the fraction of light backscattered by the sample that is mode matched with the local oscillator beam, and $\Delta L(t)$ is the displacement of the sample.

This signal can be normalized by the total power received by the two photodiodes, which yields

$$A(t) = \frac{P_1(t) - P_2(t)}{P_1(t) + P_2(t)} = \sqrt{2f_{sc}} \cos\left(2\pi \frac{\Delta L(t)}{\lambda}\right). \quad (2)$$

For the case where $\Delta L(t)$ fluctuates over many wavelengths, the backscattered light fraction is simply obtained as the normalized signal variance $\text{Var}(A(t)) = f_{sc}$. Note that this assumes that the backscattered light is perfectly aligned and mode matched with the local oscillator beam of the BHD.

To achieve a large position modulation, the sample is placed on a breadboard suspended on four metal wires at an angle of $\sim 45^\circ$ to the vertical, similar to a Newton's cradle. This allows a free pendulum motion along the beam axis, while restricting the motion in the orthogonal plane. After a gentle touch, the free motion of that suspension creates a decaying sinusoidal motion with an amplitude of a few hundred wavelengths and quality factor ~ 1000 . The motion Doppler shifts the backscattered light frequency and create a quasi-sinusoidal signal with a time-dependent frequency $f(t) = \frac{2v(t)}{\lambda}$ proportional to the instantaneous bench speed. This results in a signal with a power spectrum spreading between 0 Hz and a few kilohertz, with a peak power just below the cutoff frequency, as shown in Fig. 2. As the sample is the only object with a large motion, the upconversion clearly identifies light that is back reflected or backscattered by the sample.

Above 500 Hz, the noise floor is shot noise limited, while below, there are significant contributions of the mechanical resonances of the various optical components used in the measurement and the 50-Hz mains AC current harmonics. To measure f_{sc} without being affected by these noise sources, we integrate the power spectrum density of A only between 500 Hz and 6 kHz, which yields a variance measurement with negligible bias as long as the peak emission is between 2 kHz and 5 kHz.

This measurement is affected by speckle, that is, by the particular random realization of the light that is backscattered. Hence

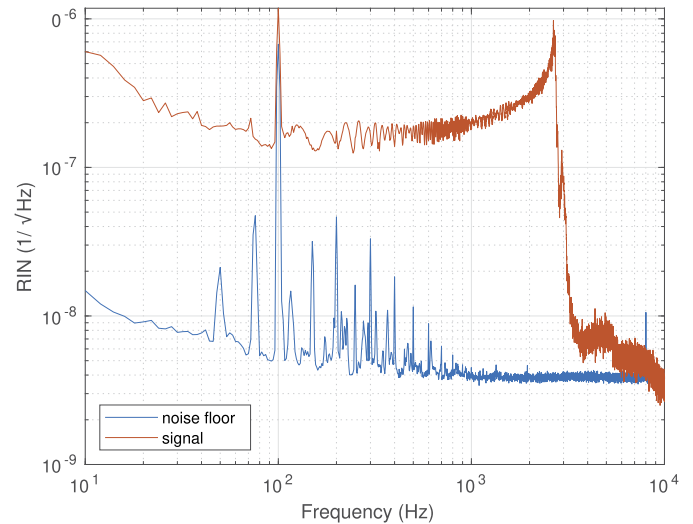


Fig. 2. Example amplitude spectral density of the normalized BHD signal A with a scattering sample of $f_{sc} = 3 \times 10^{-10}$ is shown in red (top line), and the average measurement noise floor without any sample in blue (bottom line).

the measured quantity is an exponentially distributed random variable. This random effect can be averaged by scanning the scattering sample in translation, with each translation by a beam radius yielding an independent measurement [17]. We scan the target surface with the aid of a motorized mirror using 49 dedicated points on the surface spanning over an area of 7×7 beam radii. This yields a measurement of the average scattering with $\frac{1}{\sqrt{49}} \approx 14\%$ statistical errors. This inherently assumes that the target scattering is uniform over the scanned surface. This is a good assumption for rough surfaces; however, for higher quality optics, localized scratches or dust particles can yield high scattering for some pointings. To mitigated this, we use a median of the 49 measurements corrected by a factor $\log 2$ to obtain a robust measurement of the exponential distribution parameter.

Relation between f_{sc} and BRDF. In the previous section, we have described how the scattered light fraction f_{sc} can be measured using a BHD. This is the quantity of interest when evaluating the impact of scattered light on gravitational wave detectors or other interferometric measurements. However, scattered light of a given object is usually characterized using its BRDF. In this section, we derive a simple analytical relation between these two quantities.

A normalized Gaussian beam with radius $w(z) = w_0 \sqrt{1 + \frac{\lambda^2(z-z_0)^2}{\pi^2 \omega_0^4}}$ and wavefront radius of curvature $R(z)$ has the following form in cylindrical coordinates:

$$E_{\text{beam}}(r, z) = \sqrt{\frac{2}{\pi w(z)^2}} \exp\left[-\left(\frac{1}{w(z)^2} + \frac{\pi i}{\lambda R(z)}\right)r^2\right]. \quad (3)$$

We mean by normalized that $\int_0^\infty 2\pi r |E_{\text{beam}}|^2 dr = 1$. For a point scatterer, the light close to the optical axis at large distance z can be approximated by a normalized spherical wave:

$$E_{\text{sc}}(r, z) = \frac{1}{\sqrt{2\pi z^2}} \exp\left[-\frac{\pi i}{\lambda z} r^2\right]. \quad (4)$$

The overlap integral of these two fields will yield the interference between a Gaussian beam and a spherical wave, i.e., a perfect

scatterer:

$$\text{Overlap} = \left| \int_0^\infty 2\pi r E_{\text{beam}} E_{\text{sc}}^* dr \right|^2 \quad (5)$$

$$= \left| \int_0^\infty \frac{2r dr}{wz} \exp \left[- \left(\frac{1}{w^2} + \frac{\pi i}{\lambda R} - \frac{\pi i}{\lambda z} \right) r^2 \right] \right|^2 \quad (6)$$

$$= \frac{1}{\frac{z^2}{w^2} + \frac{\pi^2}{\lambda^2} \left(\frac{1}{R} - \frac{1}{z} \right) wz} \quad (7)$$

This expression can be further approximated by evaluating it in the Gaussian beam far field, i.e., assuming that z is many Rayleigh ranges from the beam waist of radius w_0 at position z_0 :

$$\text{Overlap} \approx \frac{1}{\frac{z^2}{w^2} + \frac{\pi^2 z_0^2 w^2}{\lambda^2 z^2}} \approx \frac{1}{\frac{\pi^2 w_0^2}{\lambda^2} + \frac{z_0^2}{w_0^2}} \approx \frac{\lambda^2}{\pi^2 w(0)^2}, \quad (8)$$

where $w(0)$ is the Gaussian beam radius at the position of the spherical wave emission.

Hence, the overlap between a Gaussian beam and backscattered light depends only on the size of the beam at the scattering surface. Although this was derived for a point scattering source centered on the beam axis, it remains true if the scattering is due to a large number of uniformly distributed point sources or due to random roughness of the surface. We will not derive this more general relation, but verify it experimentally in the results section.

A normalized spherical wave is equivalent to a BRDF of $\frac{1}{\pi \cos(\theta)}$, where θ is the incidence angle on the scattering object. Hence for a scattering object, the backscattered light fraction is simply obtained by replacing the spherical wave BRDF by the BRDF of the sample object:

$$f_{\text{sc}} = \text{Overlap} \times \pi \text{BRDF}(\theta) \cos \theta = \text{BRDF}(\theta) \frac{\lambda^2 \cos \theta}{\pi w(0)^2}. \quad (9)$$

Results. We have performed measurements using the setup described in the measurement setup section. The alignment of the backscattered field with the local oscillator beam was verified using a flat mirror instead of the scattering target shown in Fig. 1. The directly backreflected beam had an interference visibility of 88%, while the maximum that was attainable was 94% given that half of the retro-reflected light was lost and sent back toward the laser. The measured backscatter fraction below was corrected for this interference visibility loss.

Backscatter as a function of beam radius. To verify the relation between backscatter fraction f_{sc} and BRDF, we measured the backscattering from a PTFE target (integrating sphere plug) as a function of beam size. PTFE is a near perfect volume Lambertian diffuser that scatters light in both polarizations with ideally a BRDF = $\frac{1}{2\pi}$ [19]. The beam radius was measured with a CCD camera and fitted with a Gaussian beam independently in the horizontal and vertical directions. The root mean square of the horizontal and vertical radius is used as the beam radius in the results below.

The beam at the output of the telescope described in the measurement setup section was converged with a 500-mm focal length lens to a waist of 85 μm and the target was placed at different locations to vary the beam size by more than one order of magnitude. The measured backscatter fraction is shown in Fig. 3 and matched well to the theoretical expectation of Eq. (9) for beam radii above 200 μm , but it was a factor of 2–3 times smaller close to the beam waist. This may be due to aberration

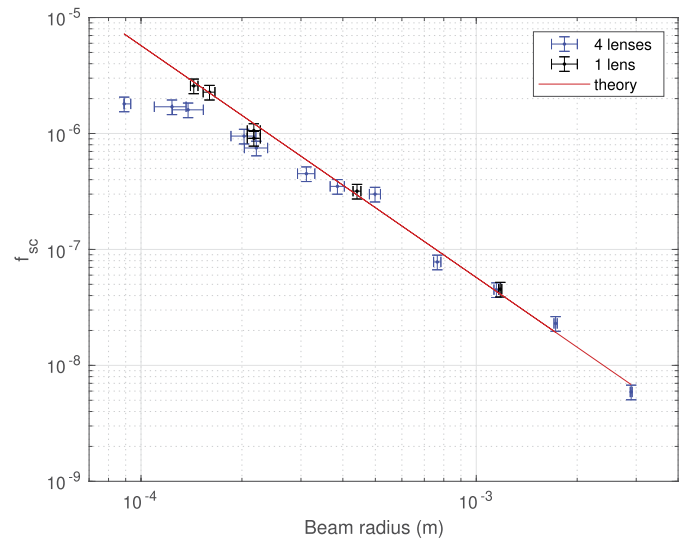


Fig. 3. Measured backscatter fraction f_{sc} as a function of beam size for the four-lens configuration (blue) and the single-lens configuration (black), compared to the expectation given by Eq. (9) in red. Vertical error bars correspond to the statistical error of the measurement due to speckle averaging, while the horizontal error bars are the target positioning errors of ± 5 mm re-stated as errors on the beam radius on the target.

in the beam converged using a single plano-convex lens. To verify this, instead of four lenses, we used a single lens with a focal length of 175 mm and a shorter optical path length. This configuration showed an excellent match at all radii down to the waist of 145 μm .

These results confirm the relation given by Eq. (9).

Backscatter as a function of incidence angle. The backscatter as a function of incidence angle was measured for a multi-band (512 nm/800 nm/1064 nm) anti-reflective coated vacuum window. The coating was measured to have a 700-ppm reflectivity at 1064 nm for an incidence angle of 0° . The 0.5° wedge of the window was placed vertically, and the incidence angle changed horizontally to measure at small angles the backscatter from only one of the two surfaces. The measured f_{sc} was converted into BRDF using Eq. (9).

The measurement result is shown in Fig. 4. Below 500 μrad , the tails of the Gaussian beam specular reflection were dominant as the beam provided by the telescope had a divergence of 160 μrad . The angular errors were due to the quadratic sum of the beam incidence angle variation of ± 30 μrad during the sample surface scan and the positioning error of ± 30 μrad provided by the window kinematic mount micrometer (Newport HR-13). Note that within 1 m of the beam waist, the Gaussian beam wavefront curvature was essentially flat, inducing negligible angular changes of less than 6 μrad across the beam radius.

At angles larger than 10 mrad, the optical configuration was changed by removing the diverging lens from the optical path to obtain a smaller beam radius of 450 μm and a ~ 15 times larger signal above the measurement noise floor. However, this introduced a much larger angular error of ± 8 mrad, as in that case, the motorized mirror motion no longer preserved the incidence angle on the sample.

For angles between 1 mrad and 10 mrad, the BRDF was proportional to $\frac{1}{\theta^2}$, which is typical for polished optics [3,9], while at angles larger than 50 mrad, the BRDF became approximately

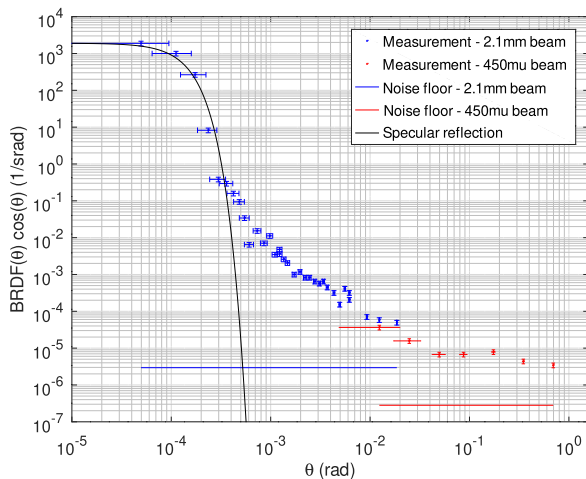


Fig. 4. Measured BRDF using a 2.1-mm radius beam (blue points) and 450- μm radius beam (right bottom points) as a function of incidence angle θ . The horizontal blue and red solid lines represent the corresponding measurement noise floor observed without a sample. The left solid line shows the expected interference from the window 700-ppm specular reflection.

independent of the incidence angle. This transition occurred at a smaller angle compared with uncoated or high reflective coated optics because the $\propto \frac{1}{\theta^2}$ term is strongly reduced by the anti-reflective coating [20,21].

Conclusion. We have proposed and implemented an interferometric measurement of backscattered light that uses relatively simple and readily available components. In a simplified case, we have derived the relation between the backscattered light fraction, the Gaussian beam radius, and the sample BRDF. This relation was verified experimentally using the proposed setup.

The measurement setup achieved an angular resolution of 160 μrad limited by beam divergence and measured backscatter for incidence angles larger than 500 μrad . In particular, it is able to measure backscatter at angles of a few mrad that are relevant for beam expanding telescope lenses in gravitational wave detectors. This allows for measuring the scattering of coated optics, which depends on the surface roughness and defects but also on the scattering reduction due to the anti-reflective coating that depends on how well the coating follows the bare optic surface.

This method can be further expanded to increase the telescope magnification by a factor of 10 to reach a beam radius of 20 mm. This should allow for measuring backscatter for angles larger than 50 μrad with a resolution of 17 μrad , and cover angles of $\sim 100 \mu\text{rad}$ to measure the most critical scattering from gravitational wave detectors core optics. As translating a large beam by several waists becomes increasingly impractical, the speckle can be instead averaged by changing the beam tilt by several beam divergence angles, for instance, in a circle at fixed incidence with respect to the sample surface.

Acknowledgment. The Virgo document number of this paper is VIR-0111A-22.

Disclosures. The authors declare no conflicts of interest.

Data availability. Data underlying the results presented in this paper are not publicly available at this time but may be obtained from the authors upon reasonable request.

REFERENCES

1. J. Aasi, B. P. Abbott, and R. Abbott, *et al.*, *Classical Quantum Gravity* **32**, 074001 (2015).
2. F. Acernese, M. Agathos, and K. Agatsuma, *et al.*, *Classical Quantum Gravity* **32**, 024001 (2015).
3. Y. Drori, J. Eichholz, T. Edo, H. Yamamoto, Y. Enomoto, G. Venugopalan, K. Arai, and R. X. Adhikari, "Scattering loss in precision metrology due to mirror roughness," arXiv:2201.05640 (2022).
4. J.-Y. Vinet, V. Brisson, S. Braccini, I. Ferrante, L. Pinard, F. Bondu, and E. Tournié, *Phys. Rev. D* **56**, 6085 (1997).
5. K. L. Dooley, J. R. Leong, and T. Adams, *et al.*, *Classical Quantum Gravity* **33**, 075009 (2016).
6. S. Soni, C. Austin, and A. Effler, *et al.*, *Classical Quantum Gravity* **38**, 025016 (2021).
7. A. Longo, S. Bianchi, W. Plastino, N. Arnaud, A. Chiummo, I. Fiori, B. Swinkels, and M. Was, *Classical Quantum Gravity* **37**, 145011 (2020).
8. M. Was, R. Gouaty, and R. Bonnand, *Classical Quantum Gravity* **38**, 075020 (2021).
9. B. Canuel, E. Genin, G. Vajente, and J. Marque, *Opt. Express* **21**, 10546 (2013).
10. "Bidirectional optical scattering facility," National Institute of Standards and Technology, <https://www.nist.gov/laboratories/tools-instruments/bidirectional-optical-scattering-facility>.
11. "Light scattering measurement systems in the VIS, UV, and IR spectral ranges," Fraunhofer Institute for Applied Optics and Precision Engineering, <https://www.iof.fraunhofer.de/en/competences/coating-and-surface-functionalization/surface-and-thin-film-characterization/scattered-light-measurement-analysis/light-scattering-measurement-systems-vis-uv-ir.html>.
12. T. Labardens, P. Chavel, Y. Sortais, M. Hébert, L. Simonot, A. Rabal, and G. Obein, *Electron. Imaging* **2021**, 140 (2021).
13. F. Magaña-Sandoval, R. X. Adhikari, V. Frolov, J. Harms, J. Lee, S. Sankar, P. R. Saulson, and J. R. Smith, *J. Opt. Soc. Am. A* **29**, 1722 (2012).
14. D. Vander-Hyde, C. Amra, M. Lequime, F. Magaña-Sandoval, J. R. Smith, and M. Zerrad, *Classical Quantum Gravity* **32**, 135019 (2015).
15. A. Kontos, B. Loggia, B. King, and N. Dziubelski, *Opt. Express* **29**, 44012 (2021).
16. S. Zeidler, T. Akutsu, Y. Torii, and Y. Aso, *Opt. Express* **27**, 16890 (2019).
17. V. Khodnevych, S. D. Pace, J.-Y. Vinet, N. Dinu-Jaeger, and M. Lintz, *Proc. SPIE* **11180**, 111807T (2019).
18. I. Khan, M. Lequime, M. Zerrad, and C. Amra, *Phys. Rev. Appl.* **16**, 044055 (2021).
19. A. Bhandari, B. Hamre, Ø. Frette, L. Zhao, J. J. Stamnes, and M. Kildemo, *Appl. Opt.* **50**, 2431 (2011).
20. C. Amra, G. Albrand, and P. Roche, *Appl. Opt.* **25**, 2695 (1986).
21. G. Soriano, M. Zerrad, and C. Amra, *Opt. Lett.* **44**, 4455 (2019).

Appendix F

Search for Gravitational Waves Associated with Gamma-Ray Bursts during the First Advanced LIGO Observing Run and Implications for the Origin of GRB 150906B



Search for Gravitational Waves Associated with Gamma-Ray Bursts during the First Advanced LIGO Observing Run and Implications for the Origin of GRB 150906B

B. P. Abbott¹, R. Abbott¹, T. D. Abbott², M. R. Abernathy³, F. Acernese^{4,5}, K. Ackley⁶, C. Adams⁷, T. Adams⁸, P. Addesso⁹, R. X. Adhikari¹, V. B. Adya¹⁰, C. Affeldt¹⁰, M. Agathos¹¹, K. Agatsuma¹¹, N. Aggarwal¹², O. D. Aguiar¹³, L. Aiello^{14,15}, A. Ain¹⁶, P. Ajith¹⁷, B. Allen^{10,18,19}, A. Allocca^{20,21}, P. A. Altin²², A. Ananyeva¹, S. B. Anderson¹, W. G. Anderson¹⁸, S. Appert¹, K. Arai¹, M. C. Araya¹, J. S. Areeda²³, N. Arnaud²⁴, K. G. Arun²⁵, S. Ascenzi^{15,26}, G. Ashton¹⁰, M. Ast²⁷, S. M. Aston⁷, P. Astone²⁸, P. Aufmuth¹⁹, C. Aulbert¹⁰, A. Avila-Alvarez²³, S. Babak²⁹, P. Bacon³⁰, M. K. M. Bader¹¹, P. T. Baker³¹, F. Baldaccini^{32,33}, G. Ballardin³⁴, S. W. Ballmer³⁵, J. C. Barayoga¹, S. E. Barclay³⁶, B. C. Barish¹, D. Barker³⁷, F. Barone^{4,5}, B. Barr³⁶, L. Barsotti¹², M. Barsuglia³⁰, D. Barta³⁸, J. Bartlett³⁷, I. Bartos³⁹, R. Bassiri⁴⁰, A. Basti^{20,21}, J. C. Batch³⁷, C. Baune¹⁰, V. Bavigadga³⁴, M. Bazzan^{41,42}, B. Bécsy⁴³, C. Beer¹⁰, M. Bejger⁴⁴, I. Belahcene²⁴, M. Belgin⁴⁵, A. S. Bell³⁶, B. K. Berger¹, G. Bergmann¹⁰, C. P. L. Berry⁴⁶, D. Bersanetti^{47,48}, A. Bertolini¹¹, J. Betzwieser⁷, S. Bhagwat³⁵, R. Bhandare⁴⁹, I. A. Bilenko⁵⁰, G. Billingsley¹, C. R. Billman⁶, J. Birch⁷, R. Birney⁵¹, O. Birnholtz¹⁰, S. Biscans^{1,12}, A. Bisht¹⁹, M. Bitossi³⁴, C. Biwer³⁵, M. A. Bizouard²⁴, J. K. Blackburn¹, J. Blackman⁵², C. D. Blair⁵³, D. G. Blair⁵³, R. M. Blair³⁷, S. Bloemen⁵⁴, O. Bock¹⁰, M. Boer⁵⁵, G. Bogaert⁵⁵, A. Bohe²⁹, F. Bondu⁵⁶, R. Bonnand⁸, B. A. Boom¹¹, R. Bork¹, V. Boschi^{20,21}, S. Bose^{16,57}, Y. Bouffanais³⁰, A. Bozzi³⁴, C. Bradaschia²¹, P. R. Brady¹⁸, V. B. Braginsky^{50,144}, M. Branchesi^{58,59}, J. E. Brau⁶⁰, T. Briant⁶¹, A. Brillet⁵⁵, M. Brinkmann¹⁰, V. Brisson²⁴, P. Brockill¹⁸, J. E. Broida⁶², A. F. Brooks¹, D. A. Brown³⁵, D. D. Brown⁴⁶, N. M. Brown¹², S. Brunetti¹, C. C. Buchanan², A. Buikema¹², T. Bulik⁶³, H. J. Bulten^{11,64}, A. Buonanno^{29,65}, D. Buskulic⁸, C. Buy³⁰, R. L. Byer⁴⁰, M. Cabero¹⁰, L. Cadonati⁴⁵, G. Cagnoli^{66,67}, C. Cahillane¹, J. Calderón Bustillo⁴⁵, T. A. Callister¹, E. Calloni^{5,68}, J. B. Camp⁶⁹, M. Canepa^{47,48}, K. C. Cannon⁷⁰, H. Cao⁷¹, J. Cao⁷², C. D. Capano¹⁰, E. Capocasa³⁰, F. Carbognani³⁴, S. Caride⁷³, J. Casanueva Diaz²⁴, C. Casentini^{15,26}, S. Caudill¹⁸, M. Cavaglia⁷⁴, F. Cavalieri²⁴, R. Cavalieri³⁴, G. Cella²¹, C. B. Cepeda¹, L. Cerboni Baiardi^{58,59}, G. Cerretani^{20,21}, E. Cesarini^{15,26}, S. J. Chamberlin⁷⁵, M. Chan³⁶, S. Chao⁷⁶, P. Charlton⁷⁷, E. Chassande-Mottin³⁰, B. D. Cheeseboro³¹, H. Y. Chen⁷⁸, Y. Chen⁵², H.-P. Cheng⁶, A. Chincarini⁴⁸, A. Chiummo³⁴, T. Chmiel⁷⁹, H. S. Cho⁸⁰, M. Cho⁶⁵, J. H. Chow²², N. Christensen⁶², Q. Chu⁵³, A. J. K. Chua⁸¹, S. Chua⁶¹, S. Chung⁵³, G. Ciani⁶, F. Clara³⁷, J. A. Clark⁴⁵, F. Cleva⁵⁵, C. Cocchiari⁷⁴, E. Coccia^{14,15}, P.-F. Cohadon⁶¹, A. Colla^{28,82}, C. G. Collette⁸³, L. Cominsky⁸⁴, M. Constancio, Jr.¹³, L. Conti⁴², S. J. Cooper⁴⁶, T. R. Corbitt², N. Cornish⁸⁵, A. Corsi⁷³, S. Cortese³⁴, C. A. Costa¹³, M. W. Coughlin⁶², S. B. Coughlin⁸⁶, J.-P. Coulon⁵⁵, S. T. Countryman³⁹, P. Couvares¹, P. B. Covas⁸⁷, E. E. Cowan⁴⁵, D. M. Coward⁵³, M. J. Cowart⁷, D. C. Coyne¹, R. Coyne⁷³, J. D. E. Creighton¹⁸, T. D. Creighton⁸⁸, J. Cripe², S. G. Crowder⁸⁹, T. J. Cullen²³, A. Cumming³⁶, L. Cunningham³⁶, E. Cuoco³⁴, T. Dal Canton⁶⁹, G. Dálya⁴³, S. L. Danilishin³⁶, S. D'Antonio¹⁵, K. Danzmann^{10,19}, A. Dasgupta⁹⁰, C. F. Da Silva Costa⁶, V. Dattilo³⁴, I. Dave⁴⁹, M. Davier²⁴, G. S. Davies³⁶, D. Davis³⁵, E. J. Daw⁹¹, B. Day⁴⁵, R. Day³⁴, S. De³⁵, D. DeBra⁴⁰, G. Debreczeni³⁸, J. Degallaix⁶⁶, M. De Laurentis^{5,68}, S. Deléglise⁶¹, W. Del Pozzo⁴⁶, T. Denker¹⁰, T. Dent¹⁰, V. Dergachev²⁹, R. De Rosa^{5,68}, R. T. DeRosa⁷, R. DeSalvo⁹, J. Devenson⁵¹, R. C. Devine³¹, S. Dhurandhar¹⁶, M. C. Diaz⁸⁸, L. Di Fiore⁵, M. Di Giovanni^{92,93}, T. Di Girolamo^{5,68}, A. Di Lieto^{20,21}, S. Di Pace^{28,82}, I. Di Palma^{28,29,82}, A. Di Virgilio²¹, Z. Doctor⁷⁸, V. Dolique⁶⁶, F. Donovan¹², K. L. Dooley⁷⁴, S. Doravari¹⁰, I. Dorrington⁹⁴, R. Douglas³⁶, M. Dovale Álvarez⁴⁶, T. P. Downes¹⁸, M. Drago¹⁰, R. W. P. Drever¹, J. C. Driggers³⁷, Z. Du⁷², M. Ducrot⁸, S. E. Dwyer³⁷, T. B. Edo⁹¹, M. C. Edwards⁶², A. Effler⁷, H.-B. Eggenstein¹⁰, P. Ehrens¹, J. Eichholz¹, S. S. Eikenberry⁶, R. A. Eisenstein¹², R. C. Essick¹², Z. Etienne³¹, T. Etzel¹, M. Evans¹², T. M. Evans⁷, R. Everett⁷⁵, M. Factourovich³⁹, V. Fafone^{14,15,26}, H. Fair³⁵, S. Fairhurst⁹⁴, X. Fan⁷², S. Farinon⁴⁸, B. Farr⁷⁸, W. M. Farr⁴⁶, E. J. Fauchon-Jones⁹⁴, M. Favata⁹⁵, M. Fays⁹⁴, H. Fehrmann¹⁰, M. M. Fejer⁴⁰, A. Fernández Galiana¹², I. Ferrante^{20,21}, E. C. Ferreira¹³, F. Ferrini³⁴, F. Fidecaro^{20,21}, I. Fiori³⁴, D. Fiorucci³⁰, R. P. Fisher³⁵, R. Flaminio^{66,96}, M. Fletcher³⁶, H. Fong⁹⁷, S. S. Forsyth⁴⁵, J.-D. Fournier⁵⁵, S. Frasca^{28,82}, F. Frasconi²¹, Z. Frei⁴³, A. Freise⁴⁶, R. Frey⁶⁰, V. Frey²⁴, E. M. Fries¹, P. Fritschel¹², V. V. Frolov⁷, P. Fulda^{6,69}, M. Fyffe⁷, H. Gabbard⁷⁴, B. U. Gadre¹⁶, S. M. Gaebel⁴⁶, J. R. Gair³⁶, L. Gammaitoni³², S. G. Gaonkar¹⁶, F. Garufi^{5,68}, G. Gaur⁹⁸, V. Gayathri⁹⁹, N. Gehrels⁶⁹, G. Gemme⁴⁸, E. Genin³⁴, A. Gennai²¹, J. George⁴⁹, L. Gergely¹⁰⁰, V. Germain⁸, S. Ghonge¹⁷, Abhirup Ghosh¹⁷, A. Ghosh¹¹, Archisman Ghosh¹⁷, S. Ghosh^{11,54}, J. A. Giaime^{2,7}, K. D. Giardino⁷, A. Giazotto²¹, K. Gill¹⁰¹, A. Glaefke³⁶, E. Goetz¹⁰, R. Goetz⁶, L. Gondan⁴³, G. González², J. M. Gonzalez Castro^{20,21}, A. Gopakumar¹⁰², M. L. Gorodetsky⁵⁰, S. E. Gossan¹, M. Gosselin³⁴, R. Gouaty⁸, A. Grado^{5,103}, C. Graef³⁶, M. Granata⁶⁶, A. Grant³⁶, S. Gras¹², C. Gray³⁷, G. Greco^{58,59}, A. C. Green⁴⁶, P. Groot⁵⁴, H. Grote¹⁰, S. Grunewald²⁹, G. M. Guidi^{58,59}, X. Guo⁷², A. Gupta¹⁶, M. K. Gupta⁹⁰, K. E. Gushwa¹, E. K. Gustafson¹, R. Gustafson¹⁰⁴, J. J. Hacker²³, B. R. Hall⁵⁷, E. D. Hall¹, G. Hammond³⁶, M. Haney¹⁰², M. M. Hanke¹⁰, J. Hanks³⁷, C. Hanna⁷⁵, J. Hanson⁷, T. Hardwick², J. Harms^{58,59}, G. M. Harry³, I. W. Harry²⁹, M. J. Hart³⁶, M. T. Hartman⁶, C.-J. Haster^{46,97}, K. Haughian³⁶, J. Healy¹⁰⁵, A. Heidmann⁶¹, M. C. Heintze⁷, H. Heitmann⁵⁵, P. Hello²⁴, G. Hemming³⁴, M. Hendry³⁶, I. S. Heng³⁶, J. Hennig³⁶, J. Henry¹⁰⁵, A. W. Heptonstall¹, M. Heurs^{10,19}, S. Hild³⁶, D. Hoak³⁴, D. Hofman⁶⁶, K. Holt⁷, D. E. Holz⁷⁸, P. Hopkins⁹⁴, J. Hough³⁶, E. A. Houston³⁶, E. J. Howell⁵³, Y. M. Hu¹⁰, E. A. Huerta¹⁰⁶, D. Huet²⁴, B. Hughey¹⁰¹, S. Husa⁸⁷, S. H. Huttner³⁶, T. Huynh-Dinh⁷, N. Indik¹⁰, D. R. Ingram³⁷, R. Inta⁷³, H. N. Isa³⁶, J.-M. Isac⁶¹, M. Isi¹, T. Isogai¹², B. R. Iyer¹⁷, K. Izumi³⁷, T. Jacqmin⁶¹, K. Jani⁴⁵, P. Jaranowski¹⁰⁷, S. Jawahar¹⁰⁸, F. Jiménez-ForTEza⁸⁷, W. W. Johnson², D. I. Jones¹⁰⁹, R. Jones³⁶, R. J. G. Jonker¹¹, L. Ju⁵³, J. Junker¹⁰, C. V. Kalaghatgi⁹⁴, V. Kalogera⁸⁶, S. Kandhasamy⁷⁴, G. Kang⁸⁰, J. B. Kanner¹, S. Karki⁶⁰, K. S. Karvinen¹⁰

M. Kasprzak², E. Katsavounidis¹², W. Katzman⁷, S. Kaufer¹⁹, T. Kaur⁵³, K. Kawabe³⁷, F. Kéfélian⁵⁵, D. Keitel⁸⁷, D. B. Kelley³⁵, R. Kennedy⁹¹, J. S. Key⁸⁸, F. Y. Khalili⁵⁰, I. Khan¹⁴, S. Khan⁹⁴, Z. Khan⁹⁰, E. A. Khazanov¹¹⁰, N. Kijbunchoo³⁷, Chunglee Kim¹¹¹, J. C. Kim¹¹², Whansun Kim¹¹³, W. Kim⁷¹, Y.-M. Kim^{111,114}, S. J. Kimbrell⁴⁵, E. J. King⁷¹, P. J. King³⁷, R. Kirchhoff¹⁰, J. S. Kissel³⁷, B. Klein⁸⁶, L. Kleybolte²⁷, S. Klimenko⁶, P. Koch¹⁰, S. M. Koehlenbeck¹⁰, S. Koley¹¹, V. Kondrashov¹, A. Kontos¹², M. Korobko²⁷, W. Z. Korth¹, I. Kowalska⁶³, D. B. Kozak¹, C. Krämer¹⁰, V. Kringel¹⁰, B. Krishnan¹⁰, A. Królak^{115,116}, G. Kuehn¹⁰, P. Kumar⁹⁷, R. Kumar⁹⁰, L. Kuo⁷⁶, A. Kutynia¹¹⁵, B. D. Lackey^{29,35}, M. Landry³⁷, R. N. Lang¹⁸, J. Lange¹⁰⁵, B. Lantz⁴⁰, R. K. Lanza¹², A. Lartaux-Vollard²⁴, P. D. Lasky¹¹⁷, M. Laxen⁷, A. Lazzarini¹, C. Lazzaro⁴², P. Leaci^{28,82}, S. Leavey³⁶, E. O. Lebigot³⁰, C. H. Lee¹¹⁴, H. K. Lee¹¹⁸, H. M. Lee¹¹¹, K. Lee³⁶, J. Lehmann¹⁰, A. Lenon³¹, M. Leonardi^{92,93}, J. R. Leong¹⁰, N. Leroy²⁴, N. Letendre⁸, Y. Levin¹¹⁷, T. G. F. Li¹¹⁹, A. Libson¹², T. B. Littenberg¹²⁰, J. Liu⁵³, N. A. Lockerbie¹⁰⁸, A. L. Lombardi⁴⁵, L. T. London⁹⁴, J. E. Lord³⁵, M. Lorenzini^{14,15}, V. Lorette¹²¹, M. Lormand⁷, G. Losurdo²¹, J. D. Lough^{10,19}, G. Lovelace²³, H. Lück^{10,19}, A. P. Lundgren¹⁰, R. Lynch¹², Y. Ma⁵², S. Macfoy⁵¹, B. Machenschalk¹⁰, M. MacInnis¹², D. M. Macleod², F. Magaña-Sandoval³⁵, E. Majorana²⁸, I. Maksimovic¹²¹, V. Malvezzi^{15,26}, N. Man⁵⁵, V. Mandic¹²², V. Mangano³⁶, G. L. Mansell²², M. Manske¹⁸, M. Mantovani³⁴, F. Marchesoni^{33,123}, F. Marion⁸, S. Márka³⁹, Z. Márka³⁹, A. S. Markosyan⁴⁰, E. Maros¹, F. Martelli^{58,59}, L. Martellini⁵⁵, I. W. Martin²⁹, D. V. Martynov¹², K. Mason¹², A. Masserot⁸, T. J. Massinger¹, M. Masso-Reid³⁶, S. Mastrogiovanni^{28,82}, F. Matichard^{1,12}, L. Matone³⁹, N. Mavalvala¹², N. Mazumder⁵⁷, R. McCarthy³⁷, D. E. McClelland²², S. McCormick⁷, C. McGrath¹⁸, S. C. McGuire¹²⁴, G. McIntyre¹, J. McIver¹, D. J. McManus²², T. McRae²², S. T. McWilliams³¹, D. Meacher^{55,75}, G. D. Meadors⁹, J. Meidam¹¹, A. Melatos¹²⁵, G. Mendell³⁷, D. Mendoza-Gandara¹⁰, R. A. Mercer¹⁸, E. L. Merilh³⁷, M. Merzougou⁵⁵, S. Meshkov¹, C. Messenger³⁶, C. Messick⁷⁵, R. Metzdriff⁶¹, P. M. Meyers¹²², F. Mezzani^{28,82}, H. Miao⁴⁶, C. Michel⁶⁶, H. Middleton⁴⁶, E. E. Mikhailov¹²⁶, L. Milano^{5,68}, A. L. Miller^{6,28,82}, A. Miller⁸⁶, B. B. Miller⁸⁶, J. Miller¹², M. Millhouse⁸⁵, Y. Minenkov¹⁵, J. Ming²⁹, S. Mirshekari¹²⁷, C. Mishra¹⁷, S. Mitra¹⁶, V. P. Mitrofanov⁵⁰, G. Mitselmakher⁶, R. Mittleman¹², A. Moggi²¹, M. Mohan³⁴, S. R. P. Mohapatra¹², M. Montani^{58,59}, B. C. Moore⁹⁵, C. J. Moore⁸¹, D. Moraru³⁷, G. Moreno³⁷, S. R. Morris⁸⁸, B. Mours⁸, C. M. Mow-Lowry⁴⁶, G. Mueller⁶, A. W. Muir⁹⁴, Arunava Mukherjee¹⁷, D. Mukherjee¹⁸, S. Mukherjee⁸⁸, N. Mukund¹⁶, A. Mullavey⁷, J. Munch⁷¹, E. A. M. Muniz²³, P. G. Murray³⁶, A. Mytidis⁶, K. Napier⁴⁵, I. Nardecchia^{15,26}, L. Naticchioni^{28,82}, G. Nelemans^{11,54}, T. J. N. Nelson⁷, M. Neri^{47,48}, M. Nery¹⁰, A. Neunzert¹⁰⁴, J. M. Newport³, G. Newton³⁶, T. T. Nguyen²², A. B. Nielsen¹⁰, S. Nissanke^{11,54}, A. Nitz¹⁰, A. Noack¹⁰, F. Nocera³⁴, D. Nolting⁷, M. E. N. Normandin⁸⁸, L. K. Nuttall³⁵, J. Oberling³⁷, E. Ochsner¹⁸, E. Oelker¹², G. H. Oggin¹²⁸, J. J. Oh¹¹³, S. H. Oh¹¹³, F. Ohme^{10,94}, M. Oliver⁸⁷, P. Oppermann¹⁰, Richard J. Oram⁷, B. O'Reilly⁷, R. O'Shaughnessy¹⁰⁵, D. J. Ottaway⁷¹, H. Overmier⁷, B. J. Owen⁷³, A. E. Pace⁷⁵, J. Page¹²⁰, A. Pai⁹⁹, S. A. Pai⁴⁹, J. R. Palamos⁶⁰, O. Palashov¹¹⁰, C. Palomba²⁸, A. Pal-Singh²⁷, H. Pan⁷⁶, C. Pankow⁸⁶, F. Pannarale⁹⁴, B. C. Pant⁴⁹, F. Paoletti^{21,34}, A. Paoli³⁴, M. A. Papa^{10,18,29}, H. R. Paris⁴⁰, W. Parker⁷, D. Pascucci³⁶, A. Pasqualetti³⁴, R. Passaquieti^{20,21}, D. Passuello²¹, B. Patricelli^{20,21}, B. L. Pearlstone³⁶, M. Pedraza¹, R. Pedurand^{66,129}, L. Pekowsky³⁵, A. Pele⁷, S. Penn¹³⁰, C. J. Perez³⁷, A. Perreca¹, L. M. Perri⁸⁶, H. P. Pfeiffer⁹⁷, M. Phelps³⁶, O. J. Piccinni^{28,82}, M. Pichot⁵⁵, F. Piergiovanni^{58,59}, V. Piero⁹, G. Pillant³⁴, L. Pinard⁶⁶, I. M. Pinto⁹, M. Pitkin³⁶, M. Poe¹⁸, R. Poggiani^{20,21}, P. Popolizio³⁴, A. Post¹⁰, J. Powell³⁶, J. Prasad¹⁶, J. W. W. Pratt¹⁰¹, V. Predoi⁹⁴, T. Prestegard^{18,122}, M. Prijatelj^{10,34}, M. Principe⁹, S. Privitera²⁹, G. A. Prodi^{92,93}, L. G. Prokhorov⁵⁰, O. Puncken¹⁰, M. Punturo³³, P. Puppò²⁸, M. Pürer²⁹, H. Qi¹⁸, J. Qin⁵³, S. Qiu¹¹⁷, V. Quetschke⁸⁸, E. A. Quintero¹, R. Quitzow-James⁶⁰, F. J. Raab³⁷, D. S. Rabeling²², H. Radkins³⁷, P. Raffai⁴³, S. Raja⁴⁹, C. Rajan⁴⁹, M. Rakhmanov⁸⁸, P. Rapagnani^{28,82}, V. Raymond²⁹, M. Razzano^{20,21}, V. Re²⁶, J. Read²³, T. Regimbau⁵⁵, L. Rei⁴⁸, S. Reid⁵¹, D. H. Reitze^{1,6}, H. Rew¹²⁶, S. D. Reyes³⁵, E. Rhoades¹⁰¹, F. Ricci^{28,82}, K. Riles¹⁰⁴, M. Rizzo¹⁰⁵, N. A. Robertson^{1,36}, R. Robie³⁶, F. Robinet²⁴, A. Rocchi¹⁵, L. Rolland⁸, J. G. Rollins¹, V. J. Roma⁶⁰, R. Romano^{4,5}, J. H. Romie⁷, D. Rosińska^{44,131}, S. Rowan³⁶, A. Rüdiger¹⁰, P. Ruggi³⁴, K. Ryan³⁷, S. Sachdev¹, T. Sadecki³⁷, L. Sadeghian¹⁸, M. Sakellariadou¹³², L. Salconi³⁴, M. Saleem⁹⁹, F. Salemi¹⁰, A. Samajdar¹³³, L. Sammut¹¹⁷, L. M. Sampson⁸⁶, E. J. Sanchez¹, V. Sandberg³⁷, J. R. Sanders³⁵, B. Sassolas⁶⁶, B. S. Sathyaprakash^{75,94}, P. R. Saulson³⁵, O. Sauter¹⁰⁴, R. L. Savage³⁷, A. Sawadsky¹⁹, P. Schale⁶⁰, J. Scheuer⁸⁶, E. Schmidt¹⁰¹, J. Schmidt¹⁰, P. Schmidt^{1,52}, R. Schnabel²⁷, R. M. S. Schofield⁶⁰, A. Schönbeck²⁷, E. Schreiber¹⁰, D. Schuette^{10,19}, S. G. Schwalbe¹⁰¹, J. Scott³⁶, S. M. Scott²², D. Sellers⁷, A. S. Sengupta¹³⁴, D. Sentenac³⁴, V. Sequino^{15,26}, A. Sergeev¹¹⁰, Y. Setyawati^{11,54}, D. A. Shaddock²², T. J. Shaffer³⁷, M. S. Shahriar⁸⁶, B. Shapiro⁴⁰, P. Shawhan⁶⁵, A. Sheperd¹⁸, D. H. Shoemaker¹², D. M. Shoemaker⁴⁵, K. Siellez⁴⁵, X. Siemens¹⁸, M. Sieniawska⁴⁴, D. Sigg³⁷, A. D. Silva¹³, A. Singer¹, L. P. Singer⁶⁹, A. Singh^{10,19,29}, R. Singh², A. Singhal¹⁴, A. M. Sintes⁸⁷, B. J. J. Slagmolen²², B. Smith⁷, J. R. Smith²³, R. J. E. Smith¹, E. J. Son¹¹³, B. Sorazu³⁶, F. Sorrentino⁴⁸, T. Souradeep¹⁶, A. P. Spencer³⁶, A. K. Srivastava⁹⁰, A. Staley³⁹, M. Steinke¹⁰, J. Steinlechner³⁶, S. Steinlechner^{27,36}, D. Steinmeyer^{10,19}, B. C. Stephens¹⁸, S. P. Stevenson⁴⁶, R. Stone⁸⁸, K. A. Strain³⁶, N. Straniero⁶⁶, G. Stratta^{58,59}, S. E. Strigin⁵⁰, R. Sturani¹²⁷, A. L. Stuver⁷, T. Z. Summerscales¹³⁵, L. Sun¹²⁵, S. Sunil⁹⁰, P. J. Sutton⁹⁴, B. L. Swinkels³⁴, M. J. Szczepańczyk¹⁰¹, A. Szolgyen⁴³, M. Tacca³⁰, D. Talukder⁶⁰, D. B. Tanner⁶, M. Tápai¹⁰⁰, A. Taracchini²⁹, R. Taylor¹, T. Theeg¹⁰, E. G. Thomas⁴⁶, M. Thomas⁷, P. Thomas³⁷, K. A. Thorne⁷, E. Thrane¹¹⁷, T. Tippens⁴⁵, S. Tiwari^{14,93}, V. Tiwari⁹⁴, K. V. Tokmakov¹⁰⁸, K. Toland³⁶, C. Tomlinson⁹¹, M. Tonelli^{20,21}, Z. Tornasi³⁶, C. I. Torrie¹, D. Töyrä⁴⁶, F. Travasso^{32,33}, G. Traylor⁷, D. Trifiro⁷⁴, J. Trinastic⁶, M. C. Tringali^{92,93}, L. Trozzo^{21,136}, M. Tse¹², R. Tso¹, M. Turconi⁵⁵, D. Tuyenbayev⁸⁸, D. Ugolini¹³⁷, C. S. Unnikrishnan¹⁰², A. L. Urban¹, S. A. Usman⁹⁴, H. Vahlbruch¹⁹, G. Vajente¹, G. Valdes⁸⁸, N. van Bakel¹¹, M. van Beuzekom¹¹, J. F. J. van den Brand^{11,64}, C. Van Den Broeck¹¹, D. C. Vander-Hyde³⁵, L. van der Schaaf¹¹, J. V. van Heijningen¹¹, A. A. van Veggel³⁶, M. Vardaro^{41,42}, V. Varma⁵², S. Vass¹, M. Vasúth³⁸, A. Vecchio⁴⁶, G. Vedovato⁴², J. Veitch⁴⁶, P. J. Veitch⁷¹, K. Venkateswara¹³⁸, G. Venugopalan¹, D. Verkindt⁸,

F. Vetranò^{58,59}, A. Vicere^{58,59}, A. D. Viets¹⁸, S. Vinciguerra⁴⁶, D. J. Vine⁵¹, J.-Y. Vinet⁵⁵, S. Vitale¹², T. Vo³⁵, H. Vocca^{32,33}, C. Vorvick³⁷, D. V. Voss⁶, W. D. Voudsen⁴⁶, S. P. Vyatchanin⁵⁰, A. R. Wade¹, L. E. Wade⁷⁹, M. Wade⁷⁹, M. Walker², L. Wallace¹, S. Walsh^{10,29}, G. Wang^{14,59}, H. Wang⁴⁶, M. Wang⁴⁶, Y. Wang⁵³, R. L. Ward²², J. Warner³⁷, M. Was⁸, J. Watchi⁸³, B. Weaver³⁷, L.-W. Wei⁵⁵, M. Weinert¹⁰, A. J. Weinstein¹, R. Weiss¹², L. Wen⁵³, P. Weßels¹⁰, T. Westphal¹⁰, K. Wette¹⁰, J. T. Whelan¹⁰⁵, B. F. Whiting⁶, C. Whittle¹¹⁷, D. Williams³⁶, R. D. Williams¹, A. R. Williamson⁹⁴, J. L. Willis¹³⁹, B. Willke^{10,19}, M. H. Wimmer^{10,19}, W. Winkler¹⁰, C. C. Wipf¹, H. Wittel^{10,19}, G. Woan³⁶, J. Woehler¹⁰, J. Worden³⁷, J. L. Wright³⁶, D. S. Wu¹⁰, G. Wu⁷, W. Yam¹², H. Yamamoto¹, C. C. Yancey⁶⁵, M. J. Yap²², Hang Yu¹², Haocun Yu¹², M. Yvert⁸, A. Zadrożny¹¹⁵, L. Zangrando⁴², M. Zanolin¹⁰¹, J.-P. Zendri⁴², M. Zevin⁸⁶, L. Zhang¹, M. Zhang¹²⁶, T. Zhang³⁶, Y. Zhang¹⁰⁵, C. Zhao⁵³, M. Zhou⁸⁶, Z. Zhou⁸⁶, X. J. Zhu⁵³, M. E. Zucker^{1,12}, J. Zweizig¹

(The LIGO Scientific Collaboration and the Virgo Collaboration),

and

R. L. Apteekar¹⁴⁰, D. D. Frederiks¹⁴⁰, S. V. Golenetskiĭ¹⁴⁰, D. V. Golovin¹⁴¹, K. Hurley¹⁴², M. L. Litvak¹⁴¹, I. G. Mitrofanov¹⁴¹, A. Rau¹⁴³, A. B. Sanin¹⁴¹, D. S. Svinkin¹⁴⁰, A. von Kienlin¹⁴³, X. Zhang¹⁴³

(The IPN Collaboration)

¹ LIGO, California Institute of Technology, Pasadena, CA 91125, USA

² Louisiana State University, Baton Rouge, LA 70803, USA

³ American University, Washington, DC 20016, USA

⁴ Università di Salerno, Fisciano, I-84084 Salerno, Italy

⁵ INFN, Sezione di Napoli, Complesso Universitario di Monte S. Angelo, I-80126 Napoli, Italy

⁶ University of Florida, Gainesville, FL 32611, USA

⁷ LIGO Livingston Observatory, Livingston, LA 70754, USA

⁸ Laboratoire d'Annecy-le-Vieux de Physique des Particules (LAPP), Université Savoie Mont Blanc, CNRS/IN2P3, F-74941 Annecy-le-Vieux, France

⁹ University of Sannio at Benevento, I-82100 Benevento, Italy and INFN, Sezione di Napoli, I-80100 Napoli, Italy

¹⁰ Albert-Einstein-Institut, Max-Planck-Institut für Gravitationsphysik, D-30167 Hannover, Germany

¹¹ Nikhef, Science Park, 1098 XG Amsterdam, The Netherlands

¹² LIGO, Massachusetts Institute of Technology, Cambridge, MA 02139, USA

¹³ Instituto Nacional de Pesquisas Espaciais, 12227-010 São José dos Campos, São Paulo, Brazil

¹⁴ INFN, Gran Sasso Science Institute, I-67100 L'Aquila, Italy

¹⁵ INFN, Sezione di Roma Tor Vergata, I-00133 Roma, Italy

¹⁶ Inter-University Centre for Astronomy and Astrophysics, Pune 411007, India

¹⁷ International Centre for Theoretical Sciences, Tata Institute of Fundamental Research, Bengaluru 560089, India

¹⁸ University of Wisconsin-Milwaukee, Milwaukee, WI 53201, USA

¹⁹ Leibniz Universität Hannover, D-30167 Hannover, Germany

²⁰ Università di Pisa, I-56127 Pisa, Italy

²¹ INFN, Sezione di Pisa, I-56127 Pisa, Italy

²² Australian National University, Canberra, Australian Capital Territory 0200, Australia

²³ California State University Fullerton, Fullerton, CA 92831, USA

²⁴ LAL, Univ. Paris-Sud, CNRS/IN2P3, Université Paris-Saclay, F-91898 Orsay, France

²⁵ Chennai Mathematical Institute, Chennai 603103, India

²⁶ Università di Roma Tor Vergata, I-00133 Roma, Italy

²⁷ Universität Hamburg, D-22761 Hamburg, Germany

²⁸ INFN, Sezione di Roma, I-00185 Roma, Italy

²⁹ Albert-Einstein-Institut, Max-Planck-Institut für Gravitationsphysik, D-14476 Potsdam-Golm, Germany

³⁰ APC, AstroParticule et Cosmologie, Université Paris Diderot, CNRS/IN2P3, CEA/Irfu, Observatoire de Paris, Sorbonne Paris Cité, F-75205 Paris Cedex 13, France

³¹ West Virginia University, Morgantown, WV 26506, USA

³² Università di Perugia, I-06123 Perugia, Italy

³³ INFN, Sezione di Perugia, I-06123 Perugia, Italy

³⁴ European Gravitational Observatory (EGO), I-56021 Cascina, Pisa, Italy

³⁵ Syracuse University, Syracuse, NY 13244, USA

³⁶ SUPA, University of Glasgow, Glasgow G12 8QQ, UK

³⁷ LIGO Hanford Observatory, Richland, WA 99352, USA

³⁸ Wigner RCP, RMKI, H-1121 Budapest, Konkoly Thege Miklós út 29-33, Hungary

³⁹ Columbia University, New York, NY 10027, USA

⁴⁰ Stanford University, Stanford, CA 94305, USA

⁴¹ Università di Padova, Dipartimento di Fisica e Astronomia, I-35131 Padova, Italy

⁴² INFN, Sezione di Padova, I-35131 Padova, Italy

⁴³ MTA Eötvös University, "Lendület" Astrophysics Research Group, Budapest 1117, Hungary

⁴⁴ Nicolaus Copernicus Astronomical Center, Polish Academy of Sciences, 00-716, Warsaw, Poland

⁴⁵ Center for Relativistic Astrophysics and School of Physics, Georgia Institute of Technology, Atlanta, GA 30332, USA

⁴⁶ University of Birmingham, Birmingham B15 2TT, UK

⁴⁷ Università degli Studi di Genova, I-16146 Genova, Italy

⁴⁸ INFN, Sezione di Genova, I-16146 Genova, Italy

⁴⁹ RRCAT, Indore MP 452013, India

⁵⁰ Faculty of Physics, Lomonosov Moscow State University, Moscow 119991, Russia

⁵¹ SUPA, University of the West of Scotland, Paisley PA1 2BE, UK

⁵² Caltech CaRT, Pasadena, CA 91125, USA

⁵³ University of Western Australia, Crawley, Western Australia 6009, Australia

⁵⁴ Department of Astrophysics/IMAPP, Radboud University Nijmegen, P.O. Box 9010, 6500 GL Nijmegen, The Netherlands

⁵⁵ Artemis, Université Côte d'Azur, CNRS, Observatoire Côte d'Azur, CS 34229, F-06304 Nice Cedex 4, France

⁵⁶ Institut de Physique de Rennes, CNRS, Université de Rennes 1, F-35042 Rennes, France

- ⁵⁷ Washington State University, Pullman, WA 99164, USA
⁵⁸ Università degli Studi di Urbino “Carlo Bo,” I-61029 Urbino, Italy
⁵⁹ INFN, Sezione di Firenze, I-50019 Sesto Fiorentino, Firenze, Italy
⁶⁰ University of Oregon, Eugene, OR 97403, USA
⁶¹ Laboratoire Kastler Brossel, UPMC-Sorbonne Universités, CNRS, ENS-PSL Research University, Collège de France, F-75005 Paris, France
⁶² Carleton College, Northfield, MN 55057, USA
⁶³ Astronomical Observatory Warsaw University, 00-478 Warsaw, Poland
⁶⁴ VU University Amsterdam, 1081 HV Amsterdam, The Netherlands
⁶⁵ University of Maryland, College Park, MD 20742, USA
⁶⁶ Laboratoire des Matériaux Avancés (LMA), CNRS/IN2P3, F-69622 Villeurbanne, France
⁶⁷ Université Claude Bernard Lyon 1, F-69622 Villeurbanne, France
⁶⁸ Università di Napoli “Federico II,” Complesso Universitario di Monte S. Angelo, I-80126 Napoli, Italy
⁶⁹ NASA/Goddard Space Flight Center, Greenbelt, MD 20771, USA
⁷⁰ RESCEU, University of Tokyo, Tokyo, 113-0033, Japan
⁷¹ University of Adelaide, Adelaide, South Australia 5005, Australia
⁷² Tsinghua University, Beijing 100084, China
⁷³ Texas Tech University, Lubbock, TX 79409, USA
⁷⁴ The University of Mississippi, University, MS 38677, USA
⁷⁵ The Pennsylvania State University, University Park, PA 16802, USA
⁷⁶ National Tsing Hua University, Hsinchu City, 30013 Taiwan, Republic of China
⁷⁷ Charles Sturt University, Wagga Wagga, New South Wales 2678, Australia
⁷⁸ University of Chicago, Chicago, IL 60637, USA
⁷⁹ Kenyon College, Gambier, OH 43022, USA
⁸⁰ Korea Institute of Science and Technology Information, Daejeon 305-806, Korea
⁸¹ University of Cambridge, Cambridge CB2 1TN, UK
⁸² Università di Roma “La Sapienza,” I-00185 Roma, Italy
⁸³ University of Brussels, Brussels B-1050, Belgium
⁸⁴ Sonoma State University, Rohnert Park, CA 94928, USA
⁸⁵ Montana State University, Bozeman, MT 59717, USA
⁸⁶ Center for Interdisciplinary Exploration & Research in Astrophysics (CIERA), Northwestern University, Evanston, IL 60208, USA
⁸⁷ Universitat de les Illes Balears, IAC3—IEEC, E-07122 Palma de Mallorca, Spain
⁸⁸ The University of Texas Rio Grande Valley, Brownsville, TX 78520, USA
⁸⁹ Bellevue College, Bellevue, WA 98007, USA
⁹⁰ Institute for Plasma Research, Bhat, Gandhinagar 382428, India
⁹¹ The University of Sheffield, Sheffield S10 2TN, UK
⁹² Università di Trento, Dipartimento di Fisica, I-38123 Povo, Trento, Italy
⁹³ INFN, Trento Institute for Fundamental Physics and Applications, I-38123 Povo, Trento, Italy
⁹⁴ Cardiff University, Cardiff CF24 3AA, UK
⁹⁵ Montclair State University, Montclair, NJ 07043, USA
⁹⁶ National Astronomical Observatory of Japan, 2-21-1 Osawa, Mitaka, Tokyo 181-8588, Japan
⁹⁷ Canadian Institute for Theoretical Astrophysics, University of Toronto, Toronto, Ontario M5S 3H8, Canada
⁹⁸ University and Institute of Advanced Research, Gandhinagar, Gujarat 382007, India
⁹⁹ IISER-TVM, CET Campus, Trivandrum Kerala 695016, India
¹⁰⁰ University of Szeged, Dóm tér 9, Szeged 6720, Hungary
¹⁰¹ Embry-Riddle Aeronautical University, Prescott, AZ 86301, USA
¹⁰² Tata Institute of Fundamental Research, Mumbai 400005, India
¹⁰³ INAF, Osservatorio Astronomico di Capodimonte, I-80131, Napoli, Italy
¹⁰⁴ University of Michigan, Ann Arbor, MI 48109, USA
¹⁰⁵ Rochester Institute of Technology, Rochester, NY 14623, USA
¹⁰⁶ NCSA, University of Illinois at Urbana-Champaign, Urbana, IL 61801, USA
¹⁰⁷ University of Białystok, 15-424 Białystok, Poland
¹⁰⁸ SUPA, University of Strathclyde, Glasgow G1 1XQ, UK
¹⁰⁹ University of Southampton, Southampton SO17 1BJ, UK
¹¹⁰ Institute of Applied Physics, Nizhny Novgorod, 603950, Russia
¹¹¹ Seoul National University, Seoul 151-742, Korea
¹¹² Inje University Gimhae, 621-749 South Gyeongsang, Korea
¹¹³ National Institute for Mathematical Sciences, Daejeon 305-390, Korea
¹¹⁴ Pusan National University, Busan 609-735, Korea
¹¹⁵ NCBJ, 05-400 Świerk-Otwock, Poland
¹¹⁶ Institute of Mathematics, Polish Academy of Sciences, 00656 Warsaw, Poland
¹¹⁷ Monash University, Victoria 3800, Australia
¹¹⁸ Hanyang University, Seoul 133-791, Korea
¹¹⁹ The Chinese University of Hong Kong, Shatin, NT, Hong Kong
¹²⁰ University of Alabama in Huntsville, Huntsville, AL 35899, USA
¹²¹ ESPCI, CNRS, F-75005 Paris, France
¹²² University of Minnesota, Minneapolis, MN 55455, USA
¹²³ Università di Camerino, Dipartimento di Fisica, I-62032 Camerino, Italy
¹²⁴ Southern University and A&M College, Baton Rouge, LA 70813, USA
¹²⁵ The University of Melbourne, Parkville, Victoria 3010, Australia
¹²⁶ College of William and Mary, Williamsburg, VA 23187, USA
¹²⁷ Instituto de Física Teórica, University Estadual Paulista/ICTP South American Institute for Fundamental Research, São Paulo SP 01140-070, Brazil
¹²⁸ Whitman College, 345 Boyer Avenue, Walla Walla, WA 99362, USA
¹²⁹ Université de Lyon, F-69361 Lyon, France
¹³⁰ Hobart and William Smith Colleges, Geneva, NY 14456, USA
¹³¹ Janusz Gil Institute of Astronomy, University of Zielona Góra, 65-265 Zielona Góra, Poland
¹³² King’s College London, University of London, London WC2R 2LS, UK

- ¹³³ IISER-Kolkata, Mohanpur, West Bengal 741252, India
¹³⁴ Indian Institute of Technology, Gandhinagar Ahmedabad Gujarat 382424, India
¹³⁵ Andrews University, Berrien Springs, MI 49104, USA
¹³⁶ Università di Siena, I-53100 Siena, Italy
¹³⁷ Trinity University, San Antonio, TX 78212, USA
¹³⁸ University of Washington, Seattle, WA 98195, USA
¹³⁹ Abilene Christian University, Abilene, TX 79699, USA
¹⁴⁰ Ioffe Institute, Politekhicheskaya 26, St. Petersburg 194021, Russia
¹⁴¹ Space Research Institute, Russian Academy of Sciences, Moscow 117997, Russia
¹⁴² University of California-Berkeley, Space Sciences Lab, 7 Gauss Way, Berkeley, CA 94720, USA
¹⁴³ Max-Planck-Institut für Extraterrestrische Physik, Giessenbachstraße 1, D-85748, Garching, Germany
 Received 2016 December 1; revised 2017 March 15; accepted 2017 March 19; published 2017 May 26

Abstract

We present the results of the search for gravitational waves (GWs) associated with γ -ray bursts detected during the first observing run of the Advanced Laser Interferometer Gravitational-Wave Observatory (LIGO). We find no evidence of a GW signal for any of the 41 γ -ray bursts for which LIGO data are available with sufficient duration. For all γ -ray bursts, we place lower bounds on the distance to the source using the optimistic assumption that GWs with an energy of $10^{-2}M_{\odot}c^2$ were emitted within the 16–500 Hz band, and we find a median 90% confidence limit of 71 Mpc at 150 Hz. For the subset of 19 short/hard γ -ray bursts, we place lower bounds on distance with a median 90% confidence limit of 90 Mpc for binary neutron star (BNS) coalescences, and 150 and 139 Mpc for neutron star–black hole coalescences with spins aligned to the orbital angular momentum and in a generic configuration, respectively. These are the highest distance limits ever achieved by GW searches. We also discuss in detail the results of the search for GWs associated with GRB 150906B, an event that was localized by the InterPlanetary Network near the local galaxy NGC 3313, which is at a luminosity distance of 54 Mpc ($z = 0.0124$). Assuming the γ -ray emission is beamed with a jet half-opening angle $\leq 30^\circ$, we exclude a BNS and a neutron star–black hole in NGC 3313 as the progenitor of this event with confidence $>99\%$. Further, we exclude such progenitors up to a distance of 102 Mpc and 170 Mpc, respectively.

Key words: binaries: close – gamma-ray burst: general – gravitational waves

1. Introduction

Gamma-ray bursts (GRBs) are among the most energetic astrophysical events observed in the electromagnetic spectrum. They are transient flashes of γ -radiation and are broadly classified as being *long* or *short*, depending on their duration and spectral hardness, mainly on the basis of data from the Burst and Transient Source Experiment on board the *Compton Gamma-Ray Observatory* (Nakar 2007; Berger 2014). Long GRBs have a duration that is greater than ~ 2 s and a softer spectrum; their origin is related to the core collapse of rapidly rotating massive stars (Woosley & Bloom 2006; Mösta et al. 2015), a hypothesis supported by observations of associated core-collapse supernovae (Hjorth & Bloom 2011). In this scenario, several (magneto)rotational instabilities may kick in and lead to the emission of gravitational waves (GWs; Modjaz 2011).

Short GRBs have a duration of less than ~ 2 s and a harder spectrum. Their progenitors are widely thought to be coalescing binary neutron star (BNS) or neutron star (NS)–black hole (BH) binary systems (Eichler et al. 1989; Paczynski 1991; Narayan et al. 1992; Lee & Ramirez-Ruiz 2007; Nakar 2007; Berger 2011), a hypothesis that was reinforced by the observation of a possible kilonova associated with GRB 130603B (Berger et al. 2013; Tanvir et al. 2013). Coalescing BNS and NS–BH

binaries—collectively NS binaries—also produce a characteristic GW signal that is detectable by the current generation of interferometric GW detectors, such as the Advanced Laser Interferometer Gravitational-Wave Observatory (LIGO) and Virgo, up to distances of hundreds of megaparsecs (Abbott et al. 2016c). GW signals associated with this class of GRBs would provide new astrophysical insight into the progenitors of these transient phenomena. Specifically, an NS binary coalescence signal in coincidence with a short GRB would confirm the NS binary merger origin. In addition, it would allow us to measure the masses and spins of the binary components—possibly enabling us to distinguish between BNS and NS–BH progenitors (Kreidberg et al. 2012; Hannam et al. 2013) and to constrain the relative merger rates of these two classes of compact binaries—as well as to place constraints on the beaming angle and the NS equation of state (Chen & Holz 2013; Pannarale & Ohme 2014; Clark et al. 2015). We note that observations of nearby long GRBs without an accompanying supernova (Della Valle et al. 2006; Fynbo et al. 2006; Gal-Yam et al. 2006) and of short GRBs that exhibit an extended γ -ray emission that is softer than the prompt spike (Gehrels et al. 2006; Norris & Bonnell 2006; Norris et al. 2010, 2011; Sakamoto et al. 2011) may blur the divide between long and short GRBs of the standard, bimodal classification. On the basis of their properties and their host environments, van Putten et al. (2014) ascribe the origin of GRBs from both categories to compact binary mergers, as for canonical short GRBs. In the case of short GRBs with and without extended emission, other studies indicate that there is no evidence to distinguish between the two populations (Fong et al. 2013; Fong & Berger 2013).

¹⁴⁴ Deceased, March 2016.



Original content from this work may be used under the terms of the [Creative Commons Attribution 3.0 licence](https://creativecommons.org/licenses/by/3.0/). Any further distribution of this work must maintain attribution to the author(s) and the title of the work, journal citation and DOI.

The first Advanced LIGO Observing Run (O1) began on 2015 September 12 and continued until 2016 January 19. During the run, the two LIGO detectors (located in Hanford, WA and Livingston, LA) were operating with instrument noise 3–4 times lower than ever measured before in their most sensitive frequency band, [100, 300] Hz; at 50 Hz, the sensitivity improvement with respect to the initial LIGO detectors was a factor of ~ 30 (for further details on detector performance, see Figure 1 in Abbott et al. 2016g, Figure 2 in Martynov et al. 2016, and discussions therein, as well as Abbott et al. 2016f and Nuttall et al. 2015). In the course of O1, the search for GWs emitted by binary BH systems yielded two unambiguously identified signals (Abbott et al. 2016j, 2016h) and a third possible signal (Abbott et al. 2016d). These successful results also sparked the first campaign to search for counterparts of Advanced LIGO sources, marking a milestone for transient astronomy and paving the way for multimessenger investigations of NS binary merger events in the years to come (Abbott et al. 2016i, 2016e).

In this paper, we present the results of a search for GWs associated with GRBs detected by the *Fermi* and *Swift* γ -ray satellites and by the InterPlanetary Network (IPN) during O1. From current observations, one expects most GRB events to be at distances that are too large for their associated GW signals to be detectable (the median redshift of the long and short GRB populations with established redshifts is ~ 2 and ~ 0.5 , respectively; Berger 2014). However, a GRB in a data set under consideration may happen to fall within the range of GW detectors. For example, the smallest observed redshift to date of an optical GRB afterglow is $z = 0.0085$ ($\simeq 36$ Mpc) for GRB 980425 (Galama et al. 1998; Kulkarni et al. 1998; Iwamoto et al. 1998; see Clark et al. 2015 for further details on the expected rate of joint short GRB and GW observations). The effort reported in this paper follows the one carried out with the initial LIGO and Virgo detectors, which found no evidence for GWs in coincidence with 508 GRBs detected between 2005 and 2010 (Aasi et al. 2014b). Three distinct searches were performed during O1: (1) a low-latency search to promptly identify coincidences in time between online GW searches and GRB events (Rapid VOEvent Coincidence Monitor or RAVEN; Urban 2016; see Section 4.1 for details), (2) a modeled search for NS binary mergers (PyGRB; Williamson et al. 2014; Nitz et al. 2016; see Section 4.2), (3) a search for generic (i.e., using minimal assumptions about the signal morphology), unmodeled GW transients (X-Pipeline; Sutton et al. 2010; see Section 4.3). We find no evidence of a GW signal associated with any of the GRBs in the sample, and we also rule out a collective signature of weak GW signals associated with the GRB population. We determine lower bounds on the distance to the progenitor of each GRB, and we constrain the fraction of observed GRB population at low redshifts.

Finally, we report on the specific case of the search for GWs associated with GRB 150906B (Golenetskii et al. 2015; Hurley et al. 2015). This event, detected by the IPN, was poorly placed for optical/infrared observations, but, as noted by Levan et al. (2015), the local galaxy NGC 3313 lies close to the GRB 150906B IPN error box, making it a viable host candidate for this event. Interestingly, NGC 3313 is at a luminosity distance of 54 Mpc and is therefore within the Advanced LIGO horizon for NS binary mergers.

2. GRB Sample

Our GRB sample contains events distributed through the Gamma-ray Coordinates Network (GCN) system,¹⁴⁵ supplemented by the *Swift*¹⁴⁶ (Lien et al. 2016) and *Fermi*¹⁴⁷ (Gruber et al. 2014; von Kienlin et al. 2014) trigger pages and the IPN (Hurley et al. 2003). Events distributed through the GCN system are ingested into the GW candidate event database (GraceDB)¹⁴⁸ within seconds of publication. The dedicated Vetting Automation and Literature Informed Database (VALID; Coyne 2015) cross-checks their time and localization parameters against the tables relative to each satellite and against the published catalog, and with automated literature searches.

In total there are 110 bursts recorded in the GCN and the IPN database during the period of interest (2015 September 12 to 2016 January 19). Twenty-three of them were detected solely by the IPN,¹⁴⁹ and about half of these were observed by a single spacecraft or two closely spaced ones and therefore could not be localized. We followed up all GRBs that occurred when at least one of the LIGO detectors was operating in a stable configuration. GW data segments that are flagged as being of poor quality are excluded from the analysis. The classification of GRBs into short and long is sometimes somewhat ambiguous. Our selection is based on the T_{90} duration, which is the time interval over which 90% of the total background-subtracted photon counts are observed. A GRB is labeled short if its $T_{90} + T_{90,\text{error}} < 2$ s. A GRB is labeled long if $T_{90} - T_{90,\text{error}} > 4$ s. The remaining GRBs are labeled ambiguous. This separates the GRB sample into 23 short GRBs, 79 long GRBs, and 8 ambiguous GRBs.

Since binary mergers are particularly strong sources of GWs, we use the modeled search for NS binaries to analyze both short GRBs and ambiguous GRBs. This ensures that we include all short GRBs in the tail of the duration distribution. This search was able to analyze 19 events, which constitute $\sim 61\%$ of the GRBs it could have targeted, had the GW detectors been operating with 100% duty cycle. This search can be run with data from one or more GW detectors (see Section 4.2), so the number is in line with the $\sim 61\%$ and $\sim 52\%$ duty cycles of the Hanford and the Livingston detectors, respectively. The generic unmodeled GW search is performed on all GRBs, regardless of their classification. In this case, results were obtained for 31 GRBs, that is, 31% of the events recorded during O1 with available sky location information. Keeping in mind that this search requires at least 660 s of data in coincidence from the two GW detectors (see Section 4.3), we note that the number is in line with the $\sim 40\%$ duty cycle of the two Advanced LIGO detectors during O1. In total, with the two methods, we were able to process 41 GRB events, that is, 41% of the events recorded during O1 that had sky location information available. Eight

¹⁴⁵ GCN Circulars Archive: http://gcn.gsfc.nasa.gov/gcn3_archive.html.

¹⁴⁶ *Swift* GRB Archive: http://swift.gsfc.nasa.gov/archive/grb_table/. *Swift*/BAT Gamma-Ray Burst Catalog: <http://swift.gsfc.nasa.gov/results/batgrbcat/>.

¹⁴⁷ FERMIGBRST—*Fermi* GBM Burst Catalog: <https://heasarc.gsfc.nasa.gov/W3Browse/fermi/fermigbrst.html>.

¹⁴⁸ Moe, B., Stephens, B., and Brady, P., GraceDB—Gravitational Wave Candidate Event Database, <https://gracedb.ligo.org/>.

¹⁴⁹ Unlike the GCN sample, the IPN sample we describe is the subset of GRBs that took place during O1 for which at least one LIGO detector was operating. For this subset, a detailed IPN sky localization was performed.

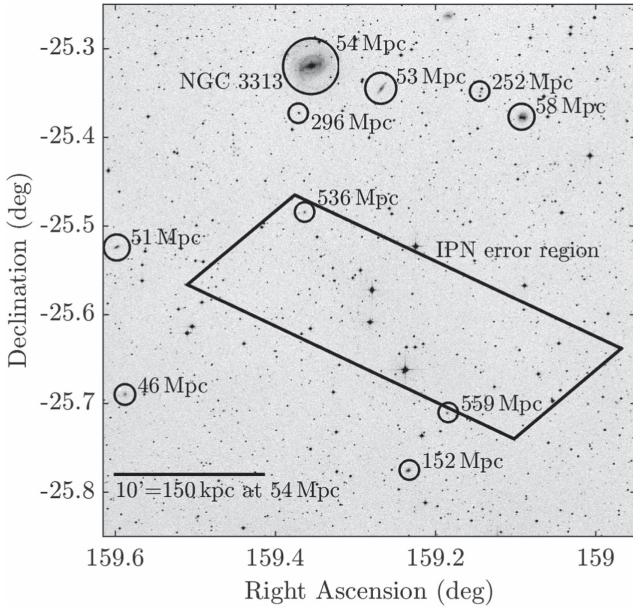


Figure 1. Overlay of the error box for GRB 150906B on the sky (Levan et al. 2015). A number of galaxies are at around 50 Mpc, while some of the galaxies within the error region are at ~ 500 Mpc (G. Dálya et al. 2016, in preparation).

of these events were analyzed in single-detector mode by the modeled search for NS binaries: the ability of this search to run with data from only one detector thus allows us to significantly increase our sample.

2.1. GRB 150906B

In addition to the GRBs in the sample we described above, we also consider GRB 150906B, an event of particular interest due to its potential proximity. It occurred on 2015 September 6 at 08:42:20.560 UTC and was detected by the IPN (Golenetskii et al. 2015; Hurley et al. 2015). At the time of GRB 150906B, the Advanced LIGO detectors were undergoing final preparations for O1. Nonetheless, the 4 km detector in Hanford was operational at that time.

GRB 150906B was observed by the *Konus–Wind*, *INTEGRAL*, *Mars Odyssey*, and *Swift* satellites. It was outside the coded field of view of the *Swift* BAT, and, consequently, localization was achieved by triangulation of the signals observed by the four satellites (Hurley et al. 2015). The localization region of GRB 150906B lies close to the local galaxy NGC 3313, which has a redshift of 0.0124 at a luminosity distance of 54 Mpc (Levan et al. 2015). This galaxy lies 130 kpc in projection from the GRB error box, a distance that is consistent with observed offsets of short GRBs from galaxies and with the expected supernova kicks imparted on NS binary systems (Berger 2011). NGC 3313 is part of a group of galaxies, and it is the brightest among this group. Other, fainter members of the group also lie close to the GRB error region, as shown in Figure 1. In addition, there are a number of known galaxies at around 500 Mpc within the error region of the GRB (Bilicki et al. 2013). For the GW search, we use a larger error region with a more conservative error assumption. Follow-up electromagnetic observations of the GRB were not possible due to its proximity to the Sun.

The *Konus–Wind* observation of GRB 150906B was further used to classify the GRB (Svinkin et al. 2015). It was observed to have a duration of $^{150} T_{50} = (0.952 \pm 0.036)$ s and $T_{90} = (1.642 \pm 0.076)$ s, which places it at the longer end of the short GRB distribution. Furthermore, GRB 150906B lies between the peaks of the short/hard and long/soft *Konus–Wind* GRB distributions in the $\log T_{50} - \log HR_{32}$ hardness-duration diagram, where $\log HR_{32}$ is the (logarithm of the) ratio of counts in the [200, 760] keV and [50, 200] keV bands (Svinkin et al. 2015). Thus, a firm classification of the GRB as either short or long is problematic.

Assuming GRB 150906B originated in NGC 3313 yields an isotropic-equivalent γ -ray energy $E_{\text{iso}} \sim 10^{49}$ erg (Levan et al. 2015). This is consistent with inferred luminosities of short GRBs with measured redshifts (Berger 2011), albeit at the lower end of the distribution of E_{iso} values. Theoretical arguments (Ruffini et al. 2015; Zhang et al. 2015) suggest that the energetics fit better with a more distant system around 500 Mpc, possibly originating from one of the galaxies within the error region.

3. Considerations on GRB Progenitors

As discussed previously, BNS and NS-BH mergers are the most plausible progenitors for the majority of short GRBs, while the progenitors of long GRBs are extreme cases of stellar collapse. In this section, we provide considerations on the main properties of the sources that we target with our searches in order to address these scenarios.

3.1. Short-duration GRBs

The modeled search for GWs emitted by NS binary mergers addresses the case of short GRB events. While not all NS binary mergers necessarily lead to a short GRB, this search looks for a GW counterpart to a short GRB event under the assumption that short GRBs are generated by NS binary mergers. In the standard scenario (Eichler et al. 1989; Paczynski 1991; Narayan et al. 1992; Nakar 2007), as the two companions spiral inward together due to the emission of GWs, the NSs are expected to tidally disrupt before the coalescence, in order to create a massive torus remnant in the surroundings of the central compact object that is formed by the binary coalescence. The matter in the torus can then power highly relativistic jets along the axis of total angular momentum (Blandford & Znajek 1977; Rosswog & Ramirez-Ruiz 2002; Lee & Ramirez-Ruiz 2007). This picture is supported by observational evidence (Berger 2011; Berger et al. 2013; Tanvir et al. 2013) and numerical simulations (e.g., Rezzolla et al. 2011; Kiuchi et al. 2015) but has not yet been fully confirmed.

The form of the GW signal emitted by a compact binary coalescence depends on the masses (m_{NS} , m_{comp}) and spins of the NS and its companion (either an NS or a BH), as well as the spatial location and orientation relative to the detector. In the remainder of this section we therefore discuss observational constraints on these properties and our choices regarding them that are folded into our search for BNS and NS-BH progenitors of short GRBs.

¹⁵⁰ Similarly to T_{90} , T_{50} is the time interval over which 50% of the total background-subtracted photon counts are observed.

Mass measurements of NSs in binary systems currently set a lower bound on the maximum possible NS mass to $(2.01 \pm 0.04) M_{\odot}$ (Antoniadis et al. 2013). On the other hand, theoretical considerations set an upper bound on the maximum NS star mass to $\sim 3 M_{\odot}$ (Rhoades & Ruffini 1974; Kalogera & Baym 1996), while the standard core-collapse supernova formation scenario restricts NS birth masses above the $1.1\text{--}1.6 M_{\odot}$ interval (Lattimer 2012; Ozel et al. 2012; Kiziltan et al. 2013). Finally, we note that the individual NS masses reported for the eight candidate BNS systems lie in the interval $[1.0, 1.49] M_{\odot}$ (Ozel & Freire 2016).

The fastest spinning pulsar ever observed rotates at a frequency of 716 Hz (Hessels et al. 2006). Assuming a mass of $1.4 M_{\odot}$ and a moment of inertia of 10^{45} g cm^2 , this corresponds to a dimensionless spin magnitude of ~ 0.4 . The highest measured spin frequency of pulsars in confirmed BNS systems is that of J0737–3039A (Burgay et al. 2003). It is equal to 44 Hz (Kramer & Wex 2009), which yields a dimensionless spin magnitude of ~ 0.05 (Brown et al. 2012). Finally, the potential BNS pulsar J1807–2500B (Lynch et al. 2012) with a spin of 4.19 ms gives a dimensionless spin magnitude of ~ 0.2 , if one assumes a pulsar mass of $1.37 M_{\odot}$ and a moment of inertia $2 \cdot 10^{45} \text{ g cm}^2$.

No observations of NS-BH systems are available to date. Notably, however, a likely NS-BH progenitor has been observed, namely Cyg X-3 (Belczynski et al. 2013). While Advanced LIGO has observed a BH with mass $36^{+5}_{-4} M_{\odot}$ in a binary BH system (Abbott et al. 2016j), and while stellar BHs with masses exceeding even $100 M_{\odot}$ are conceivable (Belczynski et al. 2014; de Mink & Belczynski 2015), mass measurements of galactic stellar-mass BHs in X-ray binaries are between 5 and 24 solar masses (Ozel et al. 2010; Farr et al. 2011; Kreidberg et al. 2012; Wiktorowicz et al. 2013). X-ray observations of accreting BHs provide a broad distribution of dimensionless spin magnitudes ranging from ~ 0.1 to above 0.95 (e.g., Miller & Miller 2014). We remark that BH dimensionless spin magnitudes inferred from observations of high-mass X-ray binaries typically have values above 0.85 and that these systems are more likely to be NS-BH system progenitors (McClintock et al. 2014).

A final property to discuss in the context of GW searches for BNS and NS-BH systems in coincidence with short GRBs is the half-opening angle θ_{jet} of the GRB jet. Relativistic beaming and collimation due to the ambient medium confine the GRB jet to θ_{jet} . In all cases, we assume that the GRB is emitted in the direction of the binary total angular momentum. The observation of prompt γ -ray emission is, therefore, indicative that the inclination of the total angular momentum with respect to the line of sight to the detectors lies within the jet cone. Estimates of θ_{jet} are based on jet breaks observed in X-ray afterglows and vary across GRBs. Indeed, many GRBs do not even exhibit a jet break. However, studies of observed jet breaks in *Swift* GRB X-ray afterglows find a mean (median) value of $\theta_{\text{jet}} = 6^{\circ}.5$ ($5^{\circ}.4$), with a tail extending almost to 25° (Racusin et al. 2009). In at least one case where no jet break is observed, the inferred lower limit is 25° and could be as high as 79° (Grupe et al. 2006). By folding in lower limits on θ_{jet} for short GRBs without opening angle measurements and the indication that $\theta_{\text{jet}} \sim 5^{\circ}\text{--}20^{\circ}$, which arises from simulations of postmerger BH accretion, Fong et al. (2015) find a median of $16^{\circ} \pm 10^{\circ}$ for θ_{jet} .

In light of all these considerations on astrophysical observations, we perform the modeled search described in Section 4.2 for NSs with masses between $1 M_{\odot}$ and $2.8 M_{\odot}$ and dimensionless spin magnitude of 0.05 at most.¹⁵¹ For the companion object, we test masses in the range $1 M_{\odot} \leq m_{\text{comp}} \leq 25 M_{\odot}$ and dimensionless spins up to 0.999. Additionally, we restrict the NS-BH search space (i.e., $m_{\text{comp}} > 2.8 M_{\odot}$) to BH masses and spins that are consistent with the presence of remnant material in the surroundings of the central BH, rather than with the direct plunge of the NS onto the BH (Pannarale & Ohme 2014). This astrophysically motivated cut excludes from our search NS-BH systems that do not allow for a GRB counterpart to be produced, even under the most optimistic assumptions regarding the NS equation of state¹⁵² and the amount of tidally disrupted NS material required to ignite the GRB emission¹⁵³ (Pannarale & Ohme 2014). Finally, we search for circularly polarized signals. As discussed in Williamson et al. (2014), this is an excellent approximation for inclination angles between the total angular momentum and the line of sight up to 30° .

3.2. Long-duration GRBs

Long GRBs are followed up by the search for unmodeled GW transients described in Section 4.3. When making quantitative statements on the basis of this search, we use two families of GW signal models: circular sine-Gaussian (CSG) and accretion disk instability (ADI) signals. The scenarios that these address are discussed below.

No precise waveform is known for stellar collapse. A wide class of scenarios involves a rotational instability developing in the GRB central engine that leads to a slowly evolving, rotating quadrupolar mass distribution. Semianalytical calculations of rotational instabilities suggest that up to $10^{-2} M_{\odot} c^2$ may be emitted in GWs (Davies et al. 2002; Fryer et al. 2002; Kobayashi & Meszaros 2003; Shibata et al. 2003; Piro & Pfahl 2007; Corsi & Meszaros 2009; Romero et al. 2010), but simulations addressing the nonextreme case of core-collapse supernovae predict an emission of up to $10^{-8} M_{\odot} c^2$ in GWs (Ott 2009). With this in mind, we use a crude but simple generic model, that is, a CSG waveform with plus (+) and cross (×) polarizations given by

$$\begin{aligned} \begin{bmatrix} h_{+}(t) \\ h_{\times}(t) \end{bmatrix} &= \frac{1}{r} \sqrt{\frac{G E_{\text{GW}}}{c^3} \frac{5}{f_0 Q}} \frac{5}{4\pi^{3/2}} \\ &\times \begin{bmatrix} (1 + \cos^2 \iota) \cos(2\pi f_0 t) \\ 2 \cos \iota \sin(2\pi f_0 t) \end{bmatrix} \exp \left[-\frac{(2\pi f_0 t)^2}{2Q^2} \right], \end{aligned} \quad (1)$$

where the signal frequency f_0 is equal to twice the rotation frequency, t is the time relative to the signal peak time, Q

¹⁵¹ The search is nonetheless effective for NS spins up to 0.4 (Nitz 2015; Abbott et al. 2016c).

¹⁵² To prescribe the cut, we use a simple piecewise polytropic equation of state (2H) that yields NSs with masses up to $\sim 2.8 M_{\odot}$ and radii of $\sim 15 \text{ km}$ (e.g., Kyutoku et al. 2010). The large NS radius value, which is above current constraints (Steiner et al. 2013; Ozel & Freire 2016), is chosen to favor tidal disruption and hence make our targeted parameter space as inclusive as possible.

¹⁵³ Namely, we target any system that leads to the presence of remnant NS debris material.

characterizes the number of cycles for which the quadrupolar mass moment is large, E_{GW} is the total radiated energy, r is the distance to the source, ι is the rotation axis inclination angle with respect to the observer, and G and c are the gravitational constant and the speed of light, respectively. The inclination angle ι can be once again linked to observations of GRB jet-opening angles: in the case of long GRBs, these are typically $\sim 5^\circ$ (Gal-Yam et al. 2006; Racusin et al. 2009). All other parameters are largely underconstrained.

In the collapsar model of long GRBs, a stellar-mass BH forms, surrounded by a massive accretion disk. An extreme scenario of emission from a stellar collapse is a “magnetically suspended” ADI (van Putten 2001; van Putten et al. 2004). This parametric model may not be a precise representation of realistic signals, but it captures the generic features of many proposed models. It is characterized by four free astrophysical parameters: the mass and the dimensionless spin parameter of the central BH, the fraction of the disk mass that forms clumps, and the accretion disk mass. Waveform parameters such as duration, frequency span, and total radiated energy can be precisely derived for a given set of astrophysical parameters. As discussed in Section 4.3, we use several combinations of values for the astrophysical parameters in order to cover the different predicted morphologies.

4. Search Methodology

A *low-latency search*, referred to as RAVEN (Urban 2016; see Section 4.1), was performed in order to potentially initiate a prompt electromagnetic follow-up effort in the case of a possible association of a GW signal with a GRB event. The method builds on the results of the online, low-latency, all-sky GW searches to look for associations between GRBs and GW candidates. Results were ready within minutes after GRB detection notices: this allows circulation of alerts to the astronomy community on a timescale that is useful for enhancing follow-up observations targeting the X-ray, optical, and radio afterglows of GRB events.

The results presented in this paper were produced by an *offline search* using (1) a templated, NS binary search method (implemented in the `PyGRB` pipeline; see Williamson et al. 2014 and references therein for a full description and Nitz et al. 2016 for the code) for triggers corresponding to short GRBs and (2) a generic method (i.e., using minimal assumptions about the signal morphology) for GW transients (implemented in the `X-Pipeline`; see Sutton et al. 2010 and Was et al. 2012 for a complete description) for all GRBs. The two methods are illustrated in Sections 4.2 and 4.3, respectively. Both of them are largely the same as for the previous analysis described in Aasi et al. (2014b) and utilized data with final quality and calibration¹⁵⁴ (Abbott et al. 2017b, 2016f). Unlike in previous studies (Abbott et al. 2010; Abadie et al. 2010, 2012a; Aasi et al. 2014b), the offline search did not require data from both interferometers to be available. However, the generic method is severely limited by nonstationary transients when data from only one interferometer are available. Hence for the generic method

we present results only for GRBs that occurred when both interferometers were available.

4.1. Rapid VOEvent Coincidence Monitor

RAVEN (Urban 2016) compares the GW triggers recorded in the low-latency all-sky GW analysis with the given time of a GRB. It provides a preliminary indication of any coincident GW candidate event and its associated significance. The `cWB` (Klimenko et al. 2016), `oLIB` (Lynch et al. 2015), `GstLAL` (Messick et al. 2017), and `MBTA` (Adams et al. 2016) pipelines perform the blind, rapid all-sky GW monitoring. `cWB` and `oLIB` search for a broad range of GW transients in the frequency range of 16–2048 Hz without prior knowledge of the signal waveforms. The `GstLAL` and `MBTA` pipelines search for GW signals from the coalescence of compact objects, using optimal matched filtering with waveforms. During O1, `MBTA` covered component masses of 1–12 M_\odot with a 5 M_\odot limit on chirp mass. `GstLAL`, instead, covered systems with component masses of 1–2.8 M_\odot and 1–16 M_\odot up to 2015 December 23; then, motivated by the discovery of GW150914, the analysis was extended to cover systems with component masses of 1–99 M_\odot and total mass less than 100 M_\odot . Both pipelines limit component spins to < 0.99 and < 0.05 for BHs and NSs,¹⁵⁵ respectively (see Abbott et al. 2016c for further details).

GW candidates from these low-latency searches were uploaded to GraceDB and compared to the GRB triggers to find any temporal coincidence in $[-600, +60]$ and $[-5, +1]$ second windows, which correspond to the delay between the GW and the GRB trigger for long and short GRBs, respectively, as discussed in the next two sections. This strategy has the advantage of being very low latency and of requiring little additional computational costs over the existing all-sky searches. RAVEN (Urban 2016) results are available to be shared with LIGO partner electromagnetic astronomy facilities¹⁵⁶ within minutes following a GRB detection.

4.2. Neutron Star Binary Search Method (`PyGRB`)

In the vast majority of short GRB progenitor scenarios, the GW signal from an NS binary coalescence is expected to precede the prompt γ -ray emission by no more than a few seconds (Lee & Ramirez-Ruiz 2007; Vedrenne & Atteia 2009). Therefore, we search for NS binary GW signals with end times that lie in an *on-source* window of $[-5, +1]$ s around the reported GRB time, as done in previous searches in LIGO and Virgo data (Abadie et al. 2012a; Aasi et al. 2014b). The method we use is described in detail in Williamson et al. (2014) and references therein; the code implementing it is available under Nitz et al. (2016).

The data are filtered in the 30 Hz–1000 Hz frequency interval through a discrete bank of $\sim 110,000$ template waveforms (Owen & Sathyaprakash 1999) that covers NS binaries with the properties discussed in Section 3.1. It is the first time that a short GRB follow-up search used a template bank that includes aligned spin systems (Brown et al. 2012; Harry et al. 2014). The bank is designed to have a 3%

¹⁵⁴ Both flavors of the search were also promptly initiated in a *medium-latency* configuration within about 20 minutes following the receipt of an appropriate GRB detection notice. This configuration requires a less accurate evaluation of the efficiency of each search and produces results within a few hours.

¹⁵⁵ `GstLAL` and `MBTA` treat as NSs components with masses below 2.8 M_\odot and 2 M_\odot , respectively.

¹⁵⁶ See program description and participation information at <http://www.ligo.org/scientists/GWEMAlerts.php>.

Table 1
Accretion Disk Instability Waveform Parameters

Waveform	M	χ	ϵ	Duration	Frequency	E_{GW}
Label	(M_{\odot})			(s)	(Hz)	($M_{\odot}c^2$)
ADI-A	5	0.30	0.050	39	135–166	0.02
ADI-B	10	0.95	0.200	9	110–209	0.22
ADI-C	10	0.95	0.040	236	130–251	0.25
ADI-D	3	0.70	0.035	142	119–173	0.02
ADI-E	8	0.99	0.065	76	111–234	0.17

Notes. The first column is the label used for the ADI waveform. The second and third columns are the mass and the dimensionless spin parameter of the central BH. The fourth column, ϵ , is the fraction of the disk mass that forms clumps, and in all cases the accretion disk mass is $1.5 M_{\odot}$. The duration, frequency span, and total radiated energy of the resulting signal are also reported in the remaining columns.

maximum loss of signal-to-noise ratio (S/N) due to discretization effects for binaries with spins aligned, or antialigned, to the orbital angular momentum over the parameter space discussed at the end of Section 3.1.

For BNS and NS-BH coalescences, we use point-particle post-Newtonian models that describe the inspiral stage, where the orbit of the binary slowly shrinks due to the emission of GWs. This is mainly motivated by the fact that the merger and postmerger regime (i.e., the GW high-frequency behavior) of these systems differs from the binary BH case. While we do have robust inspiral-merger-ringdown binary BH waveforms (Taracchini et al. 2014; Khan et al. 2016), efforts to obtain accurate, complete waveform models for NS binaries are still underway (Lackey et al. 2014; Bernuzzi et al. 2015; Pannarale et al. 2015; Barkett et al. 2016; Haas et al. 2016; Hinderer et al. 2016). Additionally, to go beyond a point-particle inspiral description, the search would have to cover all feasible NS equations of state, at the expense of a significant increase in its computational costs. Each template is therefore modeled with the “TaylorT4” time-domain, post-Newtonian inspiral approximant (Buonanno et al. 2003), filtered against the coherently combined data, and peaks in the matched filter coherent S/N are recorded. Additional signal consistency tests are used to eliminate the effect of non-Gaussian transients in the data and to generate a reweighted coherent S/N (see Williamson et al. 2014 for its formal definition), which forms the detection statistic (Allen 2005; Harry & Fairhurst 2011).

After the filtering and the consistency tests, the event with the largest reweighted coherent S/N (provided that this is greater than 6) in the on-source window is retained as a candidate GW signal. In order to assess the significance of the candidate, the detector background noise distribution is estimated using data from a time period surrounding the on-source data, when a GW signal is not expected to be present. This is known as the *off-source* data and is processed identically to the on-source data. Specifically, the same data-quality cuts and consistency tests are applied, and the same sky positions relative to the GW detector network are used. The NS binary search method requires a minimum of 1658 s of off-source data, which it splits into as many 6 s trials as possible. In order to increase the number of background

trials, when data from more than one detector are available, the data streams are time-shifted multiple times and reanalyzed for each time shift. The template that produces the largest reweighted coherent S/N in each 6 s off-source time window is retained as a trigger. These are used to calculate a p -value¹⁵⁷ to the on-source loudest event by comparing it to the distribution of loudest off-source triggers in terms of the detection statistics. The p -value is calculated by counting the fraction of background trials containing an event with a greater reweighted coherent S/N than the loudest on-source event. Any candidate events with p -values below 10% are subjected to additional follow-up studies to determine if the events can be associated with some non-GW noise artifact. Further details on the methods used to search for NS binary signals in coincidence with short GRBs can be found in Harry & Fairhurst (2011) and Williamson et al. (2014).

The efficiency of the NS binary search method for recovering relevant GW signals is evaluated via the addition in software of simulated signals to the data. In order to assess performance, these data are filtered with the same bank of templates used for the search. This provides a means of placing constraints on the short GRB progenitor in the event of no detection in the on-source. All simulated signals are modeled using the “TaylorT2” time-domain, post-Newtonian inspiral approximant (Blanchet et al. 1996). We note that this approximant differs from the one used to build the templates. This choice is designed to account for the disagreement among existing inspiral waveform models in our efficiency assessment (see Nitz et al. 2013 on this topic). Further, this approximant allows for generic spin configurations. We inject three sets of simulated inspiral signals; these correspond to (1) BNS systems with a generic spin configuration, (2) NS-BH systems with a generic spin configuration, and (3) NS-BH systems with an aligned spin configuration. We build both a generic and an aligned spin injection set in the NS-BH case in order to assess the impact of precession on the search sensitivity for rapidly spinning and highly precessing systems (as is the NS-BH case in contrast to the BNS case). The considerations illustrated in Section 3.1 motivate the following choices for the parameters that characterize the three families:

NS masses: These are chosen from a Gaussian distribution centered at $1.4 M_{\odot}$, with a width of $0.2 M_{\odot}$ and $0.4 M_{\odot}$ in the BNS and the NS-BH case, respectively (Ozel et al. 2012; Kiziltan et al. 2013). The larger width for NS-BH binaries reflects the greater uncertainty arising from a lack of observed NS-BH systems.

BH masses: These are Gaussian distributed with a mean of $10 M_{\odot}$ and a width of $6 M_{\odot}$. Additionally, they are restricted to being less than $15 M_{\odot}$, because the disagreement between different Taylor approximants dominates beyond this point (Nitz et al. 2013).

Dimensionless spins: These are drawn uniformly over the intervals $[0, 0.4]$ and $[0, 0.98]$ for NSs and BHs, respectively. For the two sets with generic spin configurations, both spins are isotropically distributed.

¹⁵⁷ A p -value is defined as the probability of obtaining such an event or a louder one in the on-source data, given the background distribution, under the null hypothesis.

Tidal disruption: NS-BH systems for which the remnant BH is not accompanied by any debris material are not included in the injected populations (Pannarale & Ohme 2014).

Inclination angle: This is uniformly distributed in cosine over the intervals $[0^\circ, 30^\circ]$ and $[150^\circ, 180^\circ]$.

Distance: Injections are distributed uniformly in distance in the intervals $[10, 300]$ Mpc and $[10, 600]$ Mpc for BNS and NS-BH systems, respectively.

When performing the efficiency assessment, we marginalize over amplitude detector calibration errors by resampling the assumed distance of each injected signal with a Gaussian distribution of 10% width (Abbott et al. 2017b, 2016f); the phase errors of $\sim 5^\circ$ have a negligible effect.

4.3. Generic Transient Search Method (X-Pipeline)

Long GRBs are associated with the gravitational collapse of massive stars. While GW emission is expected to accompany such events, its details may vary from event to event. We therefore search for any GW transient without assuming a specific signal shape; this type of search is performed for short GRB events as well. We use the time interval starting from 600 s before each GRB trigger and ending either 60 s after the trigger or at the T_{90} time (whichever is larger) as the *on-source* window to search for a GW signal. This window is large enough to take into account most plausible time delays between a GW signal from a progenitor and the onset of the γ -ray signal (Koshut et al. 1995; Aloy et al. 2000; MacFadyen et al. 2001; Zhang et al. 2003; Lazzati 2005; Wang & Meszaros 2007; Burlon et al. 2008, 2009; Lazzati et al. 2009; Vedrenne & Atteia 2009). The search is performed on the most sensitive GW band of 16–500 Hz. Above 300 Hz, the GW energy necessary to produce a detectable signal increases sharply as $\propto f^4$ (see Figure 2 of Abbott et al. 2017a), and hence the detector sensitivity is highly biased against high-frequency emission scenarios.

The method used to search for generic GW transients follows the one used in previous GRB analyses (Abadie et al. 2012a; Aasi et al. 2014a, 2014b) and is described in detail in Sutton et al. (2010) and Was et al. (2012). The on-source data for each GRB are processed by the search pipeline to generate multiple time-frequency maps of the data stream using short Fourier transforms with duration at all powers of two between 1/128 s and 2 s. The maps are generated after coherently combining data from the detectors, taking into account the antenna response and noise level of each detector. The time-frequency maps are scanned for clusters of pixels with energy significantly higher than the one expected from background noise. These are referred to as “events” and are characterized by a ranking statistic based on energy. We also perform consistency tests based on the signal correlations measured between the detectors. The event with the highest ranking statistic is taken to be the best candidate for a GW signal for that GRB; it is referred to as the “loudest event.” The strategy to associate a p -value with the loudest event is the same as the one adopted by the NS binary search but with off-source trials of ~ 660 s duration.

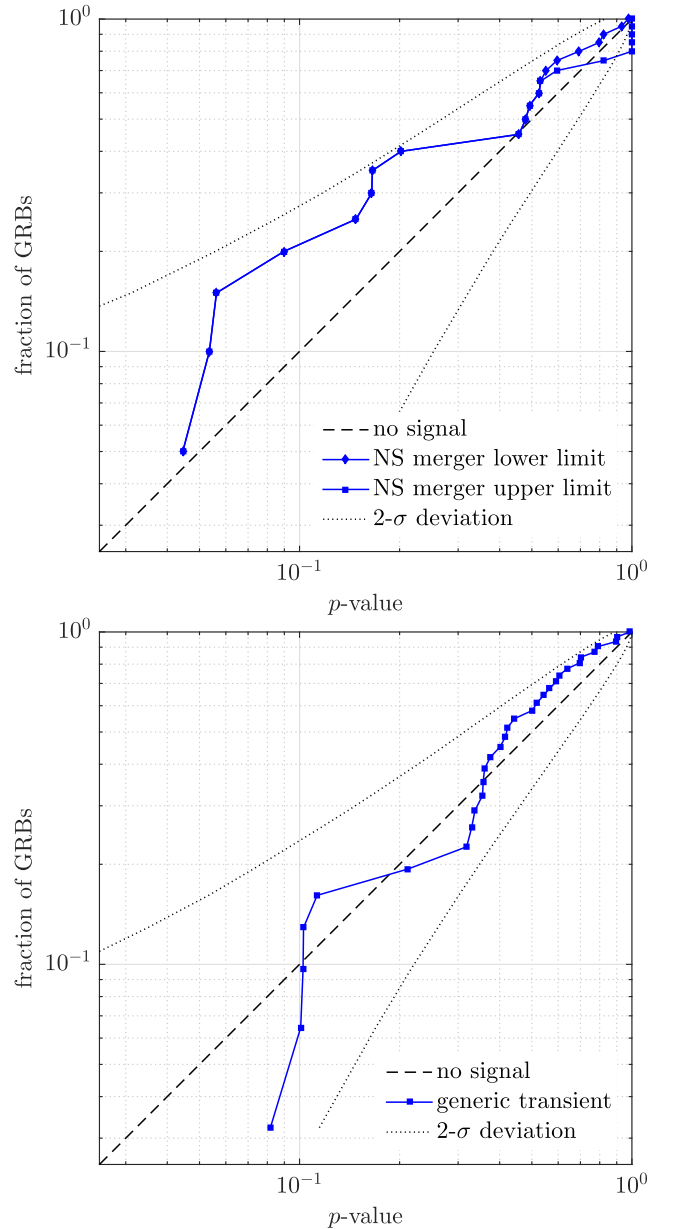


Figure 2. Cumulative distribution of p -values from the analysis of 20 short-duration GRBs for the evidence of an NS binary merger GW signal (top) and 31 GRBs for the evidence of a GW transient associated with the burst (bottom). The expected distribution under the no-signal hypothesis is indicated by the dashed line, and the 2σ deviation of that distribution is indicated by the dotted line. For GRBs with no event in the on-source, we provide an upper bound on the p -value equal to 1 and a lower bound determined by counting the fraction of background trials that yield no event: this explains the feature in the top right corner of the top panel.

As for the NS binary search method, the efficiency of this search at recovering relevant GW signals is evaluated by the addition in software of simulated signals to the data. The simulated waveforms are chosen to cover the search parameter space; they belong to three types of signals that embrace different potential signal morphologies: NS binary inspiral signals, stellar collapse (represented by CSGs), and disk instability models (represented by ADI

Table 2
Median 90% Confidence Level Exclusion Distances $D_{90\%}$

Short GRBs	BNS	NS-BH Aligned Spins	NS-BH Generic Spins		
$D_{90\%}$ [Mpc]	90	150	139		
All GRBs	CSG	CSG	CSG	CSG	CSG
	70 Hz	100 Hz	150 Hz	300 Hz	
$D_{90\%}$ [Mpc]	88	89	71	30	
All GRBs	ADI	ADI	ADI	ADI	ADI
	A	B	C	D	E
$D_{90\%}$ [Mpc]	31	97	39	15	36

Notes. The short GRB analysis assumes an NS binary progenitor. When all GRBs are analyzed, a circular sine-Gaussian (CSG) or an accretion disk instability (ADI) model is used.

waveforms).¹⁵⁸ In particular, the generic time-frequency excess power method used is equally efficient for descending (ADI) and ascending (NS binary) chirps. Because this paper reports results for NS binaries only when these are obtained with the dedicated, modeled search outlined in Section 4.2, we will limit the discussion to the case of the other two signal families.

CSG: For the standard siren CSG signals defined in Equation (1), we assume an optimistic emission of energy in GWs of $E_{\text{GW}} = 10^{-2} M_{\odot} c^2$. As discussed in Section 3, this is an upper bound on the predictions: our conclusions thus represent upper bounds, as we work under the optimistic assumption that every GRB emits $10^{-2} M_{\odot} c^2$ of energy in GWs. Further, we construct four sets of such waveforms with a fixed Q factor of 9 and varying center frequency (70, 100, 150, and 300 Hz).

ADI: The extreme scenario of ADIs (van Putten 2001; van Putten et al. 2004) provides long-lasting waveforms that the unmodeled search has the ability to recover. We chose the same sets of parameters used in a previous long-transient search (Abbott et al. 2016b) to cover the different predicted morphologies. The values of the parameters are listed in Table 1. As in previous searches, the clumps in the disk are assumed to be forming at a distance of 100 km from the BH innermost stable circular orbit (Ott & Santamaría 2013), which is the typical distance of the transition to a neutrino opaque disk where the accretion disk is expected to have the largest linear density (Lee et al. 2005; Chen & Beloborodov 2007). This constitutes a deviation from the original model that brings the GW emission from ~ 1 kHz to a few hundred Hz, where the detectors are more sensitive, thus providing a reasonable means of testing the ability of the search to detect signals in this

¹⁵⁸ In general, the sensitivity of an excess power search compared to ideal match filtering scales as $V^{0.25}$, where V is the time-frequency volume of the signal (Anderson et al. 2001). In practice, the sensitivity of this search compared to ideal match filtering is similar for CSGs, a factor of ~ 2 poorer for NS merger signals, and a factor of ~ 3 poorer for ADI signals. We refer the interested reader to Sutton et al. (2010) for further details.

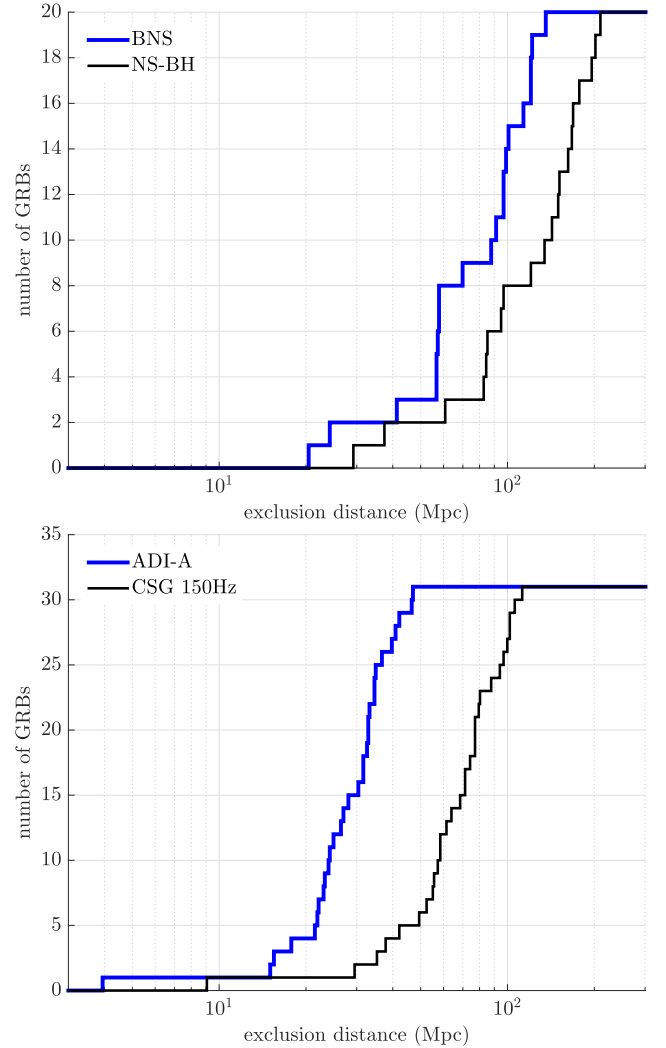


Figure 3. Cumulative histograms of the exclusion distances at the 90% confidence level for BNS and NS-BH systems across the sample of short GRBs (top) and for ADI-A and CSG GW transients at 150 Hz across the sample of all GRBs analyzed with the generic transient search (bottom). Both ADI-A and CSG at 150 Hz signals have an emission energy $\sim 10^{-2} M_{\odot} c^2$, but for ADI-A the energy is spread over a ~ 100 times longer duration, which explains the difference in exclusion distances.

frequency band and with amplitudes comparable to the original ADI formulation. We note that in the previous search for long-duration signals associated with GRBs (Aasi et al. 2013), these signals were normalized to obtain $E_{\text{GW}} = 0.1 M_{\odot} c^2$. These waveforms are tapered by a Tukey window with 1 s at the start and end of the waveform to avoid artifacts from the unphysical sharp start and end of these waveforms.

Finally, calibration errors are folded into the result by jittering the signal amplitude and time of arrival at each detector, following a wider Gaussian distribution of 20% in amplitude and 20 degrees in phase, as this search used the preliminary Advanced LIGO calibration that had greater uncertainties (Tuyenbayev et al. 2017).

5. Results

A search for GWs in coincidence with GRBs was performed during O1. We analyzed a total of 31 GRBs using the generic

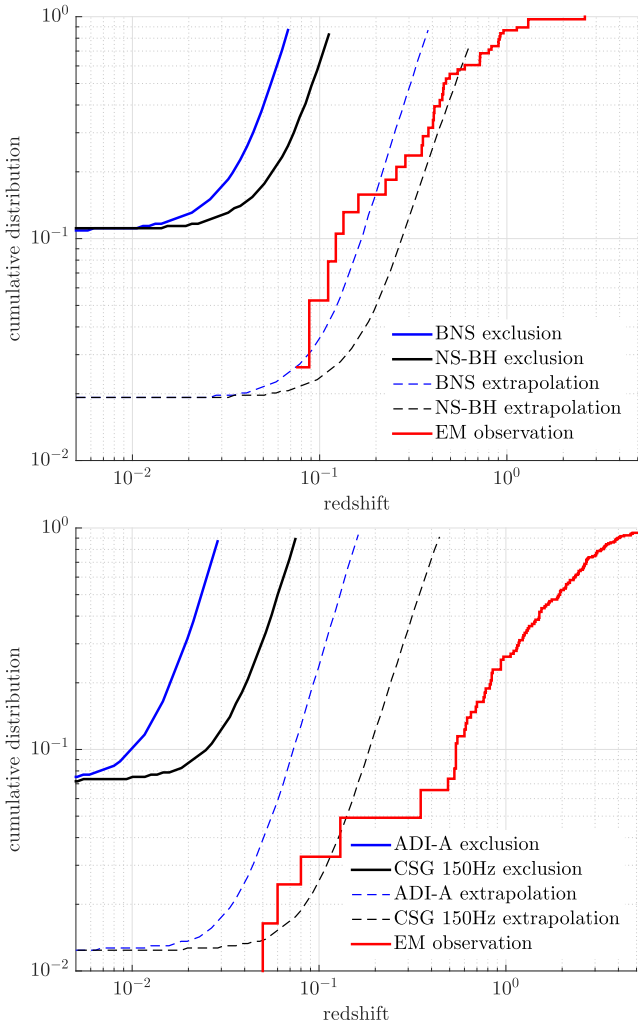


Figure 4. Combined exclusion distance for 20 short GRBs analyzed with the coalescence search for both a BNS and an NS-BH progenitor (top) and for all 31 GRBs analyzed with the generic transient search for ADI-A and standard siren CSG GW transients at 150 Hz with an energy of $E_{\text{GW}} = 10^{-2} M_{\odot} c^2$ (bottom). We exclude at 90% confidence level cumulative distance distributions that pass through the region above the solid curves. For reference, the red staircase curve shows the cumulative distribution of measured redshifts for short GRBs (top; Leibler & Berger 2010; Fong et al. 2015; Siellez et al. 2016) and *Swift* GRBs (bottom; Jakobsson et al. 2006, 2012). The dashed curves are an extrapolation of these results to 2 years of Advanced LIGO operation at design sensitivity.

transient method and 19 GRBs, classified as short or ambiguous, using the NS binary search method. In addition, we used the NS binary search method to analyze GRB 150906B, which occurred prior to 2015 September 12. The detailed list of analyzed GRBs and the search results are provided in Table 3 in the Appendix.

Overall, the RAVEN (Urban 2016) analysis yielded no temporal coincidences between GW candidates from low-latency searches and GRB triggers. With the two offline searches, we found no noteworthy individual events, nor evidence for a collective signature of weak GW signals associated with the GRB population. The distribution of observed p -values is shown in Figure 2; for GRBs with no

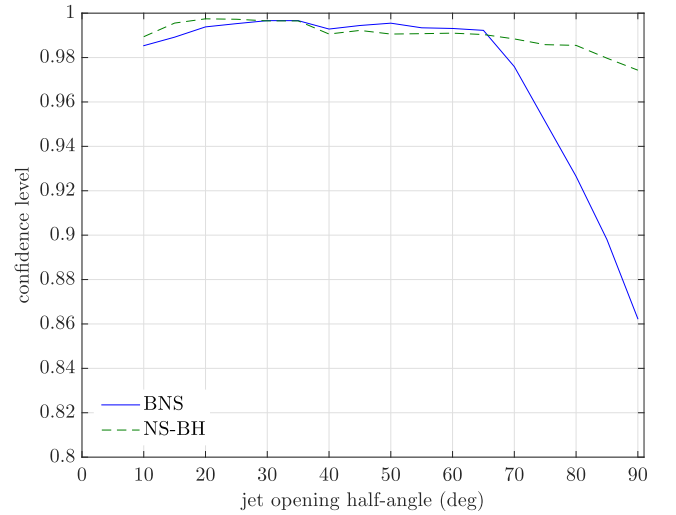


Figure 5. Exclusion confidence level for binaries at 54 Mpc from Earth as a function of the jet opening half-angle θ_{jet} of the binary. The simulated signals were performed with a uniform distribution in the cosine of the inclination angle ι , hence with a small number of cases at low ι . This causes a small decrease in confidence for jet angles below 20° due to a larger statistical uncertainty.

event in the on-source, we provide an upper bound on the p -value equal to 1 and a lower bound determined by counting the fraction of background trials that yield no event: this explains the feature in the top right corner of the top panel. These p -values are combined using the weighted binomial test (Abadie et al. 2012a) to quantitatively assess the population consistency with the no-signal hypothesis. This test looks at the lowest 5% of p -values weighted by the prior probability of detection based on the GW sensitivity at the time of and from the direction of the GRB. The NS binary (generic transient) search method yielded a combined p -value of 57% (75%).

Given that the analyses returned no significant event, we place limits on GW emission based both on binary mergers in the case of short GRBs and on generic GW transient signal models for all 42 GRBs in our sample. For a given signal morphology, the GW analysis efficiently recovers signals up to a certain distance that depends on the sensitivity of the detectors at the time and sky position of a given GRB event. We quote a 90% confidence level lower limit on the distance $D_{90\%}$ to each GRB progenitor, that is, the distance at which 90% of simulated signals are recovered with a ranking statistic that is greater than the largest value actually measured. The quoted exclusion distances are marginalized over systematic errors introduced by the mismatch of a true GW signal and the waveforms used in the simulations, and over amplitude and phase errors from the calibration of the detector data. The median exclusion distances are summarized in Table 2, while the cumulative distributions of exclusion distances for a subset of injected signal populations are shown in Figure 3. For short GRBs, the median exclusion distance is between 90 and 150 Mpc depending on the assumed NS binary progenitor, whereas for all GRBs and a generic GW signal model, the median exclusion distance is between 15 Mpc and

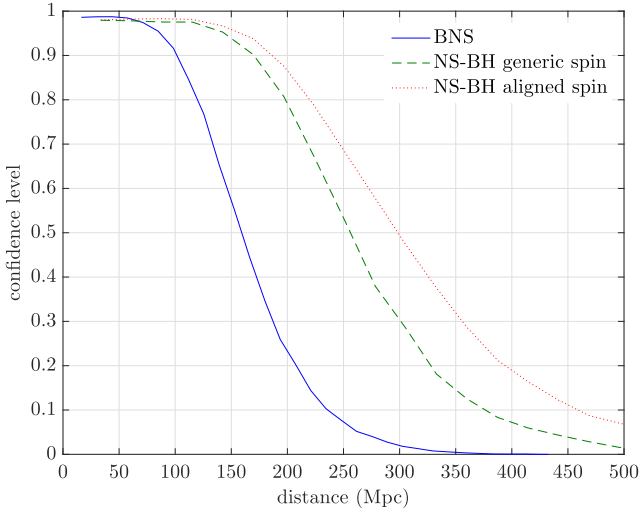


Figure 6. Exclusion confidence level for three populations of simulated binary merger signals as a function of distance, given LIGO observations at the time of GRB 150906B.

100 Mpc. The results for the NS binary search can be compared to the ranges reported in Tables 1 and 2 of Abbott et al. (2016c) for the all-time, all-sky search for GWs emitted by BNS and NS-BH systems in O1. Both searches are most sensitive to aligned-spin NS-BH binaries and least sensitive to BNS binaries. This hierarchy is determined by the masses and by the degree of spin misalignment involved in the simulated source populations: all else being equal, GW detectors are less sensitive to lower mass systems because these have smaller GW amplitudes, while searches performed with aligned spin templates progressively lose in efficiency as precession effects in the source become more and more marked. Further, as discussed by Williamson et al. (2014), the targeted, coherent search is sensitive to distances that are 20%–25% greater than those achieved by a coincident all-sky search. This explains why the distances reported here are greater than those in Abbott et al. (2016c). Clearly, this is a rough comparison because the injected populations considered here and by the all-sky all-time search are different, particularly with regards to the choice of BH masses and to the restriction set on the inclination angle.

By combining results from all analyzed GRBs, we place exclusions on GRB progenitor populations. To do this, we use a simple population model, where all GRB progenitors have the same GW emission (standard sirens), and perform exclusions on cumulative distance distributions. We parameterize the distance distribution with two components: a fraction F of GRBs distributed with a constant comoving density rate up to a luminosity distance R , and a fraction $1 - F$ at effectively infinite distance. This simple model yields a parameterization of astrophysical GRB distance distribution models that predict a uniform local rate density and a more complex dependence at redshift higher than 0.1, given that the high-redshift part of the distribution is beyond the sensitivity of current GW detectors. The exclusion is then performed in the (F, R) plane. (For details of this method, see Appendix B of Abadie et al. 2012a.) The exclusion for BNS and NS-BH

sources is shown in the top panel of Figure 4. The bottom panel instead shows the exclusion for the ADI-A model and for GW transient signals modeled as CSGs at 150 Hz, under the optimistic assumption that the energy emitted in GWs by every GRB is $E_{\text{GW}} = 10^{-2} M_{\odot} c^2$. For comparison, we plot the redshift distribution of short GRBs (or for all GRBs observed by *Swift*). In neither case does the exclusion line come close to the observed population redshift, indicating that it would have been unlikely to observe an event in this analysis.

An extrapolation of these results to 2 years of operation at Advanced LIGO design sensitivity, which is a factor of ~ 3 better than the one obtained during O1 (Abbott et al. 2016a; Martynov et al. 2016), is shown in Figure 4. For short GRBs, the observations will then probe the nearby tail of the distribution and therefore the validity of the NS binary merger origin of short GRBs. Long GRB observations, however, will only probe nearby faint GRB events at redshift ~ 0.1 , either achieving a detection from a nearby GRB or excluding that all nearby long GRBs have a very energetic GW emission with $E_{\text{GW}} \sim 10^{-2} M_{\odot} c^2$. In this respect, under the less optimistic assumption that $E_{\text{GW}} \sim 10^{-4} M_{\odot} c^2$ for all nearby long GRBs, would shift the extrapolated CSG exclusion region to redshifts that are an order of magnitude lower (see, e.g., Figure 7 in Aasi et al. 2014b). These extrapolations and conclusions are consistent with previous extrapolations (Aasi et al. 2014b).

5.1. GRB 150906B

If NGC 3313 were indeed the host of an NS binary merger progenitor of GRB 150906B, Advanced LIGO should have detected a GW signal associated with the event, given the proximity of this galaxy located at a luminosity distance of 54 Mpc from Earth. A similar hypothesis was previously tested with the initial LIGO detectors for GRB 051103 and GRB 070201, the error boxes of which overlapped the M81/M82 group of galaxies and M31, respectively (Abbott et al. 2008; Abadie et al. 2012b). In both cases, a binary merger scenario was excluded with greater than 90% confidence, and the preferred scenario is that these events were extragalactic soft-gamma-repeater flares.

The NS binary search described in Section 4.2 found no evidence for a GW signal produced at the time and sky position of GRB 150906B. The most significant candidate event in the on-source region around the time of the GRB had a p -value of 53%.

This null-detection result allows us to compute the frequentist confidence with which our search excludes a binary coalescence in NGC 3313. This confidence includes both the search efficiency at recovering signals as well as our uncertainty in measuring such efficiency. Figure 5 shows the exclusion confidence for BNS and NS-BH systems as a function of the jet half-opening angle θ_{jet} , assuming a distance¹⁵⁹ to NGC 3313 of 54 Mpc and that the NS binary inclination angle ι between the total angular momentum axis and the line of sight is distributed uniformly in $\cos \iota$ up to θ_{jet} . If we assume an isotropic (i.e., unbeamed) γ -ray emission from

¹⁵⁹ To account for the detector calibration errors in the pre-O1 stage during which GRB 150906B occurred, the simulated signals added in software to the data for this study were jittered with a Gaussian distribution of 20% in amplitude and 20° in phase.

GRB 150906B, the possibility of a BNS coalescence progenitor is excluded with $\gtrsim 86\%$ confidence. Taking a fiducial jet half-opening angle upper limit of 30° (or equivalently a maximum binary inclination angle of this size), the exclusion confidence rises to $\gtrsim 99.7\%$. NS-BH systems with isotropic emission are excluded at $\gtrsim 97\%$ confidence, which rises to $\gtrsim 99.7\%$ for $\theta_{\text{jet}} \leq 30^\circ$.

The increase in exclusion confidence for smaller jet angles is due to the fact that the average amplitude of the GW signal from an NS binary coalescence is larger for systems for which the orbital plane is viewed “face-on” (where the detector receives the flux from both GW polarizations) than for systems viewed “edge-on” (where the detector receives the flux from just one GW polarization); small jet angles imply a system closer to face-on.

To determine the distance up to which we can exclude, with 90% confidence, a binary coalescence as the progenitor of GRB 150906B, we assume beamed emission with a maximum opening angle of 30° and compute the distance at which 90% of injected BNS, generic spin NS-BH, and aligned spin NS-BH signals are recovered louder than the loudest on-source event. The result is shown in Figure 6. BNS systems are excluded with 90% confidence out to a distance of 102 Mpc, while generic and aligned spin NS-BH systems are excluded with the same confidence at 170 Mpc and 186 Mpc, respectively. This is consistent with theoretical arguments based on γ -ray spectrum and fluence that place the progenitor of GRB 150906B at more than 270 Mpc (Ruffini et al. 2015; Zhang et al. 2015), possibly in one of the several known galaxies at around 500 Mpc within the error region (Bilicki et al. 2013).

6. Conclusion

We have analyzed data from O1 to look for GWs coincident with GRBs that occurred during this period, using both a modeled search for BNS and NS-BH systems and an unmodeled search for GW transients. No GW was detected in coincidence with a GRB by either search. We set lower limits on the distance for each GRB for various GW emission models. The median of these distance limits is higher than distance limits placed by all previous modeled and unmodeled searches (e.g., Abadie et al. 2012a; Aasi et al. 2014b). We also combined these lower limits into an exclusion on the GRB redshift distribution. This exclusion is a factor of a few away from the short and long GRB distributions measured by γ -ray satellites.

With 2 years of observation at design sensitivity, Advanced LIGO will probe the observed redshift distribution. At that point, either a GW detection in association with a short GRB will take place, or the result will be in tension with the NS binary merger progenitor scenario for short GRBs. For long GRBs, a lack of detection would only constrain the most extreme scenarios of GW emission from a strongly rotating stellar core collapse.

We also analyzed data from the LIGO Hanford detector to look for a GW signal associated with GRB 150906B. No evidence was found for a GW signal associated with this GRB. The sensitivity of the modeled search allows us to confidently

exclude the hypothesis that an NS binary in NGC 3313 was the progenitor of GRB 150906B. If the event indeed occurred in NGC 3313, then it would have had to defy the setup of the modeled search. In this case, and in light of the problematic classification of GRB 150906B discussed in Section 2, this GRB may most probably have been due to a stellar core collapse or a giant flare from a soft-gamma repeater. Alternatively, GRB 150906B may have simply originated from an NS binary merger in one of the more distant galaxies at 500 Mpc, compatible with the sky location of the event.

The authors gratefully acknowledge the support of the United States National Science Foundation (NSF) for the construction and operation of the LIGO Laboratory and Advanced LIGO as well as the Science and Technology Facilities Council (STFC) of the United Kingdom, the Max-Planck-Society (MPS), and the State of Niedersachsen/Germany for support of the construction of Advanced LIGO and construction and operation of the GEO600 detector. Additional support for Advanced LIGO was provided by the Australian Research Council. The authors gratefully acknowledge the Italian Istituto Nazionale di Fisica Nucleare (INFN), the French Centre National de la Recherche Scientifique (CNRS), and the Foundation for Fundamental Research on Matter supported by the Netherlands Organisation for Scientific Research for the construction and operation of the Virgo detector and the creation and support of the EGO consortium. The authors also gratefully acknowledge research support from these agencies as well as by the Council of Scientific and Industrial Research of India, Department of Science and Technology, India, Science & Engineering Research Board (SERB), India, Ministry of Human Resource Development, India, the Spanish Ministerio de Economía y Competitividad, the Conselleria d’Economia i Competitivitat and Conselleria d’Educació Cultura i Universitats of the Govern de les Illes Balears, the National Science Centre of Poland, the European Commission, the Royal Society, the Scottish Funding Council, the Scottish Universities Physics Alliance, the Hungarian Scientific Research Fund (OTKA), the Lyon Institute of Origins (LIO), the National Research Foundation of Korea, Industry Canada and the Province of Ontario through the Ministry of Economic Development and Innovation, the Natural Science and Engineering Research Council Canada, Canadian Institute for Advanced Research, the Brazilian Ministry of Science, Technology, and Innovation, Fundação de Amparo à Pesquisa do Estado de São Paulo (FAPESP), Russian Foundation for Basic Research, the Leverhulme Trust, the Research Corporation, Ministry of Science and Technology (MOST), Taiwan and the Kavli Foundation. The authors gratefully acknowledge the support of the NSF, STFC, MPS, INFN, CNRS, and the State of Niedersachsen/Germany for provision of computational resources. K. Hurley is grateful for IPN support under NASA grant NNX15AU74G. R.L. Apteekar and S.V. Golenetskii gratefully acknowledge support from RFBR grants 15-02-00532-i and 16-29-13009-ofi-m.

Appendix Results Table

Table 3
Analyzed GRB Sample and Search Results

GRB Name	UTC Time	R.A.	Decl.	Satellite(s)	Type	Network	BNS	$D_{90\%}$ (Mpc)			
								NS-BH		GW Burst	
								Generic Spins	Aligned Spins	ADI A	CSG 150 Hz
150906B	08:42:25	10 ^h 36 ^m 57 ^s	−25°36′	IPN	Ambiguous	H1	102	170	186
150912600	14:24:31	21 ^h 25 ^m 26 ^s	73°16′	<i>Fermi</i>	Short	H1L1	88	150	150	28	71
150912A	10:37:38	16 ^h 33 ^m 46 ^s	−21°02′	<i>Fermi</i>	Long	H1L1	47	113
150919A	20:43:18	08 ^h 51 ^m 50 ^s	44°04′	IPN	Short	H1	58	83	102
150922883	21:11:32	18 ^h 16 ^m 34 ^s	−50°28′	<i>Fermi</i>	Ambiguous	H1L1	71	122	122
150922A	05:37:29	19 ^h 31 ^m 50 ^s	−2°15′	<i>Fermi</i>	Short	H1L1	100	163	183	27	69
150923297	07:07:36	21 ^h 07 ^m 12 ^s	31°49′	<i>Fermi</i>	Short	H1L1	98	144	187	33	88
150923429	10:18:17	17 ^h 51 ^m 14 ^s	−40°40′	<i>Fermi</i>	Short	H1L1	136	213	241	41	97
150925A	04:09:28	15 ^h 10 ^m 08 ^s	−19°38′	<i>Swift</i>	Long	H1L1 [†]	23	50
151001348	08:20:35	16 ^h 26 ^m 57 ^s	−10°08′	<i>Fermi</i>	Long	H1L1 [†]	33	81
151006A	09:55:01	9 ^h 49 ^m 42 ^s	70°30′	<i>Swift</i>	Long	H1L1 [†]	31	64
151009949	22:47:03	14 ^h 48 ^m 00 ^s	63°43′	<i>Fermi</i>	Long	H1L1	42	95
151019	08:05:28	6 ^h 37 ^m 49 ^s	79°08′	IPN	Long	H1L1	15	30
151022577	13:51:02	7 ^h 21 ^m 28 ^s	40°14′	<i>Fermi</i>	Short	H1L1	115	179	206	47	102
151022A	14:06:32	23 ^h 16 ^m 47 ^s	55°49′	<i>Swift</i>	Long	H1L1 [†]	25	58
151023A	13:43:04	18 ^h 03 ^m 56 ^s	−8°19′	<i>Swift</i>	Long	H1L1	35	80
151024179	04:17:53	15 ^h 31 ^m 26 ^s	22°57′	<i>Fermi</i>	Ambiguous	H1	25	30	48
151027B	22:40:40	5 ^h 04 ^m 52 ^s	−6°27′	<i>Swift</i>	Long	H1L1 [†]	40	102
151029A	07:49:39	2 ^h 34 ^m 08 ^s	−35°21′	<i>Swift</i>	Long	H1L1	16	35
151107B	20:24:52	2 ^h 05 ^m 12 ^s	45°35′	<i>Fermi</i>	Long	H1L1 [†]	4	9
151112A	13:44:48	0 ^h 08 ^m 12 ^s	−61°40′	<i>Swift</i>	Long	H1L1	37	100
151114A	09:59:50	8 ^h 03 ^m 45 ^s	−61°03′	<i>Swift</i>	Ambiguous	L1	42	61	75
151117	01:37:03	1 ^h 44 ^m 32 ^s	18°39′	IPN	Long	H1L1	33	77
151121	06:56:27	19 ^h 35 ^m 22 ^s	7°20′	IPN	Short	H1L1	32	59
151126	04:03:03	13 ^h 05 ^m 20 ^s	0°07′	IPN	Short	H1L1	122	203	217	35	78
151127A	09:08:49	1 ^h 17 ^m 54 ^s	−82°46′	<i>Swift</i>	Short	H1L1	97	152	165	33	78
151130160	03:50:50	9 ^h 05 ^m 04 ^s	−18°49′	<i>Fermi</i>	Long	H1L1	18	62
151202565	13:33:49	21 ^h 45 ^m 58 ^s	−24°40′	<i>Fermi</i>	Short	H1	121	198	226
151218857	20:33:31	0 ^h 37 ^m 48 ^s	−30°44′	<i>Fermi</i>	Ambiguous	H1L1	21	38	35
151219	09:11:16	14 ^h 34 ^m 01 ^s	12°57′	IPN	Long	H1L1	24	55
151219567	13:36:22	23 ^h 24 ^m 45 ^s	11°22′	<i>Fermi</i>	Long	H1L1 [†]	32	71
151222A	08:10:13	23 ^h 40 ^m 43 ^s	36°42′	<i>Fermi</i>	Short	H1L1	59	96	104	22	38
151227A	01:44:07	13 ^h 42 ^m 00 ^s	65°52′	<i>Fermi</i>	Ambiguous	H1L1	57	97	108	23	56
151227B	05:13:48	19 ^h 11 ^m 33 ^s	31°56′	<i>Fermi</i>	Long	H1L1	22	53
151228A	03:05:12	14 ^h 16 ^m 01 ^s	−17°41′	<i>Swift</i>	Short	H1	122	169	200
151229486	11:40:06	23 ^h 05 ^m 58 ^s	6°55′	<i>Fermi</i>	Short	H1	57	86	93
151231A	10:37:47	4 ^h 22 ^m 31 ^s	−61°32′	<i>Fermi</i>	Long	H1L1 [†]	27	75
151231B	13:38:08	10 ^h 00 ^m 19 ^s	28°49′	<i>Fermi</i>	Short	L1	58	85	96
160101A	00:43:53	14 ^h 38 ^m 36 ^s	−13°49′	<i>Fermi</i>	Long	H1L1	35	107
160103	17:39:04	13 ^h 14 ^m 53 ^s	−23°26′	IPN	Long	H1L1	22	42
160111115	02:45:03	20 ^h 40 ^m 57 ^s	−32°47′	<i>Fermi</i>	Long	H1L1	24	59
160111A	07:22:02	03 ^h 02 ^m 31 ^s	28°51′	IPN	Short	H1	91	135	151

Notes. Information and limits on associated GW emission for each of the analyzed GRBs. The first six columns are as follows: the GRB name in YYMMDD format, the trigger time, the sky position used for the GW search (R.A. and decl.), the satellite whose sky localization is used, and the GRB classification type. The seventh column gives the GW detector network used: here H1 refers to the interferometer in Hanford, WA, and L1 to the one in Livingston, LA; a † denotes cases in which the on-source window of the generic transient search is extended to cover the GRB duration ($T_{90} > 60$ s). Columns 8–12 display the 90% confidence lower limits on the exclusion distance to the GRB ($D_{90\%}$) for several emission scenarios: BNS, generic and aligned spin NS-BH, accretion disk instability (ADI)-A, and circular sine-Gaussian (CSG) GW burst at 150 Hz with total radiated energy $E_{\text{GW}} = 10^{-2} M_{\odot} c^2$. When the use of only the generic transient or the NS binary search method was possible, only a subset of exclusion distances is shown. For GRB 150922883 and GRB 151218857, there were not enough data from both LIGO detectors to run the generic GW transient search, so results are reported for the NS binary coalescence search only. The short GRB 151121 was localized by the IPN with an error box area of about 106 square degrees; it was therefore not analyzed with the modeled search due to the high computational costs this would have required and the negligible increase in sensitivity rendered by a targeted search (Aasi et al. 2014b).

References

Aasi, J., Abadie, J., Abbott, B. P., et al. 2013, *PhRvD*, **88**, 122004
Aasi, J., Abbott, B. P., Abbott, R., et al. 2014a, *PhRvD*, **89**, 122004
Aasi, J., Abbott, B. P., Abbott, R., et al. 2014b, *PhRvL*, **113**, 011102

Abadie, J., Abbott, B. P., Abbott, R., et al. 2010, *ApJ*, **715**, 1453
Abadie, J., Abbott, B. P., Abbott, R., et al. 2012a, *ApJ*, **760**, 12
Abadie, J., Abbott, B. P., Abbott, T. D., et al. 2012b, *ApJ*, **755**, 2
Abbott, B. P., Abbott, R., Abbott, T. D., et al. 2016a, *LRR*, **19**, 1
Abbott, B. P., Abbott, R., Abbott, T. D., et al. 2016b, *PhRvD*, **93**, 042005

- Abbott, B. P., Abbott, R., Abbott, T. D., et al. 2016c, *ApJL*, **832**, 21
- Abbott, B. P., Abbott, R., Abbott, T. D., et al. 2016d, *PhRvX*, **6**, 041015
- Abbott, B. P., Abbott, R., Abbott, T. D., et al. 2016e, *ApJS*, **225**, 8
- Abbott, B. P., Abbott, R., Abbott, T. D., et al. 2016f, *CQGra*, **33**, 134001
- Abbott, B. P., Abbott, R., Abbott, T. D., et al. 2016g, *PhRvL*, **116**, 131103
- Abbott, B. P., Abbott, R., Abbott, T. D., et al. 2016h, *PhRvL*, **116**, 241103
- Abbott, B. P., Abbott, R., Abbott, T. D., et al. 2016i, *ApJ*, **826**, L13
- Abbott, B. P., Abbott, R., Abbott, T. D., et al. 2016j, *PhRvL*, **116**, 061102
- Abbott, B. P., Abbott, R., Abbott, T. D., et al. 2017a, *PhRvD*, **95**, 042003
- Abbott, B. P., Abbott, R., Abbott, T. D., et al. 2017b, *PhRvD*, **95**, 062003
- Abbott, B. P., Abbott, R., Acernese, F., et al. 2010, *ApJ*, **715**, 1438
- Abbott, B. P., Abbott, R., Adhikari, R., et al. 2008, *ApJ*, **681**, 1419
- Adams, T., Buskulic, D., Germain, V., et al. 2016, *CQGra*, **33**, 175012
- Allen, B. 2005, *PhRvD*, **71**, 062001
- Aloy, M. A., Mueller, E., Ibanez, J. M., Marti, J. M., & MacFadyen, A. 2000, *ApJL*, **531**, L119
- Anderson, W. G., Brady, P. R., Creighton, J. D. E., & Flanagan, E. E. 2001, *PhRvD*, **63**, 042003
- Antoniadis, J., Freire, P. C. C., Wex, N., et al. 2013, *Sci*, **340**, 6131
- Barkett, K., Scheel, M. A., Haas, R., et al. 2016, *PhRvD*, **93**, 044064
- Belczynski, K., Bulik, T., Mandel, I., et al. 2013, *ApJ*, **764**, 96
- Belczynski, K., Buonanno, A., Cantiello, M., et al. 2014, *ApJ*, **789**, 120
- Berger, E. 2011, *NewAR*, **55**, 1
- Berger, E. 2014, *ARA&A*, **52**, 43
- Berger, E., Fong, W., & Chornock, R. 2013, *ApJL*, **774**, L23
- Bernuzzi, S., Dietrich, T., & Nagar, A. 2015, *PhRvL*, **115**, 091101
- Bilicki, M., Jarrett, T. H., Peacock, J. A., Cluver, M. E., & Steward, L. 2013, arXiv:1311.5246
- Bilicki, M., Jarrett, T. H., Peacock, J. A., Cluver, M. E., & Steward, L. 2014, *ApJS*, **210**, 9
- Blanchet, L., Iyer, B. R., Will, C. M., & Wiseman, A. G. 1996, *CQGra*, **13**, 575
- Blandford, R. D., & Znajek, R. L. 1977, *MNRAS*, **179**, 433
- Brown, D. A., Harry, I., Lundgren, A., & Nitz, A. H. 2012, *PhRvD*, **86**, 084017
- Buonanno, A., Chen, Y., & Vallisneri, M. 2003, *PhRvD*, **67**, 104025 [Erratum: *PhRvD*, **74**, 029904 (2006)]
- Burgay, M., D'Amico, N., Possenti, A., et al. 2003, *Natur*, **426**, 531
- Burlon, D., Ghirlanda, G., Ghisellini, G., et al. 2008, *ApJL*, **685**, L19
- Burlon, D., Ghirlanda, G., Ghisellini, G., Greiner, J., & Celotti, A. 2009, *A&A*, **505**, 569
- Chen, H.-Y., & Holz, D. E. 2013, *PhRvL*, **111**, 181101
- Chen, W.-X., & Beloborodov, M. 2007, *ApJ*, **657**, 383
- Clark, J., Evans, H., Fairhurst, S., et al. 2015, *ApJ*, **809**, 53
- Corsi, A., & Meszaros, P. 2009, *ApJ*, **702**, 1171
- Coyne, R. 2015, PhD thesis, The George Washington Univ.
- Davies, M. B., King, A., Rosswog, S., & Wynn, G. 2002, *ApJL*, **579**, L63
- de Mink, S. E., & Belczynski, K. 2015, *ApJ*, **814**, 58
- Della Valle, M., Chincarini, G., Panagia, N., et al. 2006, *Natur*, **444**, 1050
- Eichler, D., Livio, M., Piran, T., & Schramm, D. N. 1989, *Natur*, **340**, 126
- Farr, W. M., Sravan, N., Cantrell, A., et al. 2011, *ApJ*, **741**, 103
- Fong, W., Berger, E., Margutti, R., & Zauderer, B. A. 2015, *ApJ*, **815**, 102
- Fong, W.-F., & Berger, E. 2013, *ApJ*, **776**, 18
- Fong, W. F., Berger, E., Chornock, R., et al. 2013, *ApJ*, **769**, 56
- Fryer, C. L., Holz, D. E., & Hughes, S. A. 2002, *ApJ*, **565**, 430
- Fynbo, J. P. U., Watson, D., Thöne, C. C., et al. 2006, *Natur*, **444**, 1047
- Galama, T. J., Vreeswijk, P. M., van Paradijs, J., et al. 1998, *Natur*, **395**, 670
- Gal-Yam, A., Fox, D. B., Price, P. A., et al. 2006, *Natur*, **444**, 1053
- Gal-Yam, A., Ofek, E. O., Poznanski, D., et al. 2006, *ApJ*, **639**, 331
- Gehrels, N., Norris, J. P., Barthelmy, S. D., et al. 2006, *Natur*, **444**, 1044
- Golenetskii, S., Aptekar, R., Frederiks, D., et al. 2015, GCN, 18259
- Gruber, D., Goldstein, A., Weller von Ahlefeld, V., et al. 2014, *ApJS*, **211**, 12
- Grupe, D., Burrows, D. N., Patel, S. K., et al. 2006, *ApJ*, **653**, 462
- Haas, R., Ott, C. D., Szilagyi, B., et al. 2016, *PhRvD*, **93**, 124062
- Hannam, M., Brown, D. A., Fairhurst, S., Fryer, C. L., & Harry, I. W. 2013, *ApJL*, **766**, L14
- Harry, I. W., & Fairhurst, S. 2011, *PhRvD*, **83**, 084002
- Harry, I. W., Nitz, A. H., Brown, D. A., et al. 2014, *PhRvD*, **89**, 024010
- Hessels, J. W. T., Ransom, S. M., Stairs, I. H., et al. 2006, *Sci*, **311**, 1901
- Hinderer, T., Taracchini, A., Foucart, F., et al. 2016, *PhRvL*, **116**, 181101
- Hjorth, J., & Bloom, J. S. 2011, *Gamma-Ray Bursts* (Cambridge: Cambridge Univ. Press) (Chapter 9)
- Hurley, K., Cline, T., Mitrofanov, I., et al. 2003, in AIP Conf. Proc. 662, *Gamma-Ray Burst and Afterglow Astronomy 2001: a Workshop celebrating the First Year of the HETE Mission* (Melville, NY: AIP), 473
- Hurley, K., Mitrofanov, I. G., Golovin, D., et al. 2015, GCN, 18258
- Iwamoto, K., Mazzali, P. A., Nomoto, K., et al. 1998, *Natur*, **395**, 672
- Jakobsson, P., Hjorth, J., Malesani, D., et al. 2012, *ApJ*, **752**, 62
- Jakobsson, P., Levan, A., Fynbo, J. P. U., et al. 2006, *A&A*, **447**, 897
- Kalogera, V., & Baym, G. 1996, *ApJL*, **470**, L61
- Khan, S., Husa, S., Hannam, M., et al. 2016, *PhRvD*, **93**, 044007
- Kiuchi, K., Sekiguchi, Y., Kyutoku, K., et al. 2015, *PhRvD*, **92**, 064034
- Kiziltan, B., Kottas, A., De Yoreo, M., & Thorsett, S. E. 2013, *ApJ*, **778**, 66
- Klimenko, S., Vedovato, G., Drago, M., et al. 2016, *PhRvD*, **93**, 042004
- Kobayashi, S., & Meszaros, P. 2003, *ApJ*, **589**, 861
- Koshut, T. M., Kouveliotou, C., Paciesas, W. S., et al. 1995, *ApJ*, **452**, 145
- Kramer, M., & Wex, N. 2009, *CQGra*, **26**, 073001
- Kreidberg, L., Bailyn, C. D., Farr, W. M., & Kalogera, V. 2012, *ApJ*, **757**, 36
- Kulkarni, S. R., Frail, D. A., Wieringa, M. H., et al. 1998, *Natur*, **395**, 663
- Kyutoku, K., Shibata, M., & Taniguchi, K. 2010, *PhRvD*, **82**, 044049 [Erratum: *PhRvD*, **84**, 049902 (2011)]
- Lackey, B. D., Kyutoku, K., Shibata, M., Brady, P. R., & Friedman, J. L. 2014, *PhRvD*, **89**, 043009
- Lattimer, J. M. 2012, *ARNPS*, **62**, 485
- Lazzati, D. 2005, *MNRAS*, **357**, 722
- Lazzati, D., Morsony, B. J., & Begelman, M. 2009, *ApJL*, **700**, L47
- Lee, W. H., & Ramirez-Ruiz, E. 2007, *NJPh*, **9**, 17
- Lee, W. H., Ramirez-Ruiz, E., & Page, D. 2005, *ApJ*, **632**, 421
- Leibler, C. N., & Berger, E. 2010, *ApJ*, **725**, 1202
- Levan, A. J., Tanvir, N. R., & Hjorth, J. 2015, GCN, 18263
- Lien, A., Sakamoto, T., Barthelmy, S. D., et al. 2016, *ApJ*, **829**, 7
- Lynch, R., Vitale, S., Essick, R., Katsavounidis, E., & Robinet, F. 2015, arXiv:1511.05955
- Lynch, R. S., Freire, P. C. C., Ransom, S. M., & Jacoby, B. A. 2012, *ApJ*, **745**, 109
- MacFadyen, A. I., Woosley, S. E., & Heger, A. 2001, *ApJ*, **550**, 410
- Martynov, D. V., Hall, E. D., Abbott, B. P., et al. 2016, *PhRvD*, **93**, 112004
- McClintock, J. E., Narayan, R., & Steiner, J. F. 2014, *SSRv*, **183**, 295
- Messick, C., Blackburn, K., Brady, P., et al. 2017, *PhRvD*, **95**, 042001
- Miller, M. C., & Miller, J. M. 2014, *PhR*, **548**, 1
- Modjaz, M. 2011, *AJ*, **332**, 434
- Mösta, P., Ott, C. D., Radice, D., et al. 2015, *Natur*, **528**, 376
- Nakar, E. 2007, *PhR*, **442**, 166
- Narayan, R., Paczynski, B., & Piran, T. 1992, *ApJL*, **395**, L83
- Nitz, A., Harry, I., Biwer, C. M., et al. 2016, ligo-cbc/pycbc: ER10 Production Release 6, Zenodo, doi:10.5281/zenodo.168077
- Nitz, A. H. 2015, PhD thesis, Syracuse Univ.
- Nitz, A. H., Lundgren, A., Brown, D. A., et al. 2013, *PhRvD*, **88**, 124039
- Norris, J. P., & Bonnell, J. T. 2006, *ApJ*, **643**, 266
- Norris, J. P., Gehrels, N., & Scargle, J. D. 2010, *ApJ*, **717**, 411
- Norris, J. P., Gehrels, N., & Scargle, J. D. 2011, *ApJ*, **735**, 23
- Nuttall, L., Massinger, T. J., & Areeda, J. o. 2015, *CQGra*, **32**, 245005
- Ott, C. D. 2009, *CQGra*, **26**, 063001
- Ott, C. D., & Santamaría, L. 2013, *Gravitational Wave Emission from Accretion Disk Instabilities—Analytic Models*, Tech. rep., LIGO-T1100093
- Owen, B. J., & Sathyaprakash, B. S. 1999, *PhRvD*, **60**, 022002
- Ozel, F., & Freire, P. 2016, *ARA&A*, **54**, 401
- Ozel, F., Psaltis, D., Narayan, R., & McClintock, J. E. 2010, *ApJ*, **725**, 1918
- Ozel, F., Psaltis, D., Narayan, R., & Villarreal, A. S. 2012, *ApJ*, **757**, 55
- Paczynski, B. 1991, *AcA*, **41**, 257
- Pannarale, F., Berti, E., Kyutoku, K., Lackey, B. D., & Shibata, M. 2015, *PhRvD*, **92**, 084050
- Pannarale, F., & Ohme, F. 2014, *ApJL*, **791**, L7
- Piro, A. L., & Pfahl, E. 2007, *ApJ*, **658**, 1173
- Racusin, J. L., Liang, E. W., Burrows, D. N., et al. 2009, *ApJ*, **698**, 43
- Rezzolla, L., Giacomazzo, B., Baiotti, L., et al. 2011, *ApJL*, **732**, L6
- Rhoades, C. E., Jr., & Ruffini, R. 1974, *PhRvL*, **32**, 324
- Romero, G. E., Reynoso, M. M., & Christiansen, H. R. 2010, *A&A*, **524**, A4
- Rosswog, S., & Ramirez-Ruiz, E. 2002, *MNRAS*, **336**, L7
- Ruffini, R., Bianco, C. L., Enderli, M., et al. 2015, GCN, 18296
- Sakamoto, T., Barthelmy, S. D., Baumgartner, W. H., et al. 2011, *ApJS*, **195**, 2
- Shibata, M., Karino, S., & Eriguchi, Y. 2003, *MNRAS*, **343**, 619
- Siellez, K., Boër, M., Gendre, B., & Regimbau, T. 2016, arXiv:1606.03043
- Steiner, A. W., Lattimer, J. M., & Brown, E. F. 2013, *ApJL*, **765**, L5
- Sutton, P. J., Jones, G., Chatterji, S., et al. 2010, *NJPh*, **12**, 053034

- Svinkin, D., Frederiks, D., & Pal'Shin, V. 2015, GCN, [18321](#)
- Tanvir, N. R., Levan, A. J., Fruchter, A. S., et al. 2013, [Natur](#), **500**, 547
- Taracchini, A., Buonanno, A., Pan, Y., et al. 2014, [PhRvD](#), **89**, 061502
- Tuyenbayev, D., Karki, S., Betzwieser, J., et al. 2017, [CQG](#), **34**, 015002
- Urban, A. L. 2016, PhD thesis, Univ. Wisconsin-Milwaukee
- van Putten, M. H. P. M. 2001, [PhRvL](#), **87**, 091101
- van Putten, M. H. P. M., Lee, G. M., Della Valle, M., Amati, L., & Levinson, A. 2014, [MNRAS](#), **444**, L58
- van Putten, M. H. P. M., Levinson, A., Lee, H. K., et al. 2004, [PhRvD](#), **69**, 044007
- Vedrenne, G., & Atteia, J.-L. 2009, *Gamma-Ray Bursts: The Brightest Explosions in the Universe* (Berlin: Springer)
- von Kienlin, A., Meegan, C. A., Paciesas, W. S., et al. 2014, [ApJS](#), **211**, 13
- Wang, X.-Y., & Meszaros, P. 2007, [ApJ](#), **670**, 1247
- Was, M., Sutton, P. J., Jones, G., & Leonor, I. 2012, [PhRvD](#), **86**, 022003
- Wiktorowicz, G., Belczynski, K., & Maccarone, T. J. 2013, arXiv:1312.5924
- Williamson, A., Biwer, C., Fairhurst, S., et al. 2014, [PhRvD](#), **90**, 122004
- Woosley, S. E., & Bloom, J. S. 2006, [ARA&A](#), **44**, 507
- Zhang, F.-W., Zhang, B., & Zhang, B. 2015, GCN, [18298](#)
- Zhang, W., Woosley, S. E., & MacFadyen, A. I. 2003, [ApJ](#), **586**, 356

Appendix G

Gravitational Waves and Gamma-Rays from a Binary Neutron Star Merger: GW170817 and GRB 170817A



Gravitational Waves and Gamma-Rays from a Binary Neutron Star Merger: GW170817 and GRB 170817A

LIGO Scientific Collaboration and Virgo Collaboration, *Fermi* Gamma-ray Burst Monitor, and INTEGRAL
(See the end matter for the full list of authors.)

Received 2017 October 6; revised 2017 October 9; accepted 2017 October 9; published 2017 October 16

Abstract

On 2017 August 17, the gravitational-wave event GW170817 was observed by the Advanced LIGO and Virgo detectors, and the gamma-ray burst (GRB) GRB 170817A was observed independently by the *Fermi* Gamma-ray Burst Monitor, and the Anti-Coincidence Shield for the Spectrometer for the *International Gamma-Ray Astrophysics Laboratory*. The probability of the near-simultaneous temporal and spatial observation of GRB 170817A and GW170817 occurring by chance is 5.0×10^{-8} . We therefore confirm binary neutron star mergers as a progenitor of short GRBs. The association of GW170817 and GRB 170817A provides new insight into fundamental physics and the origin of short GRBs. We use the observed time delay of $(+1.74 \pm 0.05)$ s between GRB 170817A and GW170817 to: (i) constrain the difference between the speed of gravity and the speed of light to be between -3×10^{-15} and $+7 \times 10^{-16}$ times the speed of light, (ii) place new bounds on the violation of Lorentz invariance, (iii) present a new test of the equivalence principle by constraining the Shapiro delay between gravitational and electromagnetic radiation. We also use the time delay to constrain the size and bulk Lorentz factor of the region emitting the gamma-rays. GRB 170817A is the closest short GRB with a known distance, but is between 2 and 6 orders of magnitude less energetic than other bursts with measured redshift. A new generation of gamma-ray detectors, and subthreshold searches in existing detectors, will be essential to detect similar short bursts at greater distances. Finally, we predict a joint detection rate for the *Fermi* Gamma-ray Burst Monitor and the Advanced LIGO and Virgo detectors of 0.1–1.4 per year during the 2018–2019 observing run and 0.3–1.7 per year at design sensitivity.

Key words: binaries: close – gamma-ray burst: general – gravitational waves

1. Introduction and Background

GW170817 and GRB 170817A mark the discovery of a binary neutron star (BNS) merger detected both as a gravitational wave (GW; LIGO Scientific Collaboration & Virgo Collaboration 2017a) and a short-duration gamma-ray burst (SGRB; Goldstein et al. 2017; Savchenko et al. 2017b). Detecting GW radiation from the coalescence of BNS and neutron star (NS)–black hole (BH) binary systems has been a major goal (Abbott et al. 2017a) of the LIGO (Aasi et al. 2015) and Virgo (Acernese et al. 2015) experiments. This was at least partly motivated by their promise of being the most likely sources of simultaneously detectable GW and electromagnetic (EM) radiation from the same source. This is important as joint detections enable a wealth of science unavailable from either messenger alone (Abbott et al. 2017f). BNS mergers are predicted to yield signatures across the EM spectrum (Metzger & Berger 2012; Piran et al. 2013), including SGRBs (Blinnikov et al. 1984; Paczynski 1986; Eichler et al. 1989; Paczynski 1991; Narayan et al. 1992), which produce prompt emission in gamma-rays and longer-lived afterglows.

A major astrophysical implication of a joint detection of an SGRB and of GWs from a BNS merger is the confirmation that these binaries are indeed the progenitors of at least some SGRBs. GRBs are classified as short or long depending on the duration of their prompt gamma-ray emission. This cut is based on spectral differences in gamma-rays and the bimodality of the observed

distribution of these durations (Dezalay et al. 1992; Kouveliotou et al. 1993). This empirical division was accompanied by hypotheses that the two classes have different progenitors. Long GRBs have been firmly connected to the collapse of massive stars through the detection of associated Type Ibc core-collapse supernovae (see Galama et al. 1998, as well as Hjorth & Bloom 2012 and references therein). Prior to the results reported here, support for the connection between SGRBs and mergers of BNSs (or NS–BH binaries) came only from indirect observational evidence (Nakar 2007; Berger et al. 2013; Tanvir et al. 2013; Berger 2014), population synthesis studies (Bloom et al. 1999; Fryer et al. 1999; Belczynski et al. 2006), and numerical simulations (e.g., Aloy et al. 2005; Rezzolla et al. 2011; Kiuchi et al. 2015; Baiotti & Rezzolla 2017; Kawamura et al. 2016; Ruiz et al. 2016). The unambiguous joint detection of GW and EM radiation from the same event confirms that BNS mergers are progenitors of (at least some) SGRBs.

In Section 2 we describe the independent observations of GW170817 by the LIGO–Virgo and of GRB 170817A by the *Fermi* Gamma-ray Burst Monitor (GBM) and by the Spectrometer on board *INTEGRAL* Anti-Coincidence Shield (SPi-ACS). In Section 3 we establish the firm association between GW170817 and GRB 170817A. In Section 4 we explore the constraints on fundamental physics that can be obtained from the time separation between the GW and EM signals. In Section 5 we explore the implications of the joint detection of GW170817 and GRB 170817A on the SGRB engine and the NS equation of state (EOS). In Section 6 we explore the implications of the comparative dimness of GRB 170817A relative to the known SGRB population and revise the

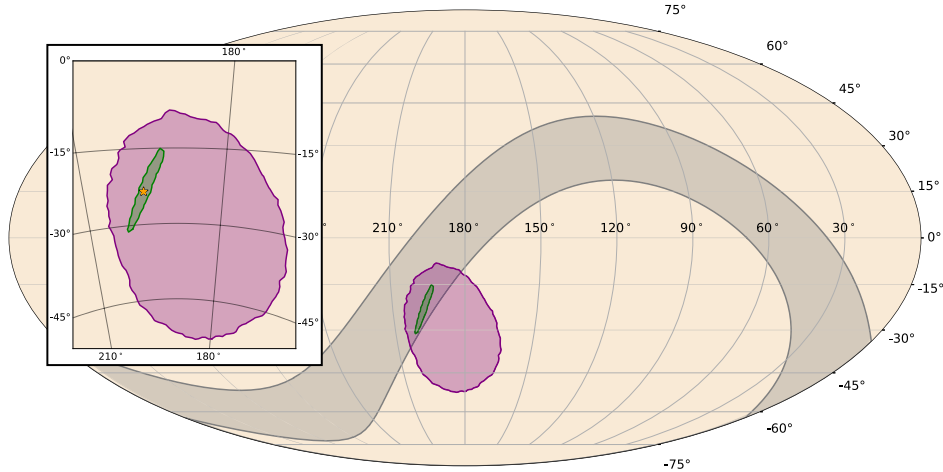


Figure 1. Final localizations. The 90% contour for the final sky-localization map from LIGO–Virgo is shown in green (LIGO Scientific Collaboration & Virgo Collaboration 2017a, 2017b, 2017c). The 90% GBM targeted search localization is overlaid in purple (Goldstein et al. 2017). The 90% annulus determined with *Fermi* and *INTEGRAL* timing information is shaded in gray (Svinkin et al. 2017). The zoomed inset also shows the position of the optical transient marked as a yellow star (Abbott et al. 2017f; Coulter et al. 2017a, 2017b). The axes are R.A. and decl. in the Equatorial coordinate system.

expectation rates for joint BNS–SGRB detections in the light of this discovery.

2. Observational Results

The observations of GW170817 and of GRB 170817A are described in detail in Abbott et al. (2017e), Goldstein et al. (2017), and Savchenko et al. (2017b). Here we summarize the observations relevant to the results presented in this Letter and report the results of two fully coherent searches for GWs from the sky location of GRB 170817A. For convenience, all measurements of time have been converted to their geocentric equivalent.

2.1. LIGO–Virgo Observation of GW170817

GW170817 is a GW signal from the inspiral of two low-mass compact objects and is the first GW observation consistent with a BNS coalescence (Abbott et al. 2017e, 2017f). GW170817 was first observed by a low-latency search (Cannon et al. 2012; Messick et al. 2017) on 2017 August 17 at 12:41:04 UTC as a single-detector trigger in the LIGO-Hanford detector (Abbott et al. 2017e; LIGO Scientific Collaboration & Virgo Collaboration 2017a). The temporal proximity of GRB 170817A was immediately identified by automatic comparison of the *Fermi*–GBM Gamma-ray Coordinates Network notice to the GW trigger (Urban 2016). Rapid offline re-analysis (Usman et al. 2016; Nitz et al. 2017b) of data from the LIGO/Virgo network confirmed the presence of a significant coincident signal in the LIGO GW detectors with a combined signal-to-noise ratio (S/N) of 32.4. The combination of observations from the LIGO and Virgo detectors allowed a precise sky position localization to an area of 28 deg^2 at 90% probability shown in green in Figure 1 (Abbott et al. 2017e; LIGO Scientific Collaboration & Virgo Collaboration 2017b). A time-frequency representation of the LIGO data containing GW170817 is shown in the bottom panel of Figure 2. The GPS time of the merger of GW170817 is $T_0^{\text{GW}} = 1187008882.430_{-0.002}^{+0.002} \text{ s}$ (Abbott et al. 2017e). At the observed signal strength, the false alarm rate of the all-sky search

for compact-object mergers is less than 1 in 80,000 years (Abbott et al. 2017e). The offline searches target binaries with (detector frame) total mass $2\text{--}500 M_{\odot}$. Signals are required to be coincident in time and mass in the LIGO detectors, but Virgo data are not used in the significance estimates of the all-sky offline search (Abbott et al. 2017e).

We present the results of two offline targeted searches that coherently combine the data from the LIGO and Virgo detectors and restrict the signal offset time and sky-location using information from the EM observation of GRB 170817A. The onset of gamma-ray emission from a BNS merger progenitor is predicted to be within a few seconds after the merger, given that the central engine is expected to form within a few seconds and that the jet propagation delays are at most of the order of the SGRB duration (see, e.g., Finn et al. 1999; Abadie et al. 2012 and references therein). The gravitational and EM waves are expected to travel at the same speed.

The first targeted search (Harry & Fairhurst 2011; Williamson et al. 2014; Abbott et al. 2017b; Nitz et al. 2017a) assumes that the source is a BNS or NS–BH binary merger and is located at the sky-position observed for the optical counterpart to GW170817 and GRB 170817A (Coulter et al. 2017a, 2017b; Abbott et al. 2017f) and that there is a $[-1, +5] \text{ s}$ time delay in the arrival of gamma-rays (determined by the GBM trigger time) compared to the binary merger time (Abbott et al. 2017b). At the detection statistic value assigned to GW170817, this search has a p -value of $<9.4 \times 10^{-6}$ ($>4.2\sigma$), with this significance estimate limited by computational resources used to estimate the noise background. The second coherent search does not assume any particular GW morphology or GRB model (Sutton et al. 2010; Was et al. 2012; Abbott et al. 2017b) and uses the GBM localization of GRB 170817A to constrain the sky location of the source. This search allows for a $[-60, +600] \text{ s}$ coincidence between the gamma-rays and the GWs in order to include potentially larger delays in collapsar models of long GRBs. At the detection-statistic value observed for GW170817, this search has a p -value of 1.3×10^{-5} (4.2σ).

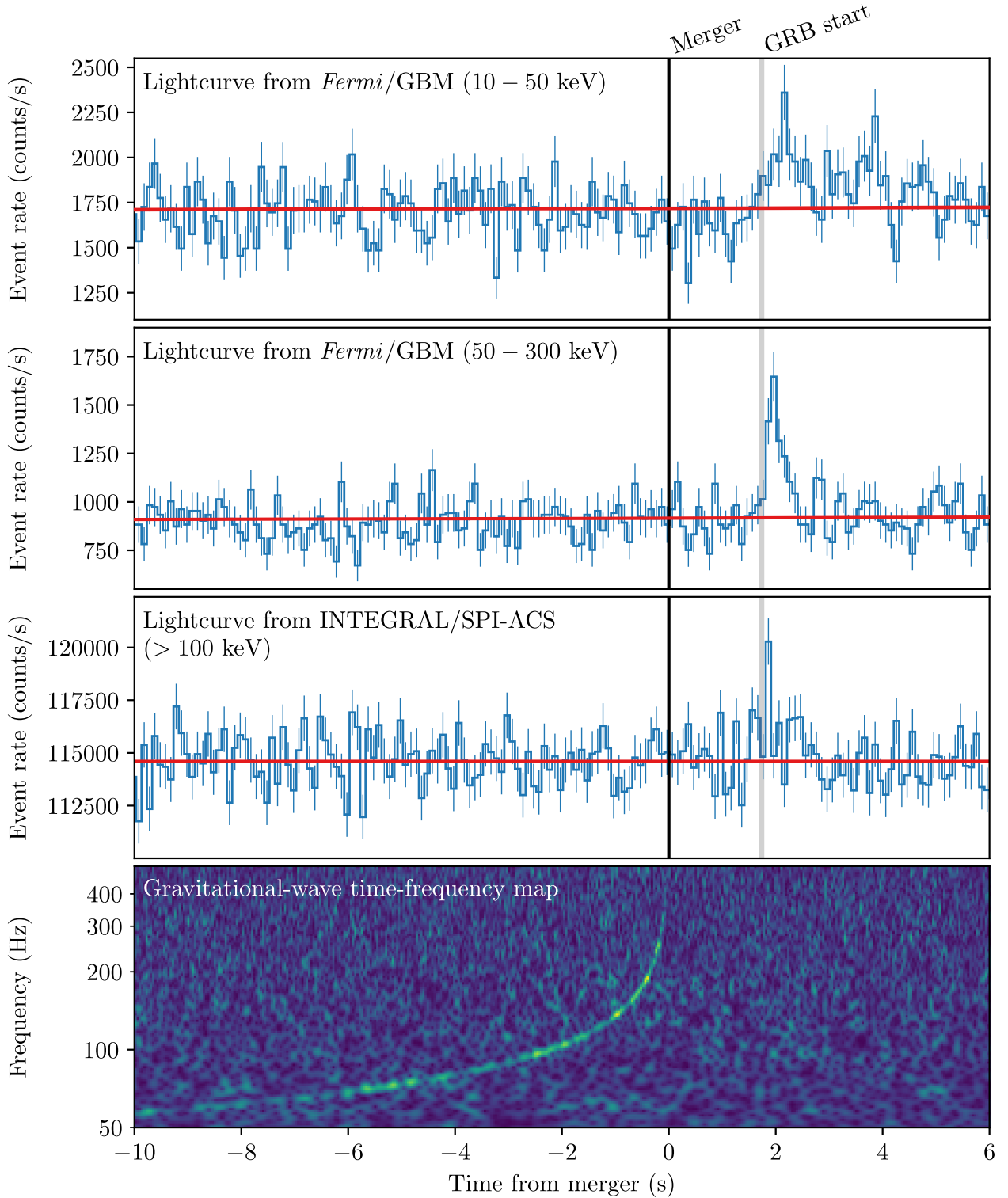


Figure 2. Joint, multi-messenger detection of GW170817 and GRB 170817A. Top: the summed GBM lightcurve for sodium iodide (NaI) detectors 1, 2, and 5 for GRB 170817A between 10 and 50 keV, matching the 100 ms time bins of the SPI-ACS data. The background estimate from Goldstein et al. (2016) is overlaid in red. Second: the same as the top panel but in the 50–300 keV energy range. Third: the SPI-ACS lightcurve with the energy range starting approximately at 100 keV and with a high energy limit of least 80 MeV. Bottom: the time-frequency map of GW170817 was obtained by coherently combining LIGO-Hanford and LIGO-Livingston data. All times here are referenced to the GW170817 trigger time T_0^{GW} .

The 90% credible intervals (Veitch et al. 2015; Abbott et al. 2017e) for the component masses (in the $m_1 \geq m_2$ convention) are $m_1 \in (1.36, 2.26) M_\odot$ and $m_2 \in (0.86, 1.36) M_\odot$, with total mass $2.82_{-0.09}^{+0.47} M_\odot$, when considering dimensionless spins with

magnitudes up to 0.89 (high-spin prior, hereafter). When the dimensionless spin prior is restricted to ≤ 0.05 (low-spin prior, hereafter), the measured component masses are $m_1 \in (1.36, 1.60) M_\odot$ and $m_2 \in (1.17, 1.36) M_\odot$, and the total mass is

$2.74_{-0.01}^{+0.04} M_{\odot}$. This result is consistent with the masses of all known BNS systems (Ozel & Freire 2016; Tauris et al. 2017). From the GW signal, the best measured combination of the masses is the chirp mass $\mathcal{M} = (m_1 m_2)^{3/5} / (m_1 + m_2)^{1/5}$, which in the detector frame is found to be $1.1977_{-0.0003}^{+0.0008} M_{\odot}$.

The detection of GW170817 triggered a campaign of EM follow-up observations which led to the identification of NGC 4993 as the host galaxy of GW170817/GRB 170817A (Coulter et al. 2017a, 2017b; Abbott et al. 2017f). We evaluate the distance to the host galaxy from the ratio of the Hubble flow velocity of the host $3017 \pm 166 \text{ km s}^{-1}$ (Abbott et al. 2017g) and two current measurements of the Hubble constant (Ade et al. 2016; Riess et al. 2016). These two distance measures are within a combined range of $(42.9 \pm 3.2) \text{ Mpc}$, which is consistent with the distance of $40_{-14}^{+8} \text{ Mpc}$ determined with GW data alone and makes GW170817 the closest GW event ever observed (Abbott et al. 2016a, 2016b, 2017c, 2017d, 2017e).

The GW data constrain the inclination angle θ_{JN} between the total angular momentum of the system and the line of sight to be anti-aligned, with $\cos \theta_{JN} \leq -0.54$ (Abbott et al. 2017e). As the binary system component masses are comparable, the NS spins have little impact on the total angular momentum which is aligned with the orbital angular momentum within a few degrees. For discussions in this Letter we will assume that the orbital and total angular momenta are aligned. The SGRB jet is expected to be perpendicular to the accretion disk of the central engine if powered by neutrino annihilation or aligned with the magnetic pole of the rotating central object (Shibata et al. 2006), hence we assume the SGRB jet is aligned with the system rotation axis. This yields a jet viewing angle $\zeta = \min(\theta_{JN}, 180^\circ - \theta_{JN}) \leq 56^\circ$. As the distance measurement is correlated with θ_{JN} , the known distance to NGC 4993 further constrains the viewing angle to $\zeta \leq 36^\circ$ or $\zeta \leq 28^\circ$ depending on the assumed value of the Hubble constant (Abbott et al. 2017g), with smaller values of the Hubble constant giving smaller misalignment angles.

2.2. Fermi-GBM Observation of GRB 170817A

GRB 170817A was autonomously detected in-orbit by the GBM flight software in a process known as “triggering.” Goldstein et al. (2017) showed the signal exceeds 5σ in three (of twelve) GBM NaI detectors. The GBM detection showed two apparently distinct components. The triggering pulse, that lasts about half a second and falls within the usual observer distributions for GBM SGRBs, is shorter and spectrally harder than the subsequent softer, weaker emission that lasts a few seconds (Goldstein et al. 2017). Summed GBM lightcurves from the relevant detectors in two energy ranges, selected to show the two distinct components, are shown in the top two panels in Figure 2. The GBM time-tagged event data is binned to match the SPI-ACS temporal resolution (100 ms) and phase (matching bin edges) to allow for an easier comparison between the gamma-ray instruments.

Goldstein et al. (2017) quantify the likelihood of GRB 170817A being an SGRB based only on gamma-ray data. This is done by comparing the measured gamma-ray properties of GRB 170817A to the known distributions of short and long GRBs. Both the duration distribution alone and the duration and spectral hardness distributions together show that GRB 170817A is three times more likely to be an SGRB than a long GRB. These analyses are performed in a standard manner, resulting in a longer duration measure than apparent from the

hard spike alone because the softer, weaker tail contributes to the calculated duration.

The final GBM localization of GRB 170817A (including systematic error) calculated by the GBM targeted search pipeline is shown in Figure 1. This pipeline performs a coherent search over all GBM detectors (NaI and BGO) and was originally developed to find gamma-ray signals below the onboard triggering threshold around GW triggers (Blackburn et al. 2015; Connaughton et al. 2016; Goldstein et al. 2016). The 50% and 90% credible regions cover $\sim 350 \text{ deg}^2$ and $\sim 1100 \text{ deg}^2$, respectively.

Fitting the main pulse in the GBM data with a parameterized function commonly used for GRB pulses indicates a gamma-ray emission onset of $0.310 \pm 0.048 \text{ s}$ before T_0^{GBM} , where T_0^{GBM} is defined as the time of the GBM trigger (Goldstein et al. 2017). Based on the position of the optical transient, the signal arrives at *Fermi* 3.176 ms before it arrives at geocenter. With this correction we find that the start of the gamma-ray emission relative to the T_0^{GW} is $(+1.74 \pm 0.05) \text{ s}$. In this Letter all derived gamma-ray results use 68% confidence levels.

The spectral analysis using the standard GBM catalog criteria uses data from the 256 ms time interval between $T_0^{\text{GBM}} - 0.192 \text{ s}$ and $T_0^{\text{GBM}} + 0.064 \text{ s}$. A fit to the “Comptonized” function, a power law with a high-energy exponential cutoff (see Goldstein et al. 2017 for a detailed explanation of this function), is preferred over both a simple power-law fit or models with more parameters. The fit produces values of $E_{\text{peak}} = (215 \pm 54) \text{ keV}$, and a poorly constrained power-law index $\alpha = 0.14 \pm 0.59$. The average flux for this interval in the 10–1000 keV range is $(5.5 \pm 1.2) \times 10^{-7} \text{ erg s}^{-1} \text{ cm}^{-2}$ with a corresponding fluence of $(1.4 \pm 0.3) \times 10^{-7} \text{ erg cm}^{-2}$. The shorter peak interval selection from $T_0^{\text{GBM}} - 0.128 \text{ s}$ to $T_0^{\text{GBM}} - 0.064 \text{ s}$ fit prefers the Comptonized function, yielding consistent parameters $E_{\text{peak}} = (229 \pm 78) \text{ keV}$, $\alpha = 0.85 \pm 1.38$, and peak energy flux in the 10–1000 keV of $(7.3 \pm 2.5) \times 10^{-7} \text{ erg s}^{-1} \text{ cm}^{-2}$. These standard fits are used to compare GRB 170817A to the rest of the SGRBs detected by GBM and to place GRB 170817A in context with the population of SGRBs with known redshift.

More detailed analysis included spectral fits to the two apparently distinct components. The main emission episode, represented by the peak in Figure 2, appears as a typical SGRB best fit by a power law with an exponential cutoff with spectral index $\alpha = -0.62 \pm 0.40$ and $E_{\text{peak}} = (185 \pm 62) \text{ keV}$ over a time interval $T_0^{\text{GBM}} - 0.320 \text{ s}$ to $T_0^{\text{GBM}} + 0.256 \text{ s}$. The time-averaged flux is $(3.1 \pm 0.7) \times 10^{-7} \text{ erg s}^{-1} \text{ cm}^{-2}$. The tail emission that appears spectrally soft is best fit by a blackbody (BB) spectrum, with temperature of $k_B T = (10.3 \pm 1.5) \text{ keV}$ and a time-averaged flux of $(0.53 \pm 0.10) \times 10^{-7} \text{ erg s}^{-1} \text{ cm}^{-2}$, with selected source interval $T_0^{\text{GBM}} + 0.832 \text{ s}$ to $T_0^{\text{GBM}} + 1.984 \text{ s}$. However, this emission is too weak and near the lower energy detection bound of GBM to completely rule out a non-thermal spectrum.

The temporal analysis yielded a T_{90} , defined as the time interval over which 90% of the burst fluence between 50–300 keV is accumulated, of $(2.0 \pm 0.5) \text{ s}$ starting at $T_0^{\text{GBM}} - 0.192 \text{ s}$. The duration extends beyond the main emission pulse due to the soft component. This analysis reports a 64 ms peak photon flux of $(3.7 \pm 0.9) \text{ photons s}^{-1} \text{ cm}^{-2}$ and occurs from $T_0^{\text{GBM}} + 0.0 \text{ s}$ to $T_0^{\text{GBM}} + 0.064 \text{ s}$. The

minimum variability timescale for GRB 170817A is (0.125 ± 0.064) s.

Using the soft spectral template of the GBM targeted search, a Band function (Band et al. 1993) with a low energy power law index of -1.9 , a high energy index of -3.7 , and an E_{peak} of 70 keV, Goldstein et al. (2017) also set 3σ flux upper limits on precursor impulsive gamma-ray emission. The limits on precursor activity out to $T_0^{\text{GBM}} - 200$ s are $(6.8\text{--}7.3) \times 10^{-7}$ erg s $^{-1}$ cm $^{-2}$ and $(2.0\text{--}2.1) \times 10^{-7}$ erg s $^{-1}$ cm $^{-2}$ for signals of 0.1 s and 1.0 s duration, respectively. The tail emission of GRB 170817A is not consistent with the general behavior of SGRBs with extended emission (Kaneko et al. 2015). We set limits on possible extended emission over 10 s intervals out to $\sim T_0^{\text{GBM}} + 100$ s is $(6.4\text{--}6.6) \times 10^{-8}$ erg s $^{-1}$ cm $^{-2}$. Additional upper limits for representative normal and harder spectra are provided in Goldstein et al. (2017) and are up to a factor of a few less constraining.

2.3. INTEGRAL SPI-ACS Observation of GRB 170817A

The orientation of *INTErnational Gamma-Ray Astrophysics Laboratory* (*INTEGRAL*) with respect to the LIGO–Virgo localization of GW170817 favored the observation by SPI-ACS and was such that the sensitivity of the Imager on Board the *INTEGRAL* Satellite (IBIS) was much lower in comparison (Savchenko et al. 2017b). For comparison of relative sensitivities of different *INTEGRAL* instruments see Savchenko et al. (2017a).

A routine follow-up search for short transients in SPI-ACS identified a single excess at $T_0^{\text{ACS}} = T_0^{\text{GW}} + 1.88$ s with $S/N = 4.6$ at the 0.1 s timescale. The correction to the geocentric system assumes the location of the optical transient and results in delay of the signal arrival to *INTEGRAL* of 148.96 ms. In order to compare the intensity of the event observed by SPI-ACS to the GBM measurement, we compute the range of fluences compatible with the SPI-ACS data in the $[-0.320$ s, $+0.256$ s] time interval centered in T_0^{GBM} , assuming the GBM best fit spectral model in the same interval. We derive a fluence estimate of $(1.4 \pm 0.4) \times 10^{-7}$ erg cm $^{-2}$ (statistical uncertainty only) in the 75–2000 keV energy range, consistent with GBM.

The significance of the association between the GBM observation of GRB 170817A and the event observed by SPI-ACS is 4.2σ . While SPI-ACS would not have alone reported this event as a GRB, it would have reported the event while searching around GW170817, with an independent association significance of 3.2σ (Savchenko et al. 2017b). SGRBs are routinely jointly detected by GBM and SPI-ACS and the association evidence from time coincidence (quoted above) as well as the consistency between the event fluences and temporal properties observed by the two instruments proves that both GBM and SPI-ACS observed the same event. The difference between the time of arrival of the signal in the SPI-ACS and GBM detectors can be exploited to improve the gamma-ray localization of GRB 170817A, which may be beneficial in future joint detections.

The significant interval of the SPI-ACS lightcurve of GRB 170817A is limited to a single pulse with a duration of 100 ms (third panel in Figure 1). GBM and SPI-ACS see the main pulse as appearing to have different durations because they are sensitive in different energy ranges. If the GBM data are shown in an energy range higher than the standard 50–300 keV, the main pulse is consistent with the 100 ms interval seen in SPI-ACS. The lightcurve observed by SPI-ACS reveals

a short rise time (<50 ms) and a rapid drop (<50 ms). We therefore constrain the pulse duration in the energy range observed by SPI-ACS ($\sim 75\text{--}2000$ keV) to less than 100 ms.

3. Unambiguous Association

The separation of GRBs into short and long classes was suggested by their duration distributions and reinforced by differences in the prompt gamma-ray emission of the two classes (Dezalay et al. 1992; Kouveliotou et al. 1993). Tying the short class to a different progenitor from the long class was strengthened by redshift measurements of their hosts (Berger 2014). Association of SGRBs with older stellar populations than long GRBs was supported by the types of galaxies that host them (Fong et al. 2013); the connection to BNS mergers was strengthened by the offsets of SGRBs afterglows from their host galaxies (Troja et al. 2008; Church et al. 2011; Fong & Berger 2013) and by the absence of supernovae following nearby, well-observed SGRBs (Fox et al. 2005; Hjorth et al. 2005a, 2005b; Bloom et al. 2006; Soderberg et al. 2006; D’Avanzo et al. 2009; Kocevski et al. 2010; Rowlinson et al. 2010; Berger et al. 2013). We provide conclusive evidence for the BNS-SGRB connection by quantifying the chance temporal and spatial coincidence for GRB 170817A and GW170817 arising from two independent astrophysical events.

To quantify the temporal agreement, we consider the null hypothesis that SGRB and GW detection events are independent Poisson processes and determine how unlikely it is to observe an unassociated SGRB within $\Delta t_{\text{SGRB-GW}} = 1.74$ s of the GW signal. GWs from a BNS merger have been detected once to date, so the p -value is $P_{\text{temporal}} = 2\Delta t_{\text{SGRB-GW}} R_{\text{GBM-SGRB}}$, where $R_{\text{GBM-SGRB}}$ is the GBM SGRB detection rate. Using the standard duration cut $T_{90} < 2$ s, GBM triggered on-board in response to 351 SGRBs in 3324 days¹⁸⁴ (the number of days between the GBM on-board trigger activation and the detection of GRB 170817A). Further, we account for the livetime of GBM, which is disabled 15% of the time to preserve detector lifetime in regions of high particle activity during transit through the South Atlantic Anomaly. Therefore, $P_{\text{temporal}} = 2(1.74 \text{ s})(351/3324 \text{ days}/0.85) = 5.0 \times 10^{-6}$, which corresponds to a 4.4σ significance in Gaussian statistics.

In order to quantify the spatial agreement of the independent GBM and LIGO–Virgo localizations, we define the statistic $\mathcal{S} = \sum_{i=1}^{N_{\text{pix}}} P_{1i} P_{2i}$, where P_1 and P_2 are the posterior probabilities from GBM and LIGO–Virgo maps and i is the HEALPix (Gorski et al. 2005) pixel index. \mathcal{S} is then compared against a background distribution generated by randomly shifting and rotating GBM posteriors from a representative sample of 164 SGRBs localized by the targeted search. We factor in the estimated localization systematic, and randomly shift and rotate each map 10 times. This background method accounts for the morphology and size distributions of GBM SGRB localizations. We find a p -value $P_{\text{spatial}} = 0.01$ that the two independent localizations agree this well by chance.

The temporal and spatial p -values are independent quantities, thus the probability that GRB 170817A and GW170817 occurred this close in time and with this level of location agreement by chance is $P_{\text{temporal}} \times P_{\text{spatial}} = (5.0 \times 10^{-6}) \times (0.01) = 5.0 \times 10^{-8}$, corresponding to a Gaussian-equivalent significance

¹⁸⁴ <https://heasarc.gsfc.nasa.gov/W3Browse/fermi/fermigbrst.html>

of 5.3σ . This unambiguous association confirms that BNS mergers are progenitors of (at least some) SGRBs.

4. Implications for Fundamental Physics

Little or no arrival delay between photons and GWs over cosmological distances is expected as the intrinsic emission times are similar and the propagation speeds of EM and GWs are thought to be identical. In this Section we discuss the implications on fundamental physics of the temporal offset of $(+1.74 \pm 0.05)$ s measured between GW170817 and GRB 170817A.

Standard EM theory minimally coupled to general relativity predicts that GWs and light propagate with identical speeds. The refractive index of vacuum is expected to be unity, and both waves are expected to be affected by background gravitational potentials in the same way. The arrival delay of only a few seconds across a distance greater than one hundred million light years places stringent constraints on deviations from fundamental principles. We use the observed temporal offset, the distance to the source, and the expected emission-time difference to place constraints on the deviation of the speed of gravity from the speed of light, and on violations of Lorentz invariance and the equivalence principle.

4.1. Speed of Gravity

Assuming a small difference in travel time Δt between photons and GWs, and the known travel distance D , the fractional speed difference during the trip can be written $\Delta v/v_{\text{EM}} \approx v_{\text{EM}}\Delta t/D$, where $\Delta v = v_{\text{GW}} - v_{\text{EM}}$ is the difference between the speed of gravity v_{GW} and the speed of light v_{EM} . This relation is less constraining for small distances, hence we conservatively use here $D = 26$ Mpc, the lower bound of the 90% credible interval on luminosity distance derived from the GW signal (Abbott et al. 2017e). If we conservatively assume that the peak of the GW signal and the first photons were emitted simultaneously, attributing the entire $(+1.74 \pm 0.05)$ s lag to faster travel by the GW signal, this time difference provides an upper bound on Δv . To obtain a lower bound on Δv , one can assume that the two signals were emitted at times differing by more than $(+1.74 \pm 0.05)$ s with the faster EM signal making up some of the difference. As a conservative bound relative to the few second delays discussed in Section 2.1, we assume the SGRB signal was emitted 10 s after the GW signal. The resulting constraint on the fractional speed difference is

$$-3 \times 10^{-15} \leq \frac{\Delta v}{v_{\text{EM}}} \leq +7 \times 10^{-16}. \quad (1)$$

The intergalactic medium dispersion has negligible impact on the gamma-ray photon speed, with an expected propagation delay many orders of magnitude smaller than our errors on v_{GW} .

Lags much longer than 10 s are proposed in alternative models (e.g., Ciolfi & Siegel 2015; Rezzolla & Kumar 2015), and emission of photons before the merger is also possible (Tsang et al. 2012). Hence, certain exotic scenarios can extend this time difference window to $(-100 \text{ s}, 1000 \text{ s})$, yielding a 2 orders of magnitude broadening of the allowed velocity range on either side. While the emission times of the two messengers are inherently model dependent, conservative assumptions yield dramatic improvements over existing indirect (Kostecký

& Russell 2017) and direct (Cornish et al. 2017) constraints, which allow for time differences of more than 1000 years. Future joint GW–GRB detection should allow disentangling the emission time difference from the relative propagation time, as only the latter is expected to depend on distance.

4.2. Lorentz Invariance Violation Limits

Within a comprehensive effective field theory description of Lorentz violation (Colladay & Kostelecký 1997, 1998; Kostelecký 2004; Tasson 2014), the relative group velocity of GWs and EM waves, is controlled by differences in coefficients for Lorentz violation in the gravitational sector and the photon sector at each mass dimension d (Kostecký & Mewes 2016, 2009, 2008; Wei et al. 2017). We focus here on the non-birefringent, non-dispersive limit at mass dimension $d = 4$, as it yields by far the most impressive results. In this case, the difference in group velocities for the two sectors takes the form

$$\Delta v = - \sum_{\ell m} Y_{\ell m}(\hat{n}) \left(\frac{1}{2} (-1)^{1+\ell} \bar{s}_{\ell m}^{(4)} - c_{(\ell)\ell m}^{(4)} \right). \quad (2)$$

The result is presented in a spherical harmonic, $Y_{\ell m}$, basis, $\bar{s}_{\ell m}^{(4)}$ and $c_{(\ell)\ell m}^{(4)}$ being spherical-basis coefficients for Lorentz violation in the gravitational and EM sectors, respectively. The direction \hat{n} refers to the sky position (provided in Coulter et al. 2017a, 2017b).

For ease of comparison with the many existing sensitivities (Shao 2014a, 2014b; Shao et al. 2017; Kostecký & Tasson 2015; Bourgoïn et al. 2016; Le Poncin-Lafitte et al. 2016; Kostecký & Russell 2017) to the $d = 4$ gravity-sector coefficients (Bailey & Kostecký 2006; Hees et al. 2016), an analysis in which the coefficients are constrained one at a time is useful (Flowers et al. 2016), with all other coefficients, including the EM sector ones, set to zero. These results are presented in Table 1 along with the best constraints for each coefficient prior to this work. These results can be compared with the isotropic A , α_{LV} Lorentz violation parametrization (Mirshekari et al. 2012) used by Abbott et al. (2017c) in dispersive GW tests. The $\alpha_{\text{LV}} = 2$ limit of this parametrization is equivalent to the isotropic limit of the framework discussed above, with $\bar{s}_{00}^{(4)} \rightarrow \sqrt{4\pi}A$. Constraints on A for $\alpha_{\text{LV}} = 2$ can be obtained from the first line of Table 1; these cannot be established within the analysis carried out in Abbott et al. (2017c).

4.3. Test of the Equivalence Principle

Probing whether EM radiation and GWs are affected by background gravitational potentials in the same way is a test of the equivalence principle (Will 2014). One way to achieve this is to use the Shapiro effect (Shapiro 1964), which predicts that the propagation time of massless particles in curved spacetime, i.e., through gravitational fields, is slightly increased with respect to the flat spacetime case. We will consider the following simple parametrized form of the Shapiro delay (Krauss & Tremaine 1988; Longo 1988; Gao et al. 2015; Kahya & Desai 2016):

$$\delta t_S = - \frac{1 + \gamma}{c^3} \int_{r_e}^{r_o} U(\mathbf{r}(l)) dl, \quad (3)$$

Table 1
Constraints on the Dimensionless Minimal Gravity Sector Coefficients

ℓ	Previous Lower	This Work Lower	Coefficient	This Work Upper	Previous Upper
0	-3×10^{-14}	-2×10^{-14}	$\bar{s}_{00}^{(4)}$	5×10^{-15}	8×10^{-5}
1	-1×10^{-13}	-3×10^{-14}	$\bar{s}_{10}^{(4)}$	7×10^{-15}	7×10^{-14}
	-8×10^{-14}	-1×10^{-14}	$-\text{Re } \bar{s}_{11}^{(4)}$	2×10^{-15}	8×10^{-14}
	-7×10^{-14}	-3×10^{-14}	$\text{Im } \bar{s}_{11}^{(4)}$	7×10^{-15}	9×10^{-14}
2	-1×10^{-13}	-4×10^{-14}	$-\bar{s}_{20}^{(4)}$	8×10^{-15}	7×10^{-14}
	-7×10^{-14}	-1×10^{-14}	$-\text{Re } \bar{s}_{21}^{(4)}$	2×10^{-15}	7×10^{-14}
	-5×10^{-14}	-4×10^{-14}	$\text{Im } \bar{s}_{21}^{(4)}$	8×10^{-15}	8×10^{-14}
	-6×10^{-14}	-1×10^{-14}	$\text{Re } \bar{s}_{22}^{(4)}$	3×10^{-15}	8×10^{-14}
	-7×10^{-14}	-2×10^{-14}	$-\text{Im } \bar{s}_{22}^{(4)}$	4×10^{-15}	7×10^{-14}

Note. Constraints on the dimensionless minimal gravity sector coefficients obtained in this work via Equations (1) and (2) appear in columns 3 and 5. The corresponding limits that predate this work and are reported in columns 2 and 6; all pre-existing limits are taken from Kostelecký & Tasson (2015), with the exception of the upper limit on $\bar{s}_{00}^{(4)}$ from Shao (2014a, 2014b). The isotropic upper bound in the first line shows greater than 10 orders of magnitude improvement. The gravity sector coefficients are constrained one at a time, by setting all other coefficients, including those from the EM sector, to zero.

where r_e and r_o denote emission and observation positions, respectively, $U(\mathbf{r})$ is the gravitational potential, and the integral is computed along the wave path. γ parametrizes a deviation from the Einstein–Maxwell theory, which minimally couples classical electromagnetism to general relativity. We allow for different values of γ for the propagation of EM and GWs (γ_{EM} and γ_{GW} , respectively, with $\gamma_{\text{EM}} = \gamma_{\text{GW}} = 1$ in the Einstein–Maxwell theory).

While obtaining the best bound on the difference between the Shapiro time delays requires modeling the potential $U(\mathbf{r})$ along the entire line of sight, we determine a conservative bound on $\gamma_{\text{GW}} - \gamma_{\text{EM}}$ by considering only the effect of the Milky Way outside a sphere of 100 kpc, and by using a Keplerian potential with a mass of $2.5 \times 10^{11} M_\odot$ (the lowest total mass within a sphere of radius 100 kpc quoted in Bland-Hawthorn & Gerhard 2016, from Gibbons et al. 2014, taking the 95% confidence lower bound) (Krauss & Tremaine 1988; Longo 1988; Gao et al. 2015). Using the same time bounds as Equation (1) we find

$$-2.6 \times 10^{-7} \leq \gamma_{\text{GW}} - \gamma_{\text{EM}} \leq 1.2 \times 10^{-6}. \quad (4)$$

The best absolute bound on γ_{EM} is $\gamma_{\text{EM}} - 1 = (2.1 \pm 2.3) \times 10^{-5}$, from the measurement of the Shapiro delay (at radio wavelengths) with the Cassini spacecraft (Bertotti et al. 2003).

5. Astrophysical Implications

The joint GW–GRB detection provides us with unprecedented information about the central engine of SGRBs. The delay between the GW and the GRB trigger times allows us to examine some basic GRB physics. This delay could be intrinsic to the central engine, reflecting the time elapsed from the moment the binary components come into contact to the formation of a remnant BH and the resulting jet. This interpretation includes the case of a relatively long-lived massive NS remnant, which has been suggested to survive from seconds to minutes after merger (see Faber & Rasio 2012; Baiotti & Rezzolla 2017 and references therein). The delay could also be due to the propagation time of the relativistic jet,

including the time it takes for the jet to break out of the dense gaseous environment produced by non-relativistic merger ejecta (Nagakura et al. 2014; Moharana & Piran 2017) and/or the emitting region to become transparent to gamma-rays (Mészáros & Rees 2000).

We first discuss the implications that the time delay between the GW and EM emission has on the physical properties of the emitting region when considering the jet propagation and transparency scenarios. Here we assume that the entire delay is due to the expansion of the emitting region and neglect any intrinsic delays between the moment of binary coalescence and the launching of the resulting jet, thus placing limits on the physical properties of the system. Then we consider the impact of the SGRB emission from an NS merger on the EOS of dense matter.

5.1. GRB Physics

The main hard peak observed for GRB 170817A lasted roughly half a second. This peak is consistent with a single intrinsic emission episode as it is well described by a single pulse (Goldstein et al. 2017), showing no evidence for significant substructure (spikes). This interpretation is consistent with the SPI-ACS observation of a single peak (Savchenko et al. 2017b). The GBM detection of GRB 170817A also shows no evidence for photons with energy > 511 keV, implying that the outflow does not require a high bulk Lorentz factor Γ to overcome photon–photon absorption at the source.

Explanations for the extreme energetics and short timescales observed in GRBs invoke a near instantaneous release of a large amount of energy in a compact volume of space (Goodman 1986; Paczynski 1986). This is commonly referred to as the fireball model, and it is the framework that we will assume for the remainder of this section. The fireball model is largely independent of the burst progenitor and focuses on the dynamics of such a system after this sudden release of energy. The resulting pair-plasma is optically thick and quickly expands under its own pressure to produce a highly relativistic outflow that coasts asymptotically with a constant Lorentz factor Γ . Within the fireball, kinetic energy is imparted to particles

entrained in the outflow, although alternative models exist in which the energy outflow occurs mostly as Poynting flux (Usov 1992; Lyutikov & Blandford 2003). The observed gamma-ray pulses are attributed to shocks internal to this relativistic outflow, which convert some of their kinetic energy into the observed EM radiation (Rees & Meszaros 1994). These shocks could produce the predominantly non-thermal emission observed in most GRBs, although non-shock heating models have also been proposed (e.g., Giannios 2006). The overall multi-pulse duration of a burst is thought to reflect the time that the inner engine was active (e.g., producing inhomogeneities in the outflow represented as shells traveling with different bulk velocities) and the variability of individual pulses reflects the size of the shells producing the emission. For a top-hat jet model, Γ is assumed constant over the jet surface and the observer never sees beyond the beaming angle $\theta_b \sim 1/\Gamma$. Therefore, the values inferred from the data are independent of the inclination angle from the total angular momentum axis of the system, as long as the viewer is within the opening angle of the jet.

We can examine the implications of the observed delay between the GW and EM signals in the internal shock scenario if we consider two shells emitted at time $t_{\text{GW}} = 0$ and time $t_{\text{GW}} + \Delta t_{\text{engine}}$. If the Lorentz factor of the second shell, γ_2 , is greater than the Lorentz factor of the first shell, γ_1 , the shells will collide at time

$$t_{\text{delay}} = \frac{\Delta t_{\text{engine}}}{1 - (\gamma_1/\gamma_2)^2}, \quad (5)$$

which is valid if $\gamma_1, \gamma_2 \gg 1$. If the shells have comparable masses, conservation of energy and momentum leads to a merged shell with Lorentz factor $\gamma_m = (\gamma_1\gamma_2)^{1/2}$. The resulting pulse profile is determined by two timescales. The rise time (which we equate to the minimum variability timescale) can be attributed to the light-crossing time of the individual emission regions and is expressed as

$$\Delta t_{\text{rise}} \approx \frac{\delta R}{2c\gamma_m^2}, \quad (6)$$

where δR is the thickness of the emitting region. The decay time reflects angular effects, where off-axis emission is delayed and affected by a varying Doppler boost due to the curvature of the relativistic shell. This timescale is essentially the difference in light-travel time between photons emitted along the line of sight and photons emitted at an angle θ along a shell of radius R . This timescale may be expressed as

$$\Delta t_{\text{decay}} = \frac{R(1 - \cos \Delta\theta)}{c} \approx \frac{R(\Delta\theta)^2}{2c} \approx \frac{R}{2c\gamma_m^2} > \Delta t_{\text{rise}}, \quad (7)$$

where we assume that the solid angle accessible to the observer is limited by relativistic beaming and thus given by $\theta \sim 1/\gamma$. At the same time, the distance that the first shell has traveled since ejection is $R_1 \approx 2c\gamma_1^2 t_{\text{delay}}$, leading to

$$\Delta t_{\text{decay}} \approx t_{\text{delay}} (\gamma_1/\gamma_2) = \frac{\Delta t_{\text{engine}}}{1 - (\gamma_1/\gamma_2)^2} \frac{\gamma_1}{\gamma_2}. \quad (8)$$

The conclusion is a linear correlation between the delay in the GW and EM signals and the resulting pulse duration, modulo

the ratio of the Lorentz factors of the two colliding shells (Fenimore et al. 1996; Kocevski et al. 2007; Krimm et al. 2007).

The relative similarity between the gamma-ray duration T_{90} and the delay between the GW and the EM emission gives $\Delta t_{\text{decay}}/t_{\text{delay}} \sim 1$, pointing to an internal shock scenario in which the difference in the Lorentz factors of the colliding shells, $\Delta\gamma$, is much smaller than their typical values, i.e., $\Delta\gamma \ll \gamma$. This would imply that the jet was launched shortly after the time of the merger and points to a relatively short Δt_{engine} time in which the central engine was active. Such a scenario would produce a collision that was relatively inefficient at converting the internal energy of the shocks to radiation, resulting in a significant isotropic equivalent kinetic energy remaining in the merged shell (Kobayashi et al. 1997; Krimm et al. 2007). This would lead to a very significant energy injection into the resulting afterglow, producing late time “refreshed shocks” (Rees & Mészáros 1998; Kumar & Piran 2000; Ramirez-Ruiz et al. 2001), which are typically not observed in the X-ray (and optical) lightcurves of SGRBs (e.g., Perley et al. 2009).

Some of these energetics constraints can be alleviated if we exclude the soft thermal emission from the gamma-ray duration estimate. In this case, the prompt non-thermal emission of $\Delta t_{\text{decay}} \simeq 0.5$ s would be due to internal shocks and the soft thermal emission would be attributed to a separate component. In this case we obtain $\Delta t_{\text{decay}}/t_{\text{delay}} \simeq 0.3$, implying $\gamma_2 \approx 3\gamma_1$. These energetics considerations may suggest that the initial hard pulse and the subsequent thermal emission observed by GBM may indeed be distinct components.

Within the context of the internal shock model, if we assume the entire $(+1.74 \pm 0.05)$ s delay between the GW and the EM emission is due to jet propagation time and use a Lorentz factor of $\gamma < 100$ for the first shell, we can estimate an upper limit to the radius of the relativistic outflow to be $R \sim 5 \times 10^{14}$ cm or ~ 30 au. The minimum variability timescale $\Delta t_{\text{rise}} = \Delta t_{\text{min}} \sim 0.125$ s (Goldstein et al. 2017) yields an upper limit on the size of the emitting region of $\delta R \sim 4 \times 10^{13}$ cm, or ~ 3 au. The ratio of the two is independent of the unknown Lorentz factor and is of order $\delta R/R \sim 10\%$.

The single-pulsed nature of the gamma-ray emission, as well as the observed $\Delta t_{\text{decay}}/t_{\text{delay}} \sim 1$, also leaves open the possibility that the GBM signal is entirely of an external shock origin. In this scenario, the relativistic outflow converts its internal energy to radiation due to its interaction with an external medium, such as the interstellar matter (Meszaros & Rees 1992). If we associate the duration of the main pulse with the deceleration time, i.e., the timescale over which the jet is significantly decelerated by interstellar matter of constant density n , in the external shock scenario (Dermer et al. 1999):

$$t_{\text{dec}} = [3E_{\text{k,iso}}/(4\pi\gamma^8 n m_p c^5)]^{1/3} = T_{\text{obs}}. \quad (9)$$

$E_{\text{k,iso}}$ is the kinetic energy of the jet calculated assuming a gamma-ray production efficiency of 20%, $m_p = 1.67 \times 10^{-27}$ kg is the proton mass, c is the speed of light, and T_{obs} is the approximate duration of the main peak. We can thus estimate

the Lorentz factor of the jet in the external shock scenario to be

$$\gamma \approx 310 \left(\frac{E_{k,\text{iso}}}{2 \times 10^{47} \text{ erg}} \right)^{1/8} \left(\frac{n}{0.1 \text{ cm}^{-3}} \right)^{-1/8} \left(\frac{T_{\text{obs}}}{0.5 \text{ s}} \right)^{-3/8}. \quad (10)$$

The deceleration radius represents the upper limit of efficient energy extraction (even for internal shocks) and can be expressed as

$$R_{\text{dec}} = 2\gamma^2 c T_{\text{obs}} = 3.0 \times 10^{15} \left(\frac{E_{k,\text{iso}}}{2 \times 10^{47} \text{ erg}} \right)^{1/4} \times \left(\frac{n}{0.1 \text{ cm}^{-3}} \right)^{-1/4} \left(\frac{T_{\text{obs}}}{0.5 \text{ s}} \right)^{1/4} \text{ cm}. \quad (11)$$

Therefore, the deceleration radius and associated Lorentz factor also serve as upper limits to the radius and Lorentz factor of the emitting region in the internal shock scenario.

The soft thermal component observed by GBM could also be due to the photosphere of the fireball before it becomes optically thin to gamma-rays. In this interpretation, the delay between the GW and the GRB trigger times may represent the time it takes for the relativistic fireball to expand and become optically thin to gamma-ray radiation. We can examine this scenario by estimating the time it takes for a fireball to become transparent to high-energy radiation in an environment similar to that of a BNS merger.

Following Mészáros & Rees (2000, hereafter MR00), we assume an outflow with an initial radius $R_0 = 6GM_{\text{BH}}/c^2$ (the innermost stable circular orbit of a Schwarzschild BH with a mass equal to M_{BH}). In our case $R_0 = 2.5 \times 10^6 \text{ cm}$, and $M_{\text{BH}} = 2.8 M_{\odot}$. Given the GBM observations, we estimate an isotropic equivalent energy of the soft thermal BB component to be $E_{\text{iso, BB}} = 1.3 \times 10^{46} \text{ erg}$ and peak isotropic luminosity of $L_{\text{iso, p}} = 1.6 \times 10^{47} \text{ erg s}^{-1}$ (see Section 6.1). We take this luminosity as an upper bound of the average luminosity, which may be estimated as $L_{\text{iso, BB}} = E_{\text{iso, BB}}/\Delta t_{\text{BB}} = 1.1 \times 10^{46} \text{ erg s}^{-1}$, where we have used a duration of the soft BB component of $\Delta t_{\text{BB}} = 1.15 \text{ s}$.

Using these parameters along with fiducial values (see Appendix B for details), we estimate the photospheric radius to be (MR00)

$$R_{\text{ph}} = \frac{L\sigma_T Y}{4\pi m_p c^3 \eta^3} = 2.01 \times 10^{13} \text{ cm} \times \left(\frac{L_0}{10^{50} \text{ erg s}^{-1}} \right) \left(\frac{\eta}{18} \right)^{-3} Y. \quad (12)$$

Where L_0 is the initial fireball luminosity, Y is the number of electrons per baryon (in our case $Y \simeq 1$), $\sigma_T = 6.65 \times 10^{-25} \text{ cm}^2$ is the Thomson cross-section, and η is the dimensionless entropy of the fireball, whose value is much smaller than the canonical one in the standard fireball model (see Appendix B). We note that L_0 can be much larger than $L_{\text{iso, BB}}$, since the fireball must expand and convert the remaining internal energy into kinetic energy of the ejecta.

The laboratory frame time needed for the fireball expanding at roughly the speed of light to reach the transparency radius is

$t_{\text{ph}} \simeq R_{\text{ph}}/c$; thus,

$$t_{\text{ph}} \simeq 672 \text{ s} \left(\frac{L_0}{10^{50} \text{ erg s}^{-1}} \right) \left(\frac{\eta}{18} \right)^{-3} Y. \quad (13)$$

Following Bianco et al. (2001), we can set an upper bound to the conversion from the laboratory to observer frame by assuming the observer is viewing the fireball at most at an angle $\cos \vartheta = v/c$:

$$t_a \simeq \frac{t_{\text{ph}}}{\gamma^2} \simeq 2.1 \text{ s} \left(\frac{L_0}{10^{50} \text{ erg s}^{-1}} \right) \left(\frac{\eta}{18} \right)^{-5} Y. \quad (14)$$

This upper bound can account for the time delay between the GW and the prompt radiation in the soft thermal peak.

Employing MR00's Equation (8) we can estimate the observer frame temperature of the expanding fireball at the photospheric radius

$$T_{\text{ph}}^{\text{obs}} = \eta T_{\text{ph}} \simeq 2.3 \text{ keV} \left(\frac{L_0}{10^{50} \text{ erg s}^{-1}} \right)^{-5/12} \times \left(\frac{R_0}{2.5 \times 10^6 \text{ cm}} \right)^{-5/6} \left(\frac{\eta}{18} \right)^{11/3} Y^{-2/3} \gamma_0^{-5/6}. \quad (15)$$

$T_{\text{ph}}^{\text{obs}}$ can then be compared to the one obtained from observational fits to the GBM data, which provide a BB temperature of $T_{\text{BB}}^{\text{obs}} \simeq 10.3 \text{ keV}$. Our result underestimates the observed BB temperature by a factor ~ 4 , but we are neglecting Comptonization effects, which may slightly raise the estimated temperature. The corresponding BB luminosity is (MR00)

$$L_{\text{ph}} \simeq 1.7 \times 10^{46} \text{ erg s}^{-1} \left(\frac{L_0}{10^{50} \text{ erg s}^{-1}} \right)^{7/12} \times \left(\frac{R_0}{2.5 \times 10^6 \text{ cm}} \right)^{-5/6} \left(\frac{\eta}{18} \right)^{8/3} Y^{-2/3} \gamma_0^{-5/6}. \quad (16)$$

As we have mentioned above, the average luminosity of the BB component is $L_{\text{iso, BB}} \simeq 1.1 \times 10^{46} \text{ erg s}^{-1}$, which is of the order of L_{ph} estimated here.

Therefore, based on the observed temperature and luminosity, the delay between the GW signal and the soft BB component can be accounted for as the time it takes the fireball photosphere to radiate. The primary challenge of this interpretation is in explaining the nature of the hard non-thermal emission preceding the BB component. If both components are the result of the same expanding fireball, the photospheric emission is expected to occur earlier than or at the same time as the non-thermal emission. This requirement can be reconciled with the GBM data if the thermal component was subdominant and indistinguishable during the initial hard non-thermal pulse.

Alternatively, energy dissipation below the photospheric radius could also provide an explanation for the timing of the two pulses (Rees & Mészáros 2005). This could be achieved through a range of possible scenarios. Energy dissipation could occur through inelastic collisions between the decoupled neutron and proton populations within the jet (Beloborodov 2010), for example, or through magnetic reconnection processes (Giannios 2006). The emitted radiation would exhibit a modified blackbody spectrum and be released at the

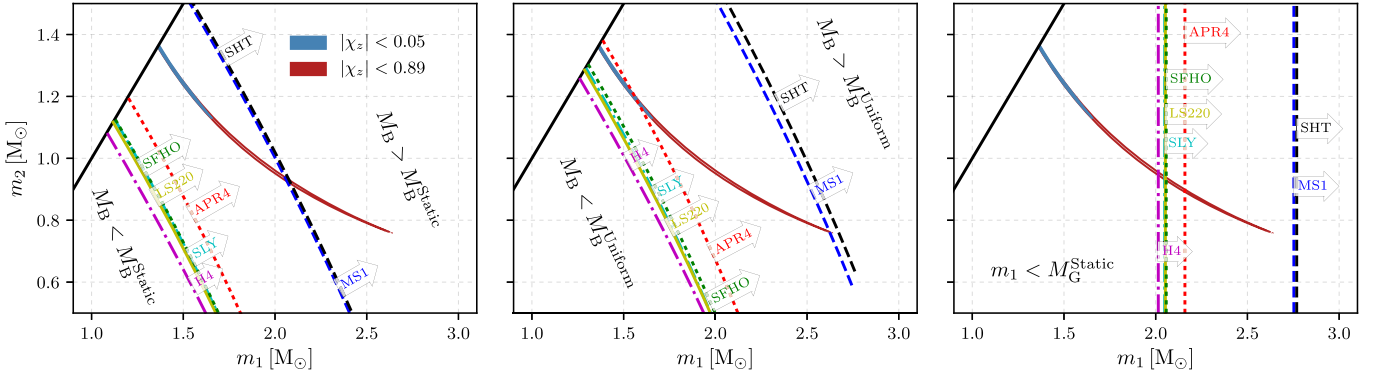


Figure 3. Critical mass boundaries for different EOSs in comparison with the 90% credible region of the gravitational masses inferred from GW170817 (prior limits on the spin magnitude, $|\chi_z|$, given in the legend). The slanted curves in the left panel and middle panel correspond to the maximum baryonic mass allowed for a single non-rotating NS (left) and for a uniformly rotating NS (middle). Arrows indicate for each EOS the region in the parameter space where the total initial baryonic mass exceeds the maximum mass for a single non-rotating or uniformly rotating NS, respectively. The right panel illustrates EOS-dependent cuts on the gravitational mass m_1 of the heavier star, with arrows indicating regions in which m_1 exceeds the maximum possible gravitational mass M_G^{Static} for non-rotating NSs. In all three panels the black solid line marks the $m_1 = m_2$ boundary, and we work in the $m_1 > m_2$ convention.

photospheric radius, resulting in similar arrival times to the thermal emission. A non-thermal pulse could also arise from a forward shock if the deceleration radius were located below the photosphere. Such a scenario would be possible if the density of the external medium were sufficiently in excess of the interstellar medium, which is a distinct possibility for such environments (Goriely et al. 2011; Bauswein et al. 2013; Hotokezaka et al. 2013).

The thermal component could also be the result of “cocoon” emission from shocked material surrounding the relativistic jet (Lazzati et al. 2017), which is expected to be softer and fainter than the non-thermal prompt emission (Ramirez-Ruiz et al. 2002; Pe’er et al. 2006). To examine this scenario, we utilize the relation between the radius of the shock breakout, duration and observed temperature proposed by Nakar & Sari (2012):

$$R = 1.4 \times 10^9 \left(\frac{t}{1 \text{ s}} \right) \left(\frac{T}{10 \text{ keV}} \right)^2 \text{ cm.} \quad (17)$$

Using the distance measurement, the blackbody spectral fit implies a radius of $R_{\text{BB}} = 3 \times 10^8 \text{ cm}$ that we can use as a proxy for the cocoon radius. This is within a factor of 4 of the relation, in spite of the fact that it applies to spherical geometry that is not guaranteed here, and the R_{BB} radius derived from the fit assumes thermal equilibrium. We thus consider this as evidence supporting the cocoon scenario.

Finally, the delay between the GW and EM signals may also be due in part to the time it takes for the relativistic jet to break out of the sub-relativistic dense ejecta surrounding the merger (Nagakura et al. 2014; Moharana & Piran 2017). We estimate that the breakout time for typical dynamical ejecta mass values of $\sim 0.1 M_\odot$ in such a merger (Hotokezaka et al. 2013) could not account for the entire observed delay. Lowering the reference isotropic kinetic luminosity of $L_{k,\text{iso}} = 10^{51} \text{ erg s}^{-1}$ assumed by Moharana & Piran (2017) could be one way to account for a larger delay. However, a luminosity below the one assumed in the breakout scenario substantially increases the likelihood of a “choked” jet that fails to break out of the surrounding medium (Aloy et al. 2005).

5.2. Neutron Star EOS Constraints

The observation of an SGRB associated with the merger of two NSs can be used to derive constraints on the EOS of NS matter (see theoretical studies by Belczynski et al. 2008; Fryer et al. 2015; Lawrence et al. 2015). To do this, we compare the measurement of the binary mass from the GW signal with two possible models of the merger remnant that powered the SGRB: (i) the merger remnant collapsed to a rotating BH with a surrounding disk that powered the SGRB (Shibata et al. 2006), or (ii) the merger formed a rapidly rotating, strongly magnetized NS (millisecond magnetar) with an accretion disk (Metzger et al. 2008).

We consider a representative sample of EOSs: SLy (Douchin & Haensel 2001), LS220 (Lattimer & Swesty 1991), SFHo (Steiner et al. 2013), H4 (Lackey et al. 2006), APR4 (Akmal et al. 1998), SHT (Shen et al. 2011), and MS1 (Müller & Serot 1996). For each EOS, we compute the maximum stable baryonic mass and gravitational mass of a non-rotating (static) NS, denoted M_B^{Static} and M_G^{Static} , respectively, and the maximum baryonic mass of a uniformly rotating NS M_B^{Uniform} (Gourgoulhon et al. 2001). The merger remnant can only collapse to a BH if its baryonic mass is larger than M_B^{Static} .

If we neglect rotational corrections, the baryonic masses m_{B1} , m_{B2} of the initial NSs are functions of their gravitational masses m_1 , m_2 only. In this approximation, a fixed total initial baryonic mass, M_B^{Initial} , corresponds to a curve in the (m_1, m_2) parameter space. In Figure 3 we show lines of M_B^{Static} and M_B^{Uniform} that bound the region of the parameter space in which the total mass of the binary is consistent with a stable non-rotating or uniformly rotating remnant, respectively. The figure also contains the 90% credible region of the gravitational masses obtained with a restricted or full spin prior (Abbott et al. 2017e). We note that the latter has a broader distribution of the component masses, such that the heavier NS can exceed M_G^{Static} for various EOS, which would correspond to either a supramassive (or even hypermassive) NS, or to a light BH. The maximum gravitational masses allowed for each EOS, M_G^{Static} , are shown in the figure as vertical lines.

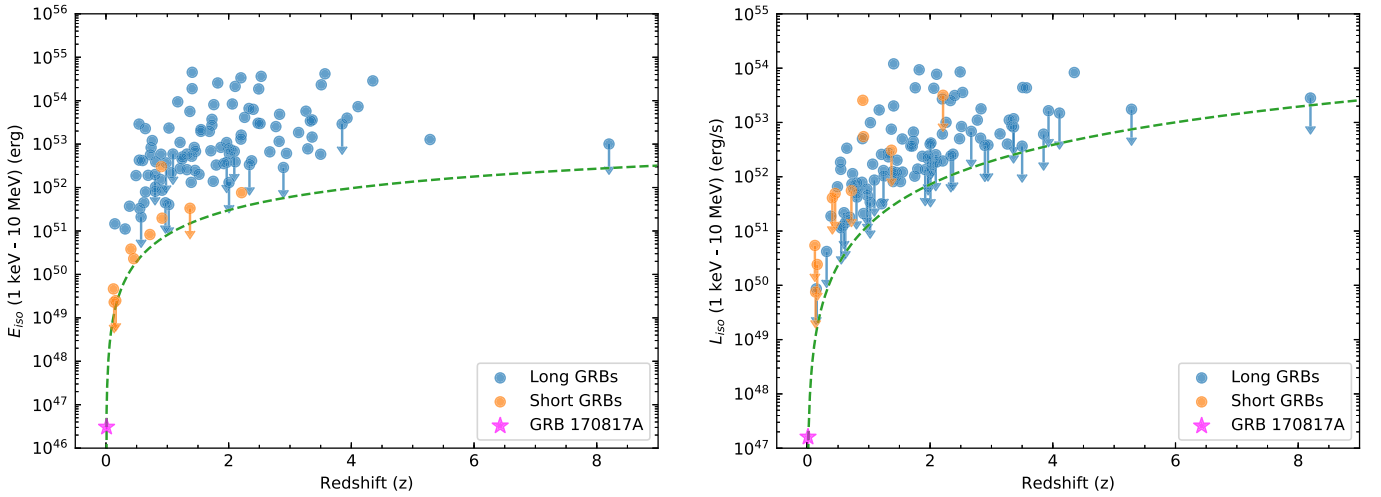


Figure 4. GRB 170817A is a dim outlier in the distributions of E_{iso} and L_{iso} , shown as a function of redshift for all GBM-detected GRBs with measured redshifts. Redshifts are taken from GRBOX (<http://www.astro.caltech.edu/grbox/grbox.php>) and Fong et al. (2015). Short- and long-duration GRBs are separated by the standard $T_{90} = 2$ s threshold. For GRBs with spectra best modeled by a power law, we take this value as an upper limit, marking them with downward pointing arrows. The power law spectra lack a constraint on the curvature, which must exist, and therefore, will overestimate the total value in the extrapolated energy range. The green curve demonstrates how the (approximate) GBM detection threshold varies as a function of redshift. All quantities are calculated in the standard 1 keV–10 MeV energy band.

Since the total baryonic mass of the system can only be reduced (by mass ejection), the maximum baryonic mass of the merger remnant and accretion disc is bound by $M_{\text{B}}^{\text{Initial}}$. From Figure 3, we can see that for the measured NS gravitational masses with the low-spin prior, the MS1 and SHT EOS could not form a BH since $M_{\text{B}}^{\text{Initial}} < M_{\text{B}}^{\text{Static}}$. Assuming that the magnitude of the spins is small, the MS1 and SHT EOS are incompatible with BH formation. If the dimensionless spins of the NSs are allowed to be larger than 0.05, BH formation is only disfavored: we find that a fraction 83% (MS1) and 84% (SHT) of the posterior distribution satisfies $M_{\text{B}}^{\text{Initial}} < M_{\text{B}}^{\text{Static}}$. For both spin priors, we find that the H4, LS220, SFHo, and SLy EOS result in $M_{\text{B}}^{\text{Initial}} > M_{\text{B}}^{\text{Uniform}}$. Even when assuming a large ejecta mass of $0.1 M_{\odot}$, the remaining mass cannot form a uniformly rotating NS. For those EOS, the merger either results in prompt BH formation or in a short-lived remnant, with a lifetime determined by the dissipation of differential rotation and/or disk accretion.

To be compatible with scenario (ii), the lifetime of the merger remnant would have to be sufficiently long to power the GRB. We note that prompt BH formation is a dynamic process accessible only to numerical relativity simulations. Although there are parameter studies (Hotokezaka et al. 2011; Bauswein et al. 2013), they only consider equal mass binaries. Considering also the error margins of those studies, we currently cannot exclude prompt collapse for the H4, LS220, SFHo, and SLy EOS. Finally, we note that for the APR4 EOS only the possibility of a stable remnant can be ruled out. More generally, only EOSs with $M_{\text{B}}^{\text{Static}} < 3.2 M_{\odot}$ are consistent with scenario (i) when assuming the low-spin prior, or with $M_{\text{B}}^{\text{Static}} < 3.7 M_{\odot}$ for the wider spin prior. These bounds were derived from the 90% credible intervals of the $M_{\text{B}}^{\text{Initial}}$ posteriors (and these, in turn, are determined for each EOS in order to account for binding energy variations). These upper limits are compatible with and complement the lower bounds on $M_{\text{G}}^{\text{Static}}$ from the observation of the most massive known pulsar, which has a mass of $(2.01 \pm 0.04) M_{\odot}$ (Antoniadis et al. 2013). In

Section 6.5 we will discuss some model-dependent implications of the lack of precursor and temporally extended gamma-ray emission from GRB 170817A on the progenitor NSs.

6. Gamma-ray Energetics of GRB 170817A and their Implications

Using the measured gamma-ray energy spectrum and the distance to the host galaxy identified by the associated optical transient, we compare the energetics of GRB 170817A to those of other SGRBs at known redshifts. Finding GRB 170817A to be subluminal, we discuss whether this dimness is an expected observational bias for joint GW–GRB detections, what insight it provides regarding the geometry of the gamma-ray emitting region, what we can learn about the population of SGRBs, update our joint detection estimates, and set limits on gamma-ray precursor and extended emission.

6.1. Isotropic Luminosity and Energetics of GRB 170817A

Using the “standard” spectral information from Goldstein et al. (2017) and the distance to the host galaxy NGC 4993 (42.9 ± 3.2 Mpc), we calculate the energetics of GRB 170817A using the standard formalisms (Bloom et al. 2001; Schaefer 2007). GRBs are believed to be relativistically beamed and their emission collimated (Rhoads 1999). Isotropic energetics are upper bounds on the true total energetics assuming the GRB is observed within the beaming angle of the brightest part of the jet. We estimate that the isotropic energy release in gamma-rays $E_{\text{iso}} = (3.1 \pm 0.7) \times 10^{46}$ erg, and the isotropic peak luminosity, $L_{\text{iso}} = (1.6 \pm 0.6) \times 10^{47}$ erg s $^{-1}$, in the 1 keV–10 MeV energy band. These energetics are from the source interval—i.e., the selected time range the analysis is run over—determined in the standard manner for GBM spectral catalog results, allowing us to compare GRB 170817A to other GRBs throughout this section. The uncertainties on the inferred isotropic energetics values here include the uncertainty on the distance to the host galaxy. As a cross check, the isotropic luminosity is also

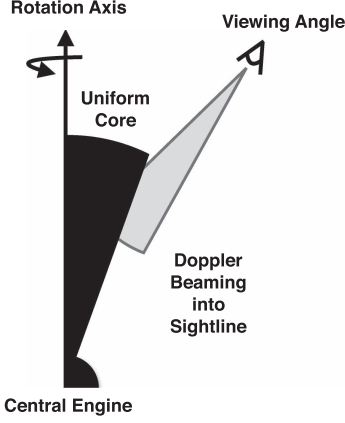
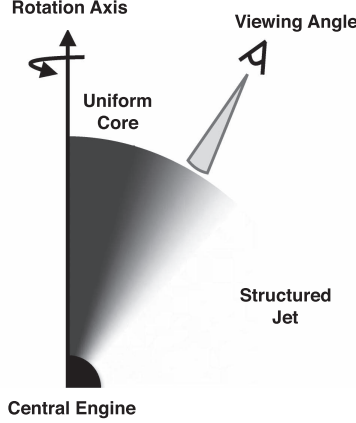
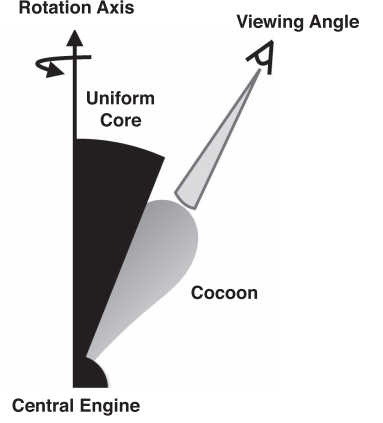
Scenario i: Uniform Top-hat Jet

Scenario ii: Structured Jet

Scenario iii: Uniform Jet + Cocoon


Figure 5. Three potential jet viewing geometries and jet profiles that could explain the observed properties of GRB 170817A, as described by scenarios (i)–(iii) in Section 6.2.

estimated using a Bayesian approach proposed by Fan (2017). Assuming a flat prior on isotropic luminosity, we obtain $L_{\text{iso}} = 1.2_{-0.6}^{+0.7} \times 10^{47} \text{ erg s}^{-1}$, which is consistent with the standard GBM approach. This Bayesian approach can be used to combine future joint GW-GRB observations to provide a redshift-independent estimate of the GRB luminosity function.

The two apparent components of GRB 170817A are sufficiently different that using an average spectrum to estimate the fluence may produce an inaccurate total luminosity. Therefore, we also estimate E_{iso} using the “detailed” fits described in Goldstein et al. (2017). Separating the hard peak best fit by a Comptonized function (a power law with an exponential cutoff) and the softer tail best fit by a BB spectrum, we estimate $E_{\text{iso,comp}} = (4.0 \pm 1.0) \times 10^{46} \text{ erg}$, and $E_{\text{iso,BB}} = (1.3 \pm 0.3) \times 10^{46} \text{ erg}$, for a total of $E_{\text{iso}} = (5.3 \pm 1.0) \times 10^{46} \text{ erg}$.

Compared to the distribution of GBM detected GRBs with measured redshift shown in Figure 4, GRB 170817A is 2 orders of magnitude closer and 2 to 6 orders of magnitude less energetic than other SGRBs. In particular, GRB 150101B was previously the weakest SGRB with a firm redshift association ($z = 0.134$; Fong et al. 2016), and its energetics (as measured by GBM) $E_{\text{iso}} = 2.3 \times 10^{49} \text{ erg}$, and $L_{\text{iso}} = 7.5 \times 10^{49} \text{ erg s}^{-1}$ are 2–3 orders of magnitude higher. As this was the previous dimmest burst, the minimum luminosity cut of $5 \times 10^{49} \text{ erg s}^{-1}$ used in Wanderman & Piran (2015) to fit a rate and an L_{iso} distribution to existing observations appeared reasonable; however, with GRB 170817A, the lower bound on the isotropic energetics distributions needs to be revised, as discussed in Section 6.4.

6.2. Implications of the Dimness on the Central Engine

The broad observed brightness distribution likely arises from a mixture of an intrinsic brightness distribution and geometric effects, which include the inclination angle of the system to Earth, the structure and width of the collimated jet itself, and the relativistic beaming angle θ_b . We consider several possibilities to explain why GRB 170817A is extremely dim (Figure 5): (i) we viewed it from beyond the half-jet opening angle θ_j for a standard top-hat model, (ii) the structure of the jet is more complicated than a simple top-hat model, (iii) the observed emission for GRB 170817A originates from a

different mechanism than for most SGRBs, or (iv) it is due solely to the intrinsic luminosity distribution and not the geometry of the system.

Scenario (i). Uniform top-hat jets (constant emissivity and Lorentz factor, Γ , within the jet aperture) with a sharp edge have been widely used to explain GRB properties, including jet breaks (Rhoads 1999). The top-hat jet is the simplest possible model for calculating off-axis parameters as it captures the basic physics of the system, but it is unable to account for smooth profiles in the Lorentz factor and the emissivity. Here the observed energetics are significantly lower than they would be if we were within θ_j .

In the top-hat scenario, off-axis values of physical quantities can be related to the on-axis values through the angle dependence of the relativistic Doppler factor:

$$\delta_D(\theta) = [\Gamma(1 - \beta \cos \theta)]^{-1} \approx 2\Gamma/(1 + \theta^2\Gamma^2), \quad (18)$$

where θ is the angle between the velocity vector v and the line of sight, and $\beta = v/c$. The relation for duration and peak energy is linear with δ_D (see, e.g., Granot et al. 2002):

$$\begin{aligned} \frac{T_{90}(\text{off-axis})}{T_{90}(\text{on-axis})} &= \frac{E_p(\text{on-axis})}{E_p(\text{off-axis})} = \frac{\delta_D(0)}{\delta_D(\theta_j - \zeta)} \\ &= \frac{1 - \beta \cos(\theta_j - \zeta)}{1 - \beta} \triangleq b \approx 1 + \Gamma^2(\zeta - \theta_j)^2, \end{aligned} \quad (19)$$

whereas $E_{\gamma,\text{iso}}(\text{off-axis})$ scales approximately $\propto b^{-2}$ for a viewing angle ζ between θ_j and $2\theta_j$. The duration in the on-axis scenario may be longer than inferred from the above equation, as the variable gamma-ray flux can be discerned above detector noise for a longer fraction of the total activity compared to emission viewed off-axis.

We use the observed quantities for GRB 170817A, $E_p \approx 200 \text{ keV}$, $E_{\gamma,\text{iso}} = 5.3 \times 10^{46} \text{ erg}$, and $T_{90} \approx 2 \text{ s}$, as values observed off-axis. If we assume that the on-axis values for GRB 170817A are consistent with typical values observed for SGRBs, we obtain $E_p = 6(b/30) \text{ MeV}$, $E_{\gamma,\text{iso}} = 5 \times 10^{49}(b/30)^2 \text{ erg}$, and $T_{90} = 7 \times 10^{-2}(b/30)^{-1} \text{ s}$. In particular using a fiducial range on $E_{\gamma,\text{iso}}(\text{on-axis})$ corresponding to the two orders of magnitude spread shown in

Figure 4 we obtain $b \approx \Gamma^2(\zeta - \theta_j)^2 \approx 30$ within a factor 3, which is a constraint on the values of Γ , ζ and θ_j .

If we assume a viewing angle of $\zeta = 30^\circ$ and $\Gamma = 300$ the uncertainty on b yields $\zeta - \theta_j \approx 1 \pm 0.5$ deg, a solid angle covering only 1% of a full sphere. Hence this configuration would require a fine tuning of the line of sight. However, if we assume $\Gamma = 30$ then the uncertainty on b yields $\zeta - \theta_j \approx 10 \pm 4$ deg, a solid angle that covers 10% of a full sphere, which is plausible without too much fine tuning. This argument only weakly depends on the particular value ζ , and illustrates that for large Γ a top-hat jet scenario is disfavored due to the sharp emission fall-off at the edges.

Scenario (ii). A more complex geometry involves a structured jet (Rossi et al. 2002, or Granot 2007 and references therein) which provides a wider range of angles from which the observer could still detect emission, and therefore does not require a fine-tuned viewing angle. Structured jet emission profiles include a uniform ultra-relativistic core surrounded by a power-law decaying wing where the energy and Lorentz factor depend on the distance from the jet axis (Pescalli et al. 2015), a Gaussian with a smooth edge and falloff outside the core (Zhang & Mészáros 2002; Kumar & Granot 2003), and a two-component jet with an ultra-relativistic narrow core and slightly slower outer jet (Frail et al. 2000; Berger et al. 2003; Racusin et al. 2008; Filgas et al. 2011), among other possibilities.

Structured jets can naturally explain the broad observed energetics distribution. Because SGRBs involve relativistic velocities, radiation is strongly beamed into angle θ_b . If the observed brightness depends on viewing geometry, i.e., is not uniform across the angle θ_j , then the part of the beam that we observe may be off-axis to the brightest part of the jet but we may still be within θ_b of some dimmer part of the emitting region, though in this case we would expect the Γ factor to vary as well.

Scenario (iii). Given the closeness of this burst it is possible that the observed emission is due to a different mechanism from other SGRBs, one that is intrinsically dim and thus undetectable at usual SGRB distances. We believe this explanation to be unlikely as the main emission episode of GRB 170817A is a typical SGRB (as measured by the observed gamma-ray properties). It is possible that the soft tail emission arises from a distinct mechanism. One explanation is “cocoon” emission from the relativistic jet shocking its surrounding non-relativistic material (Lazzati et al. 2017). We showed that “cocoon” emission could explain the thermal tail in Section 5.1. A possible full model for GRB 170817A is off-axis emission from a top-hat jet providing the main emission episode, with “cocoon” emission arising from the jet’s interaction with the surrounding torus that powers the main jet. The softer emission is near the detection limits of GBM and would not be detected to much greater distances, suggesting it may be a common property of SGRBs that is otherwise missed.

Scenario (iv). If GRB 170817A is viewed within both the collimated jet and the beaming angle, and the emission is constant across the traditional top-hat jet, then GRB 170817A is intrinsically much dimmer by orders of magnitude compared to other observed GRBs. This would mean that top-hat jets have an intrinsic distribution covering 6 orders of magnitude, which is difficult to envision given the limited mass ranges in the merger of two NSs (although see Metzger & Berger (2012)

and references therein). A broader intrinsic luminosity distribution might be accommodated if we assume that at least some SGRBs arise from the merging of an NS with a BH. It is possible, for example, that the brightest events may arise from NS–BH mergers with optimal mass ratio and spin parameters. Another possibility is that this broad luminosity range could arise from other properties of the system, such as the magnetic field strength of the progenitors or the intrinsic jet-opening angle distribution.

Observations of GW170817/GRB 170817A at other wavelengths (which are not explored in this *Letter*) will be necessary for a full understanding of this event. For example, evidence for X-ray emission that only arises at late times may provide evidence for this event occurring off-axis (see, e.g., Mészáros et al. 1998; Granot et al. 2002; Yamazaki et al. 2002). However, future joint detections of GW-GRB events can also provide a fuller understanding of the intrinsic energetics distributions and the effect geometry has on our observed brightness. Here the inclination constraint is not particularly informative as the inclination angle constraint, $\zeta \leq 36^\circ$, is comparable to the highest lower limit for a half-jet opening angle, $\theta_j > 25$ deg (Fong et al. 2015). If this is truly off-axis from a top-hat jet then it is unlikely to be a common occurrence. Only joint GW–EM detections will reveal if the intrinsic brightness varies according to the type of progenitor.

The updated expected joint detection rates in Section 6.4 suggest inferences on populations of joint detections may be possible sooner than previously thought.

6.3. Observational Bias Against Low-luminosity GRBs

The fact that GRB 170817A is orders of magnitude dimmer than the population of SGRBs with known redshifts raises the questions: (i) is it unexpectedly dim, and (ii) is there a population of SGRBs with comparable luminosities (and distances) that we are not detecting? We explore here whether the gap in luminosity compared to more luminous SGRBs is a result of the instrumental sensitivity for the detection of either the prompt or the afterglow emission of SGRBs, or whether our problem lies in the association of SGRBs to their host galaxies and thus redshift.

Burns et al. (2016) examine the observed relationship between redshift and gamma-ray fluence for SGRBs with known redshift and find no strong correlation. SGRBs that appear extremely bright are likely to be nearby because their inferred luminosities would otherwise be unrealistic, but SGRBs near the detection threshold of (current) GRB detectors are as likely to be nearby as far away. The intrinsically dim part of the SGRB luminosity distribution is detectable only at short distances.

GRB 170817A is our only clear case of a subluminal SGRB with known distance, so we investigate the maximum distance at which it could have triggered GBM. Assuming the event occurred at the same time and viewing geometry with respect to *Fermi*, with comparable detector background rates, we find that GRB 170817A could have been $\sim 30\%$ dimmer before falling below the on-board triggering threshold (Goldstein et al. 2017), corresponding to a maximum detection distance of about 50 Mpc. An approximate measure of the detectability distance given optimal detection conditions (e.g., low background, good geometry) suggests the maximum distance we could have detected this burst is about 80 Mpc—closer than any

other SGRB with a firmly determined redshift. While the GW horizon has been considered the limiting factor for joint detections with EM signals, this joint detection shows that we now must also account for an SGRB detection horizon given the sensitivity of the current gamma-ray observatories.

In addition to limited gamma-ray detector sensitivity, determining the redshift from EM observations alone is more difficult for SGRBs than for long GRBs. The fraction of SGRBs with detected X-ray afterglows for *Swift* BAT detected bursts is $\sim 75\%$ (Fong et al. 2015), compared to over 90% for long GRBs.¹⁸⁵ It is possible that SGRBs with subluminal prompt gamma-ray emission also have correspondingly weaker X-ray afterglows, and these could account for a large fraction of the quarter of SGRBs without X-ray detections. Even when the X-ray afterglows are detected, they are fainter and thus fade below detectability threshold faster than the afterglows of long GRBs, making direct measurement of the redshift from the afterglow exceedingly rare (Fong et al. 2015). For SGRBs, the redshift is instead usually determined from the host galaxy. This requires first that the afterglow be tied to a particular host galaxy, which can be difficult because the SGRB progenitors sometimes lie outside their putative hosts, owing to the natal kicks induced by the supernovae that produced the compact objects in the progenitor system (Wong et al. 2010). A well-localized (\sim few arcseconds) SGRB afterglow is associated with a galaxy within a small angular distance on the sky, using probabilistic arguments about chance alignment, and then the redshift of the host galaxy is measured.

Appendix B lists all SGRBs with possible redshifts. Most of the list was compiled by combining three relatively complete and recent literature samples (Fong et al. 2015; Lien et al. 2016; Siellez et al. 2016). Nearly all of these were detected by *Swift* BAT. It has been suggested that the BAT SGRB distribution is contaminated by the short tail of the long GRB distribution (Bromberg et al. 2013). Burns et al. (2016) find that the BAT sample is not significantly more contaminated than the GBM sample and the redshift distribution based on *Swift* BAT SGRBs is therefore a valid proxy for the redshift distribution of GBM SGRBs in the following discussion.

Berger (2010) discuss “hostless” SGRBs, which are well-localized SGRBs that have no obvious associated host galaxy despite deep observational limits. They suggested the hosts could be nearby galaxies at larger angular offset to the afterglow than others farther away, but also put forward the possibility of more distant, undetected hosts. Tunnicliffe et al. (2014) show that hostless SGRBs have an excess of nearby galaxies within a few arcminutes, relative to long GRBs or random positions, suggesting that at least some of these hostless SGRBs have nearby hosts. Therefore, the traditional assignment of probability of an SGRB to a host galaxy based solely on angular offset from a well-localized afterglow may exclude real associations with larger offsets, which are more likely to be measured for nearby events.

Tunnicliffe et al. (2014) also includes the closest potential host for an SGRB prior to GRB 170817A, with 81 Mpc for GRB 111020A. If real, this association implies an extremely low E_{iso} of $\sim 10^{46}$ erg, similar to GRB 170817A. In light of the secure association of GRB 170817A with GW170817, a subenergetic E_{iso} may no longer be a reason to doubt subluminal nearby SGRB host associations, and may suggest

a reconsideration of very nearby host galaxies with large projected angular offsets for hostless SGRBs. We include these putative host associations in Table 2. Also included are SGRBs with extended emission and bursts that have durations exceeding the standard T_{90} cut but are believed to be short based on other evidence such as spectral hardness. Asterisks indicate bursts, where the *Swift* BAT $T_{90} < 2$ s, that have localizations of a few arcseconds or better (as larger localizations increase the chance of false associations due to chance alignment), and for which the angular offset of the afterglow from the host fulfills standard association criteria. For further analysis this restricted sample is our “gold sample,” and the full sample the “total sample.”

One outstanding question is why we have not detected other SGRBs as close as GRB 170817A. We have established that bursts as dim as GRB 170817A will not be detected by current gamma-ray instruments if they lie much farther away than GRB 170817A. This raises questions about GRBs with luminosities between GRB 170817A and the rest of the GRBs with known luminosities. Some of these are surely being detected, albeit with unassigned redshifts and thus luminosities. While there are only ~ 40 SGRBs with possible redshifts, several hundreds have been detected without an assigned redshift. Nearby, subluminal SGRBs surely lie among them. There is a lower priority for following-up weak SGRBs, so if nearby events are systematically detected as weak bursts they may not have the required follow-up observations at lower wavelengths to determine the distance to the burst. It could also be that these weak bursts also have lower brightness at lower wavelengths, making them harder to detect even with follow-up observations. Lastly, we could be detecting these bursts in gamma-rays and X-rays, but failing to properly associate them with their hosts as discussed above.

GRB 170817A is unique in that its distance was first measured by GWs, which are currently detectable out to limited distances (roughly 100 Mpc) compared to other SGRBs with known redshifts (see Table 2). This is analogous to the first association of long GRBs with supernovae. Long GRBs have redshifts systematically higher than SGRBs (Coward et al. 2013). The long burst GRB 980425 is the closest GRB to date with a measured distance (and the only GRB of any class closer than GRB 170817A), and it was the first long GRB associated with a supernovae. GRB 980425 was 4 orders of magnitude less energetic than other GRBs detected at that time (Galama et al. 1998). Because supernovae are less luminous than long GRBs, the long GRBs that are associated with supernovae are systematically closer than the average population. Because of the Malmquist bias, a bias toward detecting intrinsically bright objects (Malmquist 1922), we only see dim long GRBs when they are nearby. This explains the subluminal nature of GRB 980425, and this observational peculiarity has been confirmed by other subluminal long GRB-SN detections, including GRB 031203/SN2003lw (Malesani et al. 2004), GRB 060218/SN2006aj (Modjaz et al. 2006), and GRB 100316D/SN2010bh (Cano et al. 2011), quantified as a population in Howell & Coward (2012). The history of GRB 980425, the other nearby subluminal long GRBs associated with supernova, and the lack of correlation between SGRB gamma-ray fluence and redshift noted by Burns et al. (2016) motivates the further development of subthreshold searches for counterparts to GW events and for subthreshold SGRBs in general. While GRB 170817A occurred nearby, and its favorable geometry

¹⁸⁵ https://swift.gsfc.nasa.gov/archive/grb_table/

to *Fermi* resulted in an on-board trigger, we anticipate that these untriggered searches of GBM and other gamma-ray data will uncover future counterparts to this GW-selected SGRB population.

Suggestions of nearby subluminescent SGRB populations existed prior to this discovery (Tanvir et al. 2005; Siellez et al. 2016). Tanvir et al. (2005) find a statistically significant correlation between a large sample of coarsely localized SGRBs detected by the Burst And Transient Source Experiment (BATSE) and a sample of nearby galaxies. Without associating individual SGRBs with a potential host, they conclude that $\sim 10\%$ of the SGRB sample could be part of a nearby subluminescent population. Siellez et al. (2016) infer the presence of a nearby subluminescent SGRB population through a study of SGRBs with known redshift in the context of BNS and NS–BH population evolution. They find an excess of actual nearby low-luminosity SGRBs using the results from their simulations, covering a broad range of assumed lifetimes for the binary system prior to merger.

Giant flares from the highly magnetized NSs known as magnetars can be detected outside our galaxy, with the sole extragalactic example tied to its host coming from SGR 0525-66, in the Large Magellanic Cloud (Evans et al. 1980). A giant flare from the galactic magnetar SGR 1806-20 showed a gamma-ray spectrum measured by the Konus–Wind instrument that was well-fit by a blackbody with temperature ~ 175 keV (Hurley et al. 2005), harder than a regular magnetar burst. This hard spectrum led to the idea that giant flares from magnetars in nearby galaxies might be a sub-population hiding among the general SGRB population (Hurley et al. 2005). Tanvir et al. (2005) found a stronger correlation of BATSE SGRBs with early-type than late-type galaxies, which is not expected if nearby SGRBs arise from giant magnetar flares in nearby galaxies, but is consistent with a BNS origin. GRB 170817A is clearly associated with a BNS merger, but even without the connection to GW170817, the spectrum of GRB 170817A in the GBM data strongly disfavored the BB fit expected for a giant magnetar flare. Another possible signature of a giant magnetar flare is the ringing in its tail at the NS period of a few seconds, which could be detected by GBM or by SPI-ACS for flares outside our galaxy providing it was close enough. A search for periodic or quasi-periodic emission in the GBM data for GRB 170817A (Goldstein et al. 2017) found no periodic modulation, providing another discriminant between SGRBs and nearby extragalactic giant magnetar flares that might be masquerading as SGRBs.

6.4. Predicted Detection Rates

The intrinsic specific volumetric SGRB rate is often quoted to be around $10 \text{ Gpc}^{-3} \text{ yr}^{-1}$ (see, e.g., Guetta & Piran 2006; Coward et al. 2012; Fong et al. 2015; with the value originating from Nakar et al. 2006, who noted that the true rate could be much higher). However, unlike GW signals, SGRBs do not have a clear relationship between the observed distance and brightness. As discussed in the previous section, this can be due to intrinsic variations in SGRB luminosities, as well as structure in the jet. In this Section, we investigate the former scenario presenting the implications of GW170817/GRB 170817A for future GW and SGRB observations in terms of a simple standard model for the SGRB luminosity distribution. Similar interpretations for other, perhaps more elaborate, models are straightforward.

We model the SGRB luminosity function as a broken power law, with a logarithmic distribution¹⁸⁶

$$\phi_o(L_{\text{iso}}) = \begin{cases} \left(\frac{L_{\text{iso}}}{L_*}\right)^{-\alpha_L} & L_{\text{iso}} < L_* \\ \left(\frac{L_{\text{iso}}}{L_*}\right)^{-\beta_L} & L_{\text{iso}} > L_* \end{cases}, \quad (20)$$

where L_{iso} is the peak isotropic luminosity (in the source frame) between 1 keV and 10 MeV, and α_L and β_L give the power law decay below and above the break at L_* .¹⁸⁷ Here, we follow Wanderman & Piran (2015) in using $L_* \simeq 2 \times 10^{52} \text{ erg s}^{-1}$, $\alpha_L \simeq 1$, and $\beta_L \simeq 2$. The other important parameter is the minimum SGRB luminosity, which determines the lower cutoff of the luminosity distribution. This is poorly constrained as only nearby low luminosity SGRBs are observable. In Wanderman & Piran (2015) the minimum luminosity is taken to be $L_{\text{min}} = 5 \times 10^{49} \text{ erg s}^{-1}$, while other studies use values ranging from $1 \times 10^{49} \text{ erg s}^{-1}$ to $\text{few} \times 10^{50} \text{ erg s}^{-1}$ (Regimbau et al. 2015). We assume a threshold value for detectability in GBM of 2 photons $\text{cm}^{-2} \text{ s}^{-1}$ for the 64 ms peak photon flux in the 50–300 keV band, which is higher than the minimum detectability value to account for the sky-dependent sensitivity of GBM. Furthermore, we model the SGRB spectrum using the Band function with parameters taken from Wanderman & Piran (2015) (namely, $E_{\text{peak}} = 800 \text{ keV}$, $\alpha_{\text{Band}} = -0.5$, and $\beta_{\text{Band}} = -2.25$). This spectrum is significantly harder than the one observed for GRB 170817A. The cumulative observed rate predicted for GBM by this base model is shown as a function of redshift in Figure 6 by the purple solid curve.

As discussed in Section 6.1, the inferred L_{iso} is $(1.6 \pm 0.6) \times 10^{47} \text{ erg s}^{-1}$, which is significantly lower than any previously detected SGRB, and thus is in tension with this model. In particular, we must extend the lower limit of the luminosity down by a factor of at least 500. At present, there is rather little information available about the low luminosity distribution due to the observational biases discussed in Section 6.3 and, consequently, there is a significant degeneracy between the minimum SGRB luminosity and the rate (Wanderman & Piran 2015). Let us consider the most straightforward extension of the above model and set $L_{\text{min}} = 1 \times 10^{47} \text{ erg s}^{-1}$ while maintaining $\alpha_L = 1$. In order to retain the same prediction for high-luminosity SGRBs, this requires a 500-fold increase in the number of SGRBs, with the majority emitting at low luminosity. The cumulative observed rate predicted for GBM by this simple extension is shown as a function of redshift in Figure 6 by the red solid curve, and is comparable to the measured BNS merger rate shown in black. This simple extension would imply SGRBs are not beamed and that essentially all BNS mergers are accompanied by at least a subluminescent SGRB.

Therefore, to reduce this tension and explore other possible extensions, we introduce an additional power law break below

¹⁸⁶ To get the linear distribution of luminosities, both α_L and β_L must be increased by 1.

¹⁸⁷ Other studies use a smaller energy band when defining the luminosity, and this has an impact on the value of L_* , although not on the slopes of the power law components.

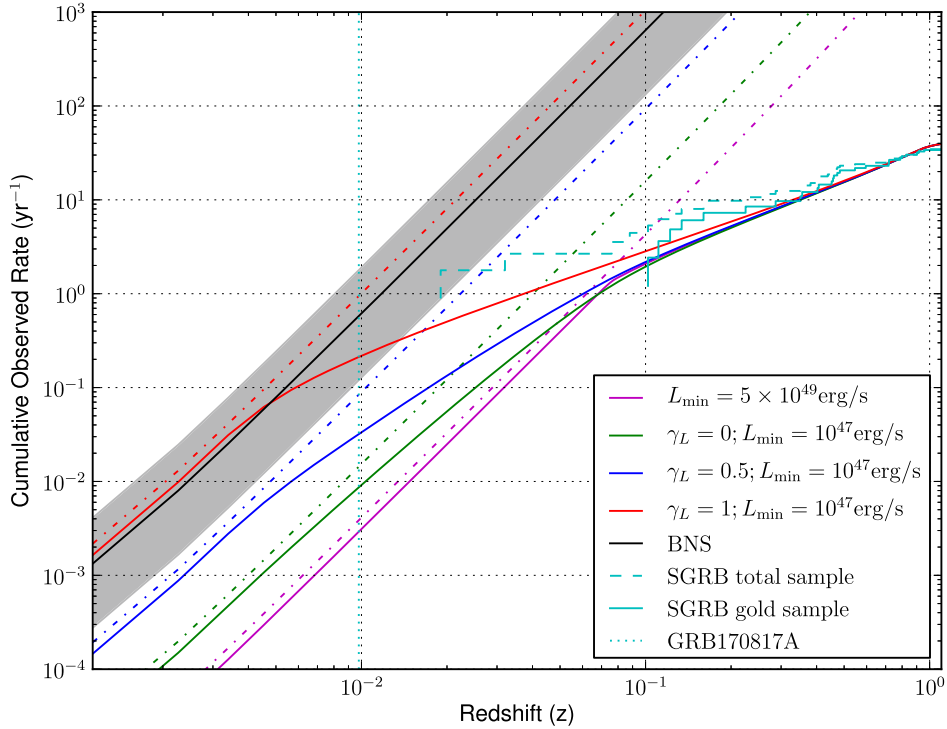


Figure 6. Predicted detection rates per year as a function of redshift. The red, blue, and green solid lines refer to the GBM observed SGRB rate assuming a minimum luminosity L_{\min} of $1 \times 10^{47} \text{ erg s}^{-1}$, and $\alpha_L = 1$, $\beta_L = 2$ and $\gamma_L = \{1, 0.5, 0\}$ in Equation (21), respectively. The purple solid line refers to the base model with L_{\min} of $5 \times 10^{49} \text{ erg s}^{-1}$. The four curves are normalized by imposing 40 triggered SGRBs per year. As γ_L increases, the observed rate is no longer volumetric at lower and lower redshifts, because a fraction of SGRBs becomes too dim to be detected. For reference, the red, blue and green dot-dashed curves show the local SGRB occurrence rate for $L_{\min} = 1 \times 10^{47} \text{ erg s}^{-1}$ and $\gamma_L = \{1, 0.5, 0\}$, respectively. The black line and gray band show the BNS merger rate $1540_{-1220}^{+3200} \text{ Gpc}^{-3} \text{ yr}^{-1}$ determined with the detection of GW170817 (Abbott et al. 2017e). For comparison, the measured SGRBs redshift distribution from Table 2 is shown in cyan, and is broadly compatible with all of the models. The dotted vertical cyan line refers to the redshift of GRB 170817A host galaxy.

$$L_{**} = 5 \times 10^{49} \text{ erg s}^{-1}:$$

$$\phi_o(L_{\text{iso}}) = \begin{cases} \left(\frac{L_{\text{iso}}}{L_{**}}\right)^{-\gamma_L} \left(\frac{L_{**}}{L_*}\right)^{-\alpha_L} & L_{\text{iso}} < L_{**} \\ \left(\frac{L_{\text{iso}}}{L_*}\right)^{-\alpha_L} & L_{**} < L_{\text{iso}} < L_* \\ \left(\frac{L_{\text{iso}}}{L_*}\right)^{-\beta_L} & L_{\text{iso}} > L_* \end{cases} \quad (21)$$

and consider three values $\gamma_L = \{1, 0.5, 0\}$ for the power law index below this second break. We normalize these three cases to 40 triggered SGRBs per year for GBM, and the $\gamma_L = 1$ case corresponds to the simple extension discussed above. For reference, Figure 6 shows the local SGRB occurrence rate for $L_{\min} = 1 \times 10^{47} \text{ erg s}^{-1}$ and $\gamma_L = \{1, 0.5, 0\}$ indicated by the red, blue, and green dotted curves, respectively, and the BNS merger rate $1540_{-1220}^{+3200} \text{ Gpc}^{-3} \text{ yr}^{-1}$ determined with the detection of GW170817 (gray band, with the mean in black; Abbott et al. 2017e). The $\gamma_L = 1$ case produces the largest number of subluminal SGRBs, and leads to a sharp departure at redshift ~ 0.005 from volumetric detection to detection limited by the GBM sensitivity. For $\gamma_L = 0$ the transition is smoother as there is only a small number of subluminal SGRBs, and the observed rate departs gradually from the occurrence rate.

When we include the luminosity of GRB 170817A by setting $L_{\min} = 1 \times 10^{47} \text{ erg s}^{-1}$ and $\gamma_L = 1$, the expected

detection rate at a redshift of $z \approx 0.1$ is around a factor of 2 higher than for the Wanderman & Piran (2015) model. At a redshift of $z \approx 0.01$, which is close to the observed redshift for GRB 170817A, rather than expecting to observe 1 event per 650 years with GBM, this is increased to 1 per year. The expected detection rate at this redshift for the $\gamma_L = 0.5$ and $\gamma_L = 0$ extensions is of roughly 1 observed event per 10 and 65 years, respectively. The expectations we obtain for GBM are consistent with the distribution of SGRBs with known redshifts reported in Table 2, in Appendix B.

Using the BNS merger volumetric rate estimated from GW170817 as a new input to the detection rate calculation presented in Abbott et al. (2017a), the LIGO–Virgo detection rate is narrowed down from 0.04–100 to ~ 1 –50 BNS coalescences during the 2018–19 observing run, with the remaining uncertainty arising in part from the not-yet-known detector sensitivities during that run. At design sensitivity, the LIGO and Virgo detectors can expect to detect ~ 6 –120 BNS coalescences per year, as opposed to the previously estimated 0.1–200 BNS coalescences per year. Inclusion of any additional BNS detections in the meantime will allow this prediction to be further sharpened.

Independently, we use the GBM detection rate as a function of redshift to predict joint GW–GRB BNS detection rates (Clark et al. 2015). Both the rates and their relative uncertainties are significantly reduced, compared to the GW-only detection rate estimates above, since the majority of distant mergers will be undetectable by GBM and the GBM

SGRB detection rate is well measured. The degree to which GBM-selected SGRBs are preferentially on-axis is unclear. When estimating the joint detection rate we include both no selection and a pure on-axis selection hypothesis, the latter implying a larger detection probability by the LIGO and Virgo detectors. During the 2018–19 observing run, we expect 0.1–1.4 joint detections per year for the GW interferometer network and GBM triggered SGRBs, with the high end of the interval corresponding to the $\alpha_L = 1$, $L_{\min} = 1 \times 10^{47} \text{ erg s}^{-1}$ extension of the luminosity function. At design sensitivity, the expected joint detection rate increases to 0.3–1.7 per year.

Future joint GW-SGRB observations will provide significant new insights into low-luminosity SGRBs. In particular, both joint observations and lower limits on distances to SGRBs not observed in GWs (e.g., GRB 150906B in Abbott et al. 2017b) will constrain the rate of nearby GRBs. Future GW observations of BNS mergers will reduce the uncertainty in the rate of such events, while observation of GW signals with no SGRB counterpart will limit the SGRB beaming angles. Finally, sub-threshold searches in GRB data around the time of GW events could significantly increase the number of joint observations.

6.5. Limits on Precursor and Extended Emission

At gamma-ray energies, SGRBs are characterized by a prompt emission episode lasting at most ~ 2 s. Observational evidence for precursor flares associated with SGRBs (Troja et al. 2010; Burns 2017; Minaev & Pozanenko 2017) and temporally extended emission (Lazzati et al. 2001; Connaughton 2002) is so far inconclusive. Given the small distance to the source, the absence of such emission from GRB 170817A provides an important data point and may constrain models that predict it. The flux upper limits set in Section 2.2 correspond to an intrinsic upper limit of $\sim 2.4 \times 10^{47} \text{ erg s}^{-1}$ for precursor emission on the 0.1 s timescale, $\sim 7.0 \times 10^{46} \text{ erg s}^{-1}$ for precursor emission on the 1.0 s timescale, and $\sim 2.2 \times 10^{46} \text{ erg s}^{-1}$ for extended emission on the 10 s timescale.

Magnetospheric interactions in NS binaries have been proposed as a source of nearly isotropic emission preceding the merger (e.g., Hansen & Lyutikov 2001; Metzger & Zivancev 2016). In the context of such models, the non-detection of precursors associated with GW170817 suggests the absence of strong magnetic fields in the last ~ 200 s before merger. Hansen & Lyutikov (2001), for instance, predict a luminosity that depends on the magnetic field B as $L \simeq 7.4 \times 10^{45} (B/10^{15} \text{ G})^2 (a/10^7 \text{ cm})^{-7} \text{ erg s}^{-1}$. We can combine this estimate with the least-constraining GBM intrinsic upper limit above and assume a final separation $a = 3 \times 10^6 \text{ cm}$ before disruption. The resulting limit is $B < 8 \times 10^{13} \text{ G}$, which is weaker than the magnetic fields of most known magnetars (Olausen & Kaspi 2014). However, the GBM upper limit still lies within the luminosity range of other similar models (Metzger & Zivancev 2016).

Resonant shattering of the NS crust has also been proposed as a source of emission prior to merger, with a maximum time delay of tens of seconds and nearly isotropic angular distribution (Tsang et al. 2012). The luminosity of such precursor emission depends on the crust breaking strain ϵ_b and the emission timescale Δt as $L \simeq 7 \times 10^{48} \epsilon_b^2 / \Delta t \text{ erg}$, from which we can derive $\epsilon_b^2 \lesssim 10^{-2} (\Delta t / 1 \text{ s})$. Assuming this mechanism took place in GW170817, and taking $\epsilon_b = 0.1$

(Horowitz & Kadau 2009), the emission either lasted more than a few seconds or happened below the GBM energy range, i.e., $\sim 10 \text{ keV}$. There might also be a dependence of the luminosity on the details of the NS EOS, although that is yet to be investigated in detail. Similarly to magnetospheric interaction, however, resonant shattering emission ultimately requires a sufficiently large magnetic field and a simple explanation for the absence of a signal is again the lack of intense magnetic fields prior to merger.

GBM and SPI-ACS observed no temporally extended gamma-ray emission for GRB 170817A. Such emission would be a signature of a long-lived NS remnant powering the SGRB and our flux limits may suggest instead that the remnant is a BH. Metzger et al. (2008) invoke a long-lived millisecond magnetar to explain SGRBs with extended gamma-ray emission (Norris & Bonnell 2006), and millisecond magnetars have also been suggested as possible causes for the plateaus seen in X-ray afterglows of some SGRBs (Rowlinson et al. 2013). The earliest X-ray observation was only performed 50 ks after GRB 170817A (Evans et al. 2017) and hence limits are only set after this time. Future observations may further constrain this scenario, e.g., radio observations on the timescale of a year (Fong et al. 2016).

We encourage the development of quantitative predictions of luminosity as a function of energy, time and physical parameters of the source, as the multiple upcoming joint observations of BNS mergers suggest the possibility of interesting constraints on the pre-merger physics.

7. Conclusion

The joint observation of GW170817 and GRB 170817A confirms the association of SGRBs with BNS mergers. With just one joint event, we have set stringent limits on fundamental physics and probed the central engine of SGRBs in ways that have not been possible with EM data alone, demonstrating the importance of multi-messenger astronomy.

The small time offset and independent localizations, though coarse, allowed an unambiguous association of these two events. Because GRB 170817A occurred nearby, an autonomous trigger on-board GBM alerted follow-up observers to the presence of a counterpart to GW170817. At design sensitivity, however, Advanced LIGO and Virgo could in principle detect GW170817 beyond the distance that any active gamma-ray observatory would trigger on a burst like GRB 170817A. Subthreshold searches for SGRBs can extend the gamma-ray horizon and the detection of GRB 170817A provides motivation for further subthreshold search development.

A joint detection at greater distance and for an SGRB with more typical energetics would allow tighter constraints on the temporal offset and the derived inferences. Should NS–BH binaries also be SGRB progenitors, only a joint detection between GW and EM can provide decisive evidence.

In this Letter we propose several explanations for the observed dimness of GRB 170817A. We suggest joint detections should be more common than previously predicted, and future observations of multiple events should enable a study of the populations of mergers and their associated SGRBs, shedding light on the jet geometry and intrinsic brightness distribution. Furthermore, detections with multiple

GW interferometers can provide more stringent constraints on the inclination angles of these systems. The joint detections of SGRBs arising from BNS and NS–BH mergers will constrain the fraction of SGRBs originating from each progenitor class.

The global network of GW detectors and wide-field gamma-ray instruments, such as *Fermi*-GBM and *INTEGRAL*/SPI-ACS, are critical to the future of multi-messenger astronomy in the GW era.

We dedicate this Letter to the memory of Neil Gehrels. His pioneering work in gamma-ray astronomy and his vision for multi-messenger astrophysics were instrumental to our discoveries.

The authors thank the referees for their invaluable comments and feedback, especially in a timely manner. The authors gratefully acknowledge the support of the United States National Science Foundation (NSF) for the construction and operation of the LIGO Laboratory and Advanced LIGO as well as the Science and Technology Facilities Council (STFC) of the United Kingdom, the Max-Planck-Society (MPS), and the State of Niedersachsen/Germany for support of the construction of Advanced LIGO and construction and operation of the GEO600 detector. Additional support for Advanced LIGO was provided by the Australian Research Council. The authors gratefully acknowledge the Italian Istituto Nazionale di Fisica Nucleare (INFN), the French Centre National de la Recherche Scientifique (CNRS) and the Foundation for Fundamental Research on Matter supported by the Netherlands Organisation for Scientific Research, for the construction and operation of the Virgo detector and the creation and support of the EGO consortium. The authors also gratefully acknowledge research support from these agencies as well as by the Council of Scientific and Industrial Research of India, the Department of Science and Technology, India, the Science & Engineering Research Board (SERB), India, the Ministry of Human Resource Development, India, the Spanish Agencia Estatal de Investigación, the Vicepresidència i Conselleria d’Innovació Recerca i Turisme and the Conselleria d’Educació i Universitat del Govern de les Illes Balears, the Conselleria d’Educació Investigació Cultura i Esport de la Generalitat Valenciana, the National Science Centre of Poland, the Swiss National Science Foundation (SNSF), the Russian Foundation for Basic Research, the Russian Science Foundation, the European Commission, the European Regional Development Funds (ERDF), the Royal Society, the Scottish Funding Council, the Scottish Universities Physics Alliance, the Hungarian Scientific Research Fund (OTKA), the Lyon Institute of Origins (LIO), the National Research, Development and Innovation Office Hungary (NKFI), the National Research Foundation of Korea, Industry Canada and the Province of Ontario through the Ministry of Economic Development and Innovation, the Natural Science and Engineering Research Council Canada, the Canadian Institute for Advanced Research, the Brazilian Ministry of Science, Technology, Innovations, and Communications, the International Center for Theoretical Physics South American Institute for Fundamental Research (ICTP-SAIFR), the Research Grants Council of Hong Kong, the National Natural Science Foundation of China (NSFC), the Leverhulme Trust, the

Research Corporation, the Ministry of Science and Technology (*MOST*), Taiwan and the Kavli Foundation. The authors gratefully acknowledge the support of the NSF, STFC, MPS, INFN, CNRS and the State of Niedersachsen/Germany for provision of computational resources.

The USRA co-authors gratefully acknowledge NASA funding through contract NNM13AA43C. The UAH co-authors gratefully acknowledge NASA funding from cooperative agreement NNM11AA01A. E.B. and T.D.C. are supported by an appointment to the NASA Postdoctoral Program at the Goddard Space Flight Center, administered by Universities Space Research Association under contract with NASA. D.K., C.A.W.H., C.M.H., and T.L. gratefully acknowledge NASA funding through the *Fermi* GBM project. Support for the German contribution to GBM was provided by the Bundesministerium für Bildung und Forschung (BMBF) via the Deutsches Zentrum für Luft und Raumfahrt (DLR) under contract number 50 QV 0301. A.v.K. was supported by the Bundesministeriums für Wirtschaft und Technologie (BMWi) through DLR grant 50 OG 1101. N.C. and J.B. acknowledge support from NSF under grant PHY-1505373. S.M.B. acknowledges support from Science Foundation Ireland under grant 12/IP/1288.

This work is based on observations with *INTEGRAL*, an ESA project with instruments and science data center funded by ESA member states (especially the PI countries: Denmark, France, Germany, Italy, Switzerland, Spain), and with the participation of Russia and the USA. The *INTEGRAL* SPI project has been completed under the responsibility and leadership of CNES. The SPI-ACS detector system has been provided by MPE Garching/Germany. The SPI team is grateful to ASI, CEA, CNES, DLR, ESA, INTA, NASA and OSTC for their support. The Italian *INTEGRAL* team acknowledges the support of ASI/INAF agreement n. 2013-025-R.1. R.D. and A.v.K. acknowledge the German *INTEGRAL* support through DLR grant 50 OG 1101. A.L. and R.S. acknowledge the support from the Russian Science Foundation (grant 14-22-00271). A.D. is funded by Spanish MINECO/FEDER grant ESP2015-65712-C5-1-R. Some of the results in this paper have been derived using the HEALPix (Gorski et al. 2005) package. We are grateful VirtualData from LABEX P2IO for enabling access to the StratusLab academic cloud. We acknowledge the continuous support by the *INTEGRAL* Users Group and the exceptionally efficient support by the teams at ESAC and ESOC for the scheduling of the targeted follow-up observations.

Appendix A

Full Derivation of Photospheric Radius

In order to explain the observed soft BB component, we present a model that simultaneously yields predictions on (1) the time difference between the GW emission and the beginning of the gamma-ray radiation, (2) the estimated temperature of the BB component ($k_B T_{\text{BB}}^{\text{obs}} = (10.3 \pm 1.5) \text{ keV}$) and (3) its average isotropic luminosity, $L_{\text{iso, BB}} = E_{\text{iso, BB}}/\Delta t_{\text{BB}} = 1.1 \times 10^{46} \text{ erg s}^{-1}$, where we have used the source interval width of the soft tail spectral fit of $\Delta t_{\text{BB}} = 1.15 \text{ s}$.

Following MR00, our model depends upon three main parameters to provide predictions of the aforementioned three observable quantities. First, the radius from which the fireball

is initiated, which is assumed to be $R_0 = 6GM_{\text{BH}}/c^2$ (the innermost stable circular orbit of a Schwarzschild BH with a mass equal to M_{BH}). In our case $R_0 = 2.5 \times 10^6$ cm, and $M_{\text{BH}} = 2.8 M_{\odot}$. From numerical models of GRB jets produced in BNS merger remnants (e.g., Aloy et al. 2005), the value of R_0 can be associated to the stagnation point of a relativistic outflow, and it is fairly well constrained to be a few gravitational radii of the BH. Second, the initial luminosity of the fireball, L_0 . This is a free parameter of the model and we note it can be much larger than $L_{\text{iso,BB}}$, since the fireball must expand from its initial volume ($\sim R_0^3$) to the size where the photosphere appears (see below). This is also needed, since the observed gamma-ray luminosity, will be a fraction $0 < \epsilon_r \leq 1$ of the total (kinetic) luminosity. Finally, the third parameter is the dimensionless entropy of the fireball, η . For a fireball baryon load \dot{M} and a luminosity L_0 , $\eta = L/(\dot{M}c^2)$. Typical values of η are larger than 100 to prevent the compactness problem (Goodman 1986), which is not an issue for GRB 170817A owing to the lack of emission detected above 511 keV. Therefore, our model may allow for values of η substantially smaller than ~ 100 . As we shall see, a combination of $L_0 \simeq 10^{50}$ erg and $\eta \simeq 18$, results in a viable model to account for the delay of GRB with respect to the GW signal and the average luminosity of the soft BB component.

The initial BB temperature in units of the electron rest mass is given by (MR00, Equation (5))

$$\Theta_0 = \left(\frac{k_{\text{B}}}{m_e c^2} \right) \left(\frac{L_0}{4\pi R_0^2 c a_r} \right)^{1/4} \simeq 1.5 \left(\frac{L_0}{10^{50} \text{ erg s}^{-1}} \right)^{1/4} \left(\frac{R_0}{2.5 \times 10^6 \text{ cm}} \right)^{-1/2}, \quad (22)$$

where $a_r = 7.57 \times 10^{-18} \text{ kg cm}^{-1} \text{ s}^{-2} \text{ K}^{-4}$ is the radiation constant. The value of Θ_0 corresponds to a comoving temperature $k_{\text{B}} T_0 \simeq 750$ keV. The radius at which the internal energy of the fireball is converted into kinetic energy, i.e., the saturation radius is

$$R_s = \eta R_0 \simeq 4.5 \times 10^7 \text{ cm} \left(\frac{\eta}{18} \right) \left(\frac{R_0}{2.5 \times 10^6 \text{ cm}} \right). \quad (23)$$

The critical baryon load η_* below which the photosphere of an expanding fireball happens after the fireball coasts at constant Lorentz factor $\gamma \simeq \eta$, i.e., at radii larger than R_s , is given by (MR00)

$$\eta_* = \left(\frac{L_0 \sigma_T Y}{4\pi m_p c^3 R_0} \right)^{1/4}, \quad (24)$$

where Y is the number of electrons per baryon, $\sigma_T = 6.65 \times 10^{-25} \text{ cm}^2$ is the Thomson cross-section. Using fiducial values, we obtain

$$\eta_* \simeq 470 \left(\frac{L_0}{10^{50} \text{ erg s}^{-1}} \right)^{1/4} \left(\frac{R_0}{2.5 \times 10^6 \text{ cm}} \right)^{-1/4} Y^{1/4}. \quad (25)$$

In the previous expression, we have taken $Y \simeq 1$, which is appropriate once pairs are not present in the system. This is the case for radii larger than R_p (MR00)

$$R_p = R_0 \frac{\Theta_0}{\Theta_p} \simeq 1.1 \times 10^8 \text{ cm} \left(\frac{L_0}{10^{50} \text{ erg s}^{-1}} \right)^{1/4} \times \left(\frac{R_0}{2.5 \times 10^6 \text{ cm}} \right)^{1/2} \left(\frac{\Theta_p}{0.03} \right)^{-1}, \quad (26)$$

where the comoving dimensionless temperature below which e^{\pm} pairs drop out of equilibrium is $\Theta_p \simeq 0.03 \simeq 17$ keV. Since we have set $\eta < \eta_*$, the photosphere will happen at a radius (MR00)

$$R_{\text{ph}} = \frac{L \sigma_T Y}{4\pi m_p c^3 \eta^3} \simeq 2 \times 10^{13} \text{ cm} \left(\frac{L_0}{10^{50} \text{ erg s}^{-1}} \right) \left(\frac{\eta}{18} \right)^{-3} Y. \quad (27)$$

Note that $R_p \ll R_{\text{ph}}$ for our choice of tunable parameters.

The laboratory frame time needed for the fireball expanding at roughly the speed of light to reach the transparency radius is $t_{\text{ph}} \simeq R_{\text{ph}}/c$, thus,

$$t_{\text{ph}} \simeq 672 \text{ s} \left(\frac{L_0}{10^{50} \text{ erg s}^{-1}} \right) \left(\frac{\eta}{18} \right)^{-3} Y. \quad (28)$$

To compute the time delay between a photon emitted at R_0 at $t = 0$ (namely, signaling the GW detection) and another one at R_{ph} , we must consider that the fireball begins its expansion from rest, in which case we shall apply the following relation between the arrival time and the time at which the photosphere appears

$$t_a \simeq t_{\text{ph}} \left(\frac{1}{2\eta^2} + 1 - \cos \vartheta \right), \quad (29)$$

where ϑ is the angle between the radial direction and the line of sight and $\cos \vartheta$ takes values only in the interval $[v/c, 1]$ (Bianco et al. 2001). Using fiducial values for η , we obtain

$$t_a^{(1)} \simeq \frac{t_{\text{ph}}}{2\eta^2} \simeq 1.0 \text{ s} \left(\frac{L_0}{10^{50} \text{ erg s}^{-1}} \right) \left(\frac{\eta}{18} \right)^{-5} Y, \quad \text{for } \cos \vartheta = 1 \quad (30)$$

$$t_a^{(2)} \simeq \frac{t_{\text{ph}}}{\eta^2} \simeq 2.1 \text{ s} \left(\frac{L_0}{10^{50} \text{ erg s}^{-1}} \right) \left(\frac{\eta}{18} \right)^{-5} Y, \quad \text{for } \cos \vartheta = v/c. \quad (31)$$

These values account for a significant fraction of the time delay between the GW and the prompt radiation in the soft thermal peak.

We can now estimate the comoving temperature of the expanding fireball at the photospheric radius (MR00)

$$k_B T_{\text{ph}} = k_B T_0 \left(\frac{R_{\text{ph}}}{R_s} \right)^{-2/3} \quad (32)$$

$$\begin{aligned} &\simeq 0.13 \text{ keV} \left(\frac{L_0}{10^{50} \text{ erg s}^{-1}} \right)^{-5/12} \left(\frac{R_0}{2.5 \times 10^6 \text{ cm}} \right)^{-5/6} \\ &\times \left(\frac{\eta}{18} \right)^{8/3} Y^{-2/3}. \end{aligned} \quad (33)$$

This corresponds to an observed temperature, $T_{\text{ph}}^{\text{obs}} = \eta T_{\text{ph}}$

$$\begin{aligned} k_B T_{\text{ph}}^{\text{obs}} &= \eta k_B T_{\text{ph}} \simeq 2.3 \text{ keV} \left(\frac{L_0}{10^{50} \text{ erg s}^{-1}} \right)^{-5/12} \\ &\times \left(\frac{R_0}{2.5 \times 10^6 \text{ cm}} \right)^{-5/6} \left(\frac{\eta}{18} \right)^{11/3} Y^{-2/3}. \end{aligned} \quad (34)$$

The corresponding BB luminosity is (MR00),

$$\begin{aligned} L_{\text{ph}} &= L_0 \left(\frac{R_{\text{ph}}}{R_s} \right)^{-2/3} \quad (35) \\ &\simeq 1.7 \times 10^{46} \text{ erg s}^{-1} \left(\frac{L_0}{10^{50} \text{ erg s}^{-1}} \right)^{7/12} \\ &\times \left(\frac{R_0}{2.5 \times 10^6 \text{ cm}} \right)^{-5/6} \left(\frac{\eta}{18} \right)^{8/3} Y^{-2/3}. \end{aligned} \quad (36)$$

Thus, with the reference values of our model for L_0 and η , we obtain $L_{\text{ph}} \simeq L_{\text{iso, BB}}$. On the other hand, $T_{\text{ph}}^{\text{obs}}$ underpredicts $T_{\text{BB}}^{\text{obs}}$ by a factor ~ 4 . Nonetheless, we are neglecting Comptonization effects, which may slightly raise the estimated temperature.

Appendix B

List of SGRBs with Associated Redshift

Table 2 is a list of possible redshifts for GRBs that have been argued to belong to the short class. The asterisks show the “gold sample” selection with standard cuts on duration ($T_{90} < 2$ s) and localization uncertainty (\sim arcsecond or better). The others include SGRBs with extended gamma-ray emission, those slightly longer than 2 s that are spectrally hard or show negligible spectral lag, and bursts that are best localized by *Swift* BAT (so a chance association is possible). Most of these redshifts come from Lien et al. (2016); Siellez et al. (2016), and Fong et al. (2015); for the original citations see references therein. They also include bursts from Tunnicliffe et al. (2014). For these bursts, and those best localized by *Swift* BAT, an individual nearby galaxy may be a chance alignment, but it is statistically unlikely that most of them are false associations.

Table 2
Probable SGRBs with Measured Redshifts

GRB	Any Claimed Redshift	Comment
161104A*	0.788	
160821B*	0.16	
160624A*	0.483	
150423A*	1.394	
150120A*	0.46	
150101B*	0.134	
141212A*	0.596	
140903A*	0.351	
140622A*	0.959	
131004A*	0.717	
130603B*	0.356	
120804A*	1.3	
111117A*	2.211	Updated value from Selsing et al. (2017)
111020A	0.019	Tunnicliffe et al. (2014)
101219A*	0.718	
100724A*	1.288	
100628A*	0.102	
100625A*	0.452	
100206A*	0.407	
100117A*	0.915	
090927	1.37	Arcminute Localization
090515*	0.403	
090510	0.903	<i>Swift</i> BAT $T_{90} > 2$ s
090426*	2.609	
090417A	0.088	Arcminute Localization
080905A*	0.122	
071227	0.381	SGRB w/Extended Emission
070923	0.076	Arcminute Localization
070809*	0.473	Tunnicliffe et al. (2014) mention of possible host at $z = 0.047$
070729*	0.8	
070724A*	0.457	
070714B	0.923	SGRB w/Extended Emission
070429B*	0.902	
061217*	0.827	
061210	0.41	SGRB w/Extended Emission
061201*	0.111	
061006	0.438	SGRB w/Extended Emission
060801*	1.13	
060502B*	0.287	
051221A*	0.546	
050906	0.032	Tunnicliffe et al. (2014)
050813*	0.72/1.8	It is unclear which redshift is correct
050724A	0.257	SGRB w/ Extended Emission
050709	0.161	Not detected by <i>Swift</i> BAT
050509B*	0.225	

References

- Aasi, J., Abbott, B. P., Abbott, R., et al. 2015, *CQGra*, 32, 074001
 Abadie, J., Abbott, B. P., Abbott, R., et al. 2012, *ApJ*, 760, 12
 Abbott, B., Abbott, R., Abbott, T., et al. 2016a, *PhRvL*, 116, 241103
 Abbott, B. P., Abbott, R., Abbott, T. D., et al. 2016b, *PhRvL*, 116, 061102
 Abbott, B. P., Abbott, R., Abbott, T. D., et al. 2017a, arXiv:1304.0670v4
 Abbott, B. P., Abbott, R., Abbott, T. D., et al. 2017b, *ApJ*, 841, 89
 Abbott, B. P., Abbott, R., Abbott, T. D., et al. 2017c, *PhRvL*, 118, 221101
 Abbott, B. P., Abbott, R., Abbott, T. D., et al. 2017d, *PhRvL*, 119, 141101
 Abbott, B. P., Abbott, R., Abbott, T. D., et al. 2017e, *PhRvL*, 119, 161101
 Abbott, B. P., Abbott, R., Abbott, T. D., et al. 2017f, *ApJL*, <https://doi.org/10.3847/2041-8213/aa91c9>
 Abbott, B. P., Abbott, R., Abbott, T. D., et al. 2017g, *Natur*, <https://doi.org/10.1038/nature24471>
 Acernese, F., Agathos, M., Agatsuma, K., et al. 2015, *CQGra*, 32, 024001
 Ade, P. A. R., Aghanim, N., Arnaud, M., et al. 2016, *A&A*, 594, A13

- Akmal, A., Pandharipande, V. R., & Ravenhall, D. G. 1998, *PhRvC*, **58**, 1804
- Aloy, M. A., Janka, H.-T., & Müller, E. 2005, *A&A*, **436**, 273
- Antoniadis, J., et al. 2013, *Sci*, **340**, 6131
- Bailey, Q. G., & Kostelecký, V. A. 2006, *PhRvD*, **74**, 045001
- Baiotti, L., & Rezzolla, L. 2017, *RPPH*, **80**, 096901
- Band, D., Matteson, J., Ford, L., et al. 1993, *ApJ*, **413**, 281
- Bauswein, A., Baumgarte, T. W., & Janka, H. T. 2013, *PhRvL*, **111**, 131101
- Bauswein, A., Goriely, S., & Janka, H.-T. 2013, *ApJ*, **773**, 78
- Belczynski, K., O’Shaughnessy, R. W., Kalogera, V., et al. 2008, *ApJL*, **680**, L129
- Belczynski, K., Perna, R., Bulik, T., et al. 2006, *ApJ*, **648**, 1110
- Beloborodov, A. M. 2010, *MNRAS*, **407**, 1033
- Berger, E. 2010, *ApJ*, **722**, 1946
- Berger, E., Fong, W., & Chornock, R. 2013, *ApJL*, **774**, L23
- Berger, E., Kulkarni, S. R., Pooley, G., et al. 2003, *Natur*, **426**, 154
- Berger, E. 2014, *ARA&A*, **52**, 43
- Bertotti, B., Iess, L., & Tortora, P. 2003, *Natur*, **425**, 374
- Bianco, C. L., Ruffini, R., & Xue, S.-S. 2001, *A&A*, **368**, 377
- Blackburn, L., Briggs, M. S., Camp, J., et al. 2015, *ApJS*, **217**, 8
- Bland-Hawthorn, J., & Gerhard, O. 2016, *ARA&A*, **54**, 529
- Blinnikov, S. I., Novikov, I. D., Perevodchikova, T. V., & Polnarev, A. G. 1984, *SvAL*, **10**, 177
- Bloom, J. S., Frail, D. A., & Sari, R. 2001, *AJ*, **121**, 2879
- Bloom, J. S., Prochaska, J. X., Pooley, D., et al. 2006, *ApJ*, **638**, 354
- Bloom, J. S., Sigurdsson, S., & Pols, O. R. 1999, *MNRAS*, **305**, 767
- Bourgoin, A., Le Poncin-Lafitte, C., Hees, A., et al. 2016, *PhRvL*, **117**, 241301
- Bromberg, O., Nakar, E., Piran, T., & Sari, R. 2013, *ApJ*, **764**, 179
- Burns, E. 2017, PhD thesis, Univ. Alabama in Huntsville
- Burns, E., Connaughton, V., Zhang, B.-B., et al. 2016, *ApJ*, **818**, 110
- Cannon, K., Cariou, R., Chapman, A., et al. 2012, *ApJ*, **748**, 136
- Cano, Z., Bersier, D., Guidorzi, C., et al. 2011, *ApJ*, **740**, 41
- Church, R. P., Levan, A. J., Davies, M. B., & Tanvir, N. 2011, *MNRAS*, **413**, 2004
- Ciolfi, R., & Siegel, D. M. 2015, *ApJL*, **798**, L36
- Clark, J., Evans, H., Fairhurst, S., et al. 2015, *ApJ*, **809**, 53
- Colladay, D., & Kostelecký, V. A. 1997, *PhRvD*, **55**, 6760
- Colladay, D., & Kostelecký, V. A. 1998, *PhRvD*, **58**, 116002
- Connaughton, V. 2002, *ApJ*, **567**, 1028
- Connaughton, V., Burns, E., Goldstein, A., et al. 2016, *ApJL*, **826**, L6
- Cornish, N., Blas, D., & Nardini, G. 2017, arXiv:1707.06101
- Coulter, D. A., Kilpatrick, C. D., Siebert, M. R., et al. 2017a, GCN, 21529, 1
- Coulter, D. A., Kilpatrick, C. D., Siebert, M. R., et al. 2017b, *Sci*, <https://doi.org/10.1126/science.aap9811>
- Coward, D., Howell, E., Branchesi, M., et al. 2013, *MNRAS*, **432**, 2141
- Coward, D. M., Howell, E. J., Piran, T., et al. 2012, *MNRAS*, **425**, 2668
- D’Avanzo, P., Malesani, D., Covino, S., et al. 2009, *A&A*, **498**, 711
- Dermer, C. D., Chiang, J., & Böttcher, M. 1999, *ApJ*, **513**, 656
- Dezalay, J.-P., Barat, C., Talon, R., et al. 1992, in AIP Conf. Ser. 265, ed. W. S. Paciesas & G. J. Fishman, 304
- Douchin, F., & Haensel, P. 2001, *A&A*, **380**, 151
- Eichler, D., Livio, M., Piran, T., & Schramm, D. N. 1989, *Natur*, **340**, 126
- Evans, P., Cenko, S. B., Kennea, J. A., et al. 2017, *Sci*, [doi:10.1126/science.aap9580](https://doi.org/10.1126/science.aap9580)
- Evans, W. D., Klebesadel, R. W., Laros, J. G., et al. 1980, *ApJL*, **237**, L7
- Faber, J. A., & Rasio, F. A. 2012, *LRR*, **15**, 8
- Fan, X., Messenger, C., & Heng, I. S. 2017, arXiv:1706.05639
- Fenimore, E. E., Madras, C. D., & Nayakshin, S. 1996, *ApJ*, **473**, 998
- Filgas, R., Krühler, T., Greiner, J., et al. 2011, *A&A*, **526**, A113
- Finn, L., Mohanty, S., & Romano, J. 1999, *PhRvD*, **60**, 121101
- Flowers, N. A., Goodge, C., & Tasson, J. D. 2016, arXiv:1612.08495
- Fong, W., & Berger, E. 2013, *ApJ*, **776**, 18
- Fong, W., Berger, E., Chornock, R., et al. 2013, *ApJ*, **769**, 56
- Fong, W., Berger, E., Margutti, R., & Zauderer, B. A. 2015, *ApJ*, **815**, 102
- Fong, W., Margutti, R., Chornock, R., et al. 2016, *ApJ*, **833**, 151
- Fong, W., Metzger, B. D., Berger, E., & Özel, F. 2016, *ApJ*, **831**, 141
- Fox, D. B., Frail, D. A., Price, P. A., et al. 2005, *Natur*, **437**, 845
- Frail, D. A., Berger, E., Galama, T., et al. 2000, *ApJL*, **538**, L129
- Fryer, C. L., Belczynski, K., Ramirez-Ruiz, E., et al. 2015, *ApJ*, **812**, 24
- Fryer, C. L., Woosley, S. E., & Hartmann, D. H. 1999, *ApJ*, **526**, 152
- Galama, T. J., Vreeswijk, P. M., van Paradijs, J., et al. 1998, *Natur*, **395**, 670
- Gao, H., Wu, X.-F., & Mészáros, P. 2015, *ApJ*, **810**, 121
- Giannios, D. 2006, *A&A*, **457**, 763
- Gibbons, S. L. J., Belokurov, V., & Evans, N. W. 2014, *MNRAS*, **445**, 3788
- Goldstein, A., Burns, E., Hamburg, R., et al. 2016, arXiv:1612.02395
- Goldstein, A., Veres, P., Burns, E., et al. 2017, *ApJL*, [doi:10.3847/2041-8213/aa8f41](https://doi.org/10.3847/2041-8213/aa8f41)
- Goodman, J. 1986, *ApJL*, **308**, L47
- Goriely, S., Bauswein, A., & Janka, H.-T. 2011, *ApJL*, **738**, L32
- Gorski, K. M., Hivon, E., Banday, A., et al. 2005, *ApJ*, **622**, 759
- Gourgoulhon, E., Grandclément, P., Taniguchi, K., Marck, J.-A., & Bonazzola, S. 2001, *PhRvD*, **63**, 064029
- Granot, J. 2007, *RMxAA*, **27**, 140
- Granot, J., Panaitescu, A., Kumar, P., & Woosley, S. E. 2002, *ApJL*, **570**, L61
- Guetta, D., & Piran, T. 2006, *A&A*, **453**, 823
- Hansen, B. M. S., & Lyutikov, M. 2001, *MNRAS*, **322**, 695
- Harry, I. W., & Fairhurst, S. 2011, *PhRvD*, **83**, 084002
- Hees, A., Bailey, Q. G., Bourgoin, A., Pihan-Le Bars, H., & Guerlin, C. 2016, *Univ*, **2**, 30
- Hjorth, J., & Bloom, J. S. 2012, in Gamma-Ray Bursts, ed. C. Kouveliotou, R. A. M. J. Wijers, & S. Woosley (Cambridge: Cambridge Univ. Press), 169
- Hjorth, J., Sollerman, J., Gorosabel, J., et al. 2005b, *ApJL*, **630**, L117
- Hjorth, J., Watson, D., Fynbo, J. P. U., et al. 2005a, *Natur*, **437**, 859
- Horowitz, C. J., & Kadau, K. 2009, *PhRvL*, **102**, 191102
- Hotokezaka, K., Kyutoku, K., Okawa, H., Shibata, M., & Kiuchi, K. 2011, *PhRvD*, **83**, 124008
- Hotokezaka, K., Kyutoku, K., & Shibata, M. 2013, *PhRvD*, **87**, 044001
- Howell, E., & Coward, D. 2012, *MNRAS*, **428**, 167
- Hurley, K., Boggs, S. E., Smith, D. M., et al. 2005, *Natur*, **434**, 1098
- Kahya, E. O., & Desai, S. 2016, *PhLB*, **756**, 265
- Kaneko, Y., Bostancı, Z. F., Göğüş, E., & Lin, L. 2015, *MNRAS*, **452**, 824
- Kawamura, T., Giacomazzo, B., Kastaun, W., et al. 2016, *PhRvD*, **94**, 064012
- Kiuchi, K., Sekiguchi, Y., Kyutoku, K., et al. 2015, *PhRvD*, **92**, 064034
- Kobayashi, S., Piran, T., & Sari, R. 1997, *ApJ*, **490**, 92
- Kocevski, D., Butler, N., & Bloom, J. S. 2007, *ApJ*, **667**, 1024
- Kocevski, D., Thöne, C. C., Ramirez-Ruiz, E., et al. 2010, *MNRAS*, **404**, 963
- Kostelecký, V. A. 2004, *PhRvD*, **69**, 105009
- Kostelecký, V. A., & Mewes, M. 2008, *ApJL*, **689**, L1
- Kostelecký, V. A., & Mewes, M. 2009, *PhRvD*, **80**, 015020
- Kostelecký, V. A., & Mewes, M. 2016, *PhLB*, **757**, 510
- Kostelecký, V. A., & Russell, N. 2017, arXiv:0801.0287v10
- Kostelecký, V. A., & Tasson, J. D. 2015, *Phys. Lett. B*, **749**, 551
- Kouveliotou, C., Meegan, C. A., Fishman, G. J., et al. 1993, *ApJL*, **413**, L101
- Krauss, L. M., & Tremaine, S. 1988, *PhRvL*, **60**, 176
- Krimm, H. A., Granot, J., Marshall, F. E., et al. 2007, *ApJ*, **665**, 554
- Kumar, P., & Granot, J. 2003, *ApJ*, **591**, 1075
- Kumar, P., & Piran, T. 2000, *ApJ*, **532**, 286
- Lackey, B. D., Nayyar, M., & Owen, B. J. 2006, *PhRvD*, **73**, 024021
- Lattimer, J. M., & Swesty, F. D. 1991, *Nucl. Phys.*, **A535**, 331
- Lawrence, S., Tervala, J. G., Bedaque, P. F., & Miller, M. C. 2015, *ApJ*, **808**, 186
- Lazzati, D., Deich, A., Morsony, B. J., & Workman, J. C. 2017, *MNRAS*, **471**, 1652
- Lazzati, D., Ramirez-Ruiz, E., & Ghisellini, G. 2001, *A&A*, **379**, L39
- Le Poncin-Lafitte, C., Hees, A., & Lambert, S. 2016, *PhRvD*, **94**, 125030
- Lien, A., Sakamoto, T., Barthelmy, S. D., et al. 2016, *ApJ*, **829**, 7
- LIGO Scientific Collaboration & Virgo Collaboration 2017a, GCN, 21505, 1
- LIGO Scientific Collaboration & Virgo Collaboration 2017b, GCN, 21513, 1
- LIGO Scientific Collaboration & Virgo Collaboration 2017c, GCN, 21527, 1
- Longo, M. J. 1988, *PhRvL*, **60**, 173
- Lyutikov, M., & Blandford, R. 2003, arXiv:astro-ph/0312347
- Malesani, D., Tagliaferri, G., Chincarini, G., et al. 2004, *ApJL*, **609**, L5
- Malmquist, K. G. 1922, *MeLuF*, **100**, 1
- Messick, C., Blackburn, K., Brady, P., et al. 2017, *PhRvD*, **95**, 042001
- Mészáros, P., & Rees, M. J. 1992, *MNRAS*, **257**, 29P
- Mészáros, P., & Rees, M. J. 2000, *ApJ*, **530**, 292
- Mészáros, P., Rees, M. J., & Wijers, R. A. M. J. 1998, *ApJ*, **499**, 301
- Metzger, B. D., & Berger, E. 2012, *ApJ*, **746**, 48
- Metzger, B. D., Quataert, E., & Thompson, T. A. 2008, *MNRAS*, **385**, 1455
- Metzger, B. D., & Zivancev, C. 2016, *MNRAS*, **461**, 4435
- Minaev, P. Y., & Pozanenko, A. S. 2017, *AstL*, **43**, 1
- Mirshekari, S., Yunes, N., & Will, C. M. 2012, *PhRvD*, **85**, 024041
- Modjaz, M., Stanek, K., Garnavich, P., et al. 2006, *ApJL*, **645**, L21
- Moharana, R., & Piran, T. 2017, arXiv:1705.02598
- Müller, H., & Serot, B. D. 1996, *NuPhA*, **606**, 508
- Nagakura, H., Hotokezaka, K., Sekiguchi, Y., Shibata, M., & Ioka, K. 2014, *ApJL*, **784**, L28
- Nakar, E. 2007, *PhR*, **442**, 166
- Nakar, E., Gal-Yam, A., & Fox, D. B. 2006, *ApJ*, **650**, 281
- Nakar, E., & Sari, R. 2012, *ApJ*, **747**, 88
- Narayan, R., Paczynski, B., & Piran, T. 1992, *ApJL*, **395**, L83

- Nitz, A., Harry, I., Brown, D., et al. 2017a, ligo-cbc/pycbc: Post-O2 Production Release 2, Zenodo, doi:10.5281/zenodo.888262
- Nitz, A. H., Dent, T., Dal Canton, T., Fairhurst, S., & Brown, D. A. 2017b, arXiv:1705.01513
- Norris, J. P., & Bonnell, J. T. 2006, *ApJ*, **643**, 266
- Olausen, S. A., & Kaspi, V. M. 2014, *ApJS*, **212**, 6
- Ozel, F., & Freire, P. 2016, *ARA&A*, **54**, 401
- Paczynski, B. 1986, *ApJL*, **308**, L43
- Paczynski, B. 1991, *AcA*, **41**, 257
- Pe'er, A., Mészáros, P., & Rees, M. J. 2006, *ApJ*, **652**, 482
- Perley, D. A., Metzger, B. D., Granot, J., et al. 2009, *ApJ*, **696**, 1871
- Pescalli, A., Ghirlanda, G., Salafia, O. S., et al. 2015, *MNRAS*, **447**, 1911
- Piran, T., Nakar, E., & Rosswog, S. 2013, *MNRAS*, **430**, 2121
- Racusin, J. L., Karpov, S. V., Sokolowski, M., et al. 2008, *Natur*, **455**, 183
- Ramirez-Ruiz, E., Celotti, A., & Rees, M. J. 2002, *MNRAS*, **337**, 1349
- Ramirez-Ruiz, E., Merloni, A., & Rees, M. J. 2001, *MNRAS*, **324**, 1147
- Rees, M. J., & Meszaros, P. 1994, *ApJL*, **430**, L93
- Rees, M. J., & Mészáros, P. 1998, *ApJL*, **496**, L1
- Rees, M. J., & Mészáros, P. 2005, *ApJ*, **628**, 847
- Regimbau, T., Siellez, K., Meacher, D., Gendre, B., & Boër, M. 2015, *ApJ*, **799**, 69
- Rezzolla, L., Giacomazzo, B., Baiotti, L., et al. 2011, *ApJL*, **732**, L6
- Rezzolla, L., & Kumar, P. 2015, *ApJ*, **802**, 95
- Rhoads, J. E. 1999, *ApJ*, **525**, 737
- Riess, A. G., Macri, L. M., Hoffmann, S. L., et al. 2016, *ApJ*, **826**, 56
- Rossi, E., Lazzati, D., & Rees, M. J. 2002, *MNRAS*, **332**, 945
- Rowlinson, A., O'Brien, P., Metzger, B., Tanvir, N., & Levan, A. J. 2013, *MNRAS*, **430**, 1061
- Rowlinson, A., Wiersema, K., Levan, A. J., et al. 2010, *MNRAS*, **408**, 383
- Ruiz, M., Lang, R. N., Paschalidis, V., & Shapiro, S. L. 2016, *ApJL*, **824**, L6
- Savchenko, V., Bazzano, A., Bozzo, E., et al. 2017a, *A&A*, **603**, A46
- Savchenko, V., Ferrigno, C., Kuulkers, E., et al. 2017b, *ApJL*, 999
- Schaefer, B. E. 2007, *ApJ*, **660**, 16
- Selsing, J., Krühler, T., Malesani, D., et al. 2017, arXiv:1707.01452
- Shao, C.-G., Chen, Y.-F., Sun, R., et al. 2017, arXiv:1707.02318
- Shao, L. 2014a, *PhRvL*, **112**, 111103
- Shao, L. 2014b, *PhRvD*, **90**, 122009
- Shapiro, I. I. 1964, *PhRvL*, **13**, 789
- Shen, G., Horowitz, C. J., & Teige, S. 2011, *PhRvC*, **83**, 035802
- Shibata, M., Duez, M. D., Liu, Y. T., Shapiro, S. L., & Stephens, B. C. 2006, *PhRvL*, **96**, 031102
- Siellez, K., Boer, M., Gendre, B., & Regimbau, T. 2016, arXiv:1606.03043
- Soderberg, A. M., Berger, E., Kasliwal, M., et al. 2006, *ApJ*, **650**, 261
- Steiner, A. W., Hempel, M., & Fischer, T. 2013, *ApJ*, **774**, 17
- Sutton, P. J., Jones, G., Chatterji, S., et al. 2010, *NJPh*, **12**, 053034
- Svinkin, D., Hurley, K., von Kienlin, A., et al. 2017, GCN, 21515
- Tanvir, N. R., Chapman, R., Levan, A. J., & Priddey, R. S. 2005, *Natur*, **438**, 991
- Tanvir, N. R., Levan, A. J., Fruchter, A. S., et al. 2013, *Natur*, **500**, 547
- Tasson, J. D. 2014, *RPPH*, **77**, 062901
- Tauris, T. M., Kramer, M., Freire, P. C. C., et al. 2017, *ApJ*, **846**, 170
- Troja, E., King, A. R., O'Brien, P. T., Lyons, N., & Cusumano, G. 2008, *MNRAS*, **385**, 10
- Troja, E., Rosswog, S., & Gehrels, N. 2010, *ApJ*, **723**, 1711
- Tsang, D., Read, J. S., Hinderer, T., Piro, A. L., & Bondarescu, R. 2012, *PhRvL*, **108**, 011102
- Tunnicliffe, R. L., Levan, A. J., Tanvir, N. R., et al. 2014, *MNRAS*, **437**, 1495
- Urban, A. L. 2016, PhD thesis, Univ. Wisconsin-Milwaukee
- Usman, S. A., Nitz, A. H., Harry, I. W., et al. 2016, *CQGra*, **33**, 215004
- Usov, V. V. 1992, *Natur*, **357**, 472
- Veitch, J., Raymond, V., Farr, B., et al. 2015, *PhRvD*, **91**, 042003
- Wanderman, D., & Piran, T. 2015, *MNRAS*, **448**, 3026
- Was, M., Sutton, P. J., Jones, G., & Leonor, I. 2012, *PhRvD*, **86**, 022003
- Wei, J.-J., Wu, X.-F., Zhang, B.-B., et al. 2017, *ApJ*, **842**, 115
- Will, C. M. 2014, *LRR*, **17**, 4
- Williamson, A., Biwer, C., Fairhurst, S., et al. 2014, *PhRvD*, **90**, 122004
- Wong, T.-W., Willems, B., & Kalogera, V. 2010, *ApJ*, **721**, 1689
- Yamazaki, R., Ioka, K., & Nakamura, T. 2002, *ApJL*, **571**, L31
- Zhang, B., & Mészáros, P. 2002, *ApJ*, **571**, 876

- B. P. Abbott¹, R. Abbott¹, T. D. Abbott², F. Acernese^{3,4}, K. Ackley^{5,6}, C. Adams⁷, T. Adams⁸, P. Addesso⁹, R. X. Adhikari¹, V. B. Adya¹⁰, C. Affeldt¹⁰, M. Afrough¹¹, B. Agarwal¹², M. Agathos¹³, K. Agatsuma¹⁴, N. Aggarwal¹⁵, O. D. Aguiar¹⁶, L. Aiello^{17,18}, A. Ain¹⁹, P. Ajith²⁰, B. Allen^{10,21,22}, G. Allen¹², A. Allocca^{23,24}, M. A. Aloy²⁵, P. A. Altin²⁶, A. Amato²⁷, A. Ananyeva¹, S. B. Anderson¹, W. G. Anderson²¹, S. V. Angelova²⁸, S. Antier²⁹, S. Appert¹, K. Arai¹, M. C. Araya¹, J. S. Areeda³⁰, N. Arnaud^{29,31}, K. G. Arun³², S. Ascenzi^{33,34}, G. Ashton¹⁰, M. Ast³⁵, S. M. Aston⁷, P. Astone³⁶, D. V. Atallah³⁷, P. Aufmuth²², C. Aubert¹⁰, K. AultONeal³⁸, C. Austin², A. Avila-Alvarez³⁰, S. Babak³⁹, P. Bacon⁴⁰, M. K. M. Bader¹⁴, S. Bae⁴¹, P. T. Baker⁴², F. Baldaccini^{43,44}, G. Ballardín³¹, S. W. Ballmer⁴⁵, S. Banagiri⁴⁶, J. C. Barayoga¹, S. E. Barclay⁴⁷, B. C. Barish¹, D. Barker⁴⁸, K. Barkett⁴⁹, F. Barone^{3,4}, B. Barr⁴⁷, L. Barsotti¹⁵, M. Barsuglia⁴⁰, D. Barta⁵⁰, J. Bartlett⁴⁸, I. Bartos^{5,51}, R. Bassiri⁵², A. Basti^{23,24}, J. C. Batch⁴⁸, M. Bawaj^{44,53}, J. C. Bayley⁴⁷, M. Bazzan^{54,55}, B. Bécsy⁵⁶, C. Beer¹⁰, M. Bejger⁵⁷, I. Belahcene²⁹, A. S. Bell⁴⁷, B. K. Berger¹, G. Bergmann¹⁰, J. J. Bero⁵⁸, C. P. L. Berry⁵⁹, D. Bersanetti⁶⁰, A. Bertolini¹⁴, J. Betzwieser⁷, S. Bhagwat⁴⁵, R. Bhandare⁶¹, I. A. Bilenko⁶², G. Billingsley¹, C. R. Billman⁵, J. Birch⁷, R. Birney⁶³, O. Birnholtz¹⁰, S. Biscans^{1,15}, S. Biscoveanu^{6,64}, A. Bisht²², M. Bitossi^{24,31}, C. Biwer⁴⁵, M. A. Bizouard²⁹, J. K. Blackburn¹, J. Blackman⁴⁹, C. D. Blair^{1,65}, D. G. Blair⁶⁵, R. M. Blair⁴⁸, S. Bloemen⁶⁶, O. Bock¹⁰, N. Bode¹⁰, M. Boer⁶⁷, G. Bogaert⁶⁷, A. Bohe³⁹, F. Bondu⁶⁸, E. Bonilla⁵², R. Bonnand⁸, B. A. Boom¹⁴, R. Bork¹, V. Boschi^{24,31}, S. Bose^{19,69}, K. Bossie⁷, Y. Bouffanais⁴⁰, A. Bozzi³¹, C. Bradaschia²⁴, P. R. Brady²¹, M. Branchesi^{17,18}, J. E. Brau⁷⁰, T. Briant⁷¹, A. Brillet⁶⁷, M. Brinkmann¹⁰, V. Brisson²⁹, P. Brockill²¹, J. E. Broida⁷², A. F. Brooks¹, D. A. Brown⁴⁵, D. D. Brown⁷³, S. Brunett¹, C. C. Buchanan², A. Buikema¹⁵, T. Bulik⁷⁴, H. J. Bulten^{14,75}, A. Buonanno^{39,76}, D. Buskulic⁸, C. Buy⁴⁰, R. L. Byer⁵², M. Cabero¹⁰, L. Cadonati⁷⁷, G. Cagnoli^{27,78}, C. Cahillane¹, J. Calderón Bustillo⁷⁷, T. A. Callister¹, E. Calloni^{4,79}, J. B. Camp⁸⁰, M. Canepa^{60,81}, P. Canizares⁶⁶, K. C. Cannon⁸², H. Cao⁷³, J. Cao⁸³, C. D. Capano¹⁰, E. Capocasa⁴⁰, F. Carbognani³¹, S. Caride⁸⁴, M. F. Carney⁸⁵, J. Casanueva Diaz²⁹, C. Casentini^{33,34}, S. Caudill^{14,21}, M. Cavaglià¹¹, F. Cavalier²⁹, R. Cavalieri³¹, G. Cella²⁴, C. B. Cepeda¹, P. Cerdá-Durán²⁵, G. Cerretani^{23,24}, E. Cesarini^{34,86}, S. J. Chamberlin⁶⁴, M. Chan⁴⁷, S. Chao⁸⁷, P. Charlton⁸⁸, E. Chase⁸⁹, E. Chassande-Mottin⁴⁰, D. Chatterjee²¹, K. Chatziioannou⁹⁰, B. D. Cheeseboro⁴², H. Y. Chen⁹¹, X. Chen⁶⁵, Y. Chen⁴⁹, H.-P. Cheng⁵, H. Chia⁵, A. Chincarini⁶⁰,

A. Chiummo³¹, T. Chmiel⁸⁵, H. S. Cho⁹², M. Cho⁷⁶, J. H. Chow²⁶, N. Christensen^{67,72}, Q. Chu⁶⁵, A. J. K. Chua¹³, S. Chua⁷¹, A. K. W. Chung⁹³, S. Chung⁶⁵, G. Ciani^{5,54,55}, R. Ciolfi^{94,95}, C. E. Cirelli⁵², A. Cirone^{60,81}, F. Clara⁴⁸, J. A. Clark⁷⁷, P. Clearwater⁹⁶, F. Cleva⁶⁷, C. Cocchieri¹¹, E. Coccia^{17,18}, P.-F. Cohadon⁷¹, D. Cohen²⁹, A. Colla^{36,97}, C. G. Collette⁹⁸, L. R. Cominsky⁹⁹, M. Constanancio Jr.¹⁶, L. Conti⁵⁵, S. J. Cooper⁵⁹, P. Corban⁷, T. R. Corbitt², I. Cordero-Carrión¹⁰⁰, K. R. Corley⁵¹, N. Cornish¹⁰¹, A. Corsi⁸⁴, S. Cortese³¹, C. A. Costa¹⁶, M. W. Coughlin^{1,72}, S. B. Coughlin⁸⁹, J.-P. Coulon⁶⁷, S. T. Countryman⁵¹, P. Couvares¹, P. B. Covas¹⁰², E. E. Cowan⁷⁷, D. M. Coward⁶⁵, M. J. Cowart⁷, D. C. Coyne¹, R. Coyne⁸⁴, J. D. E. Creighton²¹, T. D. Creighton¹⁰³, J. Cripe², S. G. Crowder¹⁰⁴, T. J. Cullen^{2,30}, A. Cumming⁴⁷, L. Cunningham⁴⁷, E. Cuoco³¹, T. Dal Canton⁸⁰, G. Dálya⁵⁶, S. L. Danilishin^{10,22}, S. D'Antonio³⁴, K. Danzmann^{10,22}, A. Dasgupta¹⁰⁵, C. F. Da Silva Costa⁵, V. Dattilo³¹, I. Dave⁶¹, M. Davier²⁹, D. Davis⁴⁵, E. J. Daw¹⁰⁶, B. Day⁷⁷, S. De⁴⁵, D. DeBra⁵², J. Degallaix²⁷, M. De Laurentis^{4,17}, S. Deléglise⁷¹, W. Del Pozzo^{23,24,59}, N. Demos¹⁵, T. Denker¹⁰, T. Dent¹⁰, R. De Pietri^{107,108}, V. Dergachev³⁹, R. De Rosa^{4,79}, R. T. DeRosa⁷, C. De Rossi^{27,31}, R. DeSalvo¹⁰⁹, O. de Varona¹⁰, J. Devenson²⁸, S. Dhurandhar¹⁹, M. C. Díaz¹⁰³, L. Di Fiore⁴, M. Di Giovanni^{95,110}, T. Di Girolamo^{4,51,79}, A. Di Lieto^{23,24}, S. Di Pace^{36,97}, I. Di Palma^{36,97}, F. Di Renzo^{23,24}, Z. Doctor⁹¹, V. Dolique²⁷, F. Donovan¹⁵, K. L. Dooley¹¹, S. Doravari¹⁰, I. Dorrington³⁷, R. Douglas⁴⁷, M. Dovale Álvarez⁵⁹, T. P. Downes²¹, M. Drago¹⁰, C. Dreissigacker¹⁰, J. C. Driggers⁴⁸, Z. Du⁸³, M. Ducrot⁸, P. Dupej⁴⁷, S. E. Dwyer⁴⁸, T. B. Edo¹⁰⁶, M. C. Edwards⁷², A. Effler⁷, H.-B. Eggenstein^{10,39}, P. Ehrens¹, J. Eichholz¹, S. S. Eikenberry⁵, R. A. Eisenstein¹⁵, R. C. Essick¹⁵, D. Estevez⁸, Z. B. Etienne⁴², T. Etzel¹, M. Evans¹⁵, T. M. Evans⁷, M. Factourovich⁵¹, V. Fafone^{17,33,34}, H. Fair⁴⁵, S. Fairhurst³⁷, X. Fan⁸³, S. Farinon⁶⁰, B. Farr⁹¹, W. M. Farr⁵⁹, E. J. Fauchon-Jones³⁷, M. Favata¹¹¹, M. Fays³⁷, C. Fee⁸⁵, H. Fehrmann¹⁰, J. Feicht¹, M. M. Fejer⁵², A. Fernandez-Galiana¹⁵, I. Ferrante^{23,24}, E. C. Ferreira¹⁶, F. Ferrini³¹, F. Fidecaro^{23,24}, D. Finstad⁴⁵, I. Fiori³¹, D. Fiorucci⁴⁰, M. Fishbach⁹¹, R. P. Fisher⁴⁵, M. Fitz-Axen⁴⁶, R. Flamini^{27,112}, M. Fletcher⁴⁷, H. Fong⁹⁰, J. A. Font^{25,113}, P. W. F. Forsyth²⁶, S. S. Forsyth⁷⁷, J.-D. Fournier⁶⁷, S. Frasca^{36,97}, F. Frasconi²⁴, Z. Frei⁵⁶, A. Freise⁵⁹, R. Frey⁷⁰, V. Frey²⁹, E. M. Fries¹, P. Fritschel¹⁵, V. V. Frolov⁷, P. Fulda⁵, M. Fyffe⁷, H. Gabbard⁴⁷, B. U. Gadre¹⁹, S. M. Gaebel⁵⁹, J. R. Gair¹¹⁴, L. Gammaitoni⁴³, M. R. Ganija⁷³, S. G. Gaonkar¹⁹, C. Garcia-Quros¹⁰², F. Garufi^{4,79}, B. Gateley⁴⁸, S. Gaudio³⁸, G. Gaur¹¹⁵, V. Gayathri¹¹⁶, N. Gehrels^{80,†}, G. Gemme⁶⁰, E. Genin³¹, A. Gennai²⁴, D. George¹², J. George⁶¹, L. Gergely¹¹⁷, V. Germain⁸, S. Ghonge⁷⁷, Abhirup Ghosh²⁰, Archisman Ghosh^{14,20}, S. Ghosh^{14,21,66}, J. A. Giaime^{2,7}, K. D. Giardino⁷, A. Giazotto²⁴, K. Gill³⁸, L. Glover¹⁰⁹, E. Goetz¹¹⁸, R. Goetz⁵, S. Gomes³⁷, B. Goncharov⁶, G. González², J. M. Gonzalez Castro^{23,24}, A. Gopakumar¹¹⁹, M. L. Gorodetsky⁶², S. E. Gossan¹, M. Gosselin³¹, R. Gouaty⁸, A. Grado^{4,120}, C. Graef⁴⁷, M. Granata²⁷, A. Grant⁴⁷, S. Gras¹⁵, C. Gray⁴⁸, G. Greco^{121,122}, A. C. Green⁵⁹, E. M. Gretarsson³⁸, P. Groot⁶⁶, H. Grote¹⁰, S. Grunewald³⁹, P. Gruning²⁹, G. M. Guidi^{121,122}, X. Guo⁸³, A. Gupta⁶⁴, M. K. Gupta¹⁰⁵, K. E. Gushwa¹, E. K. Gustafson¹, R. Gustafson¹¹⁸, O. Halim^{17,18}, B. R. Hall⁶⁹, E. D. Hall¹⁵, E. Z. Hamilton³⁷, G. Hammond⁴⁷, M. Haney¹²³, M. M. Hanke¹⁰, J. Hanks⁴⁸, C. Hanna⁶⁴, M. D. Hannam³⁷, O. A. Hannuksela⁹³, J. Hanson⁷, T. Hardwick², J. Harms^{17,18}, G. M. Harry¹²⁴, I. W. Harry³⁹, M. J. Hart⁴⁷, C.-J. Haster⁹⁰, K. Haughian⁴⁷, J. Healy⁵⁸, A. Heidmann⁷¹, M. C. Heintze⁷, H. Heitmann⁶⁷, P. Hello²⁹, G. Hemming³¹, M. Hendry⁴⁷, I. S. Heng⁴⁷, J. Hennig⁴⁷, A. W. Heptonstall¹, M. Heurs^{10,22}, S. Hild⁴⁷, T. Hinderer⁶⁶, D. Hoak³¹, D. Hofman²⁷, K. Holt⁷, D. E. Holz⁹¹, P. Hopkins³⁷, C. Horst²¹, J. Hough⁴⁷, E. A. Houston⁴⁷, E. J. Howell⁶⁵, A. Hreibi⁶⁷, Y. M. Hu¹⁰, E. A. Huerta¹², D. Huet²⁹, B. Hughey³⁸, S. Husa¹⁰², S. H. Huttner⁴⁷, T. Huynh-Dinh⁷, N. Indik¹⁰, R. Inta⁸⁴, G. Intini^{36,97}, H. N. Isa⁴⁷, J.-M. Isac⁷¹, M. Isi¹, B. R. Iyer²⁰, K. Izumi⁴⁸, T. Jacqmin⁷¹, K. Jani⁷⁷, P. Jaranowski¹²⁵, S. Jawahar⁶³, F. Jiménez-Forzeza¹⁰², W. W. Johnson², N. K. Johnson-McDaniel¹³, D. I. Jones¹²⁶, R. Jones⁴⁷, R. J. G. Jonker¹⁴, L. Ju⁶⁵, J. Junker¹⁰, C. V. Kalaghatgi³⁷, V. Kalogera⁸⁹, B. Kamai¹, S. Kandhasamy⁷, G. Kang⁴¹, J. B. Kanner¹, S. J. Kapadia²¹, S. Karki⁷⁰, K. S. Karvinen¹⁰, M. Kasprzak², W. Kastaun¹⁰, M. Katolik¹², E. Katsavounidis¹⁵, W. Katzman⁷, S. Kaufer²², K. Kawabe⁴⁸, F. Kéfélian⁶⁷, D. Keitel⁴⁷, A. J. Kembal¹², R. Kennedy¹⁰⁶, C. Kent³⁷, J. S. Key¹²⁷, F. Y. Khalili⁶², I. Khan^{17,34}, S. Khan¹⁰, Z. Khan¹⁰⁵, E. A. Khazanov¹²⁸, N. Kijbunchoo²⁶, Chunglee Kim¹²⁹, J. C. Kim¹³⁰, K. Kim⁹³, W. Kim⁷³, W. S. Kim¹³¹, Y.-M. Kim⁹², S. J. Kimbrell⁷⁷, E. J. King⁷³, P. J. King⁴⁸, M. Kinley-Hanlon¹²⁴, R. Kirchhoff¹⁰, J. S. Kissel⁴⁸, L. Kleybolte³⁵, S. Klimentenko⁵, T. D. Knowles⁴², P. Koch¹⁰, S. M. Koehlenbeck¹⁰, S. Koley¹⁴, V. Kondrashov¹, A. Kontos¹⁵, M. Korobko³⁵, W. Z. Korth¹, I. Kowalska⁷⁴, D. B. Kozak¹, C. Krämer¹⁰, V. Kringel¹⁰, B. Krishnan¹⁰, A. Królak^{132,133}, G. Kuehn¹⁰, P. Kumar⁹⁰, R. Kumar¹⁰⁵, S. Kumar²⁰, L. Kuo⁸⁷, A. Kutynia¹³², S. Kwang²¹, B. D. Lackey³⁹, K. H. Lai⁹³, M. Landry⁴⁸, R. N. Lang¹³⁴, J. Lange⁵⁸, B. Lantz⁵², R. K. Lanza¹⁵, A. Lartaux-Vollard²⁹, P. D. Lasky⁶, M. Laxen⁷, A. Lazzarini¹, C. Lazzaro⁵⁵, P. Leaci^{36,97}, S. Leavey⁴⁷, C. H. Lee⁹², H. K. Lee¹³⁵, H. M. Lee¹³⁶, H. W. Lee¹³⁰, K. Lee⁴⁷, J. Lehmann¹⁰, A. Lenon⁴², M. Leonardi^{95,110}, N. Leroy²⁹, N. Letendre⁸, Y. Levin⁶, T. G. F. Li⁹³, S. D. Linker¹⁰⁹, T. B. Littenberg¹³⁷, J. Liu⁶⁵, R. K. L. Lo⁹³, N. A. Lockerbie⁶³, L. T. London³⁷, J. E. Lord⁴⁵, M. Lorenzini^{17,18}, V. Lorette¹³⁸, M. Lormand⁷, G. Losurdo²⁴, J. D. Lough¹⁰, C. O. Lousto⁵⁸, G. Lovelace³⁰, H. Lück^{10,22}, D. Lumaca^{33,34}, A. P. Lundgren¹⁰, R. Lynch¹⁵, Y. Ma⁴⁹, R. Macas³⁷, S. Macfoy²⁸, B. Machenschalk¹⁰, M. MacInnis¹⁵, D. M. Macleod³⁷, I. Magaña Hernandez²¹, F. Magaña-Sandoval⁴⁵, L. Magaña Zertuche⁴⁵, R. M. Magee⁶⁴, E. Majorana³⁶, I. Maksimovic¹³⁸, N. Man⁶⁷, V. Mandic⁴⁶, V. Mangano⁴⁷, G. L. Mansell²⁶, M. Manske^{21,26}, M. Mantovani³¹, F. Marchesoni^{44,53}, F. Marion⁸, S. Márka⁵¹, Z. Márka⁵¹, C. Markakis¹², A. S. Markosyan⁵², A. Markowitz¹, E. Maros¹, A. Marquina¹⁰⁰, F. Martelli^{121,122}, L. Martellini⁶⁷, I. W. Martin⁴⁷, R. M. Martin¹¹¹, D. V. Martynov¹⁵, K. Mason¹⁵, E. Massera¹⁰⁶, A. Masserot⁸, T. J. Massinger¹,

M. Masso-Reid⁴⁷, S. Mastrogianni^{36,97}, A. Matas⁴⁶, F. Matichard^{1,15}, L. Matone⁵¹, N. Mavalvala¹⁵, N. Mazumder⁶⁹, R. McCarthy⁴⁸, D. E. McClelland²⁶, S. McCormick⁷, L. McCuller¹⁵, S. C. McGuire¹³⁹, G. McIntyre¹, J. McIver¹, D. J. McManus²⁶, L. McNeill⁶, T. McRae²⁶, S. T. McWilliams⁴², D. Meacher⁶⁴, G. D. Meadors^{10,39}, M. Mehmet¹⁰, J. Meidam¹⁴, E. Mejuto-Villa⁹, A. Melatos⁹⁶, G. Mendell⁴⁸, R. A. Mercer²¹, E. L. Merilh⁴⁸, M. Merzougui⁶⁷, S. Meshkov¹, C. Messenger⁴⁷, C. Messick⁶⁴, R. Metzдорff⁷¹, P. M. Meyers⁴⁶, H. Miao⁵⁹, C. Michel²⁷, H. Middleton⁵⁹, E. E. Mikhailov¹⁴⁰, L. Milano^{4,79}, A. L. Miller^{5,36,97}, B. B. Miller⁸⁹, J. Miller¹⁵, M. Millhouse¹⁰¹, M. C. Milovich-Goff¹⁰⁹, O. Minazzoli^{67,141}, Y. Minenkov³⁴, J. Ming³⁹, C. Mishra¹⁴², S. Mitra¹⁹, V. P. Mitrofanov⁶², G. Mitselmakher⁵, R. Mittleman¹⁵, D. Moffa⁸⁵, A. Moggi²⁴, K. Mogushi¹¹, M. Mohan³¹, S. R. P. Mohapatra¹⁵, M. Montani^{121,122}, C. J. Moore¹³, D. Moraru⁴⁸, G. Moreno⁴⁸, S. R. Morris¹⁰³, B. Mours⁸, C. M. Mow-Lowry⁵⁹, G. Mueller⁵, A. W. Muir³⁷, Arunava Mukherjee¹⁰, D. Mukherjee²¹, S. Mukherjee¹⁰³, N. Mukund¹⁹, A. Mullavey⁷, J. Munch⁷³, E. A. Muñoz⁴⁵, M. Muratore³⁸, P. G. Murray⁴⁷, K. Napier⁷⁷, I. Nardecchia^{33,34}, L. Naticchioni^{36,97}, R. K. Nayak¹⁴³, J. Neilson¹⁰⁹, G. Nelemans^{14,66}, T. J. N. Nelson⁷, M. Nery¹⁰, A. Neunzert¹¹⁸, L. Nevin¹, J. M. Newport¹²⁴, G. Newton^{47,‡}, K. K. Y. Ng⁹³, T. T. Nguyen²⁶, D. Nichols⁶⁶, A. B. Nielsen¹⁰, S. Nissanke^{14,66}, A. Nitz¹⁰, A. Noack¹⁰, F. Nocera³¹, D. Nolting⁷, C. North³⁷, L. K. Nuttall³⁷, J. Oberling⁴⁸, G. D. O’Dea¹⁰⁹, G. H. Oggin¹⁴⁴, J. J. Oh¹³¹, S. H. Oh¹³¹, F. Ohme¹⁰, M. A. Okada¹⁶, M. Oliver¹⁰², P. Oppermann¹⁰, Richard J. Oram⁷, B. O’Reilly⁷, R. Ormiston⁴⁶, L. F. Ortega⁵, R. O’Shaughnessy⁵⁸, S. Ossokine³⁹, D. J. Ottaway⁷³, H. Overmier⁷, B. J. Owen⁸⁴, A. E. Pace⁶⁴, J. Page¹³⁷, M. A. Page⁶⁵, A. Pai^{116,145}, S. A. Pai⁶¹, J. R. Palamos⁷⁰, O. Palashov¹²⁸, C. Palomba³⁶, A. Pal-Singh³⁵, Howard Pan⁸⁷, Huang-Wei Pan⁸⁷, B. Pang⁴⁹, P. T. H. Pang⁹³, C. Pankow⁸⁹, F. Pannarale³⁷, B. C. Pant⁶¹, F. Paoletti²⁴, A. Paoli³¹, M. A. Papa^{10,21,39}, A. Parida¹⁹, W. Parker⁷, D. Pascucci⁴⁷, A. Pasqualetti³¹, R. Passaquieti^{23,24}, D. Passuello²⁴, M. Patil¹³³, B. Patricelli^{24,146}, B. L. Pearlstone⁴⁷, M. Pedraza¹, R. Pedurand^{27,147}, L. Pekowsky⁴⁵, A. Pele⁷, S. Penn¹⁴⁸, C. J. Perez⁴⁸, A. Perreca^{1,95,110}, L. M. Perri⁸⁹, H. P. Pfeiffer^{39,90}, M. Phelps⁴⁷, O. J. Piccinni^{36,97}, M. Pichot⁶⁷, F. Piergiovanni^{121,122}, V. Pierro⁹, G. Pillant³¹, L. Pinard²⁷, I. M. Pinto⁹, M. Pirello⁴⁸, M. Pitkin⁴⁷, M. Poe²¹, R. Poggiani^{23,24}, P. Popolizio³¹, E. K. Porter⁴⁰, A. Post¹⁰, J. Powell^{47,149}, J. Prasad¹⁹, J. W. W. Pratt³⁸, G. Pratten¹⁰², V. Predoi³⁷, T. Prestegard²¹, M. Prijatelj¹⁰, M. Principe⁹, S. Privitera³⁹, G. A. Prodi^{95,110}, L. G. Prokhorov⁶², O. Puncken¹⁰, M. Punturo⁴⁴, P. Puppo³⁶, M. Pürerer³⁹, H. Qi²¹, V. Quetschke¹⁰³, E. A. Quintero¹, R. Quitzow-James⁷⁰, F. J. Raab⁴⁸, D. S. Rabeling²⁶, H. Radkins⁴⁸, P. Raffai⁵⁶, S. Raja⁶¹, C. Rajan⁶¹, B. Rajbhandari⁸⁴, M. Rakhmanov¹⁰³, K. E. Ramirez¹⁰³, A. Ramos-Buades¹⁰², P. Rapagnani^{36,97}, V. Raymond³⁹, M. Razzano^{23,24}, J. Read³⁰, T. Regimbau⁶⁷, L. Rei⁶⁰, S. Reid⁶³, D. H. Reitze^{1,5}, W. Ren¹², S. D. Reyes⁴⁵, F. Ricci^{36,97}, P. M. Ricker¹², S. Rieger¹⁰, K. Riles¹¹⁸, M. Rizzo⁵⁸, N. A. Robertson^{1,47}, R. Robie⁴⁷, F. Robinet²⁹, A. Rocchi³⁴, L. Rolland⁸, J. G. Rollins¹, V. J. Roma⁷⁰, R. Romano^{3,4}, C. L. Romel⁴⁸, J. H. Romie⁷, D. Rosińska^{57,150}, M. P. Ross¹⁵¹, S. Rowan⁴⁷, A. Rüdiger¹⁰, P. Ruggi³¹, G. Rutins²⁸, K. Ryan⁴⁸, S. Sachdev¹, T. Sadecki⁴⁸, L. Sadeghian²¹, M. Sakellariadou¹⁵², L. Salconi³¹, M. Saleem¹¹⁶, F. Salemi¹⁰, A. Samajdar¹⁴³, L. Sammut⁶, L. M. Sampson⁸⁹, E. J. Sanchez¹, L. E. Sanchez¹, N. Sanchis-Gual²⁵, V. Sandberg⁴⁸, J. R. Sanders⁴⁵, B. Sassolas²⁷, B. S. Sathyaprakash^{37,64}, P. R. Saulson⁴⁵, O. Sauter¹¹⁸, R. L. Savage⁴⁸, A. Sawadsky³⁵, P. Schale⁷⁰, M. Scheel⁴⁹, J. Scheuer⁸⁹, J. Schmidt¹⁰, P. Schmidt^{1,66}, R. Schnabel³⁵, R. M. S. Schofield⁷⁰, A. Schönbeck³⁵, E. Schreiber¹⁰, D. Schuette^{10,22}, B. W. Schulte¹⁰, B. F. Schutz^{10,37}, S. G. Schwalbe³⁸, J. Scott⁴⁷, S. M. Scott²⁶, E. Seidel¹², D. Sellers⁷, A. S. Sengupta¹⁵³, D. Sentenac³¹, V. Sequino^{17,33,34}, A. Sergeev¹²⁸, D. A. Shaddock²⁶, T. J. Shaffer⁴⁸, A. A. Shah¹³⁷, M. S. Shahriar⁸⁹, M. B. Shaner¹⁰⁹, L. Shao³⁹, B. Shapiro⁵², P. Shawhan⁷⁶, A. Sheperd²¹, D. H. Shoemaker¹⁵, D. M. Shoemaker⁷⁷, K. Siellez⁷⁷, X. Siemens²¹, M. Sieniawska⁵⁷, D. Sigg⁴⁸, A. D. Silva¹⁶, L. P. Singer⁸⁰, A. Singh^{10,22,39}, A. Singhal^{17,36}, A. M. Sintes¹⁰², B. J. J. Slagmolen²⁶, B. Smith⁷, J. R. Smith³⁰, R. J. E. Smith^{1,6}, S. Somala¹⁵⁴, E. J. Son¹³¹, J. A. Sonnenberg²¹, B. Sorazu⁴⁷, F. Sorrentino⁶⁰, T. Souradeep¹⁹, A. P. Spencer⁴⁷, A. K. Srivastava¹⁰⁵, K. Staats³⁸, A. Staley⁵¹, M. Steinke¹⁰, J. Steinlechner^{35,47}, S. Steinlechner³⁵, D. Steinmeyer¹⁰, S. P. Stevenson^{59,149}, R. Stone¹⁰³, D. J. Stops⁵⁹, K. A. Strain⁴⁷, G. Stratta^{121,122}, S. E. Strigin⁶², A. Strunk⁴⁸, R. Sturani¹⁵⁵, A. L. Stuver⁷, T. Z. Summerscales¹⁵⁶, L. Sun⁹⁶, S. Sunil¹⁰⁵, J. Suresh¹⁹, P. J. Sutton³⁷, B. L. Swinkels³¹, M. J. Szczepańczyk³⁸, M. Tacca¹⁴, S. C. Tait⁴⁷, C. Talbot⁶, D. Talukder⁷⁰, D. B. Tanner⁵, M. Tápai¹¹⁷, A. Taracchini³⁹, J. D. Tasson⁷², J. A. Taylor¹³⁷, R. Taylor¹, S. V. Tewari¹⁴⁸, T. Theeg¹⁰, F. Thies¹⁰, E. G. Thomas⁵⁹, M. Thomas⁷, P. Thomas⁴⁸, K. A. Thorne⁷, K. S. Thorne⁴⁹, E. Thrane⁶, S. Tiwari^{17,95}, V. Tiwari³⁷, K. V. Tokmakov⁶³, K. Toland⁴⁷, M. Tonelli^{23,24}, Z. Tornasi⁴⁷, A. Torres-Forné²⁵, C. I. Torrie¹, D. Töyrä⁵⁹, F. Travasso^{31,44}, G. Traylor⁷, J. Tringali⁵, M. C. Tringali^{95,110}, L. Trozzo^{24,157}, K. W. Tsang¹⁴, M. Tse¹⁵, R. Tso¹, L. Tsukada⁸², D. Tsuna⁸², D. Tuyenbayev¹⁰³, K. Ueno²¹, D. Ugolini¹⁵⁸, C. S. Unnikrishnan¹¹⁹, A. L. Urban¹, S. A. Usman³⁷, H. Vahlbruch²², G. Vajente¹, G. Valdes², N. van Bakel¹⁴, M. van Beuzekom¹⁴, J. F. J. van den Brand^{14,75}, C. Van Den Broeck^{14,159}, D. C. Vander-Hyde⁴⁵, L. van der Schaaf¹⁴, J. V. van Heijningen¹⁴, A. A. van Veggel⁴⁷, M. Vardaro^{54,55}, V. Varma⁴⁹, S. Vass¹, M. Vasúth⁵⁰, A. Vecchio⁵⁹, G. Vedovato⁵⁵, J. Veitch⁴⁷, P. J. Veitch⁷³, K. Venkateswara¹⁵¹, G. Venugopalan¹, D. Verkindt⁸, F. Vetrano^{121,122}, A. Viceré^{121,122}, A. D. Viets²¹, S. Vinciguerra⁵⁹, D. J. Vine²⁸, J.-Y. Vinet⁶⁷, S. Vitale¹⁵, T. Vo⁴⁵, H. Vocca^{43,44}, C. Vorvick⁴⁸, S. P. Vyatchanin⁶², A. R. Wade¹, L. E. Wade⁸⁵, M. Wade⁸⁵, R. Walet¹⁴, M. Walker³⁰, L. Wallace¹, S. Walsh^{10,21,39}, G. Wang^{17,122}, H. Wang⁵⁹, J. Z. Wang⁶⁴, W. H. Wang¹⁰³, Y. F. Wang⁹³, R. L. Ward²⁶, J. Warner⁴⁸, M. Was⁸, J. Watchi⁹⁸, B. Weaver⁴⁸, L.-W. Wei^{10,22}, M. Weinert¹⁰, A. J. Weinstein¹, R. Weiss¹⁵, L. Wen⁶⁵, E. K. Wessel¹², P. Weßels¹⁰, J. Westerweck¹⁰, T. Westphal¹⁰, K. Wette²⁶, J. T. Whelan⁵⁸, S. E. Whitcomb¹, B. F. Whiting⁵

C. Whittle⁶, D. Wilken¹⁰, D. Williams⁴⁷, R. D. Williams¹, A. R. Williamson⁶⁶, J. L. Willis^{1,160}, B. Willke^{10,22}, M. H. Wimmer¹⁰, W. Winkler¹⁰, C. C. Wipf¹, H. Wittel^{10,22}, G. Woan⁴⁷, J. Woehler¹⁰, J. Wofford⁵⁸, K. W. K. Wong⁹³, J. Worden⁴⁸, J. L. Wright⁴⁷, D. S. Wu¹⁰, D. M. Wysocki⁵⁸, S. Xiao¹, H. Yamamoto¹, C. C. Yancey⁷⁶, L. Yang¹⁶¹, M. J. Yap²⁶, M. Yazback⁵, Hang Yu¹⁵, Haocun Yu¹⁵, M. Yvert⁸, A. Zadrożny¹³², M. Zanolin³⁸, T. Zelenova³¹, J.-P. Zeng⁵⁵, M. Zevin⁸⁹, L. Zhang¹, M. Zhang¹⁴⁰, T. Zhang⁴⁷, Y.-H. Zhang⁵⁸, C. Zhao⁶⁵, M. Zhou⁸⁹, Z. Zhou⁸⁹, S. J. Zhu^{10,39}, X. J. Zhu⁶, A. B. Zimmerman⁹⁰, M. E. Zucker^{1,15}, J. Zweizig¹,

(LIGO Scientific Collaboration and Virgo Collaboration)

E. Burns⁸⁰, P. Veres¹⁶², D. Kocevski¹³⁷, J. Racusin⁸⁰, A. Goldstein¹⁶³, V. Connaughton¹⁶³, M. S. Briggs^{162,164}, L. Blackburn^{15,165}, R. Hamburg^{162,164}, C. M. Hui¹³⁷, A. von Kienlin¹⁶⁶, J. McEnery⁸⁰, R. D. Preece^{162,164}, C. A. Wilson-Hodge¹³⁷, E. Bissaldi^{167,168}, W. H. Cleveland¹⁶³, M. H. Gibby¹⁶⁹, M. M. Giles¹⁶⁹, R. M. Kippen¹⁷⁰, S. McBreen¹⁷¹, C. A. Meegan¹⁶², W. S. Paciesas¹⁶³, S. Poolakkil^{162,164}, O. J. Roberts¹⁶³, M. Stanbro¹⁶⁴,

(Fermi Gamma-ray Burst Monitor)

and

V. Savchenko¹⁷², C. Ferrigno¹⁷², E. Kuulkers¹⁷³, A. Bazzano¹⁷⁴, E. Bozzo¹⁷², S. Brandt¹⁷⁵, J. Chenevez¹⁷⁵, T. J.-L. Courvoisier¹⁷², R. Diehl¹⁶⁶, A. Domingo¹⁷⁶, L. Hanlon¹⁷⁷, E. Jourdain¹⁷⁸, P. Laurent^{40,179}, F. Lebrun¹⁸⁰, A. Lutovinov¹⁸¹, S. Mereghetti¹⁸², L. Natalucci¹⁷⁴, J. Rodi¹⁷⁴, J.-P. Roques¹⁷⁸, R. Sunyaev^{181,183}, and P. Ubertini¹⁷⁴

(INTEGRAL)

[†] Deceased, 2017 February.

[‡] Deceased, 2016 December.

¹ LIGO, California Institute of Technology, Pasadena, CA 91125, USA

² Louisiana State University, Baton Rouge, LA 70803, USA

³ Università di Salerno, Fisciano, I-84084 Salerno, Italy

⁴ INFN, Sezione di Napoli, Complesso Universitario di Monte S. Angelo, I-80126 Napoli, Italy

⁵ University of Florida, Gainesville, FL 32611, USA

⁶ OzGrav, School of Physics & Astronomy, Monash University, Clayton, VIC 3800, Australia

⁷ LIGO Livingston Observatory, Livingston, LA 70754, USA

⁸ Laboratoire d'Annecy-le-Vieux de Physique des Particules (LAPP), Université Savoie Mont Blanc, CNRS/IN2P3, F-74941 Annecy, France

⁹ University of Sannio at Benevento, I-82100 Benevento, Italy and INFN, Sezione di Napoli, I-80100 Napoli, Italy

¹⁰ Max Planck Institute for Gravitational Physics (Albert Einstein Institute), D-30167 Hannover, Germany

¹¹ The University of Mississippi, University, MS 38677, USA

¹² NCSA, University of Illinois at Urbana-Champaign, Urbana, IL 61801, USA

¹³ University of Cambridge, Cambridge CB2 1TN, UK

¹⁴ Nikhef, Science Park, 1098 XG Amsterdam, The Netherlands

¹⁵ LIGO, Massachusetts Institute of Technology, Cambridge, MA 02139, USA

¹⁶ Instituto Nacional de Pesquisas Espaciais, 12227-010 São José dos Campos, São Paulo, Brazil

¹⁷ Gran Sasso Science Institute (GSSI), I-67100 L'Aquila, Italy

¹⁸ INFN, Laboratori Nazionali del Gran Sasso, I-67100 Assergi, Italy

¹⁹ Inter-University Centre for Astronomy and Astrophysics, Pune 411007, India

²⁰ International Centre for Theoretical Sciences, Tata Institute of Fundamental Research, Bengaluru 560089, India

²¹ University of Wisconsin-Milwaukee, Milwaukee, WI 53201, USA

²² Leibniz Universität Hannover, D-30167 Hannover, Germany

²³ Università di Pisa, I-56127 Pisa, Italy

²⁴ INFN, Sezione di Pisa, I-56127 Pisa, Italy

²⁵ Departamento de Astronomía y Astrofísica, Universitat de València, E-46100 Burjassot, València, Spain

²⁶ OzGrav, Australian National University, Canberra, ACT 0200, Australia

²⁷ Laboratoire des Matériaux Avancés (LMA), CNRS/IN2P3, F-69622 Villeurbanne, France

²⁸ SUPA, University of the West of Scotland, Paisley PA1 2BE, UK

²⁹ LAL, Univ. Paris-Sud, CNRS/IN2P3, Université Paris-Saclay, F-91898 Orsay, France

³⁰ California State University Fullerton, Fullerton, CA 92831, USA

³¹ European Gravitational Observatory (EGO), I-56021 Cascina, Pisa, Italy

³² Chennai Mathematical Institute, Chennai 603103, India

³³ Università di Roma Tor Vergata, I-00133 Roma, Italy

³⁴ INFN, Sezione di Roma Tor Vergata, I-00133 Roma, Italy

³⁵ Universität Hamburg, D-22761 Hamburg, Germany

³⁶ INFN, Sezione di Roma, I-00185 Roma, Italy

³⁷ Cardiff University, Cardiff CF24 3AA, UK

³⁸ Embry-Riddle Aeronautical University, Prescott, AZ 86301, USA

³⁹ Max Planck Institute for Gravitational Physics (Albert Einstein Institute), D-14476 Potsdam-Golm, Germany

⁴⁰ APC, AstroParticule et Cosmologie, Université Paris Diderot, CNRS/IN2P3, CEA/Irfu, Observatoire de Paris, Sorbonne Paris Cité, F-75205 Paris Cedex 13, France

⁴¹ Korea Institute of Science and Technology Information, Daejeon 34141, Korea

⁴² West Virginia University, Morgantown, WV 26506, USA

⁴³ Università di Perugia, I-06123 Perugia, Italy

- ⁴⁴ INFN, Sezione di Perugia, I-06123 Perugia, Italy
⁴⁵ Syracuse University, Syracuse, NY 13244, USA
⁴⁶ University of Minnesota, Minneapolis, MN 55455, USA
⁴⁷ SUPA, University of Glasgow, Glasgow G12 8QQ, UK
⁴⁸ LIGO Hanford Observatory, Richland, WA 99352, USA
⁴⁹ Caltech CaRT, Pasadena, CA 91125, USA
⁵⁰ Wigner RCP, RMKI, H-1121 Budapest, Konkoly Thege Miklós út 29-33, Hungary
⁵¹ Columbia University, New York, NY 10027, USA
⁵² Stanford University, Stanford, CA 94305, USA
⁵³ Università di Camerino, Dipartimento di Fisica, I-62032 Camerino, Italy
⁵⁴ Università di Padova, Dipartimento di Fisica e Astronomia, I-35131 Padova, Italy
⁵⁵ INFN, Sezione di Padova, I-35131 Padova, Italy
⁵⁶ Institute of Physics, Eötvös University, Pázmány P. s. 1/A, Budapest 1117, Hungary
⁵⁷ Nicolaus Copernicus Astronomical Center, Polish Academy of Sciences, 00-716, Warsaw, Poland
⁵⁸ Rochester Institute of Technology, Rochester, NY 14623, USA
⁵⁹ University of Birmingham, Birmingham B15 2TT, UK
⁶⁰ INFN, Sezione di Genova, I-16146 Genova, Italy
⁶¹ RRCAT, Indore MP 452013, India
⁶² Faculty of Physics, Lomonosov Moscow State University, Moscow 119991, Russia
⁶³ SUPA, University of Strathclyde, Glasgow G1 1XQ, UK
⁶⁴ The Pennsylvania State University, University Park, PA 16802, USA
⁶⁵ OzGrav, University of Western Australia, Crawley, WA 6009, Australia
⁶⁶ Department of Astrophysics/IMAPP, Radboud University Nijmegen, P.O. Box 9010, 6500 GL Nijmegen, The Netherlands
⁶⁷ Artemis, Université Côte d'Azur, Observatoire Côte d'Azur, CNRS, CS 34229, F-06304 Nice Cedex 4, France
⁶⁸ Institut FOTON, CNRS, Université de Rennes 1, F-35042 Rennes, France
⁶⁹ Washington State University, Pullman, WA 99164, USA
⁷⁰ University of Oregon, Eugene, OR 97403, USA
⁷¹ Laboratoire Kastler Brossel, UPMC-Sorbonne Universités, CNRS, ENS-PSL Research University, Collège de France, F-75005 Paris, France
⁷² Carleton College, Northfield, MN 55057, USA
⁷³ OzGrav, University of Adelaide, Adelaide, SA 5005, Australia
⁷⁴ Astronomical Observatory Warsaw University, 00-478 Warsaw, Poland
⁷⁵ VU University Amsterdam, 1081 HV Amsterdam, The Netherlands
⁷⁶ University of Maryland, College Park, MD 20742, USA
⁷⁷ Center for Relativistic Astrophysics, Georgia Institute of Technology, Atlanta, GA 30332, USA
⁷⁸ Université Claude Bernard Lyon 1, F-69622 Villeurbanne, France
⁷⁹ Università di Napoli 'Federico II,' Complesso Universitario di Monte S. Angelo, I-80126 Napoli, Italy
⁸⁰ NASA Goddard Space Flight Center, Greenbelt, MD 20771, USA
⁸¹ Dipartimento di Fisica, Università degli Studi di Genova, I-16146 Genova, Italy
⁸² RESCEU, University of Tokyo, Tokyo, 113-0033, Japan
⁸³ Tsinghua University, Beijing 100084, China
⁸⁴ Texas Tech University, Lubbock, TX 79409, USA
⁸⁵ Kenyon College, Gambier, OH 43022, USA
⁸⁶ Museo Storico della Fisica e Centro Studi e Ricerche Enrico Fermi, I-00184 Roma, Italy
⁸⁷ National Tsing Hua University, Hsinchu City, 30013 Taiwan, Republic of China
⁸⁸ Charles Sturt University, Wagga Wagga, NSW 2678, Australia
⁸⁹ Center for Interdisciplinary Exploration & Research in Astrophysics (CIERA), Northwestern University, Evanston, IL 60208, USA
⁹⁰ Canadian Institute for Theoretical Astrophysics, University of Toronto, Toronto, ON M5S 3H8, Canada
⁹¹ University of Chicago, Chicago, IL 60637, USA
⁹² Pusan National University, Busan 46241, Korea
⁹³ The Chinese University of Hong Kong, Shatin, NT, Hong Kong
⁹⁴ INAF, Osservatorio Astronomico di Padova, I-35122 Padova, Italy
⁹⁵ INFN, Trento Institute for Fundamental Physics and Applications, I-38123 Povo, Trento, Italy
⁹⁶ OzGrav, University of Melbourne, Parkville, VIC 3010, Australia
⁹⁷ Università di Roma "La Sapienza," I-00185 Roma, Italy
⁹⁸ Université Libre de Bruxelles, Brussels B-1050, Belgium
⁹⁹ Sonoma State University, Rohnert Park, CA 94928, USA
¹⁰⁰ Departamento de Matemáticas, Universitat de València, E-46100 Burjassot, València, Spain
¹⁰¹ Montana State University, Bozeman, MT 59717, USA
¹⁰² Universitat de les Illes Balears, IAC3—IEEC, E-07122 Palma de Mallorca, Spain
¹⁰³ The University of Texas Rio Grande Valley, Brownsville, TX 78520, USA
¹⁰⁴ Bellevue College, Bellevue, WA 98007, USA
¹⁰⁵ Institute for Plasma Research, Bhat, Gandhinagar 382428, India
¹⁰⁶ The University of Sheffield, Sheffield S10 2TN, UK
¹⁰⁷ Dipartimento di Scienze Matematiche, Fisiche e Informatiche, Università di Parma, I-43124 Parma, Italy
¹⁰⁸ INFN, Sezione di Milano Bicocca, Gruppo Collegato di Parma, I-43124 Parma, Italy
¹⁰⁹ California State University, Los Angeles, 5151 State University Dr, Los Angeles, CA 90032, USA
¹¹⁰ Università di Trento, Dipartimento di Fisica, I-38123 Povo, Trento, Italy
¹¹¹ Montclair State University, Montclair, NJ 07043, USA
¹¹² National Astronomical Observatory of Japan, 2-21-1 Osawa, Mitaka, Tokyo 181-8588, Japan
¹¹³ Observatori Astronòmic, Universitat de València, E-46980 Paterna, València, Spain
¹¹⁴ School of Mathematics, University of Edinburgh, Edinburgh EH9 3FD, UK
¹¹⁵ University and Institute of Advanced Research, Koba Institutional Area, Gandhinagar Gujarat 382007, India
¹¹⁶ IISER-TVM, CET Campus, Trivandrum Kerala 695016, India
¹¹⁷ University of Szeged, Dóm tér 9, Szeged 6720, Hungary
¹¹⁸ University of Michigan, Ann Arbor, MI 48109, USA

- ¹¹⁹ Tata Institute of Fundamental Research, Mumbai 400005, India
- ¹²⁰ INAF, Osservatorio Astronomico di Capodimonte, I-80131 Napoli, Italy
- ¹²¹ Università degli Studi di Urbino “Carlo Bo,” I-61029 Urbino, Italy
- ¹²² INFN, Sezione di Firenze, I-50019 Sesto Fiorentino, Firenze, Italy
- ¹²³ Physik-Institut, University of Zurich, Winterthurerstrasse 190, 8057 Zurich, Switzerland
- ¹²⁴ American University, Washington, DC 20016, USA
- ¹²⁵ University of Białystok, 15-424 Białystok, Poland
- ¹²⁶ University of Southampton, Southampton SO17 1BJ, UK
- ¹²⁷ University of Washington Bothell, 18115 Campus Way NE, Bothell, WA 98011, USA
- ¹²⁸ Institute of Applied Physics, Nizhny Novgorod, 603950, Russia
- ¹²⁹ Korea Astronomy and Space Science Institute, Daejeon 34055, Korea
- ¹³⁰ Inje University Gimhae, South Gyeongsang 50834, Korea
- ¹³¹ National Institute for Mathematical Sciences, Daejeon 34047, Korea
- ¹³² NCBJ, 05-400 Świerk-Otwock, Poland
- ¹³³ Institute of Mathematics, Polish Academy of Sciences, 00656 Warsaw, Poland
- ¹³⁴ Hillsdale College, Hillsdale, MI 49242, USA
- ¹³⁵ Hanyang University, Seoul 04763, Korea
- ¹³⁶ Seoul National University, Seoul 08826, Korea
- ¹³⁷ NASA Marshall Space Flight Center, Huntsville, AL 35812, USA
- ¹³⁸ ESPCI, CNRS, F-75005 Paris, France
- ¹³⁹ Southern University and A&M College, Baton Rouge, LA 70813, USA
- ¹⁴⁰ College of William and Mary, Williamsburg, VA 23187, USA
- ¹⁴¹ Centre Scientifique de Monaco, 8 quai Antoine Ier, MC-98000, Monaco
- ¹⁴² Indian Institute of Technology Madras, Chennai 600036, India
- ¹⁴³ IISER-Kolkata, Mohanpur, West Bengal 741252, India
- ¹⁴⁴ Whitman College, 345 Boyer Avenue, Walla Walla, WA 99362, USA
- ¹⁴⁵ Indian Institute of Technology Bombay, Powai, Mumbai, Maharashtra 400076, India
- ¹⁴⁶ Scuola Normale Superiore, Piazza dei Cavalieri 7, I-56126 Pisa, Italy
- ¹⁴⁷ Université de Lyon, F-69361 Lyon, France
- ¹⁴⁸ Hobart and William Smith Colleges, Geneva, NY 14456, USA
- ¹⁴⁹ OzGrav, Swinburne University of Technology, Hawthorn VIC 3122, Australia
- ¹⁵⁰ Janusz Gil Institute of Astronomy, University of Zielona Góra, 65-265 Zielona Góra, Poland
- ¹⁵¹ University of Washington, Seattle, WA 98195, USA
- ¹⁵² King’s College London, University of London, London WC2R 2LS, UK
- ¹⁵³ Indian Institute of Technology, Gandhinagar Ahmedabad Gujarat 382424, India
- ¹⁵⁴ Indian Institute of Technology Hyderabad, Sangareddy, Khandi, Telangana 502285, India
- ¹⁵⁵ International Institute of Physics, Universidade Federal do Rio Grande do Norte, Natal RN 59078-970, Brazil
- ¹⁵⁶ Andrews University, Berrien Springs, MI 49104, USA
- ¹⁵⁷ Università di Siena, I-53100 Siena, Italy
- ¹⁵⁸ Trinity University, San Antonio, TX 78212, USA
- ¹⁵⁹ Van Swinderen Institute for Particle Physics and Gravity, University of Groningen, Nijenborgh 4, 9747 AG Groningen, The Netherlands
- ¹⁶⁰ Abilene Christian University, Abilene, TX 79699, USA
- ¹⁶¹ Colorado State University, Fort Collins, CO 80523, USA
- ¹⁶² Center for Space Plasma and Aeronomic Research, University of Alabama in Huntsville, 320 Sparkman Drive, Huntsville, AL 35899, USA
- ¹⁶³ Science and Technology Institute, Universities Space Research Association, Huntsville, AL 35805, USA
- ¹⁶⁴ Space Science Department, University of Alabama in Huntsville, 320 Sparkman Drive, Huntsville, AL 35899, USA
- ¹⁶⁵ Harvard-Smithsonian Center for Astrophysics, 60 Garden St, Cambridge, MA 02138, USA
- ¹⁶⁶ Max-Planck-Institut für extraterrestrische Physik, Giessenbachstrasse 1, D-85748 Garching, Germany
- ¹⁶⁷ Politecnico di Bari, Via Edoardo Orabona, 4, I-70126 Bari BA, Italy
- ¹⁶⁸ Istituto Nazionale di Fisica Nucleare, Sezione di Bari, I-70126 Bari, Italy
- ¹⁶⁹ Jacobs Technology, Inc., Huntsville, AL 35806, USA
- ¹⁷⁰ Los Alamos National Laboratory, PO Box 1663, Los Alamos, NM 87545, USA
- ¹⁷¹ School of Physics, University College Dublin, Belfield, Stillorgan Road, Dublin 4, Ireland
- ¹⁷² ISDC, Department of Astronomy, University of Geneva, Chemin d’Écogia, 16 CH-1290 Versoix, Switzerland
- ¹⁷³ European Space Research and Technology Centre (ESA/ESTEC), Keplerlaan 1, 2201 AZ Noordwijk, The Netherlands
- ¹⁷⁴ INAF-Institute for Space Astrophysics and Planetology, Via Fosso del Cavaliere 100, I-00133 Roma, Italy
- ¹⁷⁵ DTU Space—National Space Institute Elektrovej—Building 327 DK-2800 Kongens Lyngby Denmark
- ¹⁷⁶ Centro de Astrobiología (CAB-CSIC/INTA, ESAC Campus), Camino bajo del Castillo S/N, E-28692 Villanueva de la Cañada, Madrid, Spain
- ¹⁷⁷ Space Science Group, School of Physics, University College Dublin, Belfield, Dublin 4, Ireland
- ¹⁷⁸ IRAP, Université de Toulouse; CNRS; UPS; CNES; 9 Av. Roche, F-31028 Toulouse, France
- ¹⁷⁹ DSM/Irfu/Service d’Astrophysique, Bat. 709 Orme des Merisiers CEA Saclay, F-91191 Gif-sur-Yvette Cedex, France
- ¹⁸⁰ APC, AstroParticule et Cosmologie, Université Paris Diderot, CNRS/IN2P3, CEA/Irfu, Observatoire de Paris Sorbonne Paris Cité, France
- ¹⁸¹ Space Research Institute of Russian Academy of Sciences, Profsoyuznaya 84/32, 117997 Moscow, Russia
- ¹⁸² INAF, IASF-Milano, via E.Bassini 15, I-20133 Milano, Italy
- ¹⁸³ Max Planck Institute for Astrophysics, Karl-Schwarzschild-Str. 1, Garching b. Munchen D-85741, Germany